Parallel Algorithms for the Solution of Large-Scale Fluid-Structure Interaction Problems in Hemodynamics

PAR

Davide FORTI

acceptée sur proposition du jury:

Prof. F. Eisenbrand, président du jury
Prof. A. Quarteroni, Dr S. Deparis, directeurs de thèse
Prof. M. Gee, rapporteur
Prof. H. van Brummelen, rapporteur
Prof. J. Hesthaven, rapporteur

ÉCOLE POLYTECHNIQUE
FÉDÉRALE DE LAUSANNE

Suisse
2016

To my grandparents: Graziosa and Quinto

Acknowledgements

Abstract

This thesis addresses the development and implementation of efficient and parallel algorithms for the numerical simulation of Fluid-Structure Interaction (FSI) problems in hemodynamics. Indeed, hemodynamic conditions in large arteries are significantly affected by the interaction of the pulsatile blood flow with the arterial wall. The simulation of fluid-structure interaction problems requires the approximation of a coupled system of Partial Differential Equations (PDEs) and the set up of efficient numerical solution strategies.

Blood is modeled as an incompressible Newtonian fluid whose dynamics is governed by the Navier-Stokes equations. Different constituive models are used to describe the mechanical response of the arterial wall; specifically, we rely on hyperelastic isotropic and anistotropic material laws. The finite element method is used for the space discretization of both the fluid and structure problems. In particular, for the Navier-Stokes equations we consider a semi-discrete formulation based on the Variational Multiscale (VMS) method. Among a wide range of possible solution strategies for the FSI problem, here we focus on strongly coupled monolithic approaches wherein the nonlinearities are treated in a fully implicit mode. To cope with the high computational complexity of the three dimensional FSI problem, a parallel solution framework is often mandatory. To this end, we develop a new block parallel preconditioner for the coupled linearized FSI system obtained after space and time discretization. The proposed preconditioner, named FaCSI, exploits the factorized form of the FSI Jacobian matrix, the use of static condensation to formally eliminate the interface degrees of freedom of the fluid equations, and the use of a SIMPLE preconditioner for unsteady Navier-Stokes equations.

In FSI problems, the different resolution requirements in the fluid and structure physical domains, as well as the presence of complex interface geometries make the use of matching fluid and structure meshes problematic. In such situations, it is much simpler to deal with discretizations that are nonconforming at the interface, provided however that the matching conditions at the interface are properly fulfilled. In this thesis we develop a novel interpolation-based method, named INTERNODES, for numerically solving partial differential equations by Galerkin methods on computational domains that are split into

Résumé

Cette thèse aborde le développement et l'implémentation d'algorithmes parallèles pour des problèmes d'interaction fluide-structure (FSI) en écoulements sanguins. En effet, les conditions hémodynamiques dans les grandes artères sont fortement influencées par les interactions entre l'écoulement pulsatile et les parois artérielles. La simulation de problèmes d'interaction fluide-structure nécessite une approximation numérique d'un système couplé d'équations aux dérivées partielles (PDE) et la mise en place de schémas numériques efficaces.

Le sang est modélisé par un fluide Newtonien incompressible dont la dynamique est régie par les équations de Navier-Stokes. La réponse mécanique des parois artérielles est représentée par plusieurs modèles constitutifs ; en particulier, des modèles hyperélastiques, anisotropes et isotropes. La méthode des éléments finis est utilisée pour discrétiser en espace les domaines fluide et solide. Une formulation semi-discrète basée sur les multi-échelles variationnelles (VMS) est utilisée pour les équations de Navier-Stokes.

Parmi les différentes stratégies pour résoudre des problèmes d'interaction fluide-structure, ce travail présente des approches monolithiques où les non-linéarités sont traitées de manière implicite. La complexité des problèmes FSI tridimensionnels implique souvent l'adoption d'une structure de résolution parallélisée. C'est pourquoi un nouveau précon-ditionneur parallèle par bloc est developpé et appliqué au système d'équations linéarisées obtenu après une discrétisation en temps et en espace. Le préconditionneur proposé, nommé FaCSI, exploite la forme factorisée de la matrice jacobienne du système FSI, l'usage de condensation statique pour explicitement éliminer les degrés de liberté des équations fluides à l'interface et l'usage d'un préconditionneur SIMPLE pour les équations de Navier-Stokes instationnaires.

Dans les problèmes FSI, les différentes exigences en résolution dans les domaines fluides et solides et la complexité des géométries d'interface rendent le traitement du maillage difficile. Dans ces cas, il est plus simple d'utiliser des maillages non conformes tout en s'assurant que les conditions à l'interface soient satisfaites. Dans cette thèse, un nouvel outil basé sur l'interpolation est développé. Appellée INTERNODES, cette méthode permet de résoudre par des méthodes de Galerkin des PDE sur des domaines

computationels divisés en plusieurs sous-domaines aux interfaces non-conformes. Ceci signifie que des maillages et/ou des degrés de polynomes à priori indépendants peuvent être utilisés pour discrétiser chaque sous-domaine. INTERNODES peut être considérée comme un alternative à la méthode mortar : elle combine la justesse de ce dernier à une facilité d'implémentation dans un code numérique.

Mots clefs : interaction fluide-structure, simulation de la mécanique des fluides, algorithmes parallèles, calcul haute performance, méthode des éléments finis, maillages non conformes, biomécanique.

Contents

Contents

List of Figures

List of Tables

Introduction

In the last decades the interest for Fluid-Structure Interaction (FSI) problems has increased significantly. Generally we deal with fluid-structure interaction problem when the effect of fluid dynamics on elastic bodies and vice-versa is of primary interest. The simulation of various processes in engineering and nature requires the coupled solution of this type of multi-physical problems. Many examples of multi-field systems can be found in practice: aeroelastic instabilities in aircrafts, turbomachinery design, modeling of cardiovascular system and wind-sail dynamics, involve fluid-structure interaction phenomena whose analysis is crucial for an accurate and efficient design. The main aspects involved in this kind of problems is the unsteady computation of the dynamics of different physical domains (i.e. multi-physics) and their coupling across moving interface conditions.

The interaction between fluid and structure takes place at the *interface* separating the two media. The pressure and shear stress exerted by the fluid result in a force which acts on the part of the structural boundary which is in contact with the fluid. This force, in turn, may deform or simply move rigidly the structure. The deformations induced by the fluid to the solid may be quite significant or negligible, depending on the pressure and velocity of the flow field and also on the material properties of the solid itself. As a consequence of the solid deformation, the fluid domain deforms accordingly, leading to a change in the flow field. Specifically, the velocity and pressure fields of the fluid will change, and therefore we need to treat the problem using a bidirectional coupled multi-physics analysis: the fluid flow and pressure fields affect the structural deformations, and the structural deformations affect the flow and pressure. To summarize, the solution of fluid-structure interaction involves the integrated and *coupled* study of the underlying fluid and structure physical phenomena.

The *fluid* and the *structure* problems themselves have been studied separately for many years in great detail. For applications stemming from real-life problems, the coupled fluid-

structure interaction problem can not be solved analytically and so it has to be studied by means of experiments or by *numerical simulation.* In this thesis we focus on fluid-structure interaction problems arising in hemodynamics. The mechanics of an internal blood flow interacting with an elastic arterial wall can be modeled by a coupled nonlinear system of partial differential equations describing the fluid flow and the deformation of the wall structure together with suitable coupling conditions. The modeling, the discretization and the design of numerical schemes to solve efficiently the *coupled* FSI problem are still challenging tasks and major topic of ongoing research. Indeed, nowadays the modeling of the cardiovascular system is receiving increasing attention from both the medical and mathematical environments because of, from the one hand, the great influence of hemodynamics on cardiovascular diseases and, from the other hand, its challenging complexity that keeps open the debate about the setting up of appropriate models and algorithms. The numerical simulation of such complex system may provide detailed and quantitative information improving the understanding of the underlying complex physical phenomena, thus helping and supporting the development of more effective clinical treatments. For instance, stress distributions in walls of in vivo arteries (transmural stresses) are a major factor driving, e.g., the processes of arteriosclerosis and arteriogenesis which are well-known to have a major relevance on the human health. Realistic predictions of transmural stress distributions require a dynamic simulation of the interaction of the blood flow with the vessel wall (fluid-structure interaction). The computational simulation of atherosclerotic arteries is important for an optimization of medical treatment by reducing the number of animal tests.

The biological complexity of the cardiovascular system poses numerous challenges for its modeling, numerical discretization and simulation. For instance, the mathematical models of the constituents of the cardiovascular system such as the arterial wall and blood should be able to reproduce their most important physiological features and the biological interactions among them. In this work blood is modeled as Newtonian incompressible fluid, see e.g. [Bazilevs et al., 2009b, Formaggia et al., 2009, Küttler et al., 2010, Crosetto et al., 2011, Bazilevs et al., 2013b]. The modeling of the arterial tissue represents a challenging task since these materials behave almost incompressibly, undergo large strains, and are characterized by a strong anisotropy. In this thesis we consider different constituive models to describe the mechanical response of the arterial wall; specifically, we rely on hyperelastic isotropic and anistotropic material laws [Holzapfel and Gasser, 2001, Schröder et al., 2004, Schröder et al., 2005, Ogden and Holzapfel, 2006, Balzani et al., 2006b, Balzani et al., 2006a, Balzani et al., 2007a, Balzani, 2006, Tricerri, 2014, Balzani et al., 2015].

We model the behavior of the blood flow dynamics (fluid) and the mechanical deformation of the arterial wall (structure) by a set of partial differential equations together with suitable coupling conditions (interaction). At this level, a first distinction between the different methodologies comes from the choice of the frame of reference in which we formulate the problem. In fluid-structure interaction, a common choice consists in

2

describing the fluid equations using an Arbitrary Lagrangian-Eulerian (ALE) frame of reference, see e.g., [Souli et al., 2000, Nobile., 2001, Wall et al., 2006, Hron and Turek, 2006, Bazilevs et al., 2008, Formaggia et al., 2009, Gee et al., 2010, Küttler et al., 2010, Crosetto et al., 2011, Bazilevs et al., 2013b] in which one needs to introduce a new equation for the fluid domain motion. In addition, the dependence of the fluid computational domain on the solution of the FSI problem introduces a further nonlinearity. A different approach may consist in using a space-time formulation of the FSI problem. It involves a discretization of the computational domain in time slabs, and each solution in a time slab is then computed sequentially (see [Tezduyar and Sathe, 2007, Tezduyar et al., 2008, Takizawa and Tezduyar, 2011, Bazilevs et al., 2013b] for a complete overview on this formulation). Another approach would be to formulate the FSI problem in a fully Eulerian frame of reference [Cottet et al., 2008, Wang et al., 2008, Richter, 2013], i.e. on a fixed fluid domain, but it additionally requires one to keep track of the position of the fluid-structure interface. In [Dunne, 2007, Rannacher and Richter, 2010, Richter, 2010], a fully Eulerian formulation of FSI is used in two dimensions to avoid the degeneration of the ALE mapping and to facilitate mesh adaptivity. Another approach is the immersed boundary method, where the fluid is written in Eulerian coordinates, while the structure is still in a Lagrangian frame of reference [Peskin, 2002, Mittal and Iaccarino, 2005, Boffi et al., 2011]. A further alternative approach to ALE methods may be based on the use of the Extended Finite Element method (XFEM) [Gerstenberger and Wall, 2008, Wall et al., 2010, Mayer et al., 2010].

The use of an ALE formulation for the fluid, together with a Lagrangian frame for the structure, yields an FSI problem that is composed by three subproblems, namely the *fluid problem*, which allows for the computation of the velocity and pressure inside the fluid domain, the *solid problem*, which describes the deformation of the vessel wall, and the so-called *geometry problem*, which accounts for the change in time of the computational fluid domain. A peculiarity in biomechanics is the similar density of the fluid and the structure which, combined with incompressible flows, leads to increased numerical effort due to the well-known added-mass effect [Causin et al., 2005, Badia et al., 2008b, Van Brummelen, 2009, Van Brummelen, 2011]. For this reason many solution schemes have been devised for this type of coupled FSI problems. A modular approach to solve the FSI problem would consist in dealing with the three problems separately. For example, one can consider the fluid-structure coupled problem using different type of interface conditions (Dirichlet-Neumann [Le Tallec and Mouro, 2001, Matthies et al., 2006, Küttler and Wall, 2008b, Langer and Yang, 2012, Langer and Yang, 2015], Robin-Robin [Badia et al., 2008b, Badia et al., 2009, Nobile et al., 2014], Robin-Neumann [Fernández et al., 2015], Neumann-Neumann [Deparis et al., 2015c], FETI [Deparis et al., 2006b], etc. [Toselli and Widlund, 2005]) to ensure the coupling. A comparison of different coupling schemes for FSI problems in hemodynamics is carried out in [Küttler et al., 2010]. A further approach makes use of a Steklov-Poincaré formulation [Deparis et al., 2006a] to enforce the coupling on the fluid-structure interface. Furthermore, one can also solve the coupled

fluid-structure problem and, separately, the geometry one, therefore in two separate steps, as in the case of the so-called Geometry Convective Explicit (GCE) scheme [Badia et al., 2008a, Crosetto et al., 2011].

Extensive work has been carried out on the development of algorithms for the solution of time-dependent FSI problems in the framework of biomechanics. The approaches are typically categorized either as segregated or as monolithic schemes although the distinction is not always straightforward. Segregated schemes can range from simple, loosely coupled fixed point iterations to schemes which still use segregated solvers but apply a much stronger coupling. Monolithic schemes may include block preconditioners constructed from segregated solvers as well as preconditioners for the fully coupled problem which are not constructed from separate solvers. In monolithic schemes all the unknowns of the FSI problem are solved simultaneously. Monolithic algorithms were investigated, e.g., in [Michler et al., 2004, Hron and Turek, 2006, Bazilevs et al., 2008, Küttler et al., 2010, Gee et al., 2010, Barker and Cai, 2010, Wu and Cai, 2014, Crosetto et al., 2011, Grandperrin, 2013]. In [Deparis et al., 2015c], we have recently compared the performance of the strongly coupled Steklov-Poincaré algorithm using the Dirichlet-Neumann, Neumann-Dirichlet, and Neumann- Neumann preconditioners with a monolithic approach preconditioned by a Dirichlet-Neumann preconditioner.

The way the coupled set of equations describing the FSI phenomena are discretized in time induces further distinctions. One approach may consist in dealing with all the nonlinearities of the problem in an implicit mode, leading to the so-called Fully Implicit (FI) strategy [Fernández and Moubachir, 2003, Heil, 2004, Tezduyar et al., 2006, Dettmer and Perić, 2007, Bazilevs et al., 2008, Heil et al., 2008, Barker and Cai, 2010, Küttler et al., 2010, Gee et al., 2010, Wu and Cai, 2014]. Although this approach is the most stable, it is also the most expensive choice. A large variety of alternative time discretizations can be devised. For instance, a Convective Explicit time discretization is used in [Crosetto et al., 2011], in which the nonlinear convective term in the unsteady Navier-Stokes equations is treated using a semi-implicit approach. Further, a Geometry-Convective Explicit discretization is proposed in [Badia et al., 2008b] wherein the moving geometry is taken at the previous time step and the convective term is treated semi-implicitly. A possible approach to deal with the nonlinearity makes use of the Aitken accelerated fixed point algorithm, see e.g. [Le Tallec and Mouro, 2001, Causin et al., 2005, Küttler and Wall, 2008a, Küttler and Wall, 2008b, Badia et al., 2008b, Deparis et al., 2006a, Matthies et al., 2006]. In this way each fixed point iteration requires one residual evaluation. Otherwise the time discretized problem can be linearized via the Newton method, either considering the full Jacobian matrix, as in [Gee et al., 2010, Fernández and Moubachir, 2003, Tezduyar et al., 2006, Grandperrin, 2013], or neglecting some of its contributions, as in [Gerbeau and Vidrascu, 2003, Degroote et al., 2009, Heil, 2004]. We notice that the FSI Jacobian matrix is often available only as matrix-vector multiplication. In these cases a matrix-free method like GMRES may be employed to solve exactly the linearized system. Each nonlinear Newton iteration requires a solve of the linearized subproblems.

4

Thus the cost of each nonlinear iteration corresponds to the cost of one residual evaluation plus a variable number of solutions of the linearized subproblems.

After spatial and time discretization, one of the key aspects which characterizes the different methodologies is the choice of the preconditioner. For instance, relying on monolithic schemes, one may use block preconditioners built upon physic-specific solvers as well as preconditioners for the fully coupled problem which are not constructed from separate solvers. Several strategies have been proposed in literature, see e.g., [Heil, 2004, Badia et al., 2008b, Badia et al., 2008c, Gee et al., 2010, Barker and Cai, 2010, Crosetto et al., 2011, Grandperrin, 2013, Wu and Cai, 2014]. Overlapping Schwarz methods within monolithic approaches were studied in different regimes of severity of the added-mass effect in [Crosetto et al., 2011] confirming successful results for 2D obtained already reported in [Barker and Cai, 2010]. A monolithic FSI approach coupling nonlinear hyperelastic solid models with Navier-Stokes equations is presented in [Hron and Turek, 2006], considering the incompressible case for the solid. A block preconditioner with Schur complements for the monolithic system is presented in [Janssen and Wick, 2010]. A scalable monolithic solver for an FSI problem coupling blood flow with a conforming arterial wall in two dimensions is presented in [Barker, 2009, Barker and Cai, 2010]. There, a Newton scheme with an explicitly computed Jacobian is applied; see also [Fernández and Moubachir, 2003, Bazilevs et al., 2008, Barker and Cai, 2010]. For the solution of the FSI linearized systems, in [Barker and Cai, 2010] the authors use a hybrid multilevel Schwarz preconditioner which uses restricted additive Schwarz on the fine level and multiplicative Schwarz on the coarse level. The parallel Newton-Krylov-Schwarz approach for the monolithic system is extended to three dimensions in [Wu and Cai, 2014], and scalability is shown for up to three thousand processors. Parallel algebraic multigrid preconditioners have recently been applied to fully monolithic ALE formulations of FSI problems in the setting of biomechanics, see, e.g., [Gee et al., 2010, Wiesner, 2015]. Specifically, in [Gee et al., 2010], the authors propose two preconditioners that apply algebraic multigrid techniques to the linearized monolithic FSI system obtained after spatial and time discretizations.

Typically, solution algorithms for fluid-structure interaction problems are derived with the assumption of conforming fluid-structure discretizations at their interface separating the two computational domains. However, due to the different resolution requirements in the fluid and structure physical domains, as well as the presence of complex interface geometries make the use of matching fluid and structure meshes problematic. In these situations, it would be much simpler to deal with discretizations that are nonconforming, provided however that the coupling conditions at the interface are properly enforced. The mortar element method is a well known and mature technique commonly used to deal with nonconforming discretizations. It has been originally introduced in the context of nonoverlapping domain partitions [Bernardi et al., 1993, Bernardi et al., 1994]. In the mortar element method the interface coupling conditions are enforced in a variational mode. The mortar element method has been already used not only in

the context of nonconforming fluid-structure interaction problems, see e.g. [Baaijens, 2001, Gerstenberger and Wall, 2008, Klöppel et al., 2011, Mayr et al., 2015, Mayer et al., 2010], but also in other challenging engineering applications, such as contact problems [Wohlmuth and Krause, 2003, Popp et al., 2009, Popp et al., 2010, Laursen et al., 2012]. In the context of nonconforming fluid-structure interaction problems, in [Popp et al., 2010] the authors make use of a dual mortar method [Wohlmuth, 2000, Puso, 2004, Lamichhane et al., 2005] with discrete Lagrange multipliers that are constructed based on a biorthogonality relation with the primal shape functions at the fluid–structure interface. Besides the mortar element method, other coupling strategies have been proposed in the framework of partitioned solution schemes for fluid-structure interaction problems, see [Farhat et al., 1998, Cho et al., 2005, De Boer et al., 2007] and references therein.

Outline of the thesis and main contributions

In this thesis we focus on the development and implementation of efficient and parallel algorithms for the numerical simulation of Fluid-Structure Interaction. We model blood as an incompressible Newtonian fluid whose dynamics is governed by the Navier-Stokes equations. Hyperelastic isotropic and anistotropic material laws are used to describe the mechanical response of the arterial wall. We use the finite element method for the spatial discretization of both the fluid and structure problems. In particular, for the Navier-Stokes equations we consider a semi-discrete formulation based on the Variational Multiscale (VMS) method. Among a wide range of possible solution strategies for the FSI problem, here we focus on strongly coupled monolithic approaches wherein all the nonlinearities of the coupled problem are treated fully-implicitly. Since the spatial discretization of the problem by finite elements may lead easily to very large linear systems of equations with several millions of degrees of freedom in three dimensions within realistic applications, we also move forward towards the development of parallel scalable preconditioners and solvers bringing the fully nonlinear fluid-structure interaction to high performance computing machines. To this end, we develop a new block parallel preconditioner, called FaCSI, for the coupled linearized FSI system obtained after space and time discretization. The proposed preconditioner uses static condensation to formally eliminate the interface degrees of freedom of the fluid equations, and a SIMPLE preconditioner for the unsteady Navier-Stokes equations. Further, to deal with fluid-structure discretizations that are nonconforming at the interface, in this thesis we develop a novel interpolation-based method, named INTERNODES, for numerically solving partial differential equations by Galerkin methods on computational domains that are split into two (or several) subdomains featuring nonconforming interfaces. INTERNODES can be regarded as an alternative to the mortar element method which combines the accuracy of the latter with an easier implementation in a numerical code. All these methods will be instrumental to an efficient parallel numerical solution of several large-scale complex problems in

hemodynamics on high performance computing machines.

This thesis is structured in two parts and six chapters. In Part I, after describing the models for the blood (the fluid) and the vessel wall (the structure), we focus on the set up and efficient numerical solution of fluid-structure interaction problems in which conforming discretizations are adopted at the fluid-structure interface. In Part II we focus on the nonconforming case, i.e. the fluid and structure dicretizations do not match at their interface.

We report below an outline of this thesis, highlighting its original contributions.

Chapter 1: the focus of this Chapter is to describe the fluid model adopted in this work. We address an efficient semi-implicit time discretization of the Navier-Stokes equations with Variational Multiscale-Large Eddy Simulation modeling. Furthermore, we develop a parallel solver based on the GMRES method preconditioned by an algebraic multigrid preconditioner. We validate the methodology developed by simulating fluid flow past a squared cylinder obstacle. We compare the performance and the results obtained by the semi-implicit approach with those generated by a fully implicit one simulating the transitional blood flow in a patient-specific healthy Aorta geometry.

Chapter 2: in this Chapter we address the mechanical modeling of the arterial tissue for large sized arteries. We start by recalling the main concepts necessary to write the equation of motion for a continuous media. Then, we address the description of isotropic linear elastic as well as a more sophisticated nonlinear anisotropic hyperelastic material model. This Chapter mainly serves the purpose of setting up the fluid-structure interaction problem carried out in the Chapter 3.

Chapter 3: here we deal with the modeling, discretization and efficient numerical solution of fluid-structure interaction problems. We propose a new block preconditioner called FaCSI for FSI simulations. We analyze the strong and weak scalability properties of FaCSI on the solution of FSI in a benchmark cylindrical configuration and on a realistic large-scale problem of hemodynamics. Furthermore, we show that FaCSI compares successfully with state of the art preconditioners for FSI.

Chapter 4: we describe a benchmark problem which aims at mimicking blood flow in idealized coronary arteries. We address precise simulation settings for the set up of an easily reproducible test which is still able to capture all the numerical difficulties arising in realistic simulations. We provide measures that may be useful for comparisons with future simulations, experiments or for code validation. Different material models are studied, including anisotropic and viscoelastic ones at finite strains. This Chapter concludes the first part of this thesis.

Chapter 5: we propose a novel interpolation based method called INTERNODES for the numerical solution of partial differential equations on domains decomposed into two

(or several) subdomains featuring nonconforming interfaces. We extensively investigate the convergence properties of INTERNODES by solving numerically an elliptic problem in which the subdomains were discretized by non-conforming Galerkin methods. We carry out comparative study with the mortar method and we show that the orders of convergence obtained by INTERNODES compare successfully with those generated by mortar.

Chapter 6: we addressed the numerical solution of FSI problems in which nonconforming discretizations are used at the interface separating the computational domain of the fluid from the one of the structure. To deal with nonconforming fluid-structure discretizations we use INTERNODES. We numerically solve the pressure wave propagation through an elastic tube and we simulate the blood flow through a patient specific femoropopliteal bypass.

All the numerical methods described in this thesis have been implemented by the author in the open-source finite element library LifeV (www.lifev.org).

This thesis contains results which have been already published in journal articles or have been submitted for publication in a similar form. Chapter 1 is based upon a joint work with L. Dedè which has already been published in [Forti and Dedè, 2015]. Chapter 2 is partially based upon a joint work with D. Balzani, S. Deparis, S. Fausten, A. Heinlein, A. Klawonn, A. Quarteroni, O. Rheinbach, and J. Schröder which has already been published in [Balzani et al., 2015]. Chapter 3 is mainly based upon a joint work with S. Deparis, G. Grandperrin and A. Quarteroni available as submitted pre-print in [Deparis et al., 2015b] and partially on a joint work with S. Deparis, A. Heinlein, A. Klawonn, A. Quarteroni and O. Rheinbach published in [Deparis et al., 2015c]. Chapter 4 is based on the numerical results published in [Balzani et al., 2015]. The numerical method presented in Chapter 5 is based on a joint work with S. Deparis, P. Gervasio and A. Quarteroni available as submitted pre-print in [Deparis et al., 2015a]; in addition, Chapter 5 is also partially based on the published paper [Deparis et al., 2014a]. Finally, a small part of Chapter 6 have been already presented in [Deparis et al., 2015d] and accepted for publication. The whole presentation, however, is original.

The conforming case Part I

1 Variational Multiscale method for Navier–Stokes equations

In this Chapter, we focus on the description of the fluid model adopted in this thesis, its numerical approximation and efficient solution in a parallel computing framework. The fluid dynamics is described by the Navier–Stokes equations (for an incompressible and Newtonian fluid) with Variational Multiscale method. The time discretization is carried out by Backward Differentiation Formulas (BDF) while in space we use the finite element method. The nonlinearities of the problem are treated using either a semi–implicit approach for which we linearize the nonlinear terms by Newton–Gregory backward polynomials, or in a fully–implicit fashion. The resulting linear system is then solved by the GMRES method preconditioned by a right multigrid preconditioner.

The contents of this Chapter, with the exception of subsection 1.6.2, have been already published in [Forti and Dedè, 2015].

1.1 Preliminaries

In this Chapter, the description of the fluid model adopted in this work, its discretization and efficient numerical solution in a parallel setting are addressed. We focus our attention on cardiovascular flows, more specifically on flows in large sized arteries in which we model the blood flow dynamics by the Navier–Stokes equations for Newtonian incompressible fluids. Rigorously speaking blood is a suspension of particles in the plasma, the latter being made of water rather than a fluid. Nevertheless, despite the complexity of the blood rheology [Robertson et al., 2009], at the scale of large arteries, a Newtonian incompressible fluid is a suitable model for blood [Formaggia et al., 2009].

Nowadays, the accurate and efficient simulation of fluid dynamics problems still represents a major challenge, even in a High Performance Computing (HPC) framework. The Direct Numerical Simulation (DNS) of fluid flows requires the full representation of the whole range of spatial and temporal scales at the discrete level [Kim et al., 1987, Moser et al., 1999, Pope, 2000]; as consequence, even for moderate Reynolds numbers, the DNS may be unfeasible for several problems of practical interest. Conversely, the study of flows by Large Eddy Simulation (LES) approaches [Nicoud and Ducros, 1999, Pope, 2000, Sagaut, 2006], only the "large" scales of the flow field are fully represented and resolved at the discrete level, while the effect of the "small" unresolved scales is taken into account by means of suitable models based on the resolved scales, thus making the computational costs more affordable; among the others, examples of established LES models there are the Smagorinsky [Smagorinsky, 1963] and dynamic Smagorinsky [Germano et al., 1991, Lilly, 1992] models.

Variational Multiscale (VMS) approximations of for the Navier-Stokes equations has been introduced in [Hughes et al., 2000, Hughes, 1995, Hughes et al., 2004] and further extended in [Hughes et al., 2001a, Hughes et al., 2001b]; since then, the so called VMS method has been widely developed and used for the numerical simulation of flows in several benchmarking and applicative contexts [Akkerman et al., 2008, Bazilevs et al., 2007, Bazilevs et al., 2009a, Bazilevs et al., 2013b, Colomés et al., 2015, Gravemeier et al., 2010, Koobus and Farhat, 2004, Hsu et al., 2010, Hughes et al., 2005]. Indeed, VMS is a flexible approach since it provides a unified framework for the definition of spatial approximation schemes which are stable, capable of controlling the numerical instabilities arising in the convective dominated regimes at high Reynolds number, and also adequate to represent the turbulence LES modeling.

The layout of the Chapter is the following: in Section 1.2 and 1.3 after recalling the Navier–Stokes equations and the VMS method, we introduce the spatial discretization of the coarse scale velocity and pressure fields by means of the finite element method. In Section 1.4, we focus on the time discretization of the problem by means of BDF formulas. Then, in Section 1.5, we describe the parallel solver developed for the fully discrete problem, as well as the multigrid preconditioner used. Numerical results are reported in Section 1.6: after validating our solver by solving the well known square cylinder benchmark problem [Koobus and Farhat, 2004], we address the blood flow dynamics in a patient specific aorta.

1.2   The Navier–Stokes equations for incompressible fluids

Let $\Omega^f \subset \mathbb{R}^d$, $d \geq 2$, be the spatial fluid domain with piecewise smooth boundary $\Gamma \equiv \partial \Omega^f$; we denote with Γ_D the subset of Γ where the essential (Dirichlet) boundary conditions are applied, while natural (Neumann) boundary conditions will be considered

on $\Gamma_N = \Gamma \backslash \Gamma_D$. The Navier–Stokes equations for an incompressible fluid read:

$$
\begin{aligned}
\rho_f \frac{\partial \mathbf{u}_f}{\partial t} + \rho_f \mathbf{u}_f \cdot \nabla \mathbf{u}_f - \nabla \cdot \boldsymbol{\sigma}_f(\mathbf{u}_f, p_f) &= \boldsymbol{f} && \text{in } \Omega^f \times (0, T), && (1.1) \\
\nabla \cdot \mathbf{u}_f &= 0 && \text{in } \Omega^f \times (0, T), && (1.2) \\
\mathbf{u}_f &= \mathbf{g} && \text{on } \Gamma_D \times (0, T), && (1.3) \\
\boldsymbol{\sigma}_f(\mathbf{u}_f, p_f) \hat{\mathbf{n}} &= \mathbf{h} && \text{on } \Gamma_N \times (0, T), && (1.4) \\
\mathbf{u}_f(0) &= \mathbf{u}_{f_0} && \text{in } \Omega^f \times \{0\}, && (1.5)
\end{aligned}
$$

where the dependent variables $\mathbf{u}_f$ and p indicate the velocity and the pressure of the fluid, respectively, ρ_f is the fluid density, $\boldsymbol{f}$ is the vector of external forces, $\hat{\mathbf{n}}$ is the outward directed unit normal vector to Γ_N, and $\boldsymbol{\sigma}_f$ is the stress tensor defined, for a Newtonian fluid, as:

$$
\boldsymbol{\sigma}_f(\mathbf{u}_f, p) = -p\mathbf{I} + 2\mu_f \boldsymbol{\epsilon}_f(\mathbf{u}_f). \tag{1.6}
$$

We denoted by μ the dynamic viscosity of the fluid and by $\mathbf{I}$ the second order identity tensor, while $\boldsymbol{\epsilon}_f(\mathbf{u}_f)$ is the strain tensor:

$$
\boldsymbol{\epsilon}_f(\mathbf{u}_f) = \frac{1}{2}(\nabla \mathbf{u}_f + (\nabla \mathbf{u}_f)^T). \tag{1.7}
$$

The functions $\mathbf{g}$ and $\mathbf{h}$ indicate the Dirichlet and Neumann data, respectively, while $\mathbf{u}_0$ is the initial data. We recall that Eqs. (1.1)–(1.5) represent the balance of momentum in convective form, the mass conservation, the essential and natural boundary conditions, and the initial condition on the velocity, respectively. In view of the spatial approximation of the Navier–Stokes equations, we introduce the infinite dimensional function spaces

$$
\begin{aligned}
\mathcal{V}_{\mathbf{g}} &= \{\mathbf{u}_f \in \left[H^1(\Omega^f) \right]^d : \mathbf{u}_f|_{\Gamma_D} = \mathbf{g}\}, \\
\mathcal{V}_{\mathbf{0}} &= \{\mathbf{u}_f \in \left[H^1(\Omega^f) \right]^d : \mathbf{u}_f|_{\Gamma_D} = \mathbf{0}\}, \\
\mathcal{Q} &= L^2(\Omega^f).
\end{aligned}
$$

In addition, we define the function spaces $\boldsymbol{\mathcal{V}}_{\mathbf{g}} = \mathcal{V}_{\mathbf{g}} \times \mathcal{Q}$ and $\boldsymbol{\mathcal{V}}_{\mathbf{0}} = \mathcal{V}_{\mathbf{0}} \times \mathcal{Q}$. Then, the weak formulation of the Navier–Stokes equations reads, for all $t \in (0, T)$:

find $\boldsymbol{U} = \boldsymbol{U}(t) = \{\mathbf{u}_f, p_f\} \in \boldsymbol{\mathcal{V}}_{\mathbf{g}}$:
$$
\left(\boldsymbol{w}, \rho_f \frac{\partial \mathbf{u}_f}{\partial t} \right) + (\boldsymbol{w}, \rho_f \mathbf{u}_f \cdot \nabla \mathbf{u}_f) + (\nabla \boldsymbol{w}, \mu_f(\nabla \mathbf{u}_f + \nabla \mathbf{u}_f^T)) - (\nabla \cdot \boldsymbol{w}, p_f) + (q, \nabla \cdot \mathbf{u}_f)
$$
$$
= (\boldsymbol{w}, \boldsymbol{f}) + (\boldsymbol{w}, \mathbf{h})_{\Gamma_N} \qquad \text{for all } \boldsymbol{W} = \{\boldsymbol{w}, q\} \in \boldsymbol{\mathcal{V}}_{\mathbf{0}},
$$

$$
(1.8)
$$

where $\mathbf{u}_f(0) = \mathbf{u}_{f_0}$; $(\cdot, \cdot)$ denotes the standard L^2 inner product with respect to the spatial domain Ω^f and $(\cdot, \cdot)_{\Gamma_N}$ the one on Γ_N.

We remark that, in certain circumstances, the solution of the Navier-Stokes equations may develop instabilities. Without entering into details, it is well known that the responsible is the dynamics induced by the non-linear convection term $\rho_f \mathbf{u}_f \cdot \nabla \mathbf{u}_f$. To measure the importance of this term compared with the diffusive part $\mu_f(\nabla \cdot (\nabla \mathbf{u}_f + \nabla \mathbf{u}_f{}^T))$ we use the Reynolds number

$$Re = \frac{\rho_f L U}{\mu_f}, \tag{1.9}$$

where L and U denote a characteristic length of the domain and velocity of the flow, respectively. If the Reynolds number is small the flow remains stable, and is called laminar. For Reynolds numbers in the range 1'000-3'000 the flow is in a transitional regime, while for Reynolds values greater than 3'000 the flow becomes turbulent and the dynamics is dominated by the nonlinear convective term.

Along the arterial tree, typical values of the Reynolds number range from 1 to 3'000 a part from the Aorta wherein during the systolic phase of the heart cycle it may reach values of approximately 4'500 [Formaggia et al., 2009]. Under normal physiological conditions, the values of the Reynolds number in the cardiovascular system do not allow for the formation of full scale turbulence. Some flow instabilities may occur at the exit of the aortic valve and are limited to the systolic phase. In this region, the Reynolds number may reach the value of few thousands only during the peak of the systole; nevertheless, there is not enough time for a full turbulent flow to develop. For example, in [Ku, 1997] the peak Reynolds number in a human Aorta has been measured to be approximately 4'000. Several factors may induce transition from laminar to turbulent flows: for instance, the increase of flow velocity because of physical exercise, or due to the presence of a stenotic artery or a prosthetic implant may produce an increase of the local Reynolds number and eventually lead to localised turbulence.

1.3   Spatial approximation: Finite Elements and VMS modeling

We consider the Variational Multiscale (VMS) [Hughes et al., 2004, Bazilevs et al., 2007] method applied to the standard weak form of the Navier–Stokes equations (1.8). The VMS method introduces an a priori decomposition of the solution into coarse and fine scales. Accordingly, the weak formulation of the Navier–Stokes equations (1.8) is split into coarse and fine scale subproblems. At the numerical level, the coarse scale solution is identified with the numerical approximation given by the finite element method, while the fine scale component needs to be modeled. We remark that the fine scale components of

the solution are often modeled analytically (in closed form), written in terms depending both on the data of the problem and the coarse scale solution, and finally substituted in the coarse scale subproblem. In virtue of a projection of the fine scale solution into the coarse one, a finite dimensional system for the coarse scale component of the solution is obtained.

Let us introduce at this point a suitable finite element discretization, specifically with piecewise Lagrange polynomials of degree $r \geq 1$ over the computational domain Ω^f that is triangulated with a mesh $\mathcal{T}_h$ of tetrahedrons. In this respect, we indicate with $X_h^r := \left\{ v_h \in C^0(\overline{\Omega}^f) \; : \; v^h|_K \in \mathbb{P}_r, \text{ for all } K \in \mathcal{T}_h \right\}$ the function space of finite element and with h_K the diameter of the mesh element $K \in \mathcal{T}_h$.

We consider a multiscale direct–sum decomposition of a general function space $\boldsymbol{\mathcal{V}}$, which can be interpreted either as $\boldsymbol{\mathcal{V}}_{\mathbf{g}}$ or $\boldsymbol{\mathcal{V}}_{\mathbf{0}}$, into the coarse and fine scales subspaces as:

$$\boldsymbol{\mathcal{V}} = \boldsymbol{\mathcal{V}}_h \oplus \boldsymbol{\mathcal{V}}', \tag{1.10}$$

where $\boldsymbol{\mathcal{V}}_h$ is the coarse scale function space associated to the finite element discretization and $\boldsymbol{\mathcal{V}}'$ is an infinite dimensional function space representing the fine scales not directly represented in the discretization. More specifically, we have $\boldsymbol{\mathcal{V}}_h = \boldsymbol{\mathcal{V}}_{h\mathbf{g}} \times \mathcal{Q}_h$ or $\boldsymbol{\mathcal{V}}_h = \boldsymbol{\mathcal{V}}_{h\mathbf{0}} \times \mathcal{Q}_h$, with $\boldsymbol{\mathcal{V}}_{h\mathbf{g}} := \boldsymbol{\mathcal{V}}_{\mathbf{g}} \cap [X_h^{r_u}]^d$, $\boldsymbol{\mathcal{V}}_{h\mathbf{0}} := \boldsymbol{\mathcal{V}}_{\mathbf{0}} \cap [X_h^{r_u}]^d$, and $\mathcal{Q}_h := \mathcal{Q} \cap X_h^{r_p}$. Then, we have from Eq. (1.10) the following decompositions:

$$\boldsymbol{w} = \boldsymbol{w}_h + \boldsymbol{w}', \tag{1.11}$$

$$q = q_h + q', \tag{1.12}$$

$$\mathbf{u}_f = \mathbf{u}_{fh} + \mathbf{u}_f', \tag{1.13}$$

$$p_f = p_{fh} + p_f'. \tag{1.14}$$

We follow the approach proposed in [Bazilevs et al., 2007], for which we decompose Eq. (1.8) into coarse and fine scale equations, we integrate by parts the fine scale terms appearing into the coarse scale equations, and finally we model the fine scale velocity and pressure variables on every $K \in \mathcal{T}_h$ as ([Bazilevs et al., 2007]):

$$\mathbf{u}_f' \simeq -\tau_M(\mathbf{u}_{fh}) \, \boldsymbol{r}_M(\mathbf{u}_{fh}, p_{fh}), \tag{1.15}$$

$$p_f' \simeq -\tau_C(\mathbf{u}_{fh}) \, r_C(\mathbf{u}_{fh}), \tag{1.16}$$

where $\boldsymbol{r}_M(\mathbf{u}_{fh}, p_{fh})$ and $r_C(\mathbf{u}_{fh})$ indicate the residuals (in strong form) of the momentum

and continuity equations, respectively:

$$
\boldsymbol{r}_M(\mathbf{u}_{fh}, p_{fh}) \;=\; \rho_f \frac{\partial \mathbf{u}_{fh}}{\partial t} + \rho_f \mathbf{u}_{fh} \cdot \nabla \mathbf{u}_{fh} + \nabla p_{fh} - \mu_f \Delta \mathbf{u}_{fh} - \boldsymbol{f}, \tag{1.17}
$$

$$
\boldsymbol{r}_C(\mathbf{u}_{fh}) \;=\; \nabla \cdot \mathbf{u}_{fh}, \tag{1.18}
$$

respectively. Moreover, τ_M and τ_C are the stabilization parameters, which on every $K \in \mathcal{T}_h$ we choose similarly to [Bazilevs et al., 2007] as:

$$
\tau_M = \tau_M(\mathbf{u}_{fh}) \;=\; \left(\frac{\sigma^2 \rho_f^2}{\Delta t^2} + \frac{\rho_f^2}{h_K^2} |\mathbf{u}_{fh}|^2 + \frac{\mu_f^2}{h_K^4} C_r \right)^{-1/2}, \tag{1.19}
$$

$$
\tau_C = \tau_C(\mathbf{u}_{fh}) \;=\; \frac{h_K^2}{\tau_M(\mathbf{u}_{fh})}, \tag{1.20}
$$

where $C_r = 60 \cdot 2^{r_u - 2}$ is a constant obtained by an inverse inequality relation [Quarteroni and Valli, 1994], σ is a constant equal to the order of the time discretization chosen and Δt is the time step. We remark that the expression chosen for the stabilization parameter τ_M does not account for the projection of the advective and diffusive terms onto the characteristic sizes of the mesh element along the Cartesian components as e.g. in [Bazilevs et al., 2007, Hsu et al., 2010, Tezduyar and Sathe, 2003], but rather it is "averaged" for simplicity over the mesh element.

Finally, the semi–discrete variational multiscale formulation of the Navier–Stokes equations written in terms of the weak residual reads, for all $t \in (0, T)$:

$$
\begin{aligned}
&\text{find } \boldsymbol{U}_h = \boldsymbol{U}_h(t) = \{\mathbf{u}_{fh}, p_{fh}\} \in \boldsymbol{\mathcal{V}}_{h\mathbf{g}} \;: \\
&\qquad\qquad A(\boldsymbol{W}_h, \boldsymbol{U}_h) - F(\boldsymbol{W}_h) \;=\; 0 \text{ for all } \boldsymbol{W}_h = \{\boldsymbol{w}_h, q_h\} \in \boldsymbol{\mathcal{V}}_{h\mathbf{0}},
\end{aligned}
$$

with $\mathbf{u}_{fh}(0) = \mathbf{u}_{fh}^0$, where:

$$
A(\boldsymbol{W}_h, \boldsymbol{U}_h) \;=\; A^{NS}(\boldsymbol{W}_h, \boldsymbol{U}_h) + A^{VMS}(\boldsymbol{W}_h, \boldsymbol{U}_h), \tag{1.21}
$$

$$
F(\boldsymbol{W}_h) \;=\; (\boldsymbol{w}_h, \boldsymbol{f}) + (\boldsymbol{w}_h, \mathbf{h})_{\Gamma_N}, \tag{1.22}
$$

with:

$$
\begin{aligned}
A^{NS}(\boldsymbol{W}_h, \boldsymbol{U}_h) \;=\; & \left(\boldsymbol{w}_h, \rho_f \frac{\partial \mathbf{u}_{fh}}{\partial t} \right) + \left(\boldsymbol{w}_h, \rho_f \mathbf{u}_{fh} \cdot \nabla \mathbf{u}_{fh} \right) \\
& + \left(\nabla \boldsymbol{w}_h, \mu_f (\nabla \mathbf{u}_{fh} + (\nabla \mathbf{u}_{fh})^T) \right) - (\nabla \cdot \boldsymbol{w}_h, p_{fh}) + (q_h, \nabla \cdot \mathbf{u}_{fh}),
\end{aligned} \tag{1.23}
$$

and

$$
\begin{aligned}
A^{VMS}(\boldsymbol{W}_h, \boldsymbol{U}_h) \;=\; & \left(\rho_f \mathbf{u}_{f_h} \cdot \nabla \boldsymbol{w}_h + \nabla q_h, \tau_M(\mathbf{u}_{f_h})\, \boldsymbol{r}_M(\mathbf{u}_{f_h}, p_{f_h})\right) \\
& + \left(\nabla \cdot \boldsymbol{w}_h, \tau_C(\mathbf{u}_{f_h})\, \boldsymbol{r}_C(\mathbf{u}_{f_h})\right) \\
& + \left(\rho_f \mathbf{u}_{f_h} \cdot (\nabla \mathbf{u}_{f_h})^T, \tau_M(\mathbf{u}_{f_h})\, \boldsymbol{r}_M(\mathbf{u}_{f_h}, p_{f_h})\right) \\
& - \left(\nabla \boldsymbol{w}_h, \tau_M(\mathbf{u}_{f_h})\, \boldsymbol{r}_M(\mathbf{u}_{f_h}, p_{f_h}) \otimes \tau_M(\mathbf{u}_{f_h})\, \boldsymbol{r}_M(\mathbf{u}_{f_h}, p_{f_h})\right).
\end{aligned}
\tag{1.24}
$$

Remark 1.1: Eq. (1.23) defines the standard terms of the Navier–Stokes equations in weak form, while Eq. (1.24) contains the terms obtained from the application of the VMS method. In this respect, the first two rows of Eq. (1.24) represents the classical Streamline-Upwind Petrov-Galerkin (SUPG) stabilization terms, while the third and fourth rows contain terms peculiar of the VMS stabilization; specifically, the third row indicates an additional stabilization term complementing the SUPG ones and finally the fourth row models the Reynolds cross-stresses [Bazilevs et al., 2007].

Remark 1.2: In this thesis we call VMS-LES formulation of the Navier-Stokes equations the case in which all the terms on the right hand side of Eq. (1.24) are accounted for. By dropping the LES terms (fourth row of Eq. (1.24)) in the definition of $A^{VMS}(\cdot, \cdot)$ we obtain what we call the VMS-SUPG formulation. As already pointed in Remark 1.1, with respect to classical the SUPG the VMS-SUPG formulation contains additional terms (third row of Eq. (1.24)) peculiar of the VMS stabilization. Thus VMS-SUPG differs from classical SUPG stabilization. We notice that the VMS-SUPG formulation may represent a suitable choice for the study of the blood flow dynamics in large arteries (being the typical Reynolds numbers in a laminar regime [Formaggia et al., 2009]).

1.4 Time discretization

We discretize in time problem (1.21) by means of Backward Differentiation Formulas (BDF) [Brenan et al., 1989, Gear, 1971, Quarteroni et al., 2007], a family of linear multistep methods for which the first order derivative is replaced by a one–sided, high order incremental ratio; such BDF schemes are often used in computational fluid dynamics, as for example in [Gervasio et al., 2006].

1.4.1 Fully implicit BDF schemes

Let us partition the time interval $[0, T]$ into N_t subintervals of equal size $\Delta t = \frac{T}{N_t}$ for which the discrete time instances are $t^n = n\,\Delta t$ for $n = 0, \ldots, N_t$. Furthermore, let us denote with $\mathbf{u}_{f_h}^n$ and $p_{f_h}^n$ the approximations of the velocity $\mathbf{u}_{f_h}$ and pressure p_{f_h} fields at the time t^n. According to the order σ of the BDF scheme, the approximation of the

time derivative of the velocity appearing in the Navier–Stokes equations reads:

$$\frac{\partial \mathbf{u}_{fh}}{\partial t} \approx \frac{\alpha_\sigma \mathbf{u}_{fh}^{n+1} - \mathbf{u}_{fh}^{n,\mathrm{BDF}\sigma}}{\Delta t},$$

(1.25)

where for BDF schemes of orders $\sigma = 1, 2, 3$ we have:

$$\mathbf{u}_{fh}^{n,\mathrm{BDF}\sigma} = \begin{cases} \mathbf{u}_{fh}^{n} & \text{if } n \geq 0, & \text{for } \sigma = 1 \ (\mathrm{BDF1}), \\ 2\mathbf{u}_{fh}^{n} - \frac{1}{2}\mathbf{u}_{fh}^{n-1} & \text{if } n \geq 1, & \text{for } \sigma = 2 \ (\mathrm{BDF2}), \\ 3\mathbf{u}_{fh}^{n} - \frac{3}{2}\mathbf{u}_{fh}^{n-1} + \frac{1}{3}\mathbf{u}_{fh}^{n-2} & \text{if } n \geq 2, & \text{for } \sigma = 3 \ (\mathrm{BDF3}), \end{cases}$$

(1.26)

and

$$\alpha_\sigma = \begin{cases} 1, & \text{for } \sigma = 1 \ (\mathrm{BDF1}), \\ \frac{3}{2}, & \text{for } \sigma = 2 \ (\mathrm{BDF2}), \\ \frac{11}{6}, & \text{for } \sigma = 3 \ (\mathrm{BDF3}), \end{cases}$$

(1.27)

We notice that the BDF1 scheme coincides with the Backward Euler method. According to the approximation of the time derivative, Eq. (1.25) is replaced in Eq. (1.21), while the other time dependent terms are evaluated at the discrete time instance t^{n+1}. In this way, after spatial and temporal discretization, the fully discrete formulation of problem (1.21) reads at time t^{n+1} and for a given BDF scheme of order σ as:

find $\mathbf{u}_{fh}^{n+1} \in \mathcal{V}_{h\mathbf{g}}$ and $p_{fh}^{n+1} \in \mathcal{Q}_h$:

$$\mathcal{R}_{VMS}(\mathbf{u}_{fh}^{n+1}, p_{fh}^{n+1}) = 0 \qquad \text{for all } \boldsymbol{w}_h \in \mathcal{V}_{h\mathbf{0}} \text{ and } q_h \in \mathcal{Q}_h, \ \forall n \geq \sigma - 1,$$

(1.28)

where

$$\mathcal{R}_{VMS}(\mathbf{u}_{fh}^{n+1}, p_{fh}^{n+1}) = \left(\boldsymbol{w}_h, \rho_f \frac{\alpha_\sigma \mathbf{u}_{fh}^{n+1} - \mathbf{u}_{fh}^{n,\mathrm{BDF}\sigma}}{\Delta t} \right) + \left(\boldsymbol{w}_h, \rho_f \mathbf{u}_{fh}^{n+1} \cdot \nabla \mathbf{u}_{fh}^{n+1} \right)$$

$$+ \left(\nabla \boldsymbol{w}_h, \mu_f \left(\nabla \mathbf{u}_{fh}^{n+1} + (\nabla \mathbf{u}_{fh}^{n+1})^T \right) \right) - \left(\nabla \cdot \boldsymbol{w}_h, p_{fh}^{n+1} \right) + \left(q_h, \nabla \cdot \mathbf{u}_{fh}^{n+1} \right)$$

$$+ \left(\rho_f \mathbf{u}_{fh}^{n+1} \cdot \nabla \boldsymbol{w}_h + \nabla q_h, \tau_M(\mathbf{u}_{fh}^{n+1}) \, \boldsymbol{r}_M(\mathbf{u}_{fh}^{n+1}, p_{fh}^{n+1}) \right) + \left(\nabla \cdot \boldsymbol{w}_h, \tau_C(\mathbf{u}_{fh}^{n+1}) \, \boldsymbol{r}_C(\mathbf{u}_{fh}^{n+1}) \right)$$

$$+ \left(\rho_f \mathbf{u}_{fh}^{n+1} \cdot (\nabla \boldsymbol{w}_h)^T, \tau_M(\mathbf{u}_{fh}^{n+1}) \, \boldsymbol{r}_M(\mathbf{u}_{fh}^{n+1}, p_{fh}^{n+1}) \right)$$

$$- \left(\nabla \boldsymbol{w}_h, \tau_M(\mathbf{u}_{fh}^{n+1}) \, \boldsymbol{r}_M(\mathbf{u}_{fh}^{n+1}, p_{fh}^{n+1}) \otimes \tau_M(\mathbf{u}_{fh}^{n+1}) \, \boldsymbol{r}_M(\mathbf{u}_{fh}^{n+1}, p_{fh}^{n+1}) \right)$$

$$- \left(\boldsymbol{w}_h, \boldsymbol{f}^{n+1} \right) - \left(\boldsymbol{w}_h, \mathbf{h}^{n+1} \right)_{\Gamma_N},$$

(1.29)

given $\mathbf{u}_{fh}^{n}, \ldots, \mathbf{u}_{fh}^{n+1-\sigma}$, with $\boldsymbol{f}^{n+1} = \boldsymbol{f}(t^{n+1})$ and $\mathbf{h}^{n+1} = \mathbf{h}(t^{n+1})$.

At each discrete time t_n, the BDF scheme yields a nonlinear problem to be solved, since (1.28) is nonlinear in the variables $\mathbf{u}_{fh}^{n+1}$ and p_{fh}^{n+1}. An approximation of this nonlinear problem can be obtained for example with the Newton method [Quarteroni et al., 2007]. This requires, at each Newton iterate k, the assembly of the Jacobian matrix J_{VMS} and the solution of the linear system:

$$J_{VMS}(\mathbf{u}_{fh,k}^{n+1}, p_{fh,k}^{n+1})(\delta\mathbf{u}_{fh}, \delta p_{fh})^T = -\mathcal{R}_{VMS}(\mathbf{u}_{fh,k}^{n+1}, p_{fh,k}^{n+1}) \tag{1.30}$$

to compute the corrections $\delta\mathbf{u}_{fh}$ and δp for the velocity and pressure variables yielding

$$\mathbf{u}_{fh,k+1}^{n+1} = \mathbf{u}_{fh,k}^{n+1} + \delta\mathbf{u}_{fh}, \quad p_{fh,k+1}^{n+1} = p_{fh,k}^{n+1} + \delta p_{fh}.$$

A fully implicit approach, although obtained for different time discretizations (e.g. generalized alpha method), has been widely used for the study of incompressible fluid flows as e.g. in [Bazilevs et al., 2007, Koobus and Farhat, 2004, Masud and Calderer, 2009]. However, while a fully implicit approach is generally yielding a stable time discretization scheme, the associated computational costs may be significantly high due to the repeated assembly of the residual vector and Jacobian matrix and the solution of the associated linear system.

1.4.2 Semi–implicit BDF schemes

To contain the computational burden associated to the use of a fully implicit BDF approach (1.28), we consider instead a semi–implicit BDF scheme derived from problem (1.28), for which the nonlinear terms in $\mathbf{u}_{fh}^{n+1}$ and p_{fh}^{n+1} are extrapolated by means of the Newton–Gregory backward polynomials [Cellier and Kofman, 2006, Rao, 2009]. Without entering into the details of the derivation, for which we refer the reader to e.g. [Cellier and Kofman, 2006, Rao, 2009], we consider the following extrapolations of orders $\sigma = 1, 2, 3$ for the velocity and pressure variables at the discrete time t_{n+1}:

$$\mathbf{u}_{fh}^{n+1,\sigma} = \begin{cases} \mathbf{u}_{fh}^n & \text{if } n \geq 0, & \text{for } \sigma = 1 \text{ (BDF1)}, \\ 2\,\mathbf{u}_{fh}^n - \mathbf{u}_{fh}^{n-1} & \text{if } n \geq 1, & \text{for } \sigma = 2 \text{ (BDF2)}, \\ 3\,\mathbf{u}_{fh}^n - 3\,\mathbf{u}_{fh}^{n-1} + \mathbf{u}_{fh}^{n-2} & \text{if } n \geq 2, & \text{for } \sigma = 3 \text{ (BDF3)}, \end{cases} \tag{1.31}$$

and similarly:

$$p_{fh}^{n+1,\sigma} = \begin{cases} p_{fh}^n & \text{if } n \geq 0, & \text{for } \sigma = 1 \text{ (BDF1)}, \\ 2\,p_{fh}^n - p_{fh}^{n-1} & \text{if } n \geq 1, & \text{for } \sigma = 2 \text{ (BDF2)}, \\ 3\,p_{fh}^n - 3\,p_{fh}^{n-1} + p_{fh}^{n-2} & \text{if } n \geq 2, & \text{for } \sigma = 3 \text{ (BDF3)}. \end{cases} \tag{1.32}$$

Starting from the fully implicit formulation (1.28), we use the above extrapolations. In this way, for a given BDF scheme of order σ, the fully discrete linearized semi–implicit formulation of problem (1.28) reads:

find $\mathbf{u}_{fh}^{n+1} \in \mathcal{V}_{h\mathbf{g}}$ and $p_{fh}^{n+1} \in \mathcal{Q}_h$:

$$\mathcal{R}_{VMS}^{\sigma}(\mathbf{u}_{fh}^{n+1}, p_{fh}^{n+1}) = 0 \qquad \text{for all } \boldsymbol{w}_h \in \mathcal{V}_{h\mathbf{0}} \text{ and } q_h \in \mathcal{Q}_h, \ \forall n \geq \sigma - 1, \quad (1.33)$$

where

$$\mathcal{R}_{VMS}^{\sigma}(\mathbf{u}_{fh}^{n+1}, p_{fh}^{n+1}) =$$

$$\left(\boldsymbol{w}_h, \rho_f \frac{\alpha_\sigma \mathbf{u}_{fh}^{n+1} - \mathbf{u}_{fh}^{n,\mathrm{BDF}\sigma}}{\Delta t}\right) + \left(\boldsymbol{w}_h, \rho_f \, \mathbf{u}_{fh}^{n+1,\sigma} \cdot \nabla \mathbf{u}_{fh}^{n+1}\right) + \left(\nabla \boldsymbol{w}_h, \mu_f \left(\nabla \mathbf{u}_{fh}^{n+1} + (\nabla \mathbf{u}_{fh}^{n+1})^T\right)\right)$$

$$- \left(\nabla \cdot \boldsymbol{w}_h, p_{fh}^{n+1}\right) + \left(q_h, \nabla \cdot \mathbf{u}_{fh}^{n+1}\right) + \left(\rho_f \, \mathbf{u}_{fh}^{n+1,\sigma} \cdot \nabla \boldsymbol{w}_h + \nabla q_h, \tau_M^{n+1,\sigma} \, \boldsymbol{r}_M^{n+1,\sigma}(\mathbf{u}_{fh}^{n+1}, p_{fh}^{n+1})\right)$$

$$+ \left(\nabla \cdot \boldsymbol{w}_h, \tau_C^{n+1,\sigma} \, \boldsymbol{r}_C(\mathbf{u}_{fh}^{n+1})\right) + \left(\rho_f \, \mathbf{u}_{fh}^{n+1,\sigma} \cdot (\nabla \boldsymbol{w}_h)^T, \tau_M^{n+1,\sigma} \boldsymbol{r}_M^{n+1,\sigma}(\mathbf{u}_{fh}^{n+1}, p_{fh}^{n+1})\right)$$

$$- \left(\nabla \boldsymbol{w}_h, \tau_M^{n+1,\sigma} \, \widehat{\boldsymbol{r}}_M^{n+1,\sigma} \otimes \tau_M^{n+1,\sigma} \, \widetilde{\boldsymbol{r}}_M^{n+1,\sigma}(\mathbf{u}_{fh}^{n+1}, p_{fh}^{n+1})\right)$$

$$- \left(\nabla \boldsymbol{w}_h, \tau_M^{n+1,\sigma} \, \widehat{\boldsymbol{r}}_M^{n+1,\sigma} \otimes \tau_M^{n+1,\sigma} \, \rho_f \, \alpha_\sigma \frac{\mathbf{u}_{fh}^{n+1}}{\Delta t}\right)$$

$$+ \left(\nabla \boldsymbol{w}_h, \tau_M^{n+1,\sigma} \, \boldsymbol{r}_M^{n+1,\sigma}(\mathbf{u}_{fh}^{n+1}, p_{fh}^{n+1}) \otimes \tau_M^{n+1,\sigma} \, \rho_f \, \frac{\mathbf{u}_{fh}^{n,BDF\sigma}}{\Delta t}\right) - \left(\boldsymbol{w}_h, \boldsymbol{f}^{n+1}\right) - \left(\boldsymbol{w}_h, \mathbf{h}^{n+1}\right)_{\Gamma_N},$$

$$(1.34)$$

given $\mathbf{u}_{fn}^{h}, \dots, \mathbf{u}_{fn+1-\sigma}^{h}$. In every $K \in \mathcal{T}_h$ the stabilization parameters are defined as follows:

$$\tau_M^{n+1,\sigma} \ := \ \left(\frac{\sigma^2 \rho_f^2}{\Delta t^2} + \frac{\rho_f^2}{h_K^2} \left|\mathbf{u}_{fh}^{n+1,\sigma}\right|^2 + \frac{\mu_f^2}{h_K^4} C_r\right)^{-1/2}, \qquad (1.35)$$

$$\tau_C^{n+1,\sigma} \ = \ \frac{h_K^2}{\tau_M^{n+1,\sigma}}, \qquad (1.36)$$

and the residuals read:

$$\boldsymbol{r}_M^{n+1,\sigma}(\mathbf{u}_{fh}^{n+1}, p_{fh}^{n+1}) \ := \ \rho_f \left(\frac{\alpha_\sigma \mathbf{u}_{fh}^{n+1} - \mathbf{u}_{fh}^{n,\mathrm{BDF}\sigma}}{\Delta t}\right) + \rho_f \, \mathbf{u}_{fh}^{n+1,\sigma} \cdot \nabla \mathbf{u}_{fh}^{n+1}$$

$$+ \nabla p_{fh}^{n+1} - \mu_f \, \Delta \mathbf{u}_{fh}^{n+1} - \boldsymbol{f}^{n+1},$$

$$\widehat{\boldsymbol{r}}_M^{n+1,\sigma} \ := \ \boldsymbol{r}_M^{n+1,\sigma}(\mathbf{u}_{fh}^{n+1,\sigma}, p_{fh}^{n+1,\sigma}),$$

$$\widetilde{\boldsymbol{r}}_M^{n+1,\sigma}(\mathbf{u}_{fh}^{n+1}, p_{fh}^{n+1}) \ := \ \rho_f \mathbf{u}_{fh}^{n+1,\sigma} \cdot \nabla \mathbf{u}_{fh}^{n+1} + \nabla p_{fh}^{n+1} - \mu_f \Delta \mathbf{u}_{fh}^{n+1} - \boldsymbol{f}^{n+1}.$$

$$(1.37)$$

Thanks to the time discretization proposed, the fully discrete semi–implicit formulation (1.33) yields a linear problem in the variables $\mathbf{u}_{f_h}^{n+1}$ and $p_{f_h}^{n+1}$ to be solved only once at each time t_n. We remark that the Newton–Gregory extrapolation of the pressure variable in Eq. (1.32) is required by the terms of the formulation which carry the LES modeling. We finally notice that a linearization of Eq. (1.28) by means of first order Fréchèt differentiation would have led to a semi–implicit formulation with a larger number of terms than in Eq. (1.33), thus resulting in a larger assembly cost.

1.5 Linear parallel solver: GMRES with multigrid preconditioner

We implemented both the fully–implicit and the semi–implicit VMS algorithms in LifeV (www.lifev.org), an open–source finite element library for the solution of problems described by PDEs in a High Performance Computing framework. In our numerical solver, the linear system arising from either Eq. (1.28) or (1.33) is solved in a parallel setting using the GMRES method preconditioned by an algebraic three levels multigrid preconditioner based on the ML package of Trilinos [Gee et al., 2006]; see e.g. [Quarteroni and Valli, 1999, Toselli and Widlund, 2005]. For the application of the ML right preconditioner to the linear system matrix we perform three sweeps of the Gauss–Seidel algorithm for pre– and post–smoothing, while the solution on the coarsest level is based on a *LU* factorization [Quarteroni et al., 2007]. In our computations, we consider the relative residual as stopping criterion for the GMRES method with tolerance equal to 10^{-6}.

1.6 Numerical Results

In Section 1.6.1 we validate our fluid solver towards the benchmark problem of the vortex shedding induced by the fluid flow past a squared cylinder at high Reynolds number [Koobus and Farhat, 2004]. The simulations are carried out for different orders of temporal and spatial discretizations and for different time steps with the aim of studying their influence on the accuracy of the numerical solution. We discuss the numerical performance of the solver and analyze the influence of the stabilization parameters on the numerical results.

As a second numerical example, in Section 1.6.2 we study the fluid dynamics in a patient-specific thoracic aorta for which the peak Reynolds number at systole is approximately 6'600. In this example, we compare the numerical results and the computational costs obtained by using a fully-implicit or semi–implicit time discretizations and the VMS-LES or VMS-SUPG formulation of the Navier-Stokes equations.
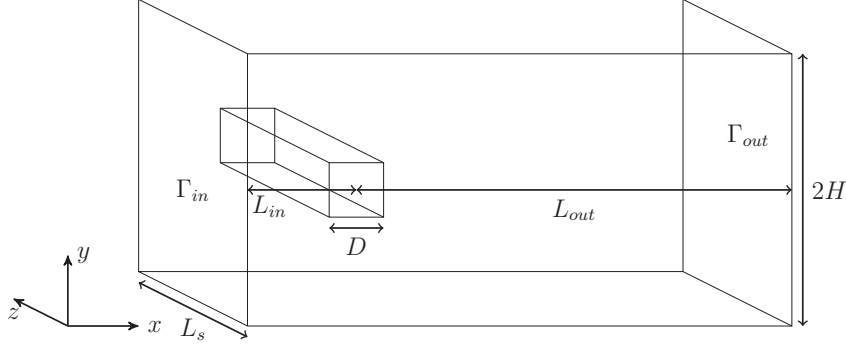
Figure 1.1: Computational domain Ω^f considered for the squared cylinder benchmark problem.

1.6.1 The benchmark problem: flow past a squared cylinder

As a validation test, we numerically simulate the flow past a squared cylinder at Reynolds number $Re = 22'000$. This problem has been already investigated both experimentally [Bearman and Obasaju, 1981, Lyn et al., 1995] and numerically by using Smagorinsky and dynamic LES models [Rodi et al., 1997, Sohankar et al., 2000], as well as with a VMS formulation for the compressible Euler equations approximated by the finite volumes method [Koobus and Farhat, 2004].

The geometrical setting considered for this benchmark problem is schematically illustrated in Figure 1.1, for which $D = 1\,m$ is the side length of the squared cylinder, $L_{in} = 4.5\,D$ and $L_{out} = 15.5\,D$ are the distances between the cylinder and the inflow and outflow surface boundaries, respectively, $L_s = 4\,D$ is the width of the domain and $H = 6.5\,D$ is the distance between the cylinder and the bottom and top walls.

Regarding the boundary conditions, at the surfaces on the top and bottom of the domain we set a null normal component of the velocity vector $\mathbf{u}_f \cdot \hat{\mathbf{n}} = 0$; similarly, at the lateral boundaries we set the normal velocity component $\mathbf{u}_f \cdot \hat{\mathbf{n}} = 0$. At the inflow of the domain Γ_{in}, we prescribe a velocity profile $\mathbf{u}_{f_{in}}(t)$ that is uniform along the inflow section and it is dependent only on time as:

$$
\mathbf{u}_{f_{in}}(t) = \begin{cases} \dfrac{V_\infty}{2}\left(1 - \cos\left(\pi\dfrac{t}{T_r}\right)\right) & \text{if } 0 \leq t < T_r, \\ V_\infty & \text{if } t \geq T_r. \end{cases}
$$

In our numerical tests we have consider $T_r = 0.3\,s$ and the reference inflow velocity $V_\infty = 22\,m/s$. At the outflow boundary Γ_{out}, we consider the following natural boundary condition [Bazilevs et al., 2009a]:

$$
-p_f\hat{\mathbf{n}} + 2\mu_f(\nabla\mathbf{u}_f + (\nabla\mathbf{u}_f)^T)\cdot\hat{\mathbf{n}} - \rho_f(\{\mathbf{u}_f\cdot\hat{\mathbf{n}}\}_-)\mathbf{u}_f = 0 \quad \text{on } \Gamma_{out}, \tag{1.38}
$$
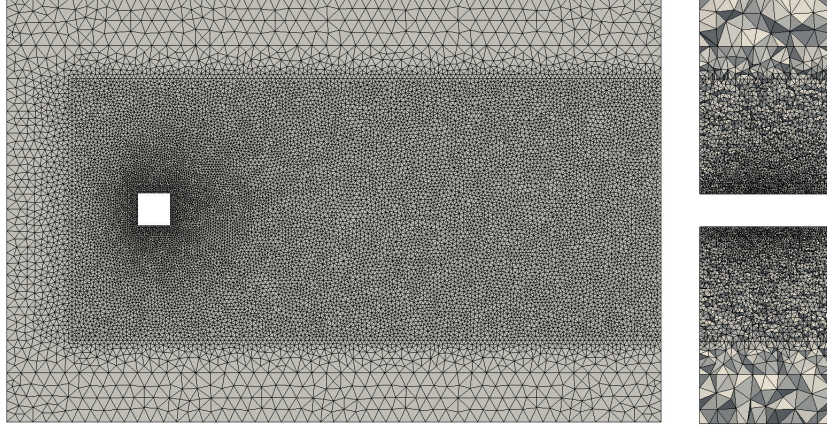
Figure 1.2: Computational mesh used for the numerical simulation of the flow past a squared cylinder.

where $\hat{\mathbf{n}}$ is the outward directed unit vector normal to Γ_{out} and $\{\mathbf{u}_f \cdot \hat{\mathbf{n}}\}_-$ denotes the negative part of $\mathbf{u}_f \cdot \hat{\mathbf{n}}$:

$$\{\mathbf{u}_f \cdot \hat{\mathbf{n}}\}_- = \begin{cases} \mathbf{u}_f \cdot \hat{\mathbf{n}} & \text{if } \mathbf{u}_f \cdot \hat{\mathbf{n}} < 0, \\ 0 & \text{if } \mathbf{u}_f \cdot \hat{\mathbf{n}} \geq 0. \end{cases}$$

The above boundary condition is introduced to weakly penalize the reverse flow induced by the vortexes at Γ_{out}, which may render unstable the discrete formulation of the problem. Indeed, we observe that only if $\mathbf{u}_f \cdot \hat{\mathbf{n}} < 0$ on Γ_{out}, the last term in the left hand side of Eq. (1.38) is active; if $\mathbf{u}_f \cdot \hat{\mathbf{n}} \geq 0$ Γ_{out}, the outflow boundary condition reduces to the well known stress–free condition. On the squared cylinder surface we impose a no slip boundary condition ($\mathbf{u}_f = \mathbf{0}$). We consider the fluid to have density $\rho_f = 1,000 \, kg/m^3$ and a dynamic viscosity $\mu_f = 1 \, Pa\,s$. In this way the Reynolds number is $Re = \dfrac{\rho_f V_\infty D}{\mu_f} = 22'000$.

We discretize the computational domain Ω^f by a mesh made of 330'764 vertices and 1'853'500 tetrahedral elements. In Figure 1.2, two images of the computational mesh $\mathcal{T}_h$ are presented: on the left we show a vertical cut plane of the mesh and on the right an horizontal cut through the squared cylinder. Along the side length of the cylinder we considered about 20 mesh elements, corresponding to a length $h_{bl} = 0.05 \, m$. We remark that the mesh size is not uniform in Ω^f and the ratio between the largest and the smallest local mesh sizes is about 10–15.

We solve the benchmark problem using the semi–implicit VMS–LES method based on the BDF formulas. We analyze the performance of the method with respect to the use of first ($\sigma = 1$) and second ($\sigma = 2$) order BDF schemes for different time steps ($\Delta t = 0.005 \, s$, $\Delta t = 0.0025 \, s$, and $\Delta t = 0.00125 \, s$) and different degrees of polynomials used for the

FE discretization	Number of dofs
$\mathbb{P}1$–$\mathbb{P}1$	1'323'056
$\mathbb{P}2$–$\mathbb{P}2$	9'209'040

Table 1.1: Number of degrees of freedom used in our simulations for the mesh of Figure 1.2.

finite element approximation, specifically $\mathbb{P}1$–$\mathbb{P}1$ and $\mathbb{P}2$–$\mathbb{P}2$. The time interval considered for the simulations is $(0, 14)$ s. In Table 1.1 we report the number of degrees of freedom associated to the discretized problem for the numerical simulations performed.

In Figure 1.3 we show a post–processing of the solution obtained by using $\mathbb{P}2$–$\mathbb{P}2$ finite elements and BDF2 scheme at time $t = 10\,s$ for $\Delta t = 0.0025\,s$, i.e. when the turbulent flow is fully developed. Figure 1.3(a) shows the coherent vortex structures characterizing the wake (we identified the structures by means of the λ_2 criterion [Jeong and Hussain, 1995]); in Figure 1.3(b), we highlight the considerable three–dimensional features of the turbulent flow occurring in the wake region adjacent to the cylinder by means of a representation of the streamlines colored by the vorticity field. Figure 1.3(c) illustrates the pressure field at a plane located at $z = 0$, as well as some significant isosurfaces; we showed only negative values of the pressure field in order to highlight the low pressure zones characterizing the center of the vortexes in the wake region. In Figure 1.3(d) we illustrate the vorticity field, both on the squared cylinder and on a cut plane at $z = 0$, on which we also show, by means of a surface LIC, the recirculation of the flow detaching from the cylinder.

In order to compare our results with those available in literature obtained by other LES methods, we compute the drag and lift coefficients on the cylinder. Let us introduce $\hat{\mathbf{v}}_\infty = \dfrac{\mathbf{v}_\infty}{\|V_\infty\|}$, that is a unit vector directed as the incoming flow, and $\hat{\mathbf{n}}_\infty$, a unit vector orthogonal to the direction $\hat{\mathbf{v}}_\infty$ of the incoming flow. The aerodynamic drag and lift coefficients for the cylinder are defined as:

$$C_D(\mathbf{u}_f, p) = -\frac{1}{q_\infty |\Gamma_{BODY}|} \oint_{\Gamma_{BODY}} (\boldsymbol{\sigma}(\mathbf{u}_f, p_f)\,\hat{\mathbf{n}}) \cdot \hat{\mathbf{v}}_\infty \, d\Gamma, \qquad (1.39)$$

$$C_L(\mathbf{u}_f, p) = \frac{1}{q_\infty |\Gamma_{BODY}|} \oint_{\Gamma_{BODY}} (\boldsymbol{\sigma}(\mathbf{u}_f, p_f)\,\hat{\mathbf{n}}) \cdot \hat{\mathbf{n}}_\infty \, d\Gamma, \qquad (1.40)$$

where $q_\infty = \frac{1}{2}\rho_f V_\infty^2$ is the dynamic pressure, and $|\Gamma_{BODY}|$ is the surface area of the cylinder; in Eq. (1.39) the minus sign takes into account that, by convention, the force is positive if acting on the fluid. In practice, we compute the aerodynamic drag and lift coefficients by means of the weak residual form ([Becker and Rannacher, 2001, Dedè, 2007, Hoffman, 2005]) which ensures higher accuracy than the direct use of Eqs. (1.39)

(a) Coherent vortex structures of the wake.

(b) Streamlines.

(c) Pressure field.

(d) Vorticity field.
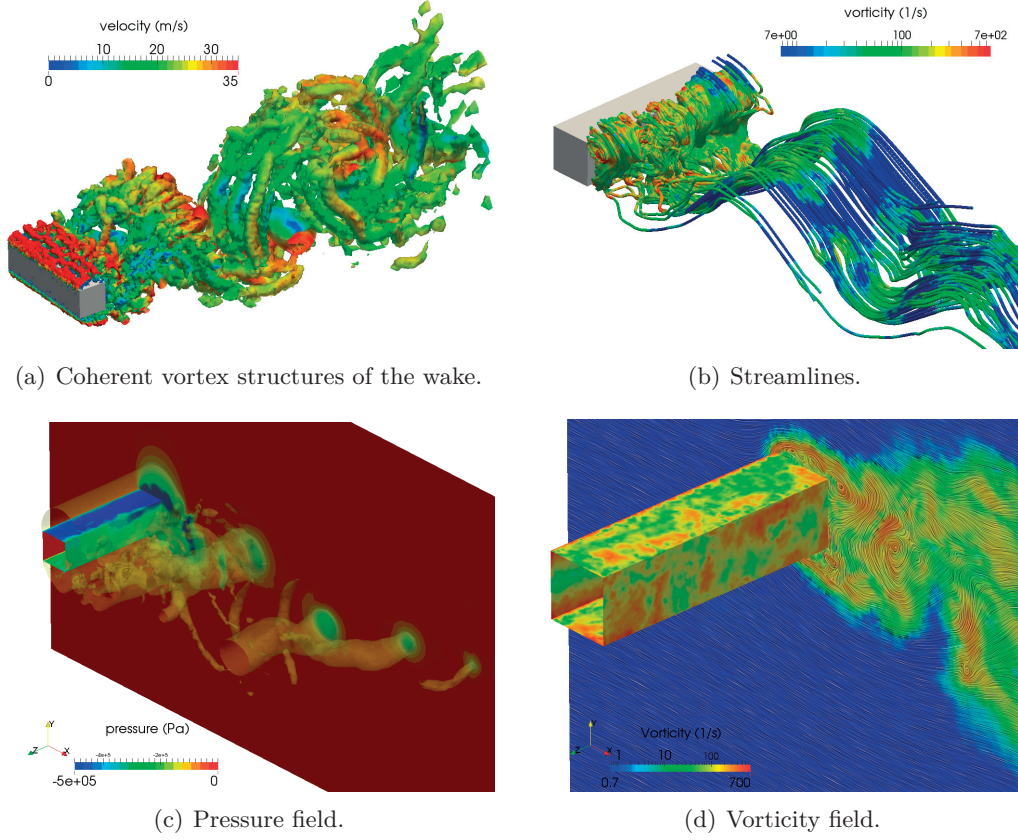
Figure 1.3: Postprocessing of the results at time $t = 10$ s. Solution obtained using $\mathbb{P}2$–$\mathbb{P}2$ finite element, BDF2, and $\Delta t = 0.0025\,s$.

and (1.40); with this aim, we use the test functions $\mathbf{d}_\infty \in \{[H^1(\Omega^f)]^d : \mathbf{d}_\infty|_{\Gamma_{BODY}} = \hat{\mathbf{v}}_\infty, \mathbf{d}_\infty|_{\partial \Omega^f \setminus \Gamma_{BODY}} = \mathbf{0}\}$ and $\mathbf{l}_\infty \in \{[H^1(\Omega^f)]^d : \mathbf{l}_\infty|_{\Gamma_{BODY}} = \hat{\mathbf{n}}_\infty, \mathbf{l}_\infty|_{\partial \Omega^f \setminus \Gamma_{BODY}} = \mathbf{0}\}$ in Eq. (1.28). In Figure 1.4 we illustrate, for the different time steps considered, the evolution of the drag (left–hand side) and lift (right–hand side) coefficients when using a first order scheme for both the spatial and the time discretizations ($\sigma = 1$ and $\mathbb{P}1$-$\mathbb{P}1$ finite elements). In the same way, Figures 1.5 and 1.6 show the evolution of the coefficients using a second order BDF scheme $\sigma = 2$ in time and a first and second order approximations in space, respectively. By a comparison of the numerical results obtained using $\mathbb{P}1$–$\mathbb{P}1$ finite element (Figures 1.4 and 1.5) we highlight the effects of the time discretization. In detail, we can observe that the amplitude of the oscillations of the lift and drag coefficients are substantially reduced when using a second order time discretization. In the same way, the results of Figures 1.5 and 1.6 (both obtained using the BDF2) allows to analyze the effects of spatial discretization on the solution. When using $\mathbb{P}1$–$\mathbb{P}1$ finite elements, the smaller Δt reduces both the amplitudes of the oscillations of lift and drag coefficients, as well as the mean drag coefficients $\overline{C}_D$. On the contrary, when a second order spatial discretization is adopted, smaller time steps lead to wider oscillations of the coefficients

FE discretization	Time step	BDF order	$\overline{C}_D$	rms(C_D)	rms(C_L)	Strouhal
	$\Delta t = 0.01$ s	1	2.51	0.250	1.59	0.127
	$\Delta t = 0.005$ s	1	2.49	0.226	1.49	0.133
	$\Delta t = 0.0025\,s$	1	2.35	0.112	1.18	0.138
	$\Delta t = 0.00125\,s$	1	2.24	0.0785	0.895	0.142
$\mathbb{P}1$–$\mathbb{P}1$						
	$\Delta t = 0.01\,s$	2	2.33	0.204	1.11	0.142
	$\Delta t = 0.005\,s$	2	2.27	0.0896	0.897	0.144
	$\Delta t = 0.0025\,s$	2	2.16	0.0622	0.658	0.146
	$\Delta t = 0.00125\,s$	2	2.05	0.0420	0.576	0.146
	$\Delta t = 0.005\,s$	2	1.98	0.102	0.580	0.142
$\mathbb{P}2$–$\mathbb{P}2$	$\Delta t = 0.0025\,s$	2	2.24	0.121	0.986	0.141
	$\Delta t = 0.00125\,s$	2	2.71	0.153	1.49	0.129

Table 1.2: Results obtained by the semi–implicit VMS–LES method by considering different time steps Δt and orders for the spatial and time discretizations.

Literature	$\overline{C}_D$	rms(C_D)	rms(C_L)	Strouhal
FV-VMS ([Koobus and Farhat, 2004])	2.10	0.18	1.08	0.136
Smagorinsky ([Rodi et al., 1997])	[1.66–2.77]	[0.1–0.27]	[0.38–1.79]	[0.07–0.15]
Dynamic LES ([Sohankar et al., 2000])	[2.00–2.32]	[0.16–0.20]	[1.23–1.54]	[0.127–0.135]

Table 1.3: Results obtained by different numerical simulations based on LES models (results between brackets indicate a range of values).

and to higher mean values of the mean of the drag.

In order to compare the numerical results with those available in literature, we evaluate the mean drag coefficient $\overline{C}_D$, the root mean square of the lift and of the drag coefficients, say rms(C_D) and rms(C_L), and the Strouhal number obtained from a Fourier analysis of the lift coefficient. In Table 1.2 we report the results predicted by the semi– implicit VMS–LES method, whereas Table 1.3 contains the values obtained by other LES methods: in particular, we consider the results obtained with the VMS–Finite Volumes method of Koobus et al. [Koobus and Farhat, 2004], LES models of Rodi et al. [Rodi et al., 1997], and Smagorinsky models of Sohankar et al. [Sohankar et al., 2000].

The choice of the time step Δt for the simulations has an important effect on the aerodynamic coefficients independently from the order of the spatial and time discretizations. Indeed, from Table 1.2 we observe that the estimation of the mean drag coefficient $\overline{C}_D$ obtained with $\Delta t = 0.005\,s$ and $\Delta t = 0.00125\,s$ varies of approximately $\pm 5\%$ with respect to the value obtained with $\Delta t = 0.0025\,s$. We notice that the use of $\mathbb{P}1$–$\mathbb{P}1$ finite elements yields a mean drag coefficient $\overline{C}_D$ that decreases as the time step gets smaller; on the contrary, by using $\mathbb{P}2$–$\mathbb{P}2$ finite element to approximate the velocity and pressure fields,
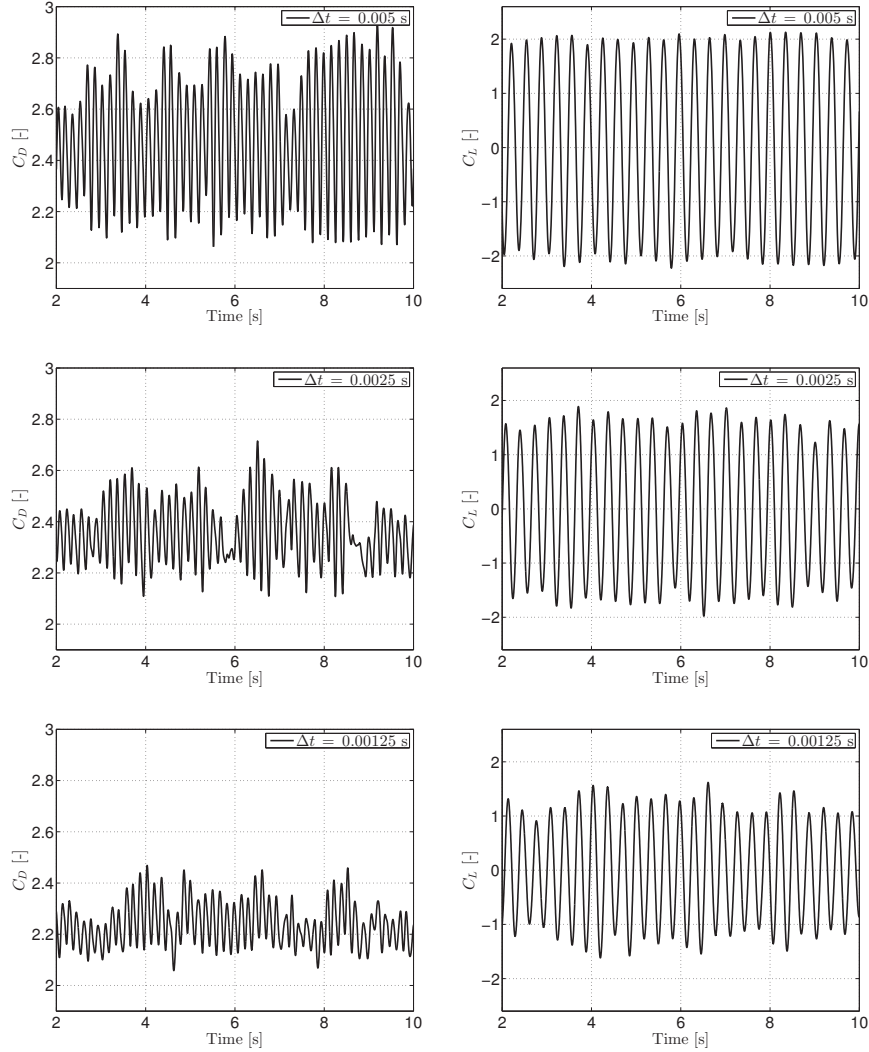
Figure 1.4: Results obtained by $\mathbb{P}1$–$\mathbb{P}1$ finite elements and the BDF1 scheme; C_D (left) and C_L (right) vs. time $t\,[s]$ for $\Delta t = 0.005\,s$ (top), $0.0025\,s$ (mid), and $0.00125\,s$ (bottom).

the value of $\overline{C}_D$ increases as Δt decreases. The same consideration follows from the analysis of the root mean square values of both the lift and drag coefficients. The results obtained using a first order spatial–time discretizations ($\mathbb{P}1$–$\mathbb{P}1$ and BDF1) are in line with those available in literature: although the largest time step under consideration leads already to an accurate prediction of the Strouhal number, the smallest one, i.e. $\Delta t = 0.00125\,s$, yields good estimation of all the coefficients. We notice that the use of a first order discretization in space and second in time ($\mathbb{P}1$–$\mathbb{P}1$ and BDF2) leads to an underestimation of the root mean square of the lift and drag coefficients with respect to the results available in literature for LES models, although the prediction of $\overline{C}_D$ is sufficiently accurate. Finally, by employing a second order space–time discretization ($\mathbb{P}2$–$\mathbb{P}2$ and BDF2) we notice that the rms(C_L) and rms(C_D) are in line with those obtained
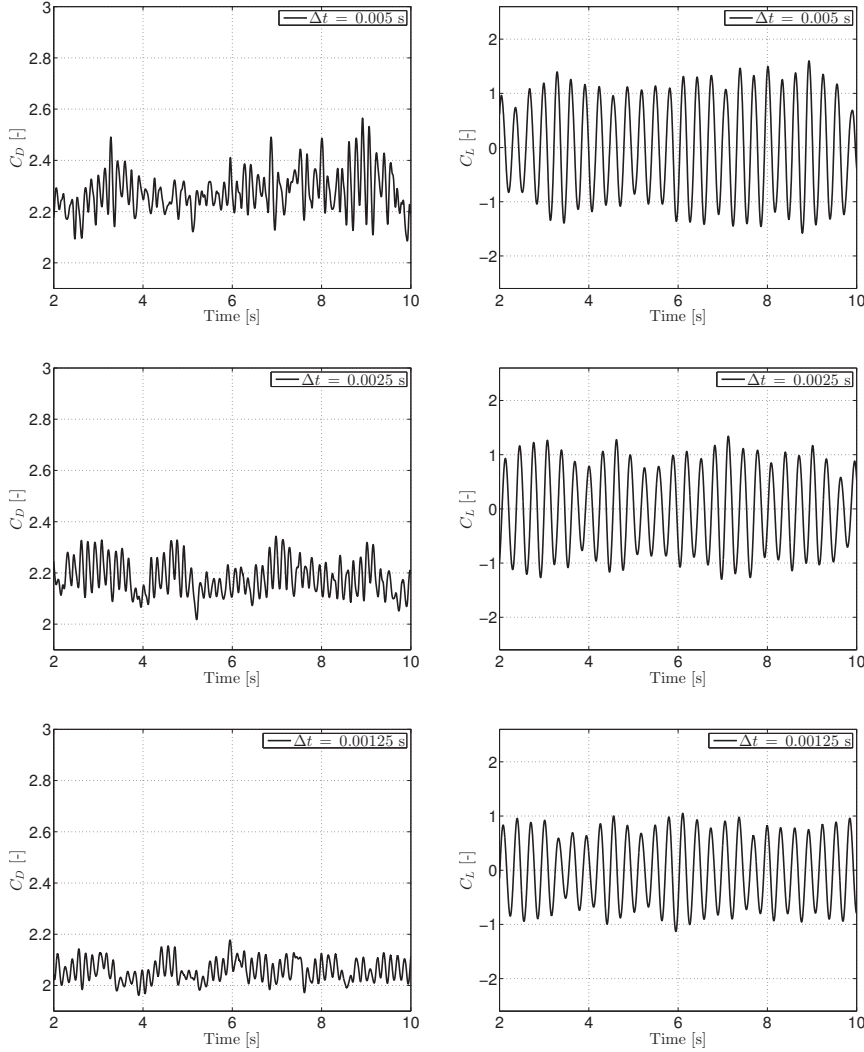
Figure 1.5: Results obtained by $\mathbb{P}1$–$\mathbb{P}1$ finite elements and the BDF2 scheme; C_D (left) and C_L (right) vs. time $t\,[s]$ for $\Delta t = 0.005\,s$ (top), $0.0025\,s$ (mid), and $0.00125\,s$ (bottom).

with other LES methods, although the smallest time step yields an overestimation of the mean drag coefficient $\overline{C}_D$.

Parallel performance of the solver

In Figure 1.7 we report a strong scalability study of the solver performed using the $\mathbb{P}2$–$\mathbb{P}2$ and BDF2 discretizations of the benchmark problem for $\Delta t = 0.0025\,s$. We recall that in this settings the total number of degrees of freedom is equal to 9'209'040. In our investigation, we consider a varying number of cores ranging from 64 to 4'096 and we monitor the time to build the preconditioner (Figure 1.7(a)), to solve the linear system by the preconditioned GMRES method (Figure 1.7(b)), and to perform a time step, i.e.
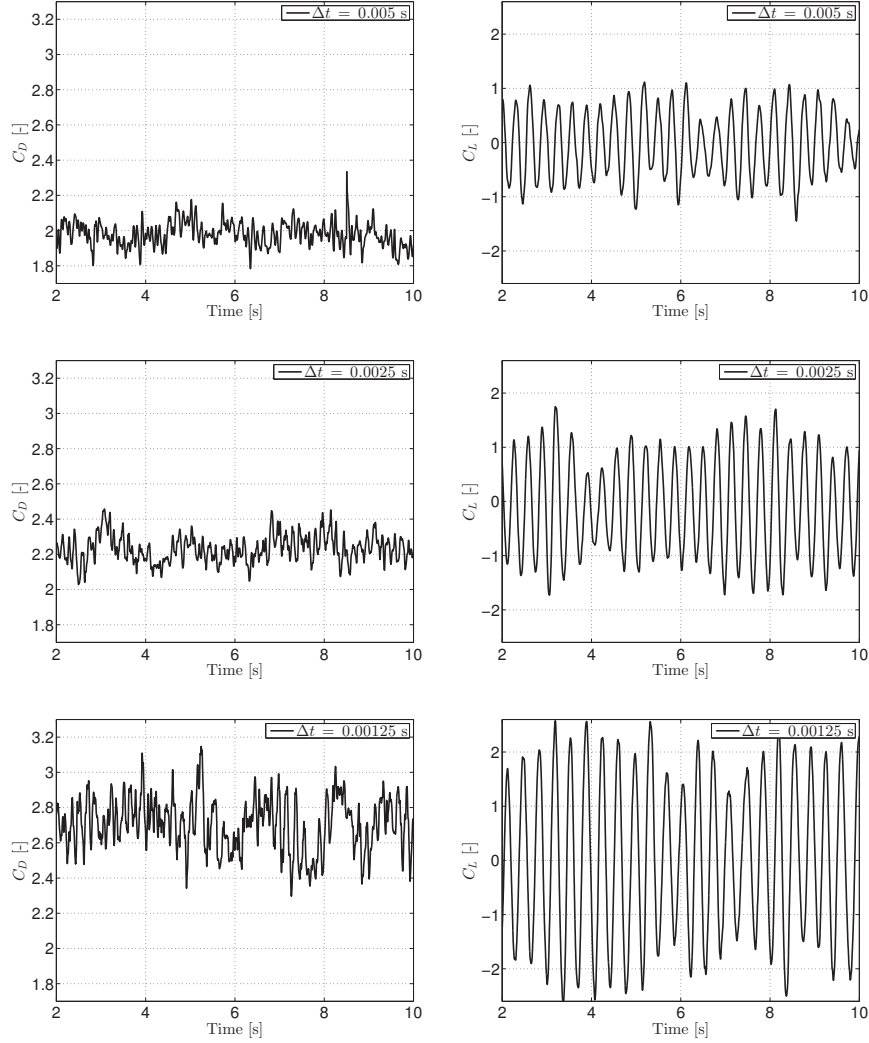
Figure 1.6: Results obtained by $\mathbb{P}2$–$\mathbb{P}2$ finite elements and the BDF2 scheme; C_D (left) and C_L (right) vs. time $t\,[s]$ for $\Delta t = 0.005\,s$ (top), $0.0025\,s$ (mid), and $0.00125\,s$ (bottom).

the sum of the time spent to update the convective and the VMS–LES terms in the assembly phase, to build the preconditioner, and to solve the linear system (Figure 1.7(c)). Furthermore, in Figure 1.7(d) we show the mean number of GMRES iterations employed to solve the linear system with the prescribed tolerance. All the computations are carried out using Piz Dora, a Cray XC40 supercomputer installed at the Swiss National Supercomputing Center (CSCS) whose main technical specifications are reported in Table 1.4.

The results reported in Figure 1.7 show the excellent scalability properties of the solver up to 2'048 cores: in fact, all the indicators scale almost perfectly and the number of iterations of the GMRES solver remains constant. More specifically, only when using

Number of compute nodes	1'256
Processor	64–bit Intel Xeon processor E5-2690v3-Haswell
Memory	64GB per node in 1'192 nodes 128GB per node in 64 nodes
Memory bandwidth	Up to 137 GB/s per node
Network	Dragonfly interconnect

Table 1.4: Piz Dora Cray XC40 technical data.

2'048 cores we start to observe an initial deterioration in the scalability of the time to build the preconditioner and to solve the linear system. Nevertheless, in terms of time to perform a time step, remarkably only with 4'096 cores we start to notice a slight deterioration of the performance. This is due to the fact that, within the overall count of the operations required to perform a time step, the assembly phase necessary to update the convective and VMS–LES stabilization terms is the most expensive, taking around

(a) Time to build the preconditioner.

(b) Time to solve the linear system.

(c) Time to complete a time step.

(d) Number of GMRES iterations.
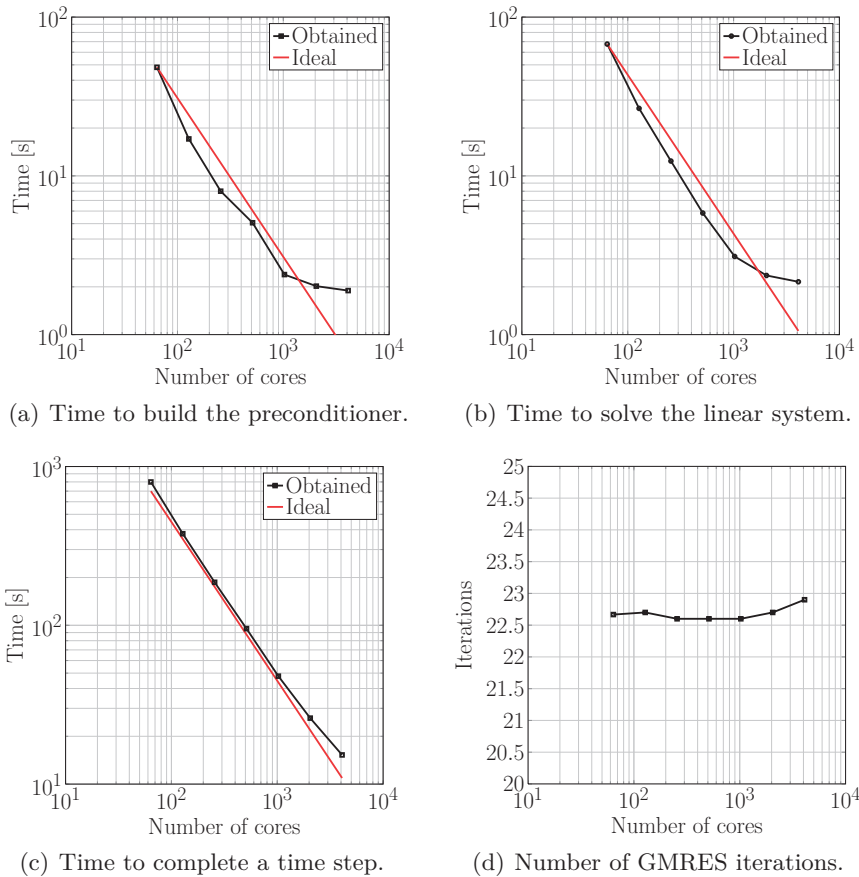
Figure 1.7: Scalability analysis of the solver. Simulations performed using $\mathbb{P}2 - \mathbb{P}2$ finite element, BDF2 and $\Delta t = 0.0025\,s$.

(a) Velocity field at time $10.0\,s$.

(b) Pressure field at time $10.0\,s$.
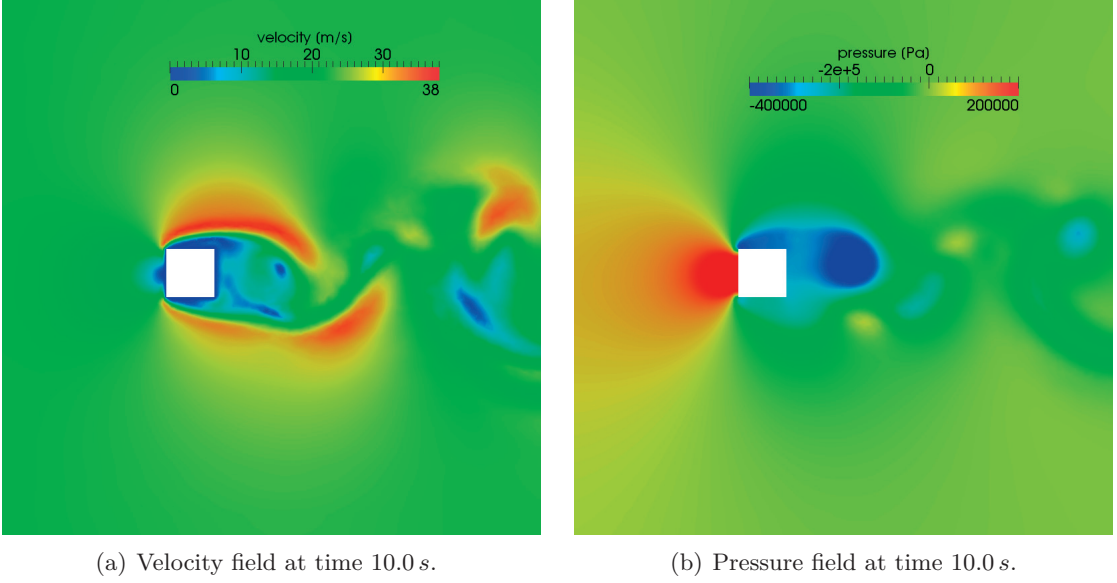
Figure 1.8: Reference velocity (a) and pressure (b) fields computed at time $t = 10.0\,s$ using $\mathbb{P}1$–$\mathbb{P}1$ finite elements and the BDF2 scheme with $\Delta t = 0.0025\,s$; the velocity field is used to evaluate the stabilization parameters $\tau_M^{n+1,\sigma}$ and $\tau_C^{n+1,\sigma}$.

the 85% of the total time spent for a time step.

Stabilization parameters

We address, for the benchmark problem at hand, the dependency of the stabilization parameters $\tau_M^{n+1,\sigma}$ and $\tau_C^{n+1,\sigma}$ of Eqs. (1.35) and (1.36) on the choice of the time step Δt. With this aim, we visualize the spatial distributions of $\tau_M^{n+1,\sigma}$ and $\tau_C^{n+1,\sigma}$ on the mid plane of the computational domain starting from the velocity field computed at the time $t = 10.0\,s$ by means of $\mathbb{P}1$–$\mathbb{P}1$ finite element and the BDF2 scheme for $\Delta t = 0.0025$ s; the corresponding computed velocity and pressure fields are reported in Figure 1.8, while the values of $\tau_M^{n+1,\sigma}$ and $\tau_C^{n+1,\sigma}$ for the time steps $\Delta t = 0.01, 0.005, 0.0025,$ and $0.00125\,s$ are reported in Figures 1.9 and 1.10. From Figure 1.9(a) we observe that the largest time step under consideration, $\Delta t = 0.01\,s$, leads to a distribution of $\tau_M^{n+1,\sigma}$ that reflects the value of the local mesh size h_K and velocity field $\mathbf{u}_{fh}^{n+1,\sigma}$. However, as the time step Δt diminishes, the magnitude of the stabilization parameter $\tau_M^{n+1,\sigma}$ diminishes and its spatial distribution only mildly depends on the local mesh size and the velocity magnitude. In fact, from the definition of $\tau_M^{n+1,\sigma}$ in Eq. (1.35), we remark that the use of small time steps tends to annihilate the dependence on h_K and $\mathbf{u}_{fh}^{n+1,\sigma}$, as it is possible to observe in Figure 1.9(d) where $\tau_M^{n+1,\sigma}$ mostly behaves as $\frac{\Delta t}{\rho_f}$ for $\Delta t \to 0$. We report in Figure 1.10 the behavior of the stabilization parameter $\tau_C^{n+1,\sigma}$ computed as in Eq. (1.36). We notice that, since mild dependencies of $\tau_M^{n+1,\sigma}$ on h_K and $\mathbf{u}_{fh}^{n+1,\sigma}$ are observed for the values of the Δt under considerations, the parameter $\tau_C^{n+1,\sigma}$ mostly depends on the

(a) $\Delta t = 0.01\,s$.

(b) $\Delta t = 0.005\,s$.

(c) $\Delta t = 0.0025\,s$.

(d) $\Delta t = 0.00125\,s$.
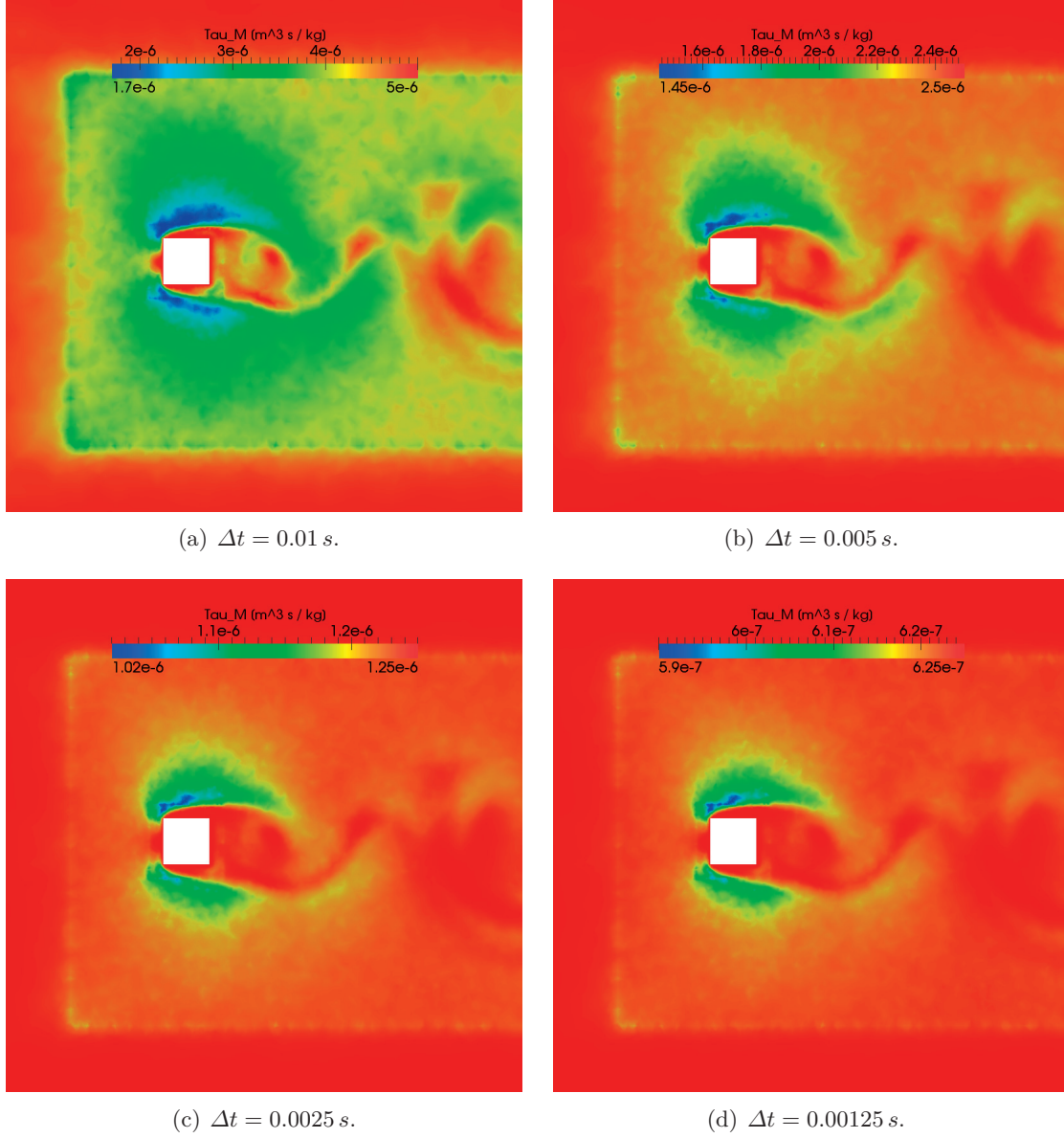
Figure 1.9: Spatial distribution (on the mid plane of Ω^f) of the stabilization parameter $\tau_M^{n+1,\sigma}$ computed from the reference velocity field of Figure 1.8(a) using $\mathbb{P}1$–$\mathbb{P}1$ finite element and the BDF2 scheme for different time steps $\Delta t = 0.01$, 0.005, 0.0025, and $0.00125\,s$.

local mesh size h_K; indeed, we have considered a variable mesh size as highlighted in Figure 1.2. As consequence, the ratio between the largest and smallest local values of $\tau_C^{n+1,\sigma}$ in Ω^f is approximatively 150 regardless of the time step Δt under consideration.

While it is well known that the stabilization parameters chosen as in Eqs. (1.35) and (1.36) degenerate as the time step decreases (see e.g. [Colomés et al., 2015, Hsu et al., 2010]),

(a) $\Delta t = 0.01\,s$.

(b) $\Delta t = 0.005\,s$.

(c) $\Delta t = 0.0025\,s$.

(d) $\Delta t = 0.00125\,s$.
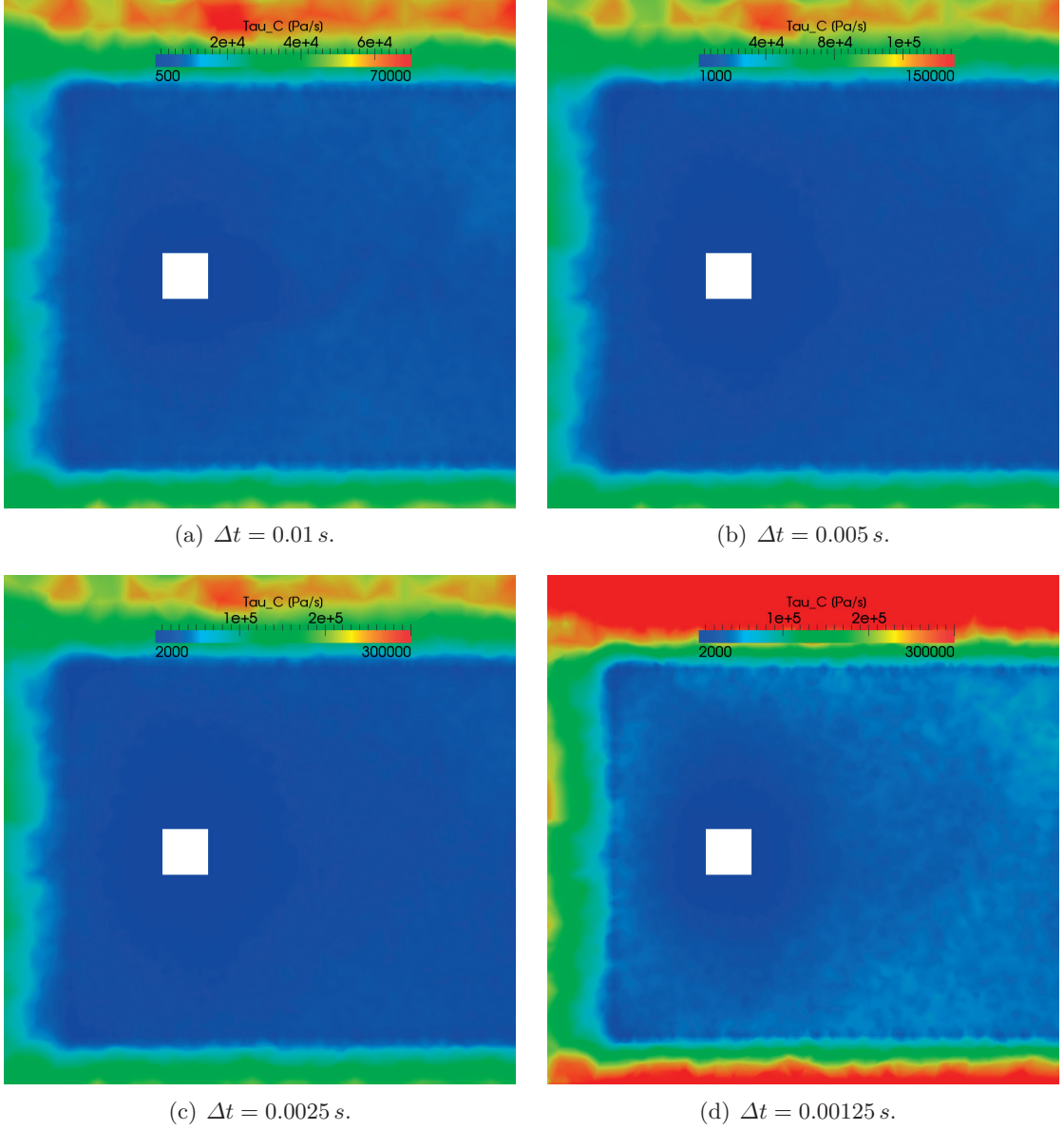
Figure 1.10: Spatial distribution (on the mid plane of Ω^f) of the stabilization parameter $\tau_C^{n+1,\sigma}$ computed from the reference velocity field of Figure 1.8(a) and the parameters $\tau_M^{n+1,\sigma}$ of Figure 1.9 using $\mathbb{P}1$–$\mathbb{P}1$ finite element and the BDF2 scheme for different time steps $\Delta t = 0.01$, 0.005, 0.0025, and $0.00125\,s$.

i.e $\tau_M^{n+1,\sigma} \sim \Delta t \to 0$ and $\tau_C^{n+1,\sigma} \sim \frac{1}{\Delta t} \to \infty$ for $\Delta t \to 0$, and hence the stabilization and turbulence LES modeling may be ineffective for relatively small values of Δt ([Colomés et al., 2015]), we stress the fact that we did not encounter any stabilization issue in our numerical simulations for the time steps under consideration. However, our experience based on numerical tests indicates that for very "small" values of Δt, i.e. when the term related to Δt in $\tau_M^{n+1,\sigma}$ is not correctly balanced with respect to the other ones, the

(a) $\widetilde{\tau}_M^{n+1,\sigma}$.

(b) $\widetilde{\tau}_C^{n+1,\sigma}$.
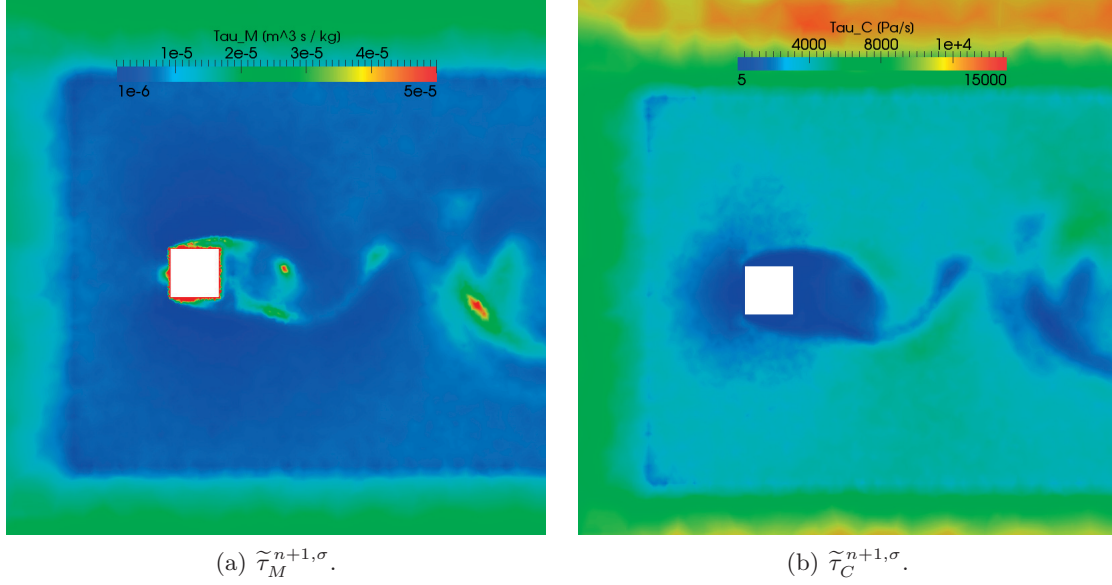
Figure 1.11: Spatial distribution (on the mid plane of Ω^f) of the stabilization parameters $\widetilde{\tau}_M^{n+1,\sigma}$ and $\widetilde{\tau}_C^{n+1,\sigma}$ computed from the reference velocity field of Figure 1.8(a) using $\mathbb{P}1$–$\mathbb{P}1$ finite element.

degeneration of the parameters $\tau_M^{n+1,\sigma}$ and $\tau_C^{n+1,\sigma}$ is reflected at the numerical level by convergence issues of the linear solver and eventually by the inability of assembling a suitable preconditioner.

An alternative formulation of the stabilization parameters of Eqs. (1.35) and (1.36) can be used by completely neglecting the effect of time dependency of the fine scale velocity $\mathbf{u}'$ in the fine scale momentum equation, where one assumes that $\frac{\partial \mathbf{u}'_f}{\partial t} \simeq 0$. This leads to consider stabilization parameters $\widetilde{\tau}_M^{n+1,\sigma}$ and $\widetilde{\tau}_C^{n+1,\sigma}$ in Eqs. (1.15) and (1.16) independent of the time step Δt, which read on every $K \in \mathcal{T}_h$:

$$
\begin{aligned}
\widetilde{\tau}_M^{\,n+1,\sigma} &= \left(\frac{\rho_f^2}{h_K^2} \left| \mathbf{u}_{fh}^{n+1,\sigma} \right|^2 + \frac{\mu_f^2}{h_K^4} C_r \right)^{-1/2}, \\
\widetilde{\tau}_C^{\,n+1,\sigma} &= \frac{h_K^2}{\widetilde{\tau}_M^{\,n+1,\sigma}}.
\end{aligned}
$$

However, we remark that we were unable to successfully perform numerical simulations by using the previous definitions of the stabilization parameters, even for different choices of Δt; specifically, we experienced convergence issues using the GMRES solver with ML preconditioner, which prevented the simulations to significantly advance beyond the time $T_v = 0.3\,s$. Our interpretation of this outcome is that a suitable preconditioner can not be "easily" assembled when the stabilization parameters $\widetilde{\tau}_M^{n+1,\sigma}$ and $\widetilde{\tau}_C^{n+1,\sigma}$ are

significantly varying in the computational domain Ω^f. Following the procedure described before, we plot in Figure 1.11 the spatial distributions of the parameters $\widetilde{\tau}_M^{n+1,\sigma}$ and $\widetilde{\tau}_C^{n+1,\sigma}$; in particular, we highlight that $\widetilde{\tau}_M^{n+1,\sigma}$ varies of approximately two orders of magnitude in Ω^f, while the ratio between the largest and smallest local values of $\widetilde{\tau}_C^{n+1,\sigma}$ is approximatively $3'000$, a value much larger than the one obtained with $\tau_C^{n+1,\sigma}$, which was about 150. We notice that $\widetilde{\tau}_M^{n+1,\sigma}$ is relatively "large" where the velocity magnitude is nearly zero, as it occurs in the boundary layers and some regions in the vortexes wake. This, in combination with the "small" mesh size h_K in the boundary layers and wake regions, renders the parameter $\widetilde{\tau}_C^{n+1,\sigma}$ relatively "small" locally in Ω^f; conversely, this becomes "large" far from the cylinder, where the mesh is locally coarse and the velocity magnitude nearly equal to V_∞.

We finally remark that the choice of the stabilization parameters may have a significant impact on the numerical results, especially if, as in this work, we take into account only in an approximate manner for the time dependencies of the fine scales using the parameters $\tau_M^{n+1,\sigma}$ and $\tau_C^{n+1,\sigma}$ of Eqs. (1.35) and (1.36). While this can be improved by using dynamic subscales models [Codina, 2002, Codina et al., 2007, Colomés et al., 2015], the latter require to solve systems of ordinary differential equations to determine the fine scale solutions $\mathbf{u}'_f$ and p'_f, which may increase the accuracy of the results, but also the computational cost of the simulations. Since in this work we focus on the efficiency aspects of the numerical solver, we decided to consider the stabilization parameters as in Eqs. (1.35) and (1.36), which nevertheless represent a common choice in literature [Bazilevs et al., 2007, Bazilevs et al., 2009a, Gamnitzer et al., 2010, Gravemeier et al., 2010, Tezduyar and Sathe, 2003].

1.6.2 Blood flow dynamics in a patient specific aorta

As a second test-case we address the study of the blood flow dynamics in a Thoracic Aorta under physiological conditions. The Thoracic Aorta is the artery that exits from the left ventricle and the ejection of the blood into this vessel is regulated by the aortic valve which opens and closes during the heart cycle. In physiological conditions, the flowrates in the aorta are the biggest along the whole cardiovascular network.

The geometrical domain of the Aorta used for the numerical simulations has been obtained through the post-processing of CT-scan images and it is illustrated in Figure 1.13. The simulations are started from fluid at rest and four heart beats are simulated before post-processing the results in order to be sure that a time periodic flow is established. The problem is approximated in space by means of $\mathbb{P}1$-$\mathbb{P}1$ finite elements while in time by a second order BDF scheme. The time step used in the numerical simulations is $\Delta t = 0.005$ s. The physical parameters that characterize the fluid are $\rho_f = 1.05$ g/cm^3 and $\mu_f = 0.035$ g/cm/s. The computational mesh used is comprised of 989'646 elements, yielding a total number of 682'892 degrees of freedom. We test our fluid solver with the focus being on

the comparison between (*i*) semi-implicit vs fully-implicit time discretizations and (*ii*) VMS-SUPG (see Remark 1.2 Section 1.3) vs VMS-LES formulation of the Navier-Stokes equations. In Figure 1.12 we report the flowrate profiles used in our simulations: they are prescribed using Dirichlet boundary conditions, i.e., mapping each flowrate through a parabolic velocity profile. At the outflow boundary Γ_{out}, we consider the boundary condition reported in Eq. (1.38).
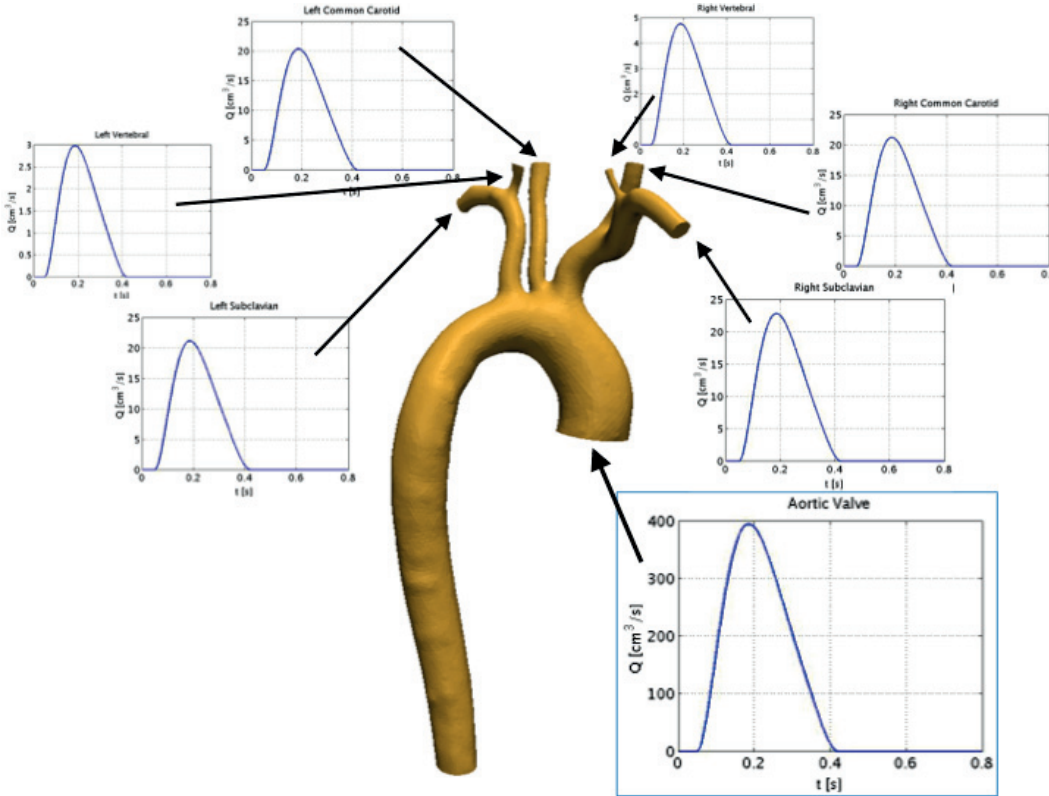
Figure 1.12: Flowrate profiles used in our simulations. At the outflow section of the domain we impose the boundary condition reported in Eq. (1.38).

In Figure 1.14 we report a post-processing of the numerical solution obtained using the semi-implicit time discretization and the VMS-LES formulation. More specifically, we visualize the streamlines of the flow colored by the velocity magnitude (left hand side) and the vortex structures (right hand side) colored by the vorticity field, at different times during the heart beat. The fluid features transitional to turbulent flows developing in the downstream part of the aorta (peak Reynolds number $Re \approx 6'600$[1]) where indeed we notice the presence of the biggest vortices right after the systolic peak which occurs at time $t = 0.19$ s (see Figure 1.14).

We aim at comparing and quantifying the differences in the numerical solutions obtained

---

[1]The Reynolds number is based on the characteristic length $L = 2.2$ cm (vessel diameter) and flow velocity $U = 100$ cm/s.
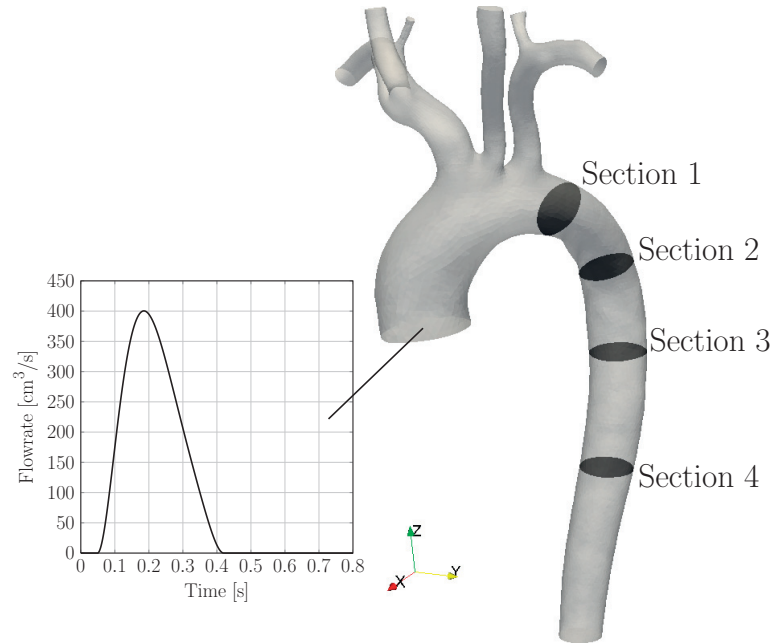
Figure 1.13: Visualization of the geometry, inflow flowrate profile and location of the cross sections at which we study the elicity of the flow.

with a semi-implicit vs fully-implicit time discretization as well as the importance of using the LES terms in the formulation. To this end, in order to highlight the differences of the flow patterns associated to the solutions obtained by the different approaches considered, we compare the secondary flows computed by means of the helicity indicator [Caputo et al., 2013]. We recall that helicity on an infinitesinal portion of fluid is defined as the scalar product of the velocity $\mathbf{u}_f$ and vorticity field, namely $(\nabla \times \mathbf{u}_f) \cdot \mathbf{u}_f$, and actually measures the alignment of the velocity and vorticity vectors. Thereby we compare, at different time steps during the heart cycle, the elicity patterns at different cross sections orthogonal to the centerlines of the geometry, see Figure 1.13. In Figure 1.15, 1.16, 1.17, 1.18 the contour plot of the helicity indicator is reported: positive values of helicity (red color) correspond to a clockwise rotation of the flow while negative values (blue color) to a counter clockwise rotation.

The results reported in Figure 1.15, 1.16, 1.17, 1.18 show that almost identical helicity patterns are obtained for both the semi-implicit and fully-implicit time discretizations (either using VMS-SUPG or the VMS-LES formulation). In the same way, we notice also that even at systole (i.e. t = 1.1925 s) the helicity plots obtained at all the cross sections considered using the VMS-SUPG and VMS-LES formulations feature very mild (almost imperceptible) differences.

Finally, in Table 1.5 we report the computational costs: we notice that the number of linear solver iterations is almost the same for all the different approaches considered. In terms of time spent to perform a single time step, we observe that the use of a
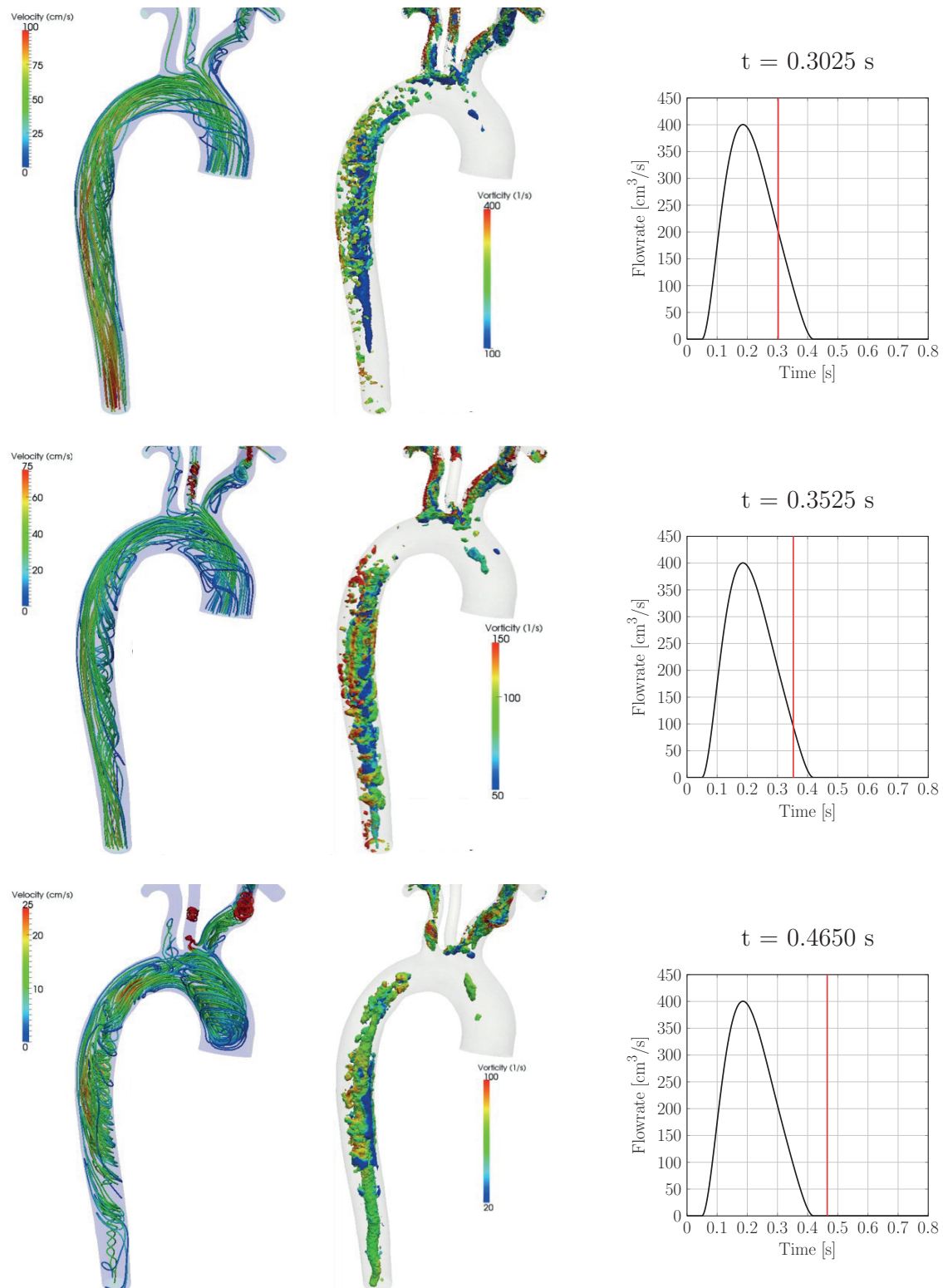
Figure 1.14: Post-processing of the simulation performed with semi-implicit time discretization and using the VMS-LES formulation. Visualization of the streamlines (left hand side) and coherent vortex structures (right hand side) at different times during the heart beat. The vortex structures are identified by means of the Q criterion [Dubief and Delcayre, 2000].

fully-implicit time discretization leads, as expected, to an increase of the computational time w.r.t. the semi-implicit case by a factor roughly equal to three (that is the number of Newton iterations performed per time step).

	GMRES iterations	Newton iterations	Time per time step
VMS-SUPG semi-implicit	29.1	-	11.8 s
VMS-SUPG fully-implicit	27.2	3.2	33.6 s
VMS-LES semi-implicit	32.9	-	14.3 s
VMS-LES fully-implicit	31.3	3.1	45.5 s

Table 1.5: Comparison of the computational costs for the different approaches considered (values averaged on the heart beats simulated).
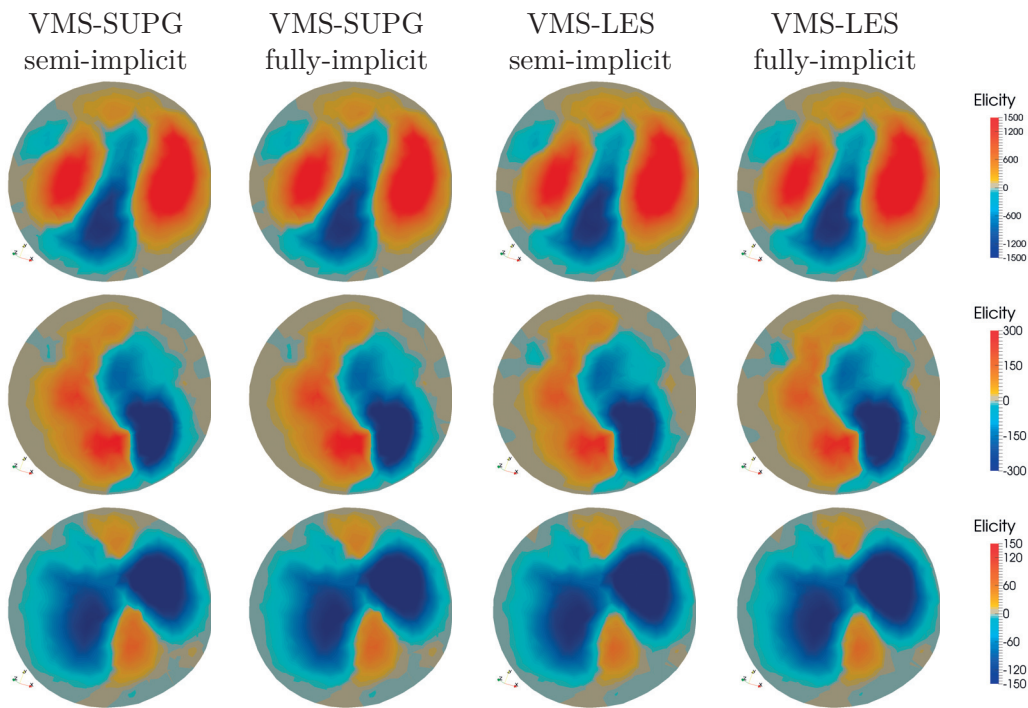
Figure 1.15: Section 1, helicity at times 0.1925 s (top), 0.3025 s (mid) and 0.4650 s (bottom).

VMS-SUPG semi-implicit	VMS-SUPG fully-implicit	VMS-LES semi-implicit	VMS-LES fully-implicit
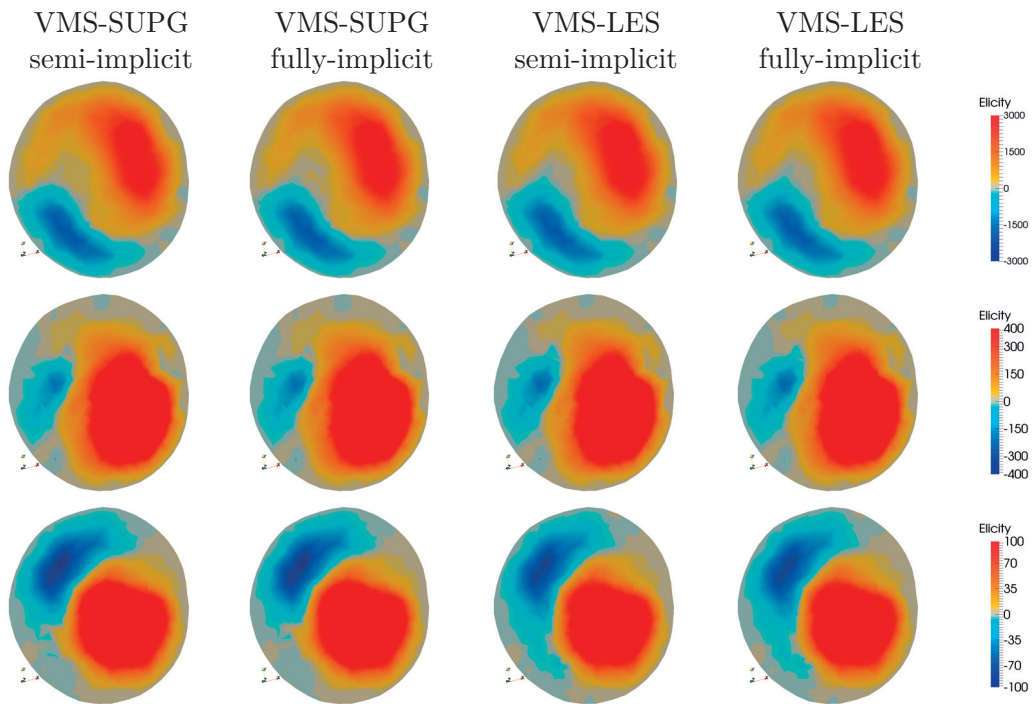
Figure 1.16: Section 2, helicity at times 0.1925 s (top), 0.3025 s (mid) and 0.4650 s (bottom).

VMS-SUPG semi-implicit	VMS-SUPG fully-implicit	VMS-LES semi-implicit	VMS-LES fully-implicit
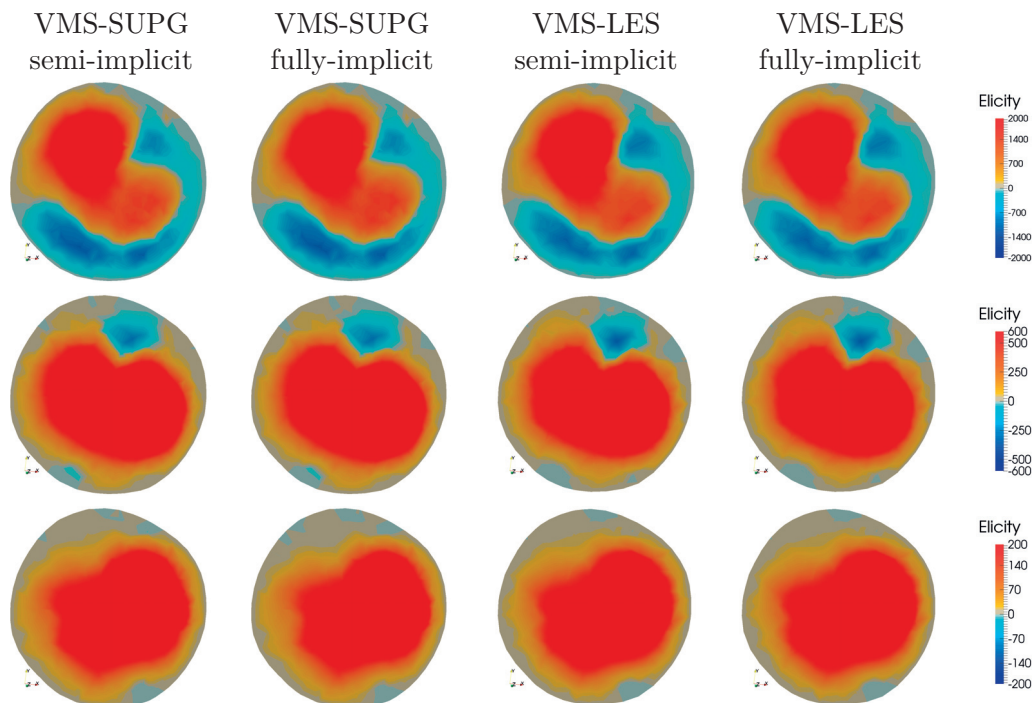
Figure 1.17: Section 3, helicity at times 0.1925 s (top), 0.3025 s (mid) and 0.4650 s (bottom).

VMS-SUPG
semi-implicit

VMS-SUPG
fully-implicit

VMS-LES
semi-implicit

VMS-LES
fully-implicit
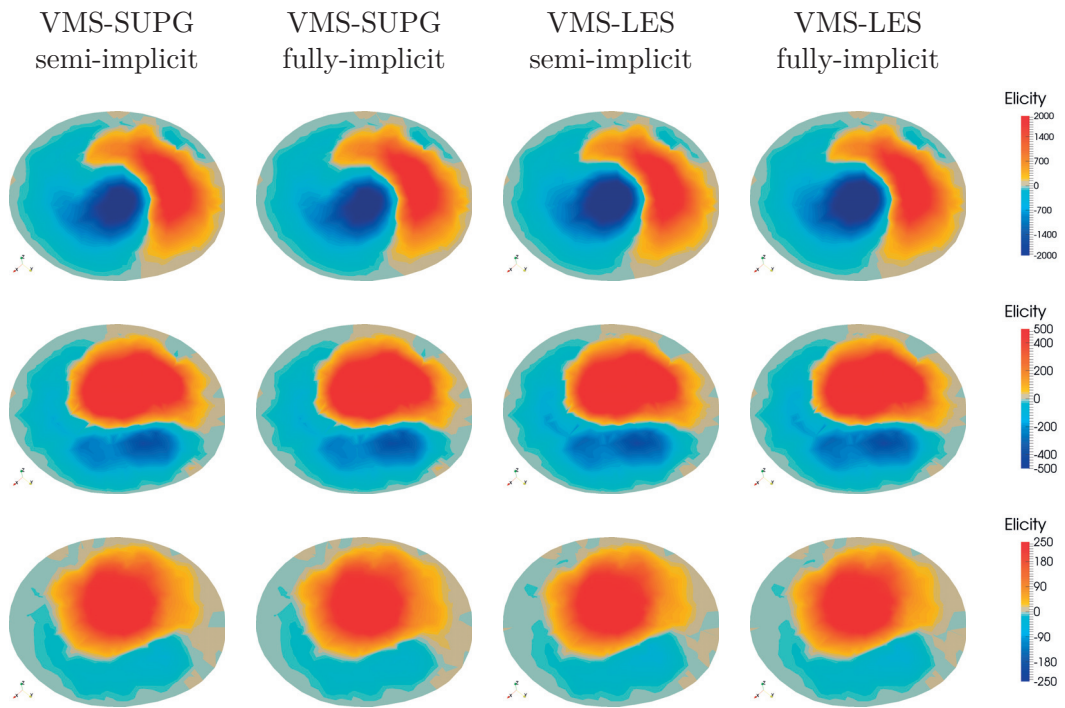
Figure 1.18: Section 4, helicity at times 0.1925 s (top), 0.3025 s (mid) and 0.4650 s (bottom).

2 Mechanical modeling for the arterial tissue

This Chapter deals with the mechanical modeling for the tissue of large sized arteries. It does not contain original contributions but rather serves the purpose of setting up of the fluid-structure interaction problem that will be addressed in Chapter 3. In Section 2.1 we briefly recall the histology and the mechanical behavior of the healty arterial tissue from a general point of view. Section 2.2 introduces the main concepts of the continuum mechanics theory, specifically the basic vectorial and tensorial notation necessary in Section 2.3 in order to write the equations of motion for a continuous media. In Section 2.4 we collect the constitutive models for the arterial tissue used in this thesis. Specifically, in Section 2.4.1 we first focus on the description of the isotropic linear elastic material model, while a more sophisticated nonlinear anisotropic hyperelastic model is then addressed in Section 2.4.2.

2.1 Biomechanics of the arterial tissue

Arterial walls of major human arteries are composite materials consisting of three main layers: the intima, media and adventitia, separated by thin elastic laminae, see Figure 2.1. The intima is the innermost, thin layer, which is mainly composed of endothelial cells. The contribution to the overall mechanical properties of the arterial wall carried by the intima layer is negligible in healty individuals. However, in pathological cases, for instance when atherosclerosis occurs, due to intima thickening and stiffening its contribution might become mechanically relevant [Holzapfel et al., 2000]. The intima is separated from the media by a dense elastic membrane called the internal elastic lamina. The media, which represents the thickest layer of the vessel wall, is the middle layer and it is mainly composed of elongated smooth muscle cells, and also elastin
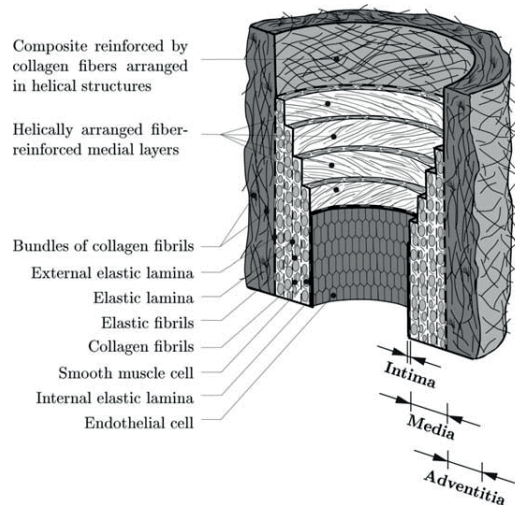
Figure 2.1: Schematic representation of the three main layers which compose a healty elastic artery. Image from [Holzapfel et al., 2000].

and collagen. Elastic fibres allow the vessel to expand with systole and contract with diastole, thereby propelling blood forward throughout the arterial tree. The media is separated from the adventitia by a dense elastic membrane called the external elastic lamina. The adventitia is the outermost layer, and it is manly composed of collagen fibrils, elastic sheets and elastic fibrils. This composition yields an anisotropic and viscoelastic material response at finite strains. Various models have been proposed in literature for the modeling of the hyperelastic response of arterial vessels, however, the essential condition of polyconvexity [Ball, 1977] was considered only since approximately 10 years. This is due to the fact that the first anisotropic polyconvex functions were just introduced in [Schröder and Neff, 2003], although later it was observed that also previously proposed anisotropic functions were indeed polyconvex, see, e.g., the function introduced in [Holzapfel et al., 2000]. Based thereon, in [Balzani et al., 2006a] a variety of polyconvex functions which a priori satisfied the condition of a stress-free reference configuration were constructed. They were compared in [Brands et al., 2008] with respect to their numerical performance using parallel iterative solvers, i.e., the FETI-DP domain decomposition method [Toselli and Widlund, 2005]. A larger structural simulation of an arterial wall for a diseased artery using one of these anisotropic, almost incompressible hyperelastic material models was then presented in [Klawonn and Rheinbach, 2010], applying a Newton-Krylov FETI-DP approach. Anisotropy, to model embedded collagen fibers, is still one of the numerical challenges present in models for soft biological tissue. In [Balzani et al., 2010] it was observed numerically that the anisotropy of soft tissue significantly affects the convergence of the Newton method as well as of the iterative linear solver but that at the same time the effect is not severe in the physiological range. Damage of the fibers from overstretch [Balzani et al., 2006b, Balzani, 2006, Balzani et al., 2007b] has been considered in computations with the FETI-DP method, for an arterial segment, in [Rheinbach, 2009, Balzani et al., 2007a]. It was observed that it poses no

additional challenge to the solver of the linearized system as it rather decreases the effect of the anisotropy.

Using these results, patient-specific simulations of arteries, neglecting the influence of the blood-flow and a viscoelastic material behavior, were shown in [Balzani et al., 2012]. Viscoelastic effects in fluid-structure interaction, using reduced models, were already considered and compared with experiments in [Čanić et al., 2006]. In [Schröder et al., 2005], it was found that the well-known model of [Holzapfel et al., 2000] also fulfills the polyconvexity condition. A model that goes beyond the concept of hyperelasticity and which includes also the viscoelastic material behavior of arteries is given in [Holzapfel and Gasser, 2001]. This approach is mainly based on the original framework for viscoelasticity at finite strains of [Simo, 1987]. However, the formulation is restricted to a volumetric-isochoric split of the strain energy function and therefore it allows for stresses induced in the fibers by a volumetric strain; cf. [Sansour, 2008]. Furthermore, the viscoelastic behavior is not only associated with the smooth muscle cells as it considers overstresses in the complete isochoric part including the response of the elastin matrix. A unified approach for the inelastic response of arterial tissues is given in [Itskov and Ehret, 2009].

2.2 Continuum mechanics, preliminaries

Let us denote by $\hat{\Omega} \subset \mathbb{R}^3$ and $\Omega_t \subset \mathbb{R}^3$ the reference and current domains configurations, respectively. In the same way, $\hat{\mathbf{x}} \in \hat{\Omega}$ and $\mathbf{x} \in \Omega_t$ are the coordinates of two points belonging to the reference and current configurations. In order to describe the kinematics of the continuum media we may adopt a frame of reference with respect to the $\hat{\mathbf{x}}$ or $\mathbf{x}$ coordinate, yielding to Lagrangian or Eulerian description of the problem, repectively. We can further define a function ϕ representing the motion, being $\phi : \hat{\Omega} \times \mathbb{R}^+ \to \Omega_t \subset \mathbb{R}^3$, such that $\phi(\hat{\mathbf{x}}, t)$ represents a deformation evolving in time. Thanks to this definition, the relations between Lagrangian and Eulerian frames of reference read:

$$
\begin{aligned}
\mathbf{x} &= \phi(\hat{\mathbf{x}}, t), \\
\hat{\mathbf{x}} &= \phi^{-1}(\mathbf{x}, t).
\end{aligned}
\tag{2.1}
$$

During motion and deformation, the displacement experienced by each point $\hat{\mathbf{x}} \in \hat{\Omega}$ is measured by the material displacement field $\hat{\mathbf{d}}_s$ which is defined by $\hat{\mathbf{d}}_s = \mathbf{x} - \hat{\mathbf{x}}$. One of the most important kinematic quantities in the framework of continuum mechanics is the deformation gradient

$$
\mathbf{F} := \frac{\partial \hat{\phi}}{\partial \hat{\mathbf{x}}} = \frac{\partial \hat{\mathbf{d}}_s}{\partial \hat{\mathbf{x}}} + \mathbf{I},
\tag{2.2}
$$

where $\dfrac{\partial \hat{\mathbf{d}}_s}{\partial \hat{\mathbf{x}}}$ represents the material gradient of $\hat{\mathbf{d}}_s$ and $\mathbf{I}$ is the second order identity tensor in $\mathbb{R}^3$. $\mathbf{F}$ locally measures the deformations experienced by the continuous body during its motion. We notice that the Jacobian of transformation (2.1) could also be interpreted as the relative volume increment between current and reference configurations, namely: $\det(\mathbf{F})d\hat{\Omega} = d\Omega$. In the sequel we will suppose that map ϕ^{-1} always exists due to the hypothesis of dealing with continuum media, i.e. during motion the body would not be lacerated, by assuming

$$J := \det(\mathbf{F}) > 0. \tag{2.3}$$

We remark that the case $J < 0$ is not considered physically admissible due to the impenetrability of matter [Holzapfel et al., 2000, Ogden, 1997].

2.3 The equation of motion for a continuous media

In this Section we briefly recall, thanks to the momentum conservation law, the equation of motion for the continuous media with respect to a Lagrangian frame of reference [Gurtin, 1982]. Let us denote by V an arbitrary control volume in the current configuration, and by ∂V its surface boundary. The conservation of momentum reads [Holzapfel et al., 2000]

$$\frac{D}{Dt}\int_V \rho_s \dot{\hat{\mathbf{d}}}_s\, dV = \int_V \rho_s \mathbf{f_s}\, dV + \int_{\partial V} \mathbf{t}\, dS, \tag{2.4}$$

where we indicated with $\mathbf{f_s}$ and $\mathbf{t}$ the force terms per unit mass and per unit surface, respectively. Thanks to the Cauchy relation $\mathbf{t} = \boldsymbol{\sigma}_s \mathbf{n}$, together with the Nanson's formula which relates the element area between the current and the reference configurations

$$\mathbf{n}dS = J\mathbf{F}^{-T}\hat{\mathbf{n}}d\hat{S} \tag{2.5}$$

we may write:

$$\frac{D}{Dt}\int_{\hat{V}} J\rho_S \dot{\hat{\mathbf{d}}}_s\, d\hat{V} = \int_{\hat{V}} J\rho_S \mathbf{f_s}\, d\hat{V} + \int_{\partial\hat{V}} J\boldsymbol{\sigma}_s\mathbf{F}^{-T}\hat{\mathbf{n}}d\hat{S}, \tag{2.6}$$

where we also adopted relation $dV = Jd\hat{V}$. At this point, in order to write the balance of momentum in Lagrangian coordinates we introduce the first Piola-Kirchhoff stress tensor

$$\boldsymbol{\Sigma}_I = J\boldsymbol{\sigma}_s\mathbf{F}^{-T}, \tag{2.7}$$

which represents a tensorial field defined on the reference configuration. By defining $\boldsymbol{\Sigma}_I$ and thanks to the divergence theorem, we rewrite Eq. (2.6) as follows:

$$\frac{D}{Dt} \int_{\hat{V}} \hat{\rho}_S \dot{\hat{\mathbf{d}}}_S \, d\hat{V} = \int_{\hat{V}} \hat{\rho}_S \mathbf{f_s} \, d\hat{V} + \int_{\hat{V}} \hat{\nabla} \cdot \boldsymbol{\Sigma}_I \, d\hat{V}. \tag{2.8}$$

Finally, adopting both the localization argument and the fact that $\hat{V}$ is fixed, we obtain:

$$\hat{\rho}_s \frac{\partial^2 \hat{\mathbf{d}}_s}{\partial t^2} - \hat{\nabla} \cdot \boldsymbol{\Sigma}_I = \hat{\rho}_s \mathbf{f_s}, \tag{2.9}$$

which represents the equation of motion for the continuous media in a Lagrangian frame of reference.

2.4 Constitutive models for the arterial tissue

To complete the derivation of the equation of motion for the continuum media, we need to characterize the constitutive law, i.e. the relationship between stress and strain. Constitutive laws are usually formulated based on empirical observations and they model the material response. The mechanical response of the large arteries wall to a given strain is mainly due to the elastin and collagen components. The former one is responsible for the elastic response in physiological conditions, while the latter activates when the strains reach a certain critical value and it is much stiffer. Furthermore the collagen component is made of fibers, which inhibit the elongation along the fiber direction. To accurately predict the mechanisms of the arterial wall one should take into account these characteristics in the constitutive law. Furthermore, as almost all biological tissues, the arterial wall is incompressible, which introduces another constraint. In literature accurate models for the arterial wall can be found in [Balzani, 2006, Holzapfel et al., 2000, Holzapfel et al., 2002, Zhao et al., 2008, Vorp et al., 1998] and references therein. We refer to [Ogden and Holzapfel, 2006, Balzani, 2006] for a complete overview of the mechanical properties and models. Complex material models, such as inelastic materials, may be found in [Simo and Hughes, 2006].

2.4.1 Isotropic linear elastic material model

In this Section, the description of an isotropic linear elastic material law suitable for the modeling of the mechanical behavior of large arteries is addressed. The material is considered as an isotropic media, thus assuming its mechanical properties independent of the direction. More specifically, isotropic constitutive models are of phenomenological type for which the tissue is assumed to behave as an isotropic material regardless of its fibrous nature. In Eq. (2.9) we observe that the tensor $\boldsymbol{\Sigma}_I$ is not symmetric. Therefore, to write the constitutive relation with respect to a symmetric tensor we introduce the

second Piola-Kirchhoff stress tensor:

$$\boldsymbol{\Sigma}_{II} = \mathbf{F}^{-1}\boldsymbol{\Sigma}_I. \tag{2.10}$$

We notice that $\boldsymbol{\Sigma}_{II}$ is symmetric and it respects the axiom of frame indifference as well. More specifically $\boldsymbol{\Sigma}_{II}$ is independent from rigid body motions (frame indifference): we can explain this concept through the introduction of a rotation tensor $\mathbf{R}$ that is orthogonal ($\mathbf{R}\mathbf{R}^T = \mathbf{I}$); by indicating with $\bar{(\cdot)}$ the rotated entities, we can write:

$$\bar{\boldsymbol{\Sigma}}_{II} = J\bar{\mathbf{F}}^{-1}\bar{\boldsymbol{\sigma}}\bar{\mathbf{F}}^{-T} = J(\mathbf{F}^{-1}\mathbf{R}^T)(\mathbf{R}\boldsymbol{\sigma}\mathbf{R}^T)(\mathbf{R}\mathbf{F}^{-T}) = \boldsymbol{\Sigma}_{II}, \tag{2.11}$$

such that $\bar{\boldsymbol{\Sigma}}_{II} = \boldsymbol{\Sigma}_{II}$. The constitutive law is written using the Green-Lagrange strain tensor:

$$\boldsymbol{\epsilon}_s = \frac{1}{2}(\mathbf{C} - \mathbf{I}), \tag{2.12}$$

where $\mathbf{C} = \mathbf{F}^T\mathbf{F}$ is the right Cauchy-Green deformation tensor. If there exists a scalar valued strain energy function ψ depending on $\boldsymbol{\epsilon}_s$, such that:

$$\frac{\partial\psi(\boldsymbol{\epsilon}_s)}{\partial\boldsymbol{\epsilon}_s} = \boldsymbol{\Sigma}_{II}(\boldsymbol{\epsilon}_s), \tag{2.13}$$

the material is called hyperelastic. Given the second Piola-Kirchhoff stress tensor, the Cauchy stress is computed as follows:

$$\boldsymbol{\sigma}_s = J^{-1}\mathbf{F}\boldsymbol{\Sigma}_{II}\mathbf{F}^T. \tag{2.14}$$

The tensor of elastic moduli $\mathbb{C}$ is then defined as the second derivative of the strain energy ψ with respect to $\boldsymbol{\epsilon}_s$

$$\mathbb{C} = \frac{\partial^2\psi(\boldsymbol{\epsilon}_s)}{\partial\boldsymbol{\epsilon}_s\partial\boldsymbol{\epsilon}_s}. \tag{2.15}$$

The St. Venant-Kirchhoff strain energy function may be used to characterize the behavior of the isotropic media

$$\psi(\boldsymbol{\epsilon}_s) = \frac{1}{2}\boldsymbol{\epsilon}_s : \mathbb{C}\boldsymbol{\epsilon}_s = \frac{\lambda_s}{2}(\text{tr}(\boldsymbol{\epsilon}_s))^2 + \mu_s\text{tr}(\boldsymbol{\epsilon}_s^2), \tag{2.16}$$

where λ_s and μ_s represent the Lamé coefficients defining the mechanical characteristics of the material. In this way, taking the derivative of (2.13) we obtain:

$$\boldsymbol{\Sigma}_{II} = \lambda_s(\text{tr}(\boldsymbol{\epsilon}_s))\mathbf{I} + 2\mu_s\boldsymbol{\epsilon}_{\mathbf{s}}. \tag{2.17}$$

Since expression (2.17) is linear, we may rewrite it into a more compact way:

$$\boldsymbol{\Sigma}_{II} = \mathbb{C} : \boldsymbol{\epsilon}_{\mathbf{s}} \quad (\text{component-wise} \quad \Sigma_{II_{ik}} = \mathbb{C}_{ikrs}\boldsymbol{\epsilon}_{s_{rs}}), \tag{2.18}$$

being $\mathbb{C}$ a fourth-order tensor. Instead of using, as shown in (2.16), the Lamé constants to characterize the St. Venant-Kirchhoff materials, we will refer hereafter to the Young modulus E and the Poisson ratio ν; Eq. (2.19) expresses the relation held between the two sets of coefficients:

$$E = \mu_s \frac{3\lambda_s + 2\mu_s}{\lambda_s + \mu_s}, \qquad \lambda_s = \frac{E\nu}{(1 - 2\nu)(1 + \nu)},$$
$$\nu = \frac{\lambda_s}{2(\lambda_s + \mu_s)}, \qquad \mu_s = \frac{E}{2(1 + \nu)}. \tag{2.19}$$

We remark that the constitutive law introduced is nonlinear in the displacement $\hat{\mathbf{d}}_s$, since both $\boldsymbol{\Sigma}_{II}$ and $\boldsymbol{\epsilon}_s$ are nonlinear in $\mathbf{F}$. Assuming small deformations we further proceed by neglecting the terms which are of order higher than one in $\boldsymbol{\epsilon}_s$, leading to the approximations

$$\boldsymbol{\epsilon}_s = \frac{1}{2}[(\hat{\nabla}\hat{\mathbf{d}}_s)^T + \hat{\nabla}\hat{\mathbf{d}}_s + ((\hat{\nabla}\hat{\mathbf{d}}_s)^T \cdot \hat{\nabla}\hat{\mathbf{d}}_s)] \approx \frac{1}{2}[(\hat{\nabla}\hat{\mathbf{d}}_s)^T + \hat{\nabla}\hat{\mathbf{d}}_s] = \widetilde{\boldsymbol{\epsilon}}_s, \tag{2.20}$$

where $\widetilde{\boldsymbol{\epsilon}}_s$ indicates the symmetric part of the displacement gradient, and

$$\lambda_s(\mathrm{tr}(\boldsymbol{\epsilon}_s))\mathbf{I} + 2\mu_s\boldsymbol{\epsilon}_s = \boldsymbol{\Sigma}_{II} = \mathbf{F}^{-1}\boldsymbol{\Sigma}_I \approx \boldsymbol{\Sigma}_I. \tag{2.21}$$

Thanks to the simplifications introduced, we obtain the equation of the linear elasticity:

$$\frac{\partial^2 \hat{\mathbf{d}}_s}{\partial t^2} - \hat{\nabla} \cdot (\lambda_s(\mathrm{tr}(\widetilde{\boldsymbol{\epsilon}}_s))\mathbf{I} + 2\mu_s\widetilde{\boldsymbol{\epsilon}}_{\mathbf{s}}) = \hat{\rho}_s\mathbf{f}_s. \tag{2.22}$$

We remark that Eq. (2.22) models the behavior of continuum media under the hypothesis of small strain, small rotations.

2.4.2 Anisotropic polyconvex hyperelastic material model

In this Section the description of an anisotropic polyconvex hyperelastic material model for the vessel wall is addressed. This model, which was originally proposed in [Balzani, 2006], is formulated in terms of classical continuum mechanics at finite strains, where the deformation gradient $\mathbf{F}$ and the right Cauchy-Green tensor $\mathbf{C} = \mathbf{F}^T\mathbf{F}$ are considered. In order to account for the anisotropy resulting mainly from the reinforcing fibers (collagen and smooth muscle cells) the concept of structural tensors is applied, see, e.g., [Boehler, 1987]. In arteries mainly two fiber family directions are arranged cross-wise helically around the wall. By assuming a weak interaction of these two families the standard approach is to consider an additively decoupled energy ψ consisting of an isotropic part ψ^{isot} for the elastin-rich ground substance and the superposition of two transversely isotropic parts $\psi_{(a)}^{\mathrm{ti},\infty}$ for the individual fiber family (a) with direction vector $\mathbf{a}_{(a)}$. The isotropic energy is considered to depend on the right Cauchy-Green tensor in order

to a priori fulfill the objectivity condition, i.e., $\psi^{\text{isot}} := \psi^{\text{isot}}(\mathbf{C})$. For the transversely isotropic part, an additional argument tensor, the structural tensor for transverse isotropy $\mathbf{M}_{(a)} = \mathbf{a}_{(a)} \otimes \mathbf{a}_{(a)}$, is considered such that $\psi_{(a)}^{\text{ti},\infty} := \psi_{(a)}^{\text{ti},\infty}(\mathbf{C}, \mathbf{M}_{(a)})$. In order to arrive at a more convenient construction of specific energy functions, a coordinate-invariant representation in terms of the principal and mixed invariants

$$I_1 = \text{tr}(\mathbf{C}) \,, \; I_2 = \text{tr}(\text{Cof}(\mathbf{C})) \,, \; I_3 = \det(\mathbf{C}) \tag{2.23}$$

and

$$J_4^{(a)} = \text{tr}(\mathbf{C}\mathbf{M}_{(a)}) \,, \; J_5^{(a)} = \text{tr}(\mathbf{C}^2\mathbf{M}_{(a)}), \quad a = 1, 2 \tag{2.24}$$

is considered. For the isotropic part, we focus on a Neo-Hooke-type representation and skip the dependency of I_2. For the transversely isotropic part note that the fifth invariant is not polyconvex by itself and thus the alternative invariant

$$K_3^{(a)} := I_1 J_4^{(a)} - J_5^{(a)}, \quad a = 1, 2 \tag{2.25}$$

is considered, see [Schröder and Neff, 2003]. Finally, the polynomial basis for the representation of the strain energy for two fiber families reads $\mathcal{P} := \{I_1, I_3, K_3^{(1)}, K_3^{(2)}\}$ and the structure of the strain energy is

$$\psi(\mathbf{C}, \mathbf{M}_{(1)}, \mathbf{M}_{(2)}) = \psi^{\text{isot}}(I_1, I_3) + \sum_{a=1}^{2} \psi_{(a)}^{\text{ti},\infty}(I_1, K_3^{(a)}), \tag{2.26}$$

cf. [Holzapfel et al., 2000]. The polyconvexity condition in the sense of [Ball, 1977] is the essential condition to ensure the existence of minimizers and material stability, cf. [Schröder et al., 2005], where the latter aspect is analyzed in terms of an accompanied localization analysis. Therefore, polyconvex energy functions have to be considered and thus, the Neo-Hooke-type function is considered for the isotropic part and for the transversely isotropic part the function for arterial tissues proposed in [Balzani et al., 2006a] is used, see also [Balzani et al., 2008], where this function is also applied in an engineering context. The two parts of the strain energy function are then given by

$$\psi^{\text{isot}} = \epsilon_1 \left(I_3^{\epsilon_2} + I_3^{-\epsilon_2} - 2 \right) + c_1 \left(I_1 I_3^{-1/3} - 3 \right) \tag{2.27}$$

and

$$\psi_{(a)}^{ti,\infty} = \alpha_1 \left\langle K_3^{(a)} - 2 \right\rangle^{\alpha_2}, \tag{2.28}$$

where the restrictions $c_1 > 0, \epsilon_1 > 0, \epsilon_2 > 1, \alpha_1 > 0$ and $\alpha_2 > 2$ ensure polyconvexity and smooth tangent moduli; the Macaulay brackets are defined as $\langle (\bullet) \rangle = 1/2(|(\bullet)| + (\bullet))$. Note that a volumetric-isochoric split is considered for the isotropic function, but not

for the transversely isotropic part in order to avoid the unphysical behavior observed in [Sansour, 2008]. The Cauchy stresses can then be computed by $\boldsymbol{\sigma} = J^{-1}\mathbf{F}\boldsymbol{\Sigma}_{II}\mathbf{F}^T$, wherein the second Piola-Kirchhoff stresses are obtained by deriving the strain energy function with respect to the right Cauchy-Green tensor, i.e., $\boldsymbol{\Sigma}_{II} = 2\partial_{\mathbf{C}}\psi(\mathbf{C})$. We remark that the hyperelastic parameters c_1, ϵ_1, ϵ_2, α_1 and α_2 that will be used for the numerical simulation of Chapter 4 are taken from [Brands et al., 2008], where they have been adjusted to experimental data of a media of a human abdominal aorta with the side constraint that an improved robustness of numerical computations can be achieved.

3 Parallel preconditioners for fluid-structure interaction problems

In Chapters 1 and 2 we addressed the models adopted for the blood (the fluid) and the arterial wall (the structure), respectively. They serve now, together with suitable coupling conditions, as the two main components for the set up of the fluid-structure interaction problem. Indeed, in this Chapter we consider fluid-structure interaction problems to model the blood flow dynamics in arteries undergoing relatively large deformations, with the focus being on their efficient numerical solution in a parallel setting.

This Chapter is organized as follows. In Section 3.1 we provide an introduction to FSI problems in the context of hemodynamics. In Section 3.2 we recall the fluid-structure interaction model adopted in this work while in Sections 3.3 and 3.4 we introduce the weak form of the equations and their spatial and temporal discretizations, respectively. Then, in Section 3.5, we address the numerical solution of the resulting nonlinear FSI system by the Newton method. In Section 3.6, we focus on the preconditioning strategy: in particular, we address the description of the preconditioner FaCSI [Deparis et al., 2015b] and how it compares with preconditioners devised from other condensed formulations. Finally, in Section 3.7, after assessing the weak and strong scalability properties of FaCSI on a benchmark problem, we apply it in the context of large- scale simulations of the blood flow in a patient-specific femoropopliteal bypass where about 150 milions of degrees of freedom are used.

The remaining part of this Chapter is taken from [Deparis et al., 2015b], with exception of a new mesh convergence study that is reported in subsection 3.7.1.

3.1 Preliminaries

The mechanics of an internal blood flow interacting with an elastic arterial wall can be modeled by a coupled nonlinear system of partial differential equations describing the fluid flow and the deformation of the wall structure together with suitable coupling conditions. A problem of this type is commonly referred to as fluid-structure interaction problem.

We are interested in the specific situation where the fluid is formulated in an Arbitrary Lagrangian Eulerian (ALE) frame of reference as in, e.g., [Nobile., 2001, Formaggia et al., 2009, Crosetto et al., 2011, Bazilevs et al., 2013a]. An alternative approach to the ALE would be to formulate the FSI problem in a fully Eulerian frame of reference [Cottet et al., 2008, Wang et al., 2008, Richter, 2013], i.e. on a fixed fluid domain, but it additionally requires one to keep track of the position of the fluid-structure interface. In [Dunne, 2007, Rannacher and Richter, 2010, Richter, 2010], a fully Eulerian formulation of FSI is used in two dimensions to avoid the degeneration of the ALE mapping and to facilitate mesh adaptivity. Another approach is that of the immersed boundary method, where the fluid is written in Eulerian coordinates, while the structure is still in a Lagrangian frame of reference [Peskin, 2002, Mittal and Iaccarino, 2005, Boffi et al., 2011]. A further alternative approach to ALE methods may be based on the use of the Extended Finite Element method (XFEM) [Gerstenberger and Wall, 2008, Wall et al., 2010, Mayer et al., 2010]. See, e.g., [Formaggia et al., 2009, Bazilevs et al., 2013a] and references therein for an overview of the subject.

The use of an ALE formulation for the fluid, together with a Lagrangian frame for the structure, yields an FSI problem that is composed by three subproblems, namely the *fluid problem*, which allows for the computation of the velocity and pressure inside the fluid domain, the *solid problem*, which describes the deformation of the vessel wall, and the so-called *geometry problem*, which accounts for the change in time of the computational fluid domain. A modular approach to solve the FSI problem would consist in dealing with the three problems separately. For example, one can consider the fluid-structure coupled problem using different type of interface conditions to ensure the coupling: Dirichlet-Neumann [Matthies et al., 2006, Küttler and Wall, 2008b, Langer and Yang, 2012, Langer and Yang, 2015], Robin-Robin [Badia et al., 2008b, Badia et al., 2009, Nobile et al., 2014], Robin-Neumann [Fernández et al., 2015], Neumann-Neumann, FETI [Deparis et al., 2006b], etc. [Toselli and Widlund, 2005]. A further approach makes use of a Steklov-Poincaré formulation [Deparis et al., 2006a] to enforce the coupling on the fluid-structure interface. Furthermore, one can also solve the coupled fluid-structure problem and, separately, the geometry one, therefore in two separate steps, as in the case of the so-called Geometry Convective Explicit (GCE) scheme [Badia et al., 2008a, Crosetto et al., 2011].

Extensive work has been carried out on the development of algorithms for the solution

of time-dependent FSI problems in the framework of biomechanics. The approaches are typically categorized either as segregated or as monolithic schemes. Segregated schemes can range from loosely coupled iterative schemes, such as simple, possibly accelerated, fixed point iterations, to schemes with a much stronger coupling which still use separate solvers for fluid and structure. Conversely, in monolithic schemes all the unknowns of the FSI problem are solved simultaneously.

Monolithic algorithms were investigated, e.g., in [Bazilevs et al., 2008, Hron and Turek, 2006, Küttler et al., 2010, Gee et al., 2010, Barker and Cai, 2010, Crosetto et al., 2011, Grandperrin, 2013, Wu and Cai, 2014]. In [Deparis et al., 2015c], we have recently compared the performance of the strongly coupled Steklov-Poincaré algorithm using the Dirichlet-Neumann, Neumann-Dirichlet, and Neumann-Neumann preconditioners have been compared with those of a monolithic approach preconditioned by a Dirichlet-Neumann preconditioner.

In this thesis, we use a monolithic solution algorithm and therefore we consider the coupled problem as a single system involving all the state variables, including the fluid domain displacement. This system is nonlinear because of the convective term in the Navier-Stokes equations, the possible nonlinearity of the constitutive law used to model the vessel wall, and the changing-in-time fluid computational domain. The time discretization of the fluid problem is carried out by second order backward differentiation formulas, while for the structure we use the Newmark method. The spatial discretization is based on finite elements: we use $\mathbb{P}2$-$\mathbb{P}1$ Lagrange polynomials for the approximation of the fluid velocity and pressure, respectively, $\mathbb{P}2$ for the structure displacement and $\mathbb{P}2$ for the ALE map, using conforming meshes at the fluid-structure interface.

After spatial and temporal discretization we solve the fully coupled nonlinear FSI system in its implicit form by using the Newton method with an exact Jacobian system, as in, e.g., [Fernández and Moubachir, 2003, Heil, 2004, Tezduyar et al., 2006, Dettmer and Perić, 2007, Bazilevs et al., 2008, Heil et al., 2008, Barker and Cai, 2010, Küttler et al., 2010, Gee et al., 2010, Wu and Cai, 2014]. Other strategies may be employed to linearize the nonlinear FSI system: for instance, one can use relaxed fixed point iterations using Aitken acceleration [Le Tallec and Mouro, 2001, Causin et al., 2005, Küttler and Wall, 2008b, Matthies et al., 2006] or inexact Newton methods [Gerbeau and Vidrascu, 2003, Degroote et al., 2009], which may not converge or converge only linearly.

The numerical solution of the fully coupled 3D FSI problem is computationally expensive; to lower the time to solution, the use of an efficient preconditioner is crucial. In this regard, several strategies have been proposed in, e.g., [Heil, 2004, Badia et al., 2008b, Badia et al., 2008c, Gee et al., 2010, Barker and Cai, 2010, Crosetto et al., 2011, Grandperrin, 2013, Wu and Cai, 2014]. Overlapping Schwarz methods within monolithic approaches were studied in different regimes of severity of the added-mass effect in [Crosetto et al., 2011] confirming successful results for 2D obtained already reported in [Barker and Cai,

2010]. A monolithic FSI approach coupling nonlinear hyperelastic solid models with Navier-Stokes is presented in [Hron and Turek, 2006], considering the incompressible case for the solid. For the solution of the linear saddle point systems a sparse direct solver, an ILU preconditioner, and a geometric multigrid method with a Vanka-type smoother are considered. A block preconditioner with Schur complements for the monolithic system is presented in [Janssen and Wick, 2010]. A scalable monolithic solver for an FSI problem coupling blood flow with a conforming arterial wall in 2D is presented [Barker, 2009, Barker and Cai, 2010]. There, a Newton scheme with an explicitly computed Jacobian is applied; see also [Fernández and Moubachir, 2003, Bazilevs et al., 2008, Barker and Cai, 2010]. For the solution of the FSI linearized systems, in [Barker and Cai, 2010] the authors use a hybrid multilevel Schwarz preconditioner which uses restricted additive Schwarz on the fine level and multiplicative Schwarz on the coarse level. The parallel Newton-Krylov-Schwarz approach for the monolithic system is extended to three dimensions in [Wu and Cai, 2014], and scalability is shown for up to three thousand processors. Parallel algebraic multigrid preconditioners have recently been applied to fully monolithic ALE formulations of FSI problems in the setting of biomechanics, see, e.g., [Gee et al., 2010, Wiesner, 2015, Mayr et al., 2015]. Specifically, in [Gee et al., 2010], the authors propose two preconditioners that apply algebraic multigrid techniques to the linearized monolithic FSI system obtained after spatial and temporal discretizations.

In this Chapter, we focus on parallel block preconditioners for FSI problems. Indeed, the mixed nature of the equations involving fluid, structure, and geometry motivates the development of preconditioners that are built upon the specific features of each of these three subproblems. These preconditioners enjoy the same modularity property of fully segregated methods where each subproblem is solved separately. Our block preconditioner, that we named FaCSI, is constructed through the following steps. First, we consider a block Gauss-Seidel approximation of the FSI Jacobian matrix: this amounts to drop the block associated to the kinematic coupling condition. This simplification can be reinterpreted as imposing (one-sided) Dirichlet boundary conditions on the structure displacement at the fluid-structure interface. Then, by a proper matrix factorization we identify three block-triangular matrices: the first matrix refers solely to the structural problem, the second one solely to the geometry and the last solely to the fluid. Special attention is paid to the fluid matrix whose saddle-point structure features the additional presence of two coupling blocks: after carrying out static condensation of the interface fluid variables, we use a SIMPLE preconditioner [Patankar and Spalding, 1972, Pernice and Tocci, 2001, Elman et al., 2006, Elman et al., 2008, ur Rehman et al., 2008, ur Rehman et al., 2009, Deparis et al., 2014b] on the reduced fluid matrix. Finally, on the approximate factorization, FaCSI is obtained by replacing the diagonal blocks referring to each physical subproblem by suitable parallel preconditioners, e.g, those based on domain decomposition or multigrid strategies. In spite of their similarities, we show in Section 3.6.2 that FaCSI differs from the block Gauss-Seidel preconditioner proposed in [Gee et al., 2010] .

3.2 Fluid structure interaction model

The fluid-structure interaction model used here consists in a fluid governed by the incompressible Navier-Stokes equations written in the Arbitrary Lagrangian Eulerian (ALE) frame of reference, coupled with a linear elastic structure, see, e.g, [Crosetto et al., 2011, Reymond et al., 2013]. It is convenient to separate the FSI problem into three coupled subproblems, namely the fluid problem, the structure problem, and the geometry problem. The latter determines the displacement of the fluid domain $\hat{\mathbf{d}}_f$ which defines in turn the ALE map. We consider $\hat{\mathbf{d}}_f$ as an harmonic extension to the fluid
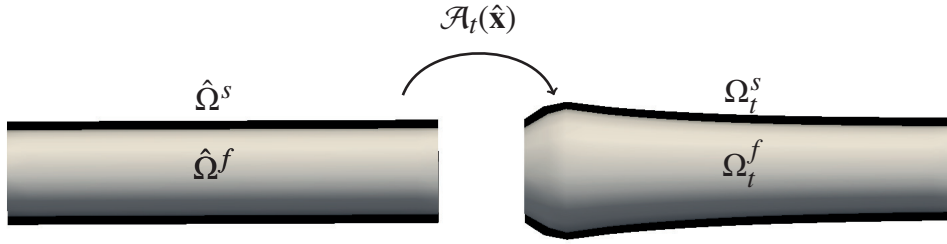
Figure 3.1: The ALE frame of reference.

reference domain $\hat{\Omega}^f \subset \mathbb{R}^3$ of the trace of the solid displacement $\hat{\mathbf{d}}_s$ at the reference fluid-structure interface $\hat{\Gamma}$:

$$
\begin{cases}
-\Delta \hat{\mathbf{d}}_f = 0 & \text{in } \hat{\Omega}^f, & \text{(3.1a)} \\
\hat{\mathbf{d}}_f = \hat{\mathbf{d}}_s & \text{on } \hat{\Gamma}. & \text{(3.1b)}
\end{cases}
$$

The solution of the geometry problem defines the ALE map $\mathcal{A}_t(\hat{\mathbf{x}}) = \hat{\mathbf{x}} + \hat{\mathbf{d}}_f(\hat{\mathbf{x}}, t)$ $\forall \hat{\mathbf{x}} \in \hat{\Omega}^f$, and the current fluid domain configuration. The Navier-Stokes equations for an incompressible fluid written in ALE coordinates read:

$$
\begin{cases}
\rho_f \left.\dfrac{\partial \mathbf{u}_f}{\partial t}\right|_{\hat{\mathbf{x}}} + \rho_f((\mathbf{u}_f - \mathbf{w}) \cdot \nabla)\mathbf{u}_f - \nabla \cdot \boldsymbol{\sigma}_f = 0 & \text{in } \Omega_t^f, & \text{(3.2a)} \\[2mm]
\nabla \cdot \mathbf{u}_f = 0 & \text{in } \Omega_t^f, & \text{(3.2b)} \\[2mm]
\mathbf{u}_f = \mathbf{h}_f & \text{on } \Gamma_D^f, \\[2mm]
\boldsymbol{\sigma}_f \mathbf{n}_f = \mathbf{g}_f & \text{on } \Gamma_N^f, \\[2mm]
\mathbf{u}_f \circ \mathcal{A}_t = \dfrac{\partial \hat{\mathbf{d}}_s}{\partial t} & \text{on } \hat{\Gamma}, & \text{(3.2c)}
\end{cases}
$$

where $\left.\frac{\partial}{\partial t}\right|_{\hat{\mathbf{x}}} = \frac{\partial}{\partial t} + \mathbf{w} \cdot \nabla$ is the ALE derivative, $\mathbf{w}(\mathbf{x}) = \frac{\partial \mathcal{A}_t(\mathbf{x})}{\partial t}$ is fluid domain velocity, $\mathbf{u}_f$ and p_f are the velocity and pressure of the fluid, respectively. In (3.2a) we denoted by ρ_f the density of the fluid and by $\boldsymbol{\sigma}_f$ the Cauchy stress tensor

$$
\boldsymbol{\sigma}_f = \mu_f(\nabla \mathbf{u}_f + (\nabla \mathbf{u}_f)^T) - p_f \mathbf{I},
$$

with $\mathbf{I}$ being the identity tensor, μ_f the dynamic viscosity of the fluid, and $\mathbf{n}_f$ the outward unit normal vector to $\partial\Omega_t^f$. The functions $\mathbf{h}_f$ and $\mathbf{g}_f$ indicate the Dirichlet and Neumann data applied at the the Dirichlet and Neumann boundaries Γ_D^f and Γ_N^f, respectively, of Ω_t^f. From (3.1b), (3.2c) and the definition of $\mathbf{w}$, we have that

$$\mathbf{u}_f \circ \mathcal{A}_t = \mathbf{w} \quad \text{on } \hat{\Gamma}. \tag{3.3}$$

We model the structure by linear elasticity in a Lagrangian frame of reference (see Chapter 2):

$$\begin{cases} \hat{\rho}_s \dfrac{\partial^2 \hat{\mathbf{d}}_s}{\partial t^2} - \nabla_{\hat{\mathbf{x}}} \cdot \boldsymbol{\Pi}(\hat{\mathbf{d}}_s) = 0 & \text{in } \hat{\Omega}^s, & \text{(3.4a)} \\[2mm] \hat{\mathbf{d}}_s = \mathbf{h}_s & \text{on } \hat{\Gamma}_D^s, \\[2mm] \boldsymbol{\Pi}(\hat{\mathbf{d}}_s)\hat{\mathbf{n}}_s = 0 & \text{on } \hat{\Gamma}_N^s, \\[2mm] \boldsymbol{\Pi}(\hat{\mathbf{d}}_s)\hat{\mathbf{n}}_s + \hat{\boldsymbol{\sigma}}_f \hat{\mathbf{n}}_f = 0 & \text{on } \hat{\Gamma}. & \text{(3.4b)} \end{cases}$$

Here $\hat{\mathbf{n}}_s$ and $\hat{\mathbf{n}}_f$ represent the outward unit normal vector to $\partial\hat{\Omega}_s$ and $\partial\hat{\Omega}_f$, respectively, $\hat{\boldsymbol{\sigma}}_f = (\det[\mathbf{F}])\,\mathbf{F}^{-T}\,\boldsymbol{\sigma}_f$ and $\mathbf{F} = \mathbf{I} + \nabla_{\hat{\mathbf{x}}}\hat{\mathbf{d}}_s$ is the deformation gradient tensor. The function $\mathbf{h}_s$ indicates the Dirichlet data applied at the Dirichlet boundary Γ_D^s of $\hat{\Omega}^s$. The material is characterized by the Young modulus E_s and the Poisson ratio ν_s, which define in turn the first Piola-Kirchhoff stress tensor

$$\boldsymbol{\Pi}(\hat{\mathbf{d}}_s) = \lambda_s \operatorname{Tr}\left(\frac{\nabla\hat{\mathbf{d}}_s + (\nabla\hat{\mathbf{d}}_s)^T}{2}\right)\mathbf{I} + \mu_s(\nabla\hat{\mathbf{d}}_s + (\nabla\hat{\mathbf{d}}_s)^T),$$

where

$$\lambda_s = \frac{E_s\nu_s}{(1-2\nu_s)(1+\nu_s)} \quad \text{and} \quad \mu_s = \frac{E_s}{2(1+\nu_s)}.$$

The coupling between these three subproblems is ensured by imposing the geometry adherence, the continuity of the velocity and the continuity of the normal component of the stresses at the interface through Equations (3.1b), (3.2c), and (3.4b), respectively. The resulting system is nonlinear due to the convective term in the fluid momentum equation, to the possible nonlinear material model and to the moving fluid domain.

3.3 Weak formulation

We follow [Nobile., 2001, Le Tallec and Mouro, 2001] to derive the weak form of the FSI problem in the nonconservative form. The velocity coupling condition is imposed strongly, while the continuity of the normal component of the stresses is imposed in weak

form. Let us introduce the following functional spaces:

$$U^f = \{\mathbf{v} = \hat{\mathbf{v}} \circ \mathcal{A}_t^{-1} \mid \hat{\mathbf{v}} \in [H^1(\hat{\Omega}^f)]^3\},$$
$$U_D^f = \{\mathbf{v} = \hat{\mathbf{v}} \circ \mathcal{A}_t^{-1} \mid \hat{\mathbf{v}} \in [H^1(\hat{\Omega}^f)]^3, \hat{\mathbf{v}} = 0 \text{ on } \Gamma_D^f\},$$
$$Q^f = \{q = \hat{q} \circ \mathcal{A}_t^{-1} \mid \hat{q} \in L^2(\hat{\Omega}^f)\},$$
$$U^s = [H^1(\hat{\Omega}^s)]^3, \ U_D^s = \{\mathbf{v} \in [H^1(\hat{\Omega}^s)]^3 \mid \mathbf{v} = 0 \text{ on } \Gamma_D^s\},$$
$$U^g = [H^1(\hat{\Omega}^f)]^3, \ U_D^g = \{\mathbf{v} \in [H^1(\hat{\Omega}^f)]^3 \mid \mathbf{v} = 0 \text{ on } \Gamma_{fixed}^f\},$$
$$U^\lambda = [H^{-1/2}(\hat{\Gamma})]^3.$$

Γ_{fixed}^f is the part of the fluid boundary $\hat{\Omega}^f$ where the domain motion is prescribed (e.g. when a portion of the fluid domain boundary is fixed). The weak form of the fluid and structure equations is standard [Formaggia et al., 2009]. We introduce an auxiliary variable $\boldsymbol{\lambda} \in U^\lambda$

$$\boldsymbol{\lambda} := \hat{\sigma}_f \hat{\mathbf{n}}_f = -\Pi(\hat{\mathbf{d}}_s)\hat{\mathbf{n}}_s \qquad \text{in } U^\lambda, \tag{3.5}$$

that can be regarded as a Lagrange multiplier used to enforce the continuity of the velocity at the interface.

We recall the notation for the Dirichlet boundary data for the fluid, structure and geometry subproblem: $\mathbf{h}_f : \Gamma_D^f \to \mathbb{R}^2$, $\mathbf{h}_s : \Gamma_D^s \to \mathbb{R}^2$, $\mathbf{h}_g : \Gamma_{fixed}^f \to \mathbb{R}^2$, respectively. The weak form of the FSI problem reads: for all $t \in (0, T]$, find $\mathbf{u}_f \in U^f$ such that $\mathbf{u}_f = \mathbf{h}_f$ on Γ_D^f, $p_f \in Q^f$, $\hat{\mathbf{d}}_s \in U^s$ such that $\hat{\mathbf{d}}_s = \mathbf{h}_s$ on Γ_D^s, $\hat{\mathbf{d}}_f \in U^g$ such that $\hat{\mathbf{d}}_f = \mathbf{h}_g$ on Γ_{fixed}^f, and $\boldsymbol{\lambda} \in U^\lambda$ satisfying

$$\int_{\Omega_t^f} \left(\rho_f \frac{\partial \mathbf{u}_f}{\partial t}\bigg|_{\hat{\mathbf{x}}} \cdot \mathbf{v}_f + \rho_f((\mathbf{u}_f - \mathbf{w}) \cdot \nabla)\mathbf{u}_f \cdot \mathbf{v}_f + \boldsymbol{\sigma}_f : \nabla \mathbf{v}_f \right) d\Omega_t^f + \int_{\hat{\Gamma}} \boldsymbol{\lambda} \cdot (\mathbf{v}_f \circ \mathcal{A}_t) \, d\hat{\gamma}$$

$$= \int_{\Gamma_N^f} \mathbf{g}_f \cdot \mathbf{v}_f \, d\gamma \qquad \forall \mathbf{v}_f \in U_D^f,$$

$$\int_{\Omega_t^f} q \, \nabla \cdot \mathbf{u}_f \, d\Omega_t^f = 0 \qquad \forall q \in Q^f, \tag{3.6}$$

$$\int_{\hat{\Omega}^s} \left(\hat{\rho}_s \frac{\partial^2 \hat{\mathbf{d}}_s}{\partial t^2} \cdot \mathbf{v}_s + \Pi(\hat{\mathbf{d}}_s) : \nabla_{\hat{\mathbf{x}}} \mathbf{v}_s \right) d\hat{\Omega}^s - \int_{\hat{\Gamma}} \boldsymbol{\lambda} \cdot \mathbf{v}_s \, d\hat{\gamma} = \int_{\Gamma_N^s} \mathbf{g}_s \cdot \mathbf{v}_s \, d\gamma \qquad \forall \mathbf{v}_s \in U_D^s,$$

$$\int_{\hat{\Gamma}} (\mathbf{u}_f \circ \mathcal{A}_t) \cdot \boldsymbol{\eta} \, d\gamma - \int_{\hat{\Gamma}} \frac{\partial \hat{\mathbf{d}}_s}{\partial t} \cdot \boldsymbol{\eta} \, d\gamma = 0 \qquad \forall \boldsymbol{\eta} \in [H^{-1/2}(\hat{\Gamma})]^3,$$

$$\int_{\hat{\Gamma}} \nabla_{\hat{\mathbf{x}}} \hat{\mathbf{d}}_f : \nabla_{\hat{\mathbf{x}}} \mathbf{v}_g \, d\hat{\Omega}^f = 0 \qquad \forall \mathbf{v}_g \in U_D^g,$$

$$\hat{\mathbf{d}}_f = \hat{\mathbf{d}}_s \qquad \text{on } \hat{\Gamma},$$

where $\mathbf{w} = \frac{\partial \hat{\mathbf{d}}_f}{\partial t}$ represents the rate of deformation of the fluid domain. In system (3.6)

integrals on $\hat{\varGamma}$ should be intended in the sense of the duality.

3.4 Temporal and spatial discretizations

We consider a Fully Implicit (FI) scheme for which all the nonlinearities are treated implicitly. We discretize the time derivative of the fluid problem by second order backward differentiation formulas [Gervasio et al., 2006, Forti and Dedè, 2015]

$$
\left.\frac{\partial \mathbf{u}_f}{\partial t}(t^{n+1})\right|_{\hat{\mathbf{x}}} \approx \frac{3\mathbf{u}_f^{n+1} - 4\mathbf{u}_f^n + \mathbf{u}_f^{n-1}}{2\Delta t}. \tag{3.7}
$$

The time discretization of the structural problem is carried out by the Newmark method [Newmark, 1959, Hughes, 2012]

$$
\frac{\partial^2 \hat{\mathbf{d}}_s}{\partial t^2}(t^{n+1}) \approx \frac{1}{\beta \Delta t^2}\hat{\mathbf{d}}_s^{n+1} - \frac{1}{\beta \Delta t^2}(\hat{\mathbf{d}}_s^n + \Delta t\,\dot{\hat{\mathbf{d}}}_s^n) - \frac{1-2\beta}{2\beta}\,\ddot{\hat{\mathbf{d}}}_s^n, \tag{3.8}
$$

where:

$$
\ddot{\hat{\mathbf{d}}}_s^n = \frac{1}{\beta \Delta t^2}\hat{\mathbf{d}}_s^n - \frac{1}{\beta \Delta t^2}(\hat{\mathbf{d}}_s^{n-1} + \Delta t\,\dot{\hat{\mathbf{d}}}_s^{n-1}) - \frac{1-2\beta}{2\beta}\,\ddot{\hat{\mathbf{d}}}_s^{n-1}, \tag{3.9}
$$

$$
\dot{\hat{\mathbf{d}}}_s^n = \dot{\hat{\mathbf{d}}}_s^{n-1} + \Delta t\,(\gamma\,\ddot{\hat{\mathbf{d}}}_s^n + (1-\gamma)\,\ddot{\hat{\mathbf{d}}}_s^{n-1}). \tag{3.10}
$$

We choose the coefficients $\gamma = 0.5$ and $\beta = 0.25$ such that the scheme is unconditionally stable and second order. In space, we consider a Galerkin finite elements approximation using $\mathbb{P}2$-$\mathbb{P}1$ Lagrange polynomials for the representation of the fluid variables $\mathbf{u}_f$ and p_f, respectively, $\mathbb{P}2$ for the structure displacement $\hat{\mathbf{d}}_s$, and $\mathbb{P}2$ for the harmonic extension $\hat{\mathbf{d}}_f$. At each time step, the resulting nonlinear system to be solved may be rewritten as

$$
\begin{pmatrix}
S(\hat{\mathbf{d}}_s^{n+1}) & + & 0 & + & 0 & - I_{\varGamma s}^T \boldsymbol{\lambda}^{n+1} \\
-I_{\varGamma s}\hat{\mathbf{d}}_s^{n+1} & + G(\hat{\mathbf{d}}_f^{n+1}) + & 0 & + & 0 \\
0 & + & 0 & + F(\mathbf{u}_f^{n+1}, p_f^{n+1}, \hat{\mathbf{d}}_f^{n+1}) + I_{\varGamma f}^T \boldsymbol{\lambda}^{n+1} \\
-\frac{\gamma}{\beta \Delta t} I_{\varGamma s}\hat{\mathbf{d}}_s^{n+1} + & 0 & + & I_{\varGamma f}\mathbf{u}_f^{n+1} & + & 0
\end{pmatrix}
=
\begin{pmatrix}
\mathbf{b}_s \\
0 \\
\mathbf{b}_f \\
\mathbf{b}_c
\end{pmatrix}. \tag{3.11}
$$

We denoted by $\hat{\mathbf{d}}_s^{n+1}$, $\hat{\mathbf{d}}_f^{n+1}$, $\mathbf{u}_f^{n+1}$, p_f^{n+1}, and $\boldsymbol{\lambda}^{n+1}$, the unknown displacement of the structure, the displacement of the fluid domain, the velocity and pressure of the fluid, and the Lagrange multipliers, respectively. We make use of an augmented formulation wherein the vector of Lagrange multipliers $\boldsymbol{\lambda}^{n+1}$ is used to impose the continuity of the velocity at the fluid-structure interface. We notice that the Lagrange multipliers may formally be removed from the set of unknowns of the problem by static condensation, as in [Gee et al., 2010, Mayr et al., 2015]. However, we remark that we do not perform static condensation at this stage because it would lead to additional implementation

difficulties in our code.

The diagonal blocks on the left hand side of (3.11) account for the discretized solid, geometry and fluid problems. We remark that F is nonlinear due to the convective term and the fact that fluid domain moves. The matrices $I_{\Gamma f}$ and $I_{\Gamma s}$ are the restriction of fluid and structure vectors to the interface and in (3.11) account for the continuity of velocities and the geometry adherence, which are imposed strongly. Their transposes account for the continuity of the normal component of the stresses, which is imposed weakly. Last row of (3.11) represents the discretized kinematic coupling condition at the fluid-structure interface:

$$I_{\Gamma f}\mathbf{u}_f - \frac{\gamma}{\beta\Delta t}I_{\Gamma s}\hat{\mathbf{d}}_s^{n+1} = \mathbf{b}_c, \tag{3.12}$$

where

$$\mathbf{b}_c = I_{\Gamma s}\dot{\hat{\mathbf{d}}}_s^n - \frac{\gamma}{\beta\Delta t}(I_{\Gamma s}\hat{\mathbf{d}}_s^n + \Delta t\, I_{\Gamma s}\dot{\hat{\mathbf{d}}}_s^n) - \Delta t\,\gamma\frac{1-2\beta}{2\beta}\,I_{\Gamma s}\ddot{\hat{\mathbf{d}}}_s^n + \Delta t\,(1-\gamma)\,I_{\Gamma s}\ddot{\hat{\mathbf{d}}}_s^n. \tag{3.13}$$

The ALE velocity $\mathbf{w}$ is approximated by second order backward differentiation formulas

$$\mathbf{w}(t^{n+1}) = \frac{d\hat{\mathbf{d}}_f}{dt}(t^{n+1}) \approx \frac{3\hat{\mathbf{d}}_f^{n+1} - 4\hat{\mathbf{d}}_f^n + \hat{\mathbf{d}}_f^{n-1}}{2\Delta t}. \tag{3.14}$$

We notice that this scheme is not compatible with Eq. (3.10) and therefore, at the discrete level, $\mathbf{w} \neq \mathbf{u}_f \circ \mathcal{A}_t$ on $\hat{\Gamma}$. To impose this equality one should use the Newmark formulas (3.9) and (3.10) also for the approximation of $\mathbf{w}$.

3.5 Solution algorithms for the FSI problem

We solve the nonlinear fully coupled FSI problem (3.11) using the Newton method as in, e.g., [Fernández and Moubachir, 2003, Tezduyar et al., 2006, Heil, 2004, Bazilevs et al., 2008]. Let us denote the solution of (3.11) at time $t^n = n\,\Delta t$ by $\mathbf{X}^n = (\hat{\mathbf{d}}_s^n, \hat{\mathbf{d}}_f^n, \mathbf{u}_f^n, p_f^n, \boldsymbol{\lambda}^n)^T$. At each timestep, we compute a sequence of approximations $\mathbf{X}_1^{n+1}$, $\mathbf{X}_2^{n+1}$, etc. until the numerical solution converges up to a prescribed tolerance. The generic $k+1$ iteration of the Newton method applied to (3.11) is described as follows. Starting from an approximation of $\mathbf{X}_k^{n+1}$, we compute the residual $\mathbf{R}_k^{n+1} = (\mathbf{r}_{\mathbf{d}_s,k}^{n+1}, \mathbf{r}_{\mathbf{d}_f,k}^{n+1}, \mathbf{r}_{u_f,k}^{n+1}, r_{p_f,k}^{n+1}, \mathbf{r}_{\lambda,k}^{n+1})^T$:

$$\mathbf{R}_k^{n+1} = \begin{pmatrix} \mathbf{b}_s \\ 0 \\ \mathbf{b}_f \\ \mathbf{b}_c \end{pmatrix} - \begin{pmatrix} S(\hat{\mathbf{d}}_{s,k}^{n+1}) & -I_{\Gamma s}^T\boldsymbol{\lambda}_k^{n+1} \\ -I_{\Gamma s}\hat{\mathbf{d}}_{s,k}^{n+1} & +G(\hat{\mathbf{d}}_{f,k}^{n+1}) \\ F(\mathbf{u}_{f,k}^{n+1}, p_{f,k}^{n+1}, \hat{\mathbf{d}}_{f,k}^{n+1}) & +I_{\Gamma f}^T\boldsymbol{\lambda}_k^{n+1} \\ -\frac{\gamma}{\beta\Delta t}\,I_{\Gamma s}\hat{\mathbf{d}}_{s,k}^{n+1} & +I_{\Gamma f}\mathbf{u}_{f,k}^{n+1} \end{pmatrix}. \tag{3.15}$$

Then, we compute the Newton correction vector $\delta \mathbf{X}_k^{n+1} = (\delta \hat{\mathbf{d}}_{s,k}^{n+1}, \delta \hat{\mathbf{d}}_{f,k}^{n+1}, \delta \mathbf{u}_{f,k}^{n+1}, \delta p_{f,k}^{n+1}, \delta \boldsymbol{\lambda}_k^{n+1})^T$ by solving the Jacobian linear system

$$J_{FSI} \, \delta \mathbf{X}_k^{n+1} = -\mathbf{R}_k^{n+1}, \tag{3.16}$$

being

$$J_{FSI} = \begin{pmatrix} \mathcal{S} & 0 & 0 & -I_{\Gamma^s}^T \\ -I_{\Gamma^s} & \mathcal{G} & 0 & 0 \\ 0 & \mathcal{D} & \mathcal{F} & I_{\Gamma^f}^T \\ -\dfrac{\gamma}{\beta \Delta t} I_{\Gamma^s} & 0 & I_{\Gamma^f} & 0 \end{pmatrix}, \tag{3.17}$$

where $\mathcal{S}$, $\mathcal{G}$ and $\mathcal{F}$ represent the linearized structure, geometry and fluid problems, respectively; $\mathcal{D}$ are the shape derivatives, i.e. the derivatives of $F(\mathbf{u}_f^{n+1}, p_f^{n+1}, \hat{\mathbf{d}}_f^{n+1})$ with respect to $\hat{\mathbf{d}}_f^{n+1}$ (for their exact computation see [Fernández and Moubachir, 2003]).

Finally, we update the solution: $\mathbf{X}_{k+1}^{n+1} = \mathbf{X}_k^{n+1} + \delta \mathbf{X}_k^{n+1}$. We stop the Newton iterations when

$$\frac{\|\mathbf{R}_k^{n+1}\|_\infty}{\|\mathbf{R}_0^{n+1}\|_\infty} \leq \epsilon, \tag{3.18}$$

where $\mathbf{R}_0^{n+1}$ is the residual at the first Newton iteration and ϵ is a given tolerance.

3.6 Preconditioning strategy

In analogy with what is proposed in [Crosetto et al., 2011], we exploit the block structure of the Jacobian matrix associated to the fully coupled FSI problem (3.11) to build our preconditioner:

$$J_{FSI} = \begin{pmatrix} \boxed{\mathcal{S}} & 0 & 0 & -I_{\Gamma^s}^T \\ -I_{\Gamma^s} & \boxed{\mathcal{G}} & 0 & 0 \\ 0 & \mathcal{D} & \boxed{\mathcal{F} \quad I_{\Gamma^f}^T} \\ -\frac{\gamma}{\beta \Delta t} I_{\Gamma^s} & 0 & \boxed{I_{\Gamma^f} \quad 0} \end{pmatrix},$$

which is lower block triangular up to the $-I_{\Gamma^s}^T$ block. By neglecting this block, we obtain the following Gauss-Seidel preconditioner for the matrix J_{FSI}:

$$P_{FSI} = \begin{pmatrix} \mathcal{S} & 0 & 0 & \boxed{0} \\ -I_{\Gamma^s} & \mathcal{G} & 0 & 0 \\ 0 & \mathcal{D} & \mathcal{F} & I_{\Gamma^f}^T \\ -\frac{\gamma}{\beta \Delta t} I_{\Gamma^s} & 0 & I_{\Gamma^f} & 0 \end{pmatrix}. \tag{3.19}$$

Having dropped $-I_{\Gamma^s}^T$ in J_{FSI} amounts to neglect the kinematic coupling condition: more precisely this can be reinterpreted as imposing (one-sided) Dirichlet boundary conditions on $\hat{\mathbf{d}}_s$ at the fluid-structure interface, see also Section 3.6.2 for more in depth comments. A similar strategy was used for a Geometry Convective Explicit (GCE) scheme in [Crosetto et al., 2011]. P_{FSI} can be factorized into three physics-specific nonsingular matrices, namely $P_{\mathcal{S}}$, $P_{\mathcal{G}}$, and $P_{\mathcal{F}}$ corresponding to the structure, the geometry, and the fluid problem, respectively:

$$P_{FSI} = \underbrace{\begin{pmatrix} \boxed{\mathcal{S}} & 0 & 0 & 0 \\ 0 & I & 0 & 0 \\ 0 & 0 & I & 0 \\ 0 & 0 & 0 & I \end{pmatrix}}_{P_{\mathcal{S}}} \underbrace{\begin{pmatrix} I & 0 & 0 & 0 \\ -I_{\Gamma^s} & \boxed{\mathcal{G}} & 0 & 0 \\ 0 & 0 & I & 0 \\ 0 & 0 & 0 & I \end{pmatrix}}_{P_{\mathcal{G}}} \underbrace{\begin{pmatrix} I & 0 & 0 & 0 \\ 0 & I & 0 & 0 \\ 0 & \mathcal{D} & \boxed{\mathcal{F} \quad I_{\Gamma^f}^T} \\ -\frac{\gamma}{\beta\Delta t} I_{\Gamma^s} & 0 & \boxed{I_{\Gamma^f} \quad 0} \end{pmatrix}}_{P_{\mathcal{F}}}. \quad (3.20)$$

$P_{\mathcal{S}}$ is block diagonal while both $P_{\mathcal{G}}$ and $P_{\mathcal{F}}$ can be further factorized into matrices featuring simpler block structures:

$$P_{\mathcal{G}} = \begin{pmatrix} I & 0 & 0 & 0 \\ -I_{\Gamma^s} & I & 0 & 0 \\ 0 & 0 & I & 0 \\ 0 & 0 & 0 & I \end{pmatrix} \begin{pmatrix} I & 0 & 0 & 0 \\ 0 & \mathcal{G} & 0 & 0 \\ 0 & 0 & I & 0 \\ 0 & 0 & 0 & I \end{pmatrix} = P_{\mathcal{G}}^{(1)} P_{\mathcal{G}}^{(2)}, \quad (3.21)$$

$$P_{\mathcal{F}} = \begin{pmatrix} I & 0 & 0 & 0 \\ 0 & I & 0 & 0 \\ 0 & \mathcal{D} & I & 0 \\ 0 & 0 & 0 & I \end{pmatrix} \begin{pmatrix} I & 0 & 0 & 0 \\ 0 & I & 0 & 0 \\ 0 & 0 & I & 0 \\ -\frac{\gamma}{\beta\Delta t} I_{\Gamma^s} & 0 & 0 & I \end{pmatrix} \begin{pmatrix} I & 0 & 0 & 0 \\ 0 & I & 0 & 0 \\ 0 & 0 & \mathcal{F} & I_{\Gamma^f}^T \\ 0 & 0 & I_{\Gamma^f} & 0 \end{pmatrix} = P_{\mathcal{F}}^{(1)} P_{\mathcal{F}}^{(2)} P_{\mathcal{F}}^{(3)}. \quad (3.22)$$

The factors $P_{\mathcal{G}}^{(1)}$, $P_{\mathcal{F}}^{(1)}$ and $P_{\mathcal{F}}^{(2)}$ can be inverted exactly (and cost-free). Since $\mathcal{S}$ and $\mathcal{G}$ appear (as diagonal blocks) in different factors, physics-specific ad-hoc preconditioners can be efficiently used to approximate their inverses. Unfortunately, this is only partially true for the fluid subproblem $\mathcal{F}$ whose saddle point structure features the additional presence of the two coupling blocks I_{Γ^f} and $I_{\Gamma^f}^T$.

We remark that factorization (3.20) has already been used in [Crosetto et al., 2011], where after factorization, the inverses of $P_{\mathcal{S}}$, $P_{\mathcal{G}}$ and $P_{\mathcal{F}}$ were approximated by the one level algebraic additive Schwarz method [Quarteroni and Valli, 1999, Toselli and Widlund, 2005].

The novelty here with respect to [Crosetto et al., 2011] consists in operating a static condensation on the interface fluid variables, and in using SIMPLE [Patankar and Spalding, 1972, Pernice and Tocci, 2001, Elman et al., 2006, Elman et al., 2008, ur Rehman et al., 2008, ur Rehman et al., 2009] to precondition the resulting reduced fluid matrix.

In fact, we notice that according to the (further) factorization (3.22) of $P_{\mathcal{F}}$, the critical term is $P_{\mathcal{F}}^{(3)}$ which corresponds to a linearized Navier-Stokes problem with additional constraints. Our goal is to replace it, after removing the Lagrange multipliers, by a convenient approximation built on an efficient SIMPLE preconditioner.

We point out that our static condensation of the interface variables is operated at the level of the fluid preconditioner. A different approach, see e.g. [Gee et al., 2010, Mayr et al., 2015], consists in removing the interface variables directly from the set of unknowns of the FSI problem (3.16). In Section 3.6.2 we will show that the corresponding block preconditioner introduced in [Gee et al., 2010] differs from ours and we will compare the results obtained by the two approaches.

3.6.1 Static condensation and approximation of $P_{\mathcal{F}}^{(3)}$ based on SIMPLE preconditioner

By static condensation of the degrees of freedom related to the Lagrange multipliers $\boldsymbol{\lambda}$, we show that the application of $P_{\mathcal{F}}^{(3)}$ is equivalent to solving a linearized Navier-Stokes problem with Dirichlet boundary conditions at the fluid-structure interface. Let us extract from $P_{\mathcal{F}}^{(3)}$ the blocks associated to the fluid and the coupling parts, yielding the following saddle-point problem:

$$
\begin{pmatrix} \begin{pmatrix} \mathcal{K} & \mathcal{B}^T \\ \mathcal{B} & 0 \end{pmatrix} & I_{\Gamma f}^T \\ I_{\Gamma f} & 0 \end{pmatrix} \begin{pmatrix} \delta\mathbf{u}_{f,k}^{n+1} \\ \delta p_{f,k}^{n+1} \\ \delta\boldsymbol{\lambda}_k^{n+1} \end{pmatrix} = \begin{pmatrix} \mathbf{r}_{\mathbf{u},k}^{n+1} \\ \mathbf{r}_{p,k}^{n+1} \\ \mathbf{r}_{\boldsymbol{\lambda},k}^{n+1} \end{pmatrix},
\tag{3.23}
$$

where we highlighted the block structure of $\mathcal{F}$

$$
\mathcal{F} = \begin{pmatrix} \mathcal{K} & \mathcal{B}^T \\ \mathcal{B} & 0 \end{pmatrix},
\tag{3.24}
$$

being $\mathcal{K}$, $\mathcal{B}$, and $\mathcal{B}^T$ the block matrices of $\mathcal{F}$ representing the linearized advection-diffusion-reaction, the divergence, and the gradient operators, respectively. We notice that the coupling matrix $I_{\Gamma f}$ features the following structure:

$$
I_{\Gamma f} = \left(I_{\Gamma^{u_f}} \vdots 0 \right),
$$

where $I_{\Gamma^{u_f}}$ is the restriction of the fluid velocity to the interface Γ. The linear system (3.23) is equivalent to:

$$
\begin{cases}
\mathcal{K}\delta\mathbf{u}_{f,k}^{n+1} + \mathcal{B}^T \delta p_{f,k}^{n+1} + I_{\Gamma^{u_f}}^T \delta\boldsymbol{\lambda}_k^{n+1} = \mathbf{r}_{\mathbf{u},k}^{n+1}, & \text{(3.25a)} \\
\mathcal{B}\delta\mathbf{u}_{f,k}^{n+1} = \mathbf{r}_{p,k}^{n+1}, & \text{(3.25b)} \\
I_{\Gamma^{u_f}}\delta\mathbf{u}_{f,k}^{n+1} = \mathbf{r}_{\boldsymbol{\lambda},k}^{n+1}. & \text{(3.25c)}
\end{cases}
$$

By splitting $\delta\mathbf{u}_{f,k}^{n+1}$ into its internal component $\delta\mathbf{u}_{f,k,i}^{n+1}$ and its interface component $\delta\mathbf{u}_{f,k,\Gamma}^{n+1}$, the first step consists in eliminating the variables $\delta\mathbf{u}_{f,k,\Gamma}^{n+1}$ using Eq. (3.25c).

The second step proceeds by replacing the newly computed variables $\delta\mathbf{u}_{f,k,\Gamma}^{n+1}$ into (3.25a) and (3.25b). This leads to a new system from which the variable $\delta\boldsymbol{\lambda}_k^{n+1}$ can be formally eliminated, yielding:

$$\delta\boldsymbol{\lambda}_k^{n+1} = I_{\Gamma^{u_f}} I_{\Gamma^{u_f}}^T \delta\boldsymbol{\lambda}_k^{n+1} = I_{\Gamma^{u_f}}\left(\mathbf{r}_{\mathbf{u}_f,k}^{n+1} - \mathcal{K}\delta\mathbf{u}_{f,k}^{n+1} - \mathcal{B}^T\delta p_{f,k}^{n+1}\right). \tag{3.26}$$

The remaining equations consist then in the system

$$\begin{pmatrix} \mathcal{K}_{ii} & \mathcal{B}_i^T \\ \mathcal{B}_i & 0 \end{pmatrix}\begin{pmatrix} \delta\mathbf{u}_{f,k,i}^{n+1} \\ \delta p_{f,k}^{n+1} \end{pmatrix} = \begin{pmatrix} \mathbf{r}_{\mathbf{u},k,i}^{n+1} - \mathcal{K}_{i\Gamma}\delta\mathbf{u}_{f,k,\Gamma}^{n+1} \\ \mathbf{r}_{p,k}^{n+1} - \mathcal{B}_\Gamma\delta\mathbf{u}_{f,k,\Gamma}^{n+1} \end{pmatrix}, \tag{3.27}$$

where $\mathcal{K}_{ii}$ and $\mathcal{B}_i^T$ are the matrices representing the linearized advection-diffusion-reaction and gradient terms, respectively, restricted to the internal degrees of freedom $\delta\mathbf{u}_{f,k,i}^{n+1}$. Eq. (3.27) features the classical saddle-point form of a system associated to the linearized Navier-Stokes equations.

At this point we replace the matrix in (3.27) by its approximation based on SIMPLE preconditioner

$$\mathcal{F} \cong \widetilde{\mathcal{F}} = \begin{pmatrix} \mathcal{K}_{ii} & 0 \\ \mathcal{B}_i & -\widetilde{S} \end{pmatrix}\begin{pmatrix} I & D^{-1}\mathcal{B}_i^T \\ 0 & I \end{pmatrix}, \tag{3.28}$$

where D is the diagonal of $\mathcal{K}_{ii}$, and $\widetilde{S} = \mathcal{B}_i D^{-1}\mathcal{B}_i^T$ the approximated Schur complement of (3.27). In the application of FaCSI, the inverses of $\mathcal{S}$, $\mathcal{G}$, $\mathcal{K}_{ii}$ and $\widetilde{S}$ are approximated by efficient preconditioners denoted by $\mathcal{H}_\mathcal{S}$, $\mathcal{H}_\mathcal{G}$, $\mathcal{H}_{\mathcal{K}_{ii}}$ and $\mathcal{H}_{\widetilde{S}}$, respectively, based, e.g., on domain decomposition or the multigrid method. This concludes the construction of the preconditioner FaCSI for J_{FSI}, which takes then the following final form:

$$P_{FaCSI} = P_\mathcal{S}^{ap} \cdot P_\mathcal{G}^{ap} \cdot P_\mathcal{F}^{ap}, \tag{3.29}$$

where:

$$P_\mathcal{S}^{ap} = \begin{pmatrix} \mathcal{H}_\mathcal{S} & 0 & 0 & 0 \\ 0 & I & 0 & 0 \\ 0 & 0 & I & 0 \\ 0 & 0 & 0 & I \end{pmatrix}, \quad P_\mathcal{G}^{ap} = \begin{pmatrix} I & 0 & 0 & 0 \\ -I_{\Gamma^s} & \mathcal{H}_\mathcal{G} & 0 & 0 \\ 0 & 0 & I & 0 \\ 0 & 0 & 0 & I \end{pmatrix} \tag{3.30}$$

and

$$
P_{\mathcal{F}}^{ap} = \begin{pmatrix} I & 0 & 0 & 0 \\ 0 & I & 0 & 0 \\ 0 & \mathcal{D} & \begin{pmatrix} I & 0 & 0 \\ 0 & I_\Gamma & 0 \\ 0 & 0 & I \end{pmatrix} & \begin{pmatrix} 0 \\ 0 \\ 0 \end{pmatrix} \\ -\frac{\gamma}{\beta\Delta t} I_{\Gamma^s} & 0 & \begin{pmatrix} 0 & 0 & 0 \end{pmatrix} & I \end{pmatrix} \begin{pmatrix} I & 0 & 0 & 0 \\ 0 & I & 0 & 0 \\ 0 & 0 & \begin{pmatrix} I & 0 & 0 \\ 0 & 0 & 0 \\ 0 & 0 & I \end{pmatrix} & \begin{pmatrix} 0 \\ I_\Gamma \\ 0 \end{pmatrix} \\ 0 & 0 & \begin{pmatrix} 0 & I_\Gamma & 0 \end{pmatrix} & I \end{pmatrix}
$$

$$
\begin{pmatrix} I & 0 & 0 & 0 \\ 0 & I & 0 & 0 \\ 0 & 0 & \begin{pmatrix} \mathcal{H}_{\mathcal{K}_{ii}} & \mathcal{K}_{i\Gamma} & 0 \\ 0 & I_\Gamma & 0 \\ \mathcal{B}_i & \mathcal{B}_\Gamma & -\mathcal{H}_{\widetilde{S}} \end{pmatrix} & \begin{pmatrix} 0 \\ I_\Gamma \\ 0 \end{pmatrix} \\ 0 & 0 & \begin{pmatrix} 0 & 0 & 0 \end{pmatrix} & I \end{pmatrix} \begin{pmatrix} I & 0 & 0 & 0 \\ 0 & I & 0 & 0 \\ 0 & 0 & \begin{pmatrix} I & 0 & D^{-1}\mathcal{B}_i^T \\ 0 & I_\Gamma & 0 \\ 0 & 0 & I \end{pmatrix} & \begin{pmatrix} 0 \\ I_\Gamma \\ 0 \end{pmatrix} \\ 0 & 0 & \begin{pmatrix} 0 & 0 & 0 \end{pmatrix} & I \end{pmatrix}
$$

$$
\begin{pmatrix} I & 0 & 0 & 0 \\ 0 & I & 0 & 0 \\ 0 & 0 & \begin{pmatrix} I & 0 & 0 \\ 0 & I_\Gamma & 0 \\ 0 & 0 & I \end{pmatrix} & \begin{pmatrix} 0 \\ 0 \\ 0 \end{pmatrix} \\ 0 & 0 & \begin{pmatrix} \mathcal{K}_{\Gamma i} & \mathcal{K}_{\Gamma\Gamma} & \mathcal{B}_\Gamma^T \end{pmatrix} & I \end{pmatrix}. \tag{3.31}
$$

For the sake of clarity, we point out that, for a given residual $\mathbf{r} = (\mathbf{r_{d_s}}, \mathbf{r_{d_f}}, \mathbf{r_{u_f}}, \mathbf{r_{p_f}}, \mathbf{r_\lambda})^T$, the application of our preconditioner amounts to solve $P_{FaCSI}\mathbf{w} = \mathbf{r}$, therefore involving the following steps:

1. Application of $(P_{\mathcal{S}}^{ap})^{-1}$: $\mathbf{w_{d_s}} = \mathcal{H}_{\mathcal{S}}^{-1}\mathbf{r_{d_s}}$.

2. Application of $(P_{\mathcal{G}}^{ap})^{-1}$: $\mathbf{w_{d_f}} = \mathcal{H}_{\mathcal{G}}^{-1}(\mathbf{r_{d_f}} + I_{\Gamma^s}\mathbf{w_{d_s}})$.

3. Application of $(P_{\mathcal{F}}^{ap})^{-1}$: compute $\mathbf{z}_F = \mathbf{r}_F - \mathcal{D}\mathbf{w_{d_f}}$ and $\mathbf{z}_\lambda = \mathbf{r}_\lambda + \frac{\gamma}{\beta\Delta t} I_{\Gamma^s}\mathbf{w_{d_s}}$. Then, after denoting by $\mathbf{w_u}$ and $\mathbf{w}_p$, $\mathbf{z_u}$ and $\mathbf{z}_p$ the velocity and pressure components of $\mathbf{w}_F$ and $\mathbf{z}_F$, respectively, thanks to (3.25c) we set $\mathbf{z_{u,\Gamma}} = \mathbf{z_\lambda}$. The application of the SIMPLE preconditioner involves the following steps:

   a) $\mathbf{y_{u,i}} = \mathcal{H}_{\mathcal{K}_{ii}}^{-1}(\mathbf{z_{u,i}} - \mathcal{K}_{i\Gamma}\mathbf{z_{u,\Gamma}})$,
   b) $\mathbf{w}_p = \mathcal{H}_{\widetilde{S}}^{-1}(\mathcal{B}_i\mathbf{y_{u,i}} - \mathbf{z}_p + \mathcal{B}_\Gamma\mathbf{z_{u,\Gamma}})$,
   c) $\mathbf{w_u} = (\mathbf{w_{u,i}}, \mathbf{w_{u,\Gamma}})^T = (\mathbf{y}_{u,i} - D^{-1}\mathcal{B}_i^T\mathbf{w}_p, \mathbf{z_{u,\Gamma}})^T$.

   Finally, we compute $\mathbf{w_\lambda} = I_{\Gamma^{u_f}}(\mathbf{z_u} - \mathcal{K}\mathbf{w_u} - \mathcal{B}^T\mathbf{w}_p)$.

In [Grandperrin, 2013] a similar factorization as in Eq. (3.20) was used, and a SIMPLE preconditioner was exploited to directly approximate the factor $P_{\mathcal{F}}^{(3)}$. However, no static

condensation was used to eliminate the interface fluid variables, yielding therefore to a different preconditioner. In Section 3.7.2 we show that static condensation substantially increases the performance with respect to the version proposed in [Grandperrin, 2013].

Note that in the following case our preconditioner may be singular and FaCSI not applicable: at both the inflow and outflow sections $\partial\Omega_f \cap \partial\Omega$, either the fluid velocity or the flow rates are prescribed; moreover at the lateral structure boundary $\partial\Omega_s \cap \partial\Omega$ a Neumann condition is enforced. Even though the whole FSI problem is well posed, the matrix $\mathcal{F}$, and therefore $P_{\mathcal{F}}$, is singular. In such a situation, a possible turnaround consists in replacing the Dirichlet condition for the velocity on the interface with an equivalent Robin condition, as done e.g. in [Crosetto, 2011]. This alternative, however, is not analyzed in this thesis.

3.6.2 Comparison with other condensed formulations

In [Gee et al., 2010] the authors consider a condensed formulation of the coupled FSI problem for which the unknowns are $\hat{\mathbf{d}}_{s,i}$, $\hat{\mathbf{d}}_{f,i}$, $\mathbf{u}_{F,i}$, $\mathbf{u}_{F,\Gamma}$ being $\hat{\mathbf{d}}_{s,i}$ and $\hat{\mathbf{d}}_{f,i}$ the structure and fluid mesh displacement associated to the internal degrees of freedom, respectively, and $\mathbf{u}_{F,.} = (\mathbf{u}_{f,.}, p_{f,.})^T$. In particular, the vector of Lagrange multipliers is condensed into the structural displacement unknowns at the interface. In our case $\boldsymbol{\lambda}$ is condensed into the fluid velocity.

The block Gauss-Seidel preconditioner of [Gee et al., 2010] (see Eq. (43) in [Gee et al., 2010]) reads:

$$M = \begin{pmatrix} \mathcal{S}_{ii} & 0 & \begin{pmatrix} 0 & 0 \end{pmatrix} \\ 0 & \mathcal{G}_{ii} & \begin{pmatrix} 0 & 0 \end{pmatrix} \\ \begin{pmatrix} \mathcal{S}_{\Gamma i} \\ 0 \end{pmatrix} & \begin{pmatrix} \mathcal{D}_{\Gamma i} \\ \mathcal{D}_{ii} \end{pmatrix} & \begin{pmatrix} \delta\mathcal{S}_{\Gamma\Gamma} + \mathcal{F}_{\Gamma\Gamma} + \delta\mathcal{D}_{\Gamma\Gamma} & \mathcal{F}_{\Gamma i} \\ \mathcal{F}_{i\Gamma} + \delta\mathcal{D}_{i\Gamma} & \mathcal{F}_{ii} \end{pmatrix} \end{pmatrix} \tag{3.32}$$

In (3.32) each matrix block (i.e. $\mathcal{S}$, $\mathcal{G}$, $\mathcal{F}$ and $\mathcal{D}$) is split into its internal (index i) and interface (index Γ) components; δ is a factor which converts displacement into velocity.

By comparing (3.19) with (3.32) we observe that the two block preconditioners are different. More specifically, the nature of the subproblems change: in (3.32) the structure bears a Dirichlet problem, the ALE is still of Dirichlet type and decoupled from the structure, while the fluid is a Neumann problem. In FaCSI, the structure bears a Neumann problem, the ALE is of Dirichlet type and it is coupled with the structure while the fluid is of Dirichlet type. Furthermore, we notice that due to the condensed formulation adopted in [Gee et al., 2010], we observe that the fluid diagonal block in (3.32) slightly differs from ours at the interface.

The aforementioned differences may be summarized by stating that the block Gauss-Seidel

preconditioner devised in [Gee et al., 2010] is of Neumann-Dirichlet type while FaCSI is of Dirichlet-Neumann type. In [Deparis et al., 2015c] a comparison of the performance of Dirichlet-Neumann, Neumann-Dirichlet and Neumann-Neumann preconditioners for the Steklov-Poincaré formulation of the FSI problem was carried out. There, it was shown that the Dirichlet-Neumann preconditioner was the most efficient in terms of requested both CPU time and linear solver iterations.

Finally, we report the equivalent form of the Gauss-Seidel preconditioner P_{FSI} (see Eq. (3.19)) for the condensed formulation of the FSI problem:

$$
M_{DN} = \begin{pmatrix} \mathcal{S}_{ii} & \delta \mathcal{S}_{i\Gamma} & 0 & 0 \\ \mathcal{S}_{\Gamma i} & \delta \mathcal{S}_{\Gamma \Gamma} & 0 & 0 \\ 0 & \delta \mathcal{G}_{i\Gamma} & \mathcal{G}_{ii} & 0 \\ 0 & \mathcal{F}_{i\Gamma} + \delta \mathcal{D}_{i\Gamma} & \mathcal{D}_{ii} & \mathcal{F}_{ii} \end{pmatrix}.
\tag{3.33}
$$

With respect to (3.32), in (3.33) we reordered the unknowns of the FSI problem. Indeed, in (3.33) the unknowns are $\hat{\mathbf{d}}_{s,i}$, $\mathbf{u}_{F,\Gamma}$, $\hat{\mathbf{d}}_{f,i}$ and $\mathbf{u}_{F,i}$. M_{DN} is a preconditioner of Dirichlet-Neumann type since the structure bears a Neumann problem, the ALE is of Dirichlet type and it is coupled with the structure, while the fluid is of Dirichlet type.

3.7   Numerical results

We test our FSI preconditioner on two different test cases: the first is an FSI example in which we study the fluid flow in a straight flexible tube, the second consists in the simulation of the hemodynamics in a femoropopliteal bypass. We measure the weak and strong scalability of the proposed preconditioner, namely the wall time and iterations count.

The FSI problem is discretized by a Fully Implicit (FI) second order scheme in time and space. The resulting nonlinear system is solved by the exact Newton method using tolerance $\epsilon = 10^{-6}$ in (3.18). We solve the linearized problem at each Newton iteration by the right preconditioned GMRES method [Saad and Schultz, 1986] which is never restarted. The stopping criterion of the linear solver is set to 10^{-6} and it is based on the residual scaled by the right hand side. We remark that since in our case the matrices associated to the harmonic extension and the structure are constant throughout the simulation, their preconditioners $\mathcal{H}_{\mathcal{S}}$ and $\mathcal{H}_{\mathcal{G}}$ are computed once and stored. Conversely, we recompute the preconditioner associated to the fluid problem, namely $\mathcal{H}_{\mathcal{K}_{ii}}$ and $\mathcal{H}_{\widetilde{S}}$, at each Newton iteration. At each time step t^{n+1}, the initial guess for the Newton method is given by the solution of the FSI problem at time t^n. In practice, better choices can be made, e.g., by taking as initial guess an extrapolation of the solutions at the previous time steps.

We have implemented our parallel algorithm in LifeV, an open-source C++ finite element

library which makes intensive use of Trilinos [Heroux et al., 2005]. Our linear iterative solver (GMRES) is based on the Belos package [Bavier et al., 2012]. In this work we consider preconditioners $\mathcal{H}_\mathcal{S}$, $\mathcal{H}_\mathcal{G}$, $\mathcal{H}_{\mathcal{K}_{ii}}$ and $\mathcal{H}_{\widetilde{S}}$ based on either the one level Algebraic Additive Schwarz (AAS) method implemented in Ifpack [Sala and Heroux, 2005] or on Algebraic Multigrid (AMG) via ML [Gee et al., 2006]. Whenever mesh coarsening is required, aggregates are computed using METIS/ParMETIS [Karypis et al., 1998, Karypis et al., 2003]. All the computations reported in this work have been made on Piz Dora at CSCS, a Cray XC40 machine whose main technical specifications are reported in Table 1.4.

3.7.1 FSI in a straight flexible tube

Our first numerical example is a benchmark problem proposed in [Nobile., 2001] and numerically solved, e.g., in [Crosetto et al., 2011, Deparis et al., 2006a, Gee et al., 2010, Wu and Cai, 2014]. The geometry of the fluid consists in a straight cylinder of length $L = 5$ cm and radius $R = 0.5$ cm, surrounded by a structure with uniform thickness $t = 0.1$ cm. A constant normal stress $\boldsymbol{\sigma} \cdot \mathbf{n} = 1.33 \times 10^4$ dyne/cm^2 is applied at the fluid inflow for $t \leq 0.003$ s, while a homogeneous Neumann boundary condition is used at the fluid outflow. The structure is clamped at both the ends. The fluid is characterized by a density $\rho_f = 1.0$ g/cm^3 and a dynamic viscosity $\mu_f = 0.03$ g/(cm s) while the structure by a density $\rho_s = 1.2$ g/cm^3, Poisson's ratio $\nu_s = 0.3$ and Young's modulus $E_s = 3 \times 10^6$ dyne/cm^2. The time step used in our simulations is $\Delta t = 10^{-4}$ s.

Mesh convergence study

To validate the solver implemented, in Figure 3.2 we show a post-processing of the numerical solution obtained by simulating 100 time steps: the results reported well compare with those in [Deparis et al., 2006a, Fernández and Moubachir, 2003, Gee et al., 2010, Wu and Cai, 2014].

(a) $t = 2$ ms.   (b) $t = 4$ ms.   (c) $t = 6$ ms.   (d) $t = 8$ ms.
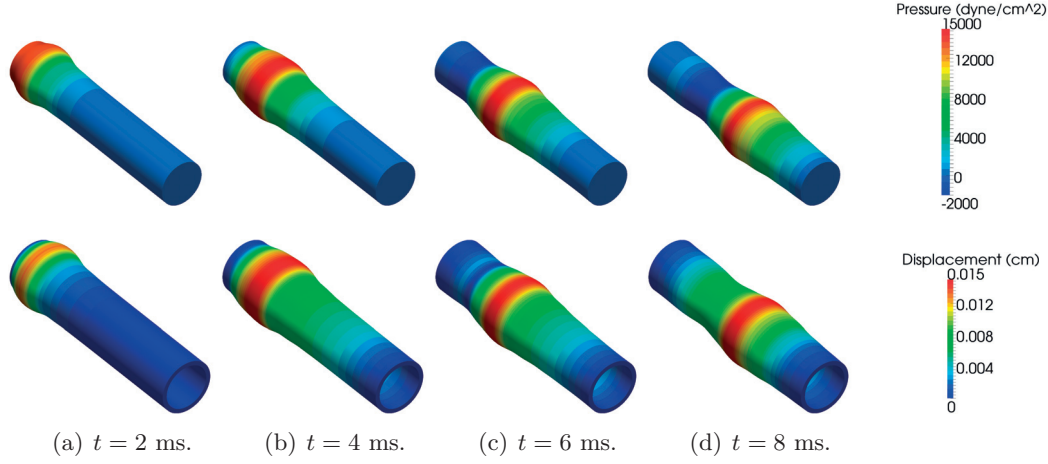
Figure 3.2: Top row: pressure wave propagation throughout the deformed fluid domain; bottom row: structural displacement. Deformation magnified by a factor 10 for visualization purpose.

Furthermore, a mesh convergence study is carried out using both "P1" and "P2" spatial discretizations, see Table 3.1. We remark that in the "P1" case, the fluid problem is stabilized using a VMS-SUPG stabilization, see Section 1.3. To this end, we consider five meshes of increasing refinement for the fluid and structure domains. In Table 3.2 we report the information of the meshes considered while in Table 3.3 and 3.4 their corresponding number of degrees of freedom obtaied using the "P1" and the "P2" discretizations. In Figure 3.3, 3.4 and 3.5 we show the mesh convergence results in terms of pressure, radial displacement and radial velocity, respectively, at the fluid-structure interface along the line between points P1 = (0.5,0.0,0.0) and P1 = (0.5,0.0,5.0).

Discretization	Fluid velocity	Fluid pressure	Structure displacement	ALE
"P1"	$\mathbb{P}1$	$\mathbb{P}1$	$\mathbb{P}1$	$\mathbb{P}1$
"P2"	$\mathbb{P}2$	$\mathbb{P}1$	$\mathbb{P}2$	$\mathbb{P}2$

Table 3.1: Discretizations used for the mesh convergence study.

	Fluid		Structure	
	# Vertices	# Tetrahedra	# Vertices	# Tetrahedra
Mesh # 1	2'337	11'040	2'460	9'600
Mesh # 2	13'603	72'000	8'052	31'680
Mesh # 3	64'943	362'400	23'028	91'200
Mesh # 4	183'300	1'045'800	60'912	272'160
Mesh # 5	285'912	1'641'180	84'816	379'440

Table 3.2: Details of the meshes used for the mesh convergence study.

	Fluid DoF	Structure DoF	Coupling DoF	Geometry DoF	Total
Mesh # 1	9'348	7'380	2'340	7'011	26'079
Mesh # 2	54'412	24'156	7'788	40'809	127'165
Mesh # 3	259'772	69'084	22'572	194'829	546'257
Mesh # 4	733'200	182'736	45'036	549'900	1'510'872
Mesh # 5	1'143'648	254'448	62'868	857'736	2'318'700

Table 3.3: Mesh convergence study: number of Degrees of Freedom (DoF) obtained using the "P1" discretization.
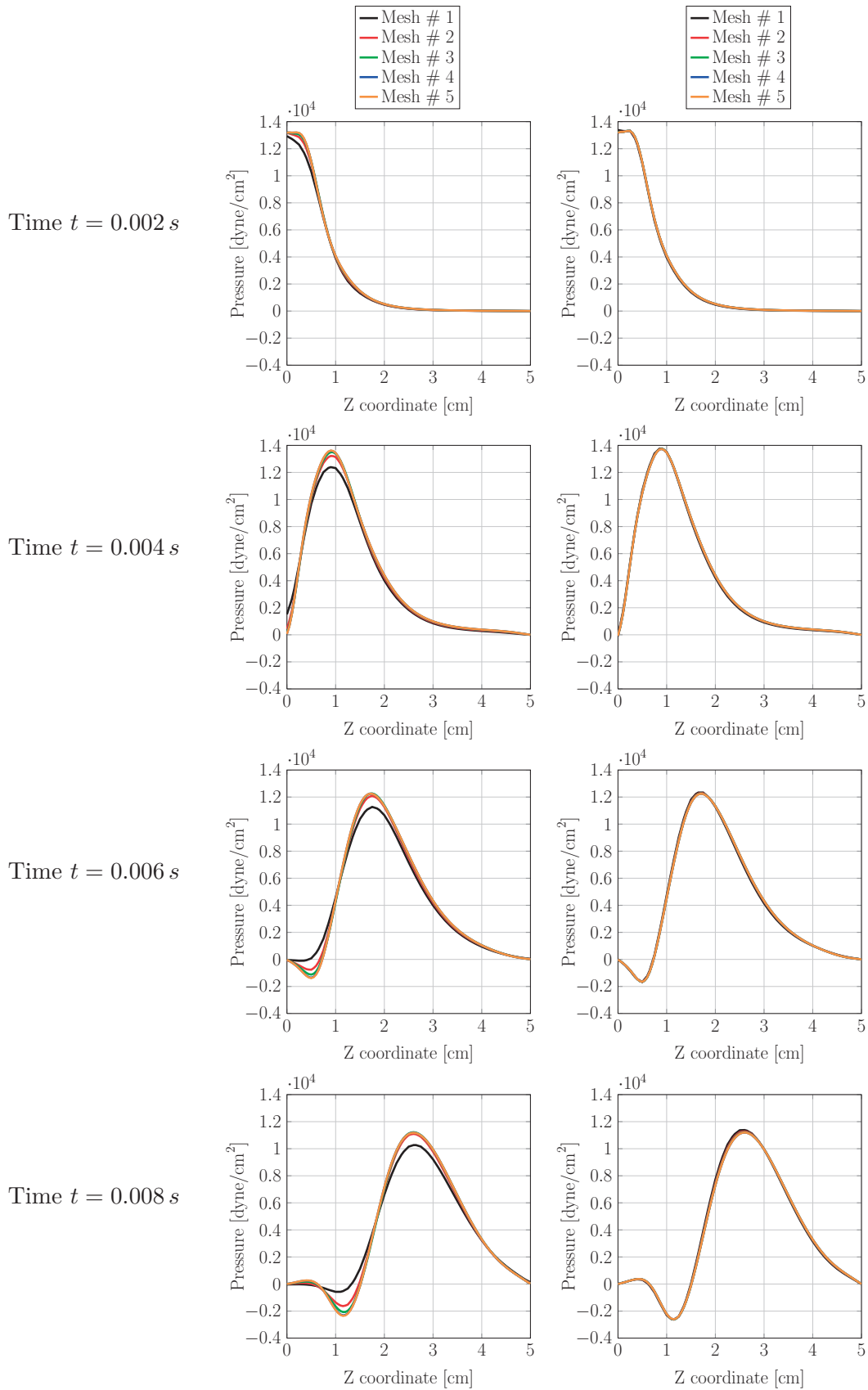
Figure 3.3: Mesh convergence of the pressure at the fluid-structure interface. Left and right columns refer to the "P1" and "P2" discretizations, respectively.
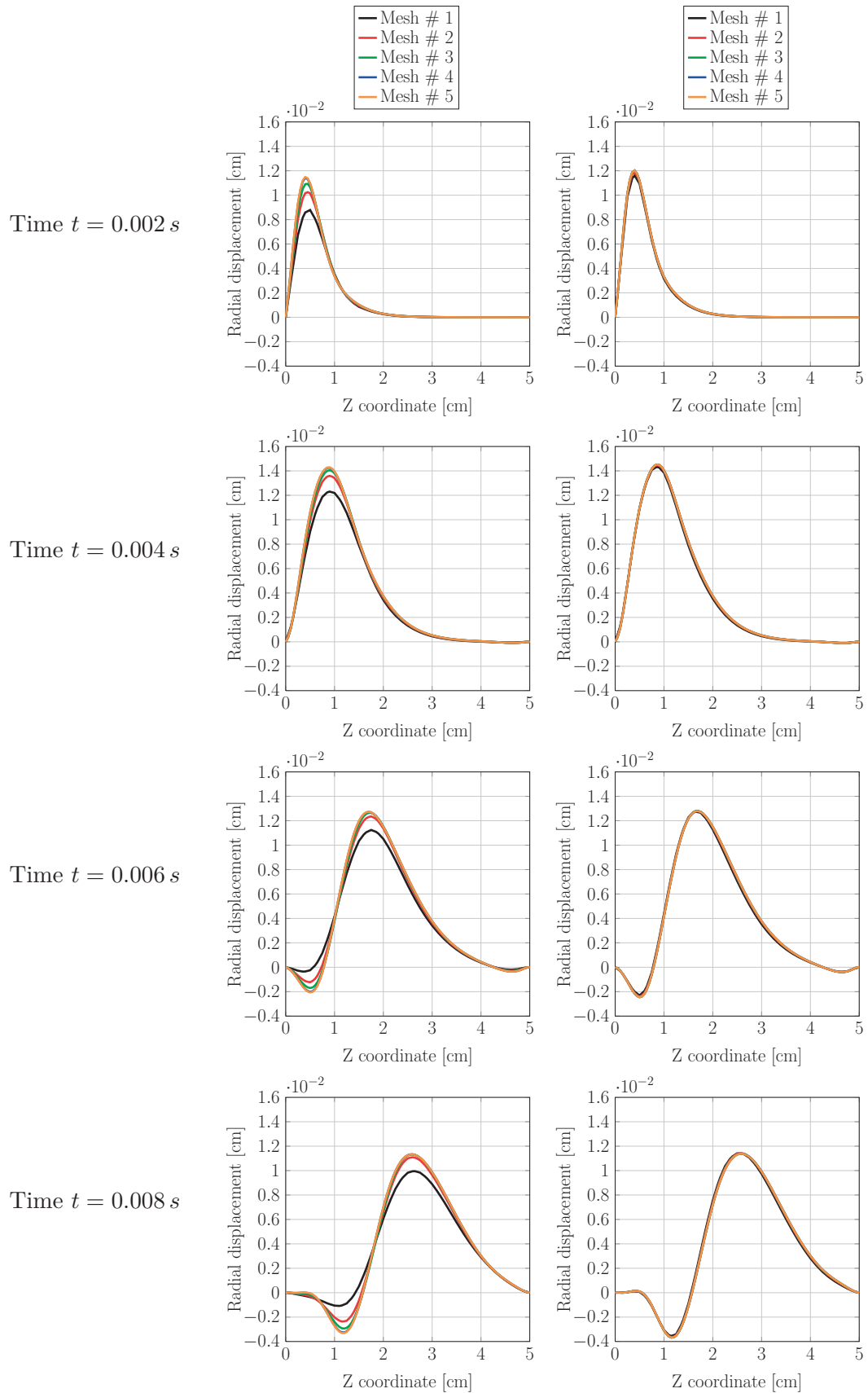
Figure 3.4: Mesh convergence of the radial displacement at the fluid-structure interface.
Left and right columns refer to the "P1" and "P2" discretizations, respectively.
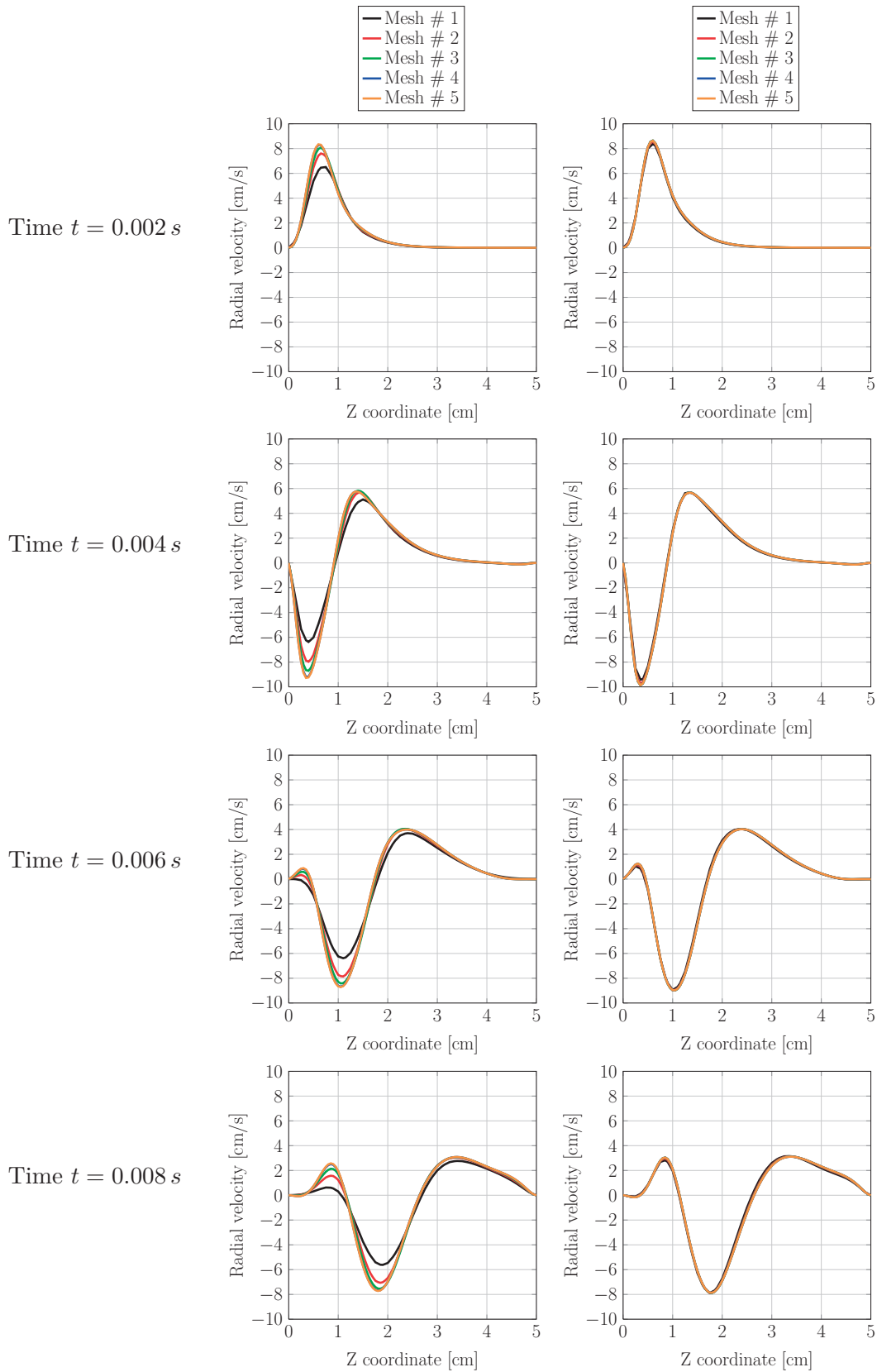
Figure 3.5: Mesh convergence of the radial velocity at the fluid-structure interface. Left and right columns refer to the "P1" and "P2" discretizations, respectively.

	Fluid DoF	Structure DoF	Coupling DoF	Geometry DoF	Total
Mesh # 1	52'152	48'600	9'480	49'815	160'047
Mesh # 2	320'338	159'720	31'416	306'735	818'209
Mesh # 3	1'568'222	458'280	90'744	1'503'279	3'620'525
Mesh # 4	4'473'327	1'274'616	180'792	4'290'027	10'218'762
Mesh # 5	6'997'815	1'775'928	238'962	6'711'903	15'724'608

Table 3.4: Mesh convergence study: number of Degrees of Freedom (DoF) obtained using the "P2" discretization.

Parallel performance of FaCSI

We are interested in studying the weak and strong scalability performance of FaCSI when different choices for $\mathcal{H}_\mathcal{S}$, $\mathcal{H}_\mathcal{G}$, $\mathcal{H}_{\mathcal{K}_{ii}}$ and $\mathcal{H}_{\widetilde{S}}$ are considered. In Table 3.5 we report the different configurations adopted to customize FaCSI for the analysis. As reported in

Configuration	Preconditioner	Approximation
set A	$\mathcal{H}_\mathcal{S}$	1 level AAS
	$\mathcal{H}_\mathcal{G}$	1 level AAS
	$\mathcal{H}_{\mathcal{K}_{ii}}$	1 level AAS
	$\mathcal{H}_{\widetilde{S}}$	1 level AAS
set B	$\mathcal{H}_\mathcal{S}$	3 level AMG, $\omega=0.79$
	$\mathcal{H}_\mathcal{G}$	3 level AMG, $\omega=1.0$
	$\mathcal{H}_{\mathcal{K}_{ii}}$	3 level AMG, $\omega=0.69$
	$\mathcal{H}_{\widetilde{S}}$	3 level AMG, $\omega=1.0$
set C	$\mathcal{H}_\mathcal{S}$	1 level AAS
	$\mathcal{H}_\mathcal{G}$	1 level AAS
	$\mathcal{H}_{\mathcal{K}_{ii}}$	3 level AMG, $\omega=0.69$
	$\mathcal{H}_{\widetilde{S}}$	3 level AMG, $\omega=1.0$

Table 3.5: Different configurations of FaCSI considered for this analysis.

Table 3.5, three different configurations are studied: in the first (set A) we consider the one level AAS preconditioner with an algebraic overlap $\delta = 2$ (i.e., roughly two times the mesh size h) for $\mathcal{H}_\mathcal{S}$, $\mathcal{H}_\mathcal{G}$, $\mathcal{H}_{\mathcal{K}_{ii}}$ and $\mathcal{H}_{\widetilde{S}}$. In set B, the 3 level AMG method is used: we consider a symmetric Gauss-Seidel smoother (ω is the damping parameter) for levels 1 and 2 while at the coarsest level, i.e. level 3, the problem is solved exactly. Set C is a combination of set A and set B: we make use of the AAS method for $\mathcal{H}_\mathcal{S}$, $\mathcal{H}_\mathcal{G}$, while the 3 level AMG method is used for $\mathcal{H}_{\mathcal{K}_{ii}}$ and $\mathcal{H}_{\widetilde{S}}$. In both Set B and Set C, for $\mathcal{H}_{\mathcal{K}_{ii}}$ we used the parameters setting NSSA (Nonsymmetric Smoothed Aggregation) of ML, while for $\mathcal{H}_{\widetilde{S}}$ we used SA (classical Smoothed Aggregation). In Set B, for both $\mathcal{H}_\mathcal{S}$, $\mathcal{H}_\mathcal{G}$ we used the DD (Domain Decomposition) parameter settings of ML.

We remark that the exact local subdomain solves for AAS as well as the exact coarse solve of the AMG preconditioner are carried out by LU factorization using the library MUMPS [Amestoy et al., 2001, Amestoy et al., 2006].

In Table 3.6 and 3.7 we report the information concerning the meshes used in our simulations and the correponding number of degrees of freedom.

	Fluid		Structure	
	# Vertices	# Tetrahedra	# Vertices	# Tetrahedra
Mesh # 1	210'090	1'202'040	65'424	292'320
Mesh # 2	559'471	3'228'960	191'080	913'920
Mesh # 3	841'341	4'880'640	300'456	1'497'600

Table 3.6: Details of the meshes used for the straight cylinder example.

	Fluid DoF	Structure DoF	Coupling DoF	Geometry DoF	Total
Mesh # 1	5'134'050	1'369'030	195'576	4'923'960	11'622'616
Mesh # 2	13'728'971	4'119'980	456'114	13'169'500	31'474'595
Mesh # 3	20'696'341	6'599'740	598'104	19'855'000	47'749'185

Table 3.7: Straight flexible tube test case: number of Degrees of Freedom (DoF).

The strong and weak scalability performance of FaCSI are tested by solving the straight flexible tube example using three sets of fluid-structure meshes (that are conforming at the interface) of increasing refinement and three different configurations of FaCSI. In Figure 3.6 and 3.7 we report the weak and strong scalability results, respectively (consisting in average values over the first 10 time steps simulated).

In the weak scalability study, the problem size (workload) assigned to each core is kept constant. In our investigation we address the cases of 30'000, 40'000 and 50'000 degrees of freedom per core. In terms of GMRES iterations (first row of Figure 3.6), we notice that FaCSI configured with set C performs better with respect to configurations of set A and set B. In fact, set C yields an iteration count which mildly depends on both the mesh size (along each curve the number of iterations vary from roughly 22 to 34 iterations) and the number of degrees of freedom per core since the three curves almost overlap. Configuration of set A leads to a number of linear iterations which on the one hand mildly depends on the core workload but on the other is rather sensitive to the mesh size (along each curve the iterations vary from roughly 30 to 60 iterations). We observe that FaCSI configured with set B yields iteration counts that are affected by both the mesh size and the number of degrees of freedom per core. We focus now on the weak scalability of the time to compute a single time step (second row of Figure 3.6). FaCSI configured with set A leads to computational times that are weakly scalable for all the core workloads taken into account. Nevertheless, comparing the results obtained by set
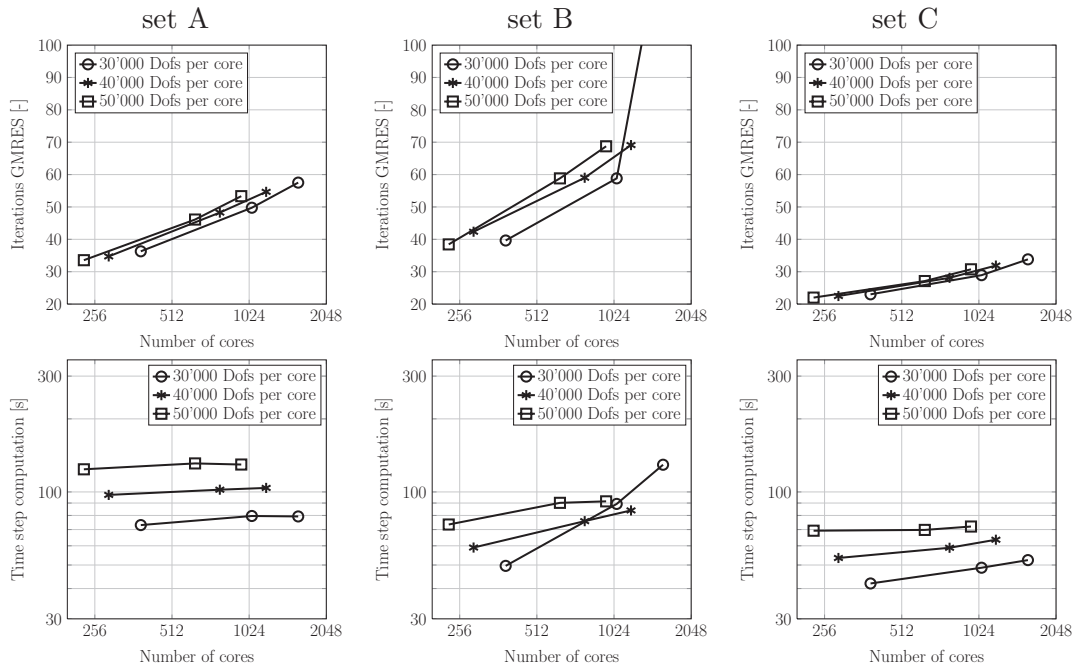
Figure 3.6: Weak scalability results obtained using three different configurations of FaCSI (see Table 3.5).

A with those generated with set B and C, we notice that set A is the most computational expensive. In particular, we highlight that the time to compute a time step using set C with 50'000 Dofs per core (which is roughly 70 s) is smaller than the one with workload 30'000 Dofs per core using set A (that is roughly 80 s). FaCSI configured with set B is not weakly scalable as the timings obtained vary significantly (in particular when 30'000 Dofs per core are used). Using set C, we notice that the time to compute a single time step is weakly scalable for a core workload of 50'000 Dofs while for 30'000 and 40'000 it increases with the cores count as the time spent by communication is larger than the actual one associated to the relatively small amount of computational work required on each individual core.

In Figure 3.7 we show the strong scalability results obtained. In the first row of Figure 3.7 we report the number of GMRES iterations, in the second row the time to build the preconditioner of the fluid problem, in the third row the time to solve the linear system while in the fourth row the time to compute a single time step. We remark that in the second row of Figure 3.7 we report the time to build only the preconditioner for the fluid problem: in fact, since the harmonic extension and the structure matrices are constant throughout the simulation, their preconditioners are built only once and stored at the beginning.

In terms of linear solver iterations we notice that FaCSI configured with set C performs better than both set A and set B (in line with what we observed in the study of the weak

scalability). Indeed, for all the 3 meshes considered, we notice that the use of set C leads to a number of linear solver iterations that is the lowest and which is less affected by the number of cores utilized.

Regarding the time to build the fluid preconditioner, although set A leads to strongly scalable results (the red curve behaves almost as the black one of the ideal scaling), we notice that up to 2'048 cores set B and set C allows for a remarkably faster computation w.r.t. set A. For instance, when a small number of cores is used, the construction of the fluid preconditioner by the algebraic multigrid method (set B and set C) is roughly ten times lower then the one of the overlapping algebraic additive Schwarz (set A). Nevertheless, although AMG leads to a very fast construction of the preconditioner, we notice that in our numerical experiments its construction scales up to 512 cores (on Mesh # 3). We remark that the curves in the second row of Figure 3.7 associated to set B and set C are overlapping since their settings for the fluid problem are the same (see Table 3.5). In terms of time to solve the linear system, we notice that with the configurations of set A FaCSI scales up to 2'048 cores, with set B until 512 cores whereas using set C linear scaling is obtained up to 1'024 cores. It is noteworthy that until 1'024 cores the solution of the linear system carried out by FaCSI customized by set C is the fastest (in particular almost two times faster than set A). The last row of Figure 3.7 shows the strong scalability of the time to compute a single time step. Strong scalability of FaCSI customized with set A, set B and set C is observed up to 4'096, 1'024 and 2'048 cores, respectively. Also in this case we notice that until FaCSI configured with set C scales linearly, it is the fastest. For instance, until 2'048 cores on Mesh # 3, we remark that the computational times associated to set A are roughly the same of those obtained by set C using, for the latter, half of the cores.

Based on the analysis presented so far we conclude that FaCSI customized with set C (i.e. using the one level AAS method for both $\mathcal{H}_\mathcal{S}$ and $\mathcal{H}_\mathcal{G}$, and the 3 level AMG method for $\mathcal{H}_{\mathcal{K}_{ii}}$ and $\mathcal{H}_{\widetilde{S}}$) is the most computationally efficient and robust with respect to the mesh size among all the configurations taken into account in our analysis.

Comparison of FaCSI with other preconditioners

We compare the performance of FaCSI (hereafter configured using set C) with some state of the art preconditioners for FSI. In particular, we compare with the two preconditioners based on algebraic multigrid techniques proposed in [Gee et al., 2010] and the one level overlapping additive Schwarz preconditioner proposed in [Wu and Cai, 2014]. In both [Wu and Cai, 2014, Gee et al., 2010] the numerical example of the pressure wave propagation throughout a flexible tube is addressed. To carry out the comparison with [Gee et al., 2010] (in which hexahedral elements were used, whereas we use tetrahedra) we solve the FSI problem using both first order and second order space discretizations (denoted as "P1" and "P2" in Table 3.8). The comparison with [Wu and Cai, 2014] is carried out
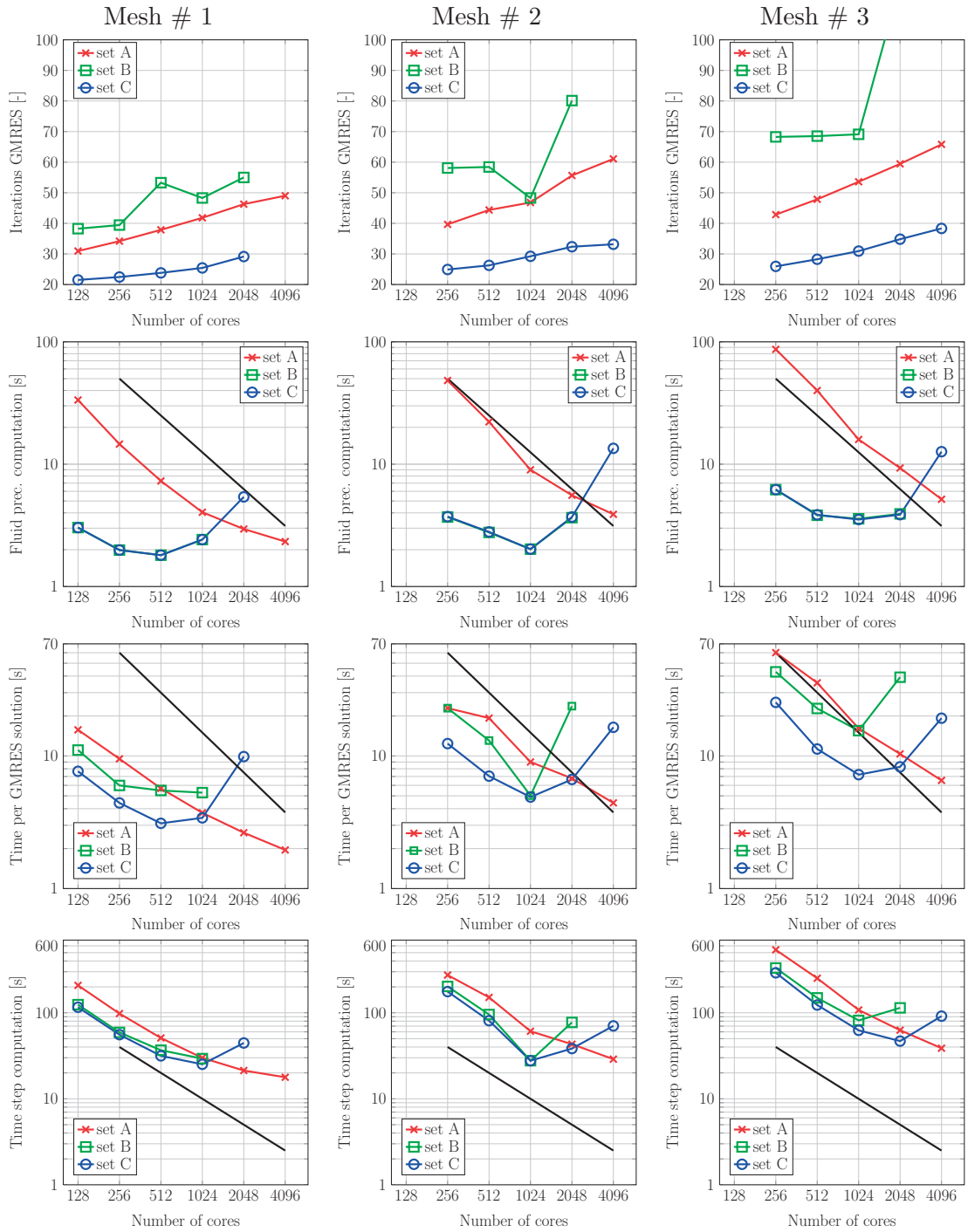
Figure 3.7: Strong scalability results obtained on meshes of increasing refinement (see Table 3.6). Black lines denote ideal scaling.

using the "P1" discretization (same settings of [Wu and Cai, 2014]). We remark that in the "P1" case, the fluid problem is stabilized using the same stabilization of [Wu and Cai, 2014].

For both the "P1" and "P2" discretizations the fluid-structure meshes have been generated such that the numbers of degrees of freedom of the fluid, structure and geometry fields are similar to those reported in [Gee et al., 2010] (see Table III discretization *pw3*). Discretization "P1" in Table 3.8 has almost the same number of degrees of freedom of the finer one used in [Wu and Cai, 2014] (that is 3.08×10^6). The comparisons of the results obtained by FaCSI with those reported in [Gee et al., 2010] and [Wu and Cai, 2014] are shown in Table 3.9 and in Figure 3.8, respectively: we notice that FaCSI well compares with both the preconditioners taken into account for the analysis.

Discretization	Fluid DoF	Structure DoF	Coupling DoF	Geometry DoF	Total
"P1"	1'539'226	456'120	75'180	1'154'420	3'224'946
"P2"	1'568'223	458'280	90'744	1'503'280	3'620'527

Table 3.8: Degrees of freedom of the discretized FSI problem for the comparisons with [Gee et al., 2010, Wu and Cai, 2014].

	# unknowns	CPUs	# GMRES
BGS(AMG), *pw3*	3'063'312	16	41.77
AMG(BGS), *pw3*	3'063'312	16	30.29
FaCSI, "P1"	3'224'946	16	23.24
FaCSI, "P2"	3'620'527	16	17.09

Table 3.9: Comparison of FaCSI with the preconditioners proposed in [Gee et al., 2010]. Note that # GMRES is the average number of GMRES iterations per Newton step (that is 3 both for us and [Gee et al., 2010]).
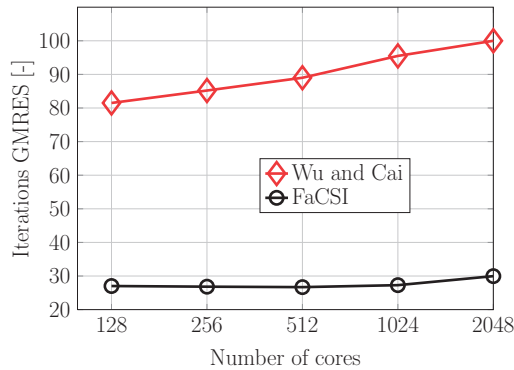
Figure 3.8: Comparison of FaCSI (using the "P1" discretization, see Table 3.8) with the overlapping additive Schwarz preconditioner proposed in [Wu and Cai, 2014] (red curve taken from right-most plot in Figure 4 of [Wu and Cai, 2014]).

3.7.2 FSI in a patient-specific femoropopliteal bypass

We consider a hemodynamic simulation in a femoropopliteal bypass. This problem has already been investigated in [Marchandise et al., 2012]. The geometric model of the

(a) Fluid domain.

(b) Structure domain.
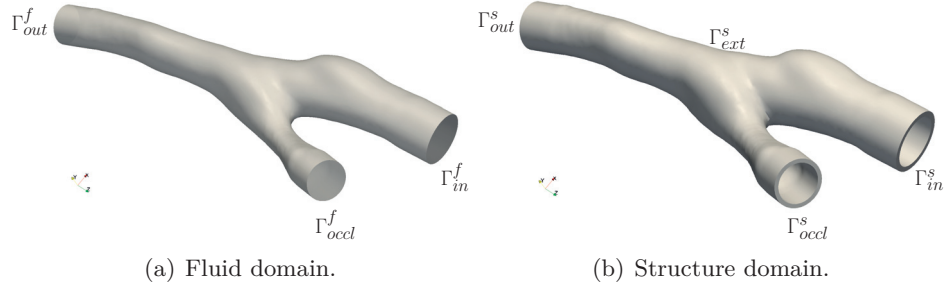
Figure 3.9: Femoropopliteal bypass test case: labels of the boundaries.

femoropopliteal bypass was obtained through a 3T MRI scanner while the computational unstructured meshes used in our simulations were generated using VMTK and Gmsh [Faggiano and Antiga, 2015]. We consider the blood characterized by a density $\rho_f = 1$ g/cm^3 and by a dynamic viscosity $\mu_f = 0.035$ g/(cm s). The physical parameters of the vessel wall are set as follows: the Young's modulus is $E_s = 4 \times 10^6$ dyne/cm^2, the Poisson's ratio is $\nu_s = 0.45$, and the density is $\rho_s = 1.2$ g/cm^3. The boundaries of the computational domain are labeled as illustrated in Figure 3.9. We impose patient-specific measured flow rate on Γ_{in}^f while homogeneous Dirichlet conditions are applied at the occluded branch Γ_{occl}^f. At the outflow section of the domain Γ_{out}^f we apply a mean pressure taken from [Colciago, 2014, Section 3.2.3], in which the same bypass geometry and inflow flow rate profile were considered. The structure is clamped at the inlets and the outlet rings Γ_{in}^s, Γ_{occl}^s and Γ_{out}^s where we impose $\hat{\mathbf{d}}_s = 0$. Homogenous Neumann boundary conditions are imposed at the outer surface of the vessel Γ_{ext}^s. The time step used is $\Delta t = 0.001$ s.

(a) Front and back view, Mesh #1.

(b) Top view: Mesh # 1 (first row) and Mesh # 2 (second row).
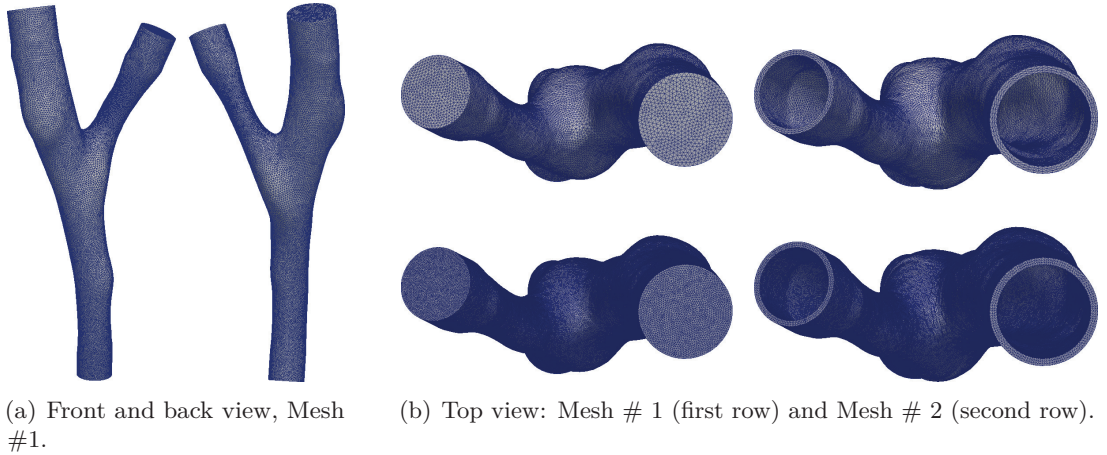
Figure 3.10: Meshes generated for the femoropopliteal bypass test case.

In our numerical simulations, we study the robustness of the proposed preconditioner with respect to the mesh size for a varying number of cores utilized. To analyze the robustness of the preconditioner proposed with respect to the mesh size, we consider

two set of fluid-structure meshes that are conforming at the interface, whose number of vertices and elements are summarized in Table 3.10. Figure 3.10 shows the computational meshes generated for the femoropopliteal bypass. In Table 3.11 we report the information concerning the number of degrees of freedom associated to the meshes used.

	Fluid		Structure	
	# Vertices	# Tetrahedra	# Vertices	# Tetrahedra
Mesh # 1	354'178	2'153'476	113'380	508'374
Mesh # 2	2'768'791	17'247'246	451'900	2'029'878

Table 3.10: Details of the coarse and fine meshes used for the femoropopliteal bypass example.

The strong scalability results of FaCSI (configured with set C of Table 3.5) are reported in Figure 3.11. In Figure 3.12 we show a post-processing of the numerical solution computed using Mesh # 2 at three time instances during the third heart beat simulated.

	Fluid DoF	Structure DoF	Coupling DoF	Geometry DoF	Total
Mesh # 1	9'029'128	2'376'720	338'295	8'674'950	20'419'093
Mesh # 2	71'480'725	9'481'350	1'352'020	68'711'934	151'026'029

Table 3.11: Femoropopliteal bypass test case: number of degrees of freedom.
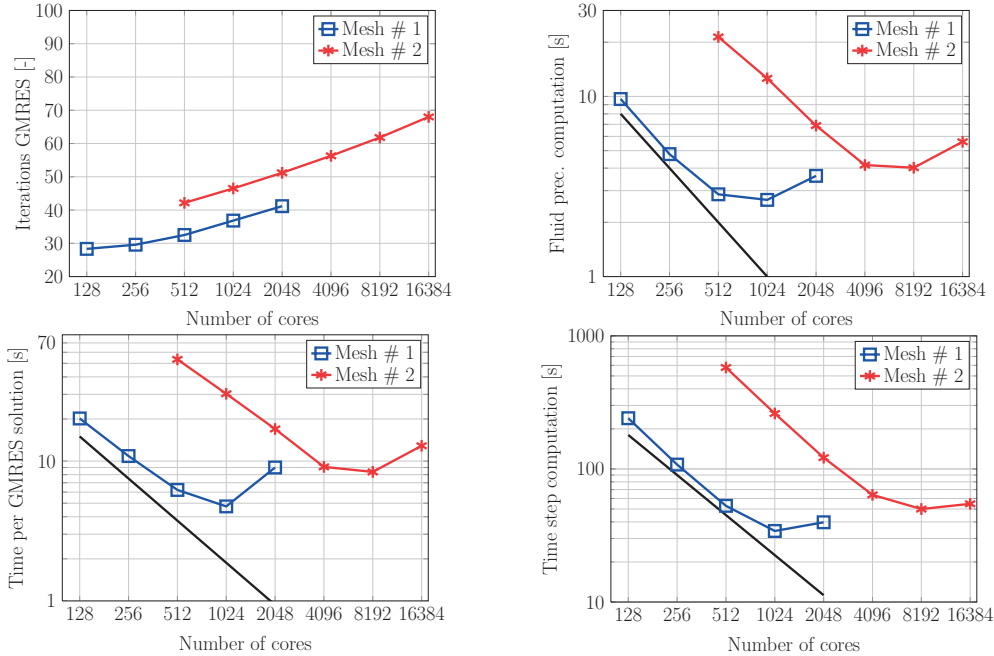
Figure 3.11: Strong scalability results for the femoropopliteal bypass example.
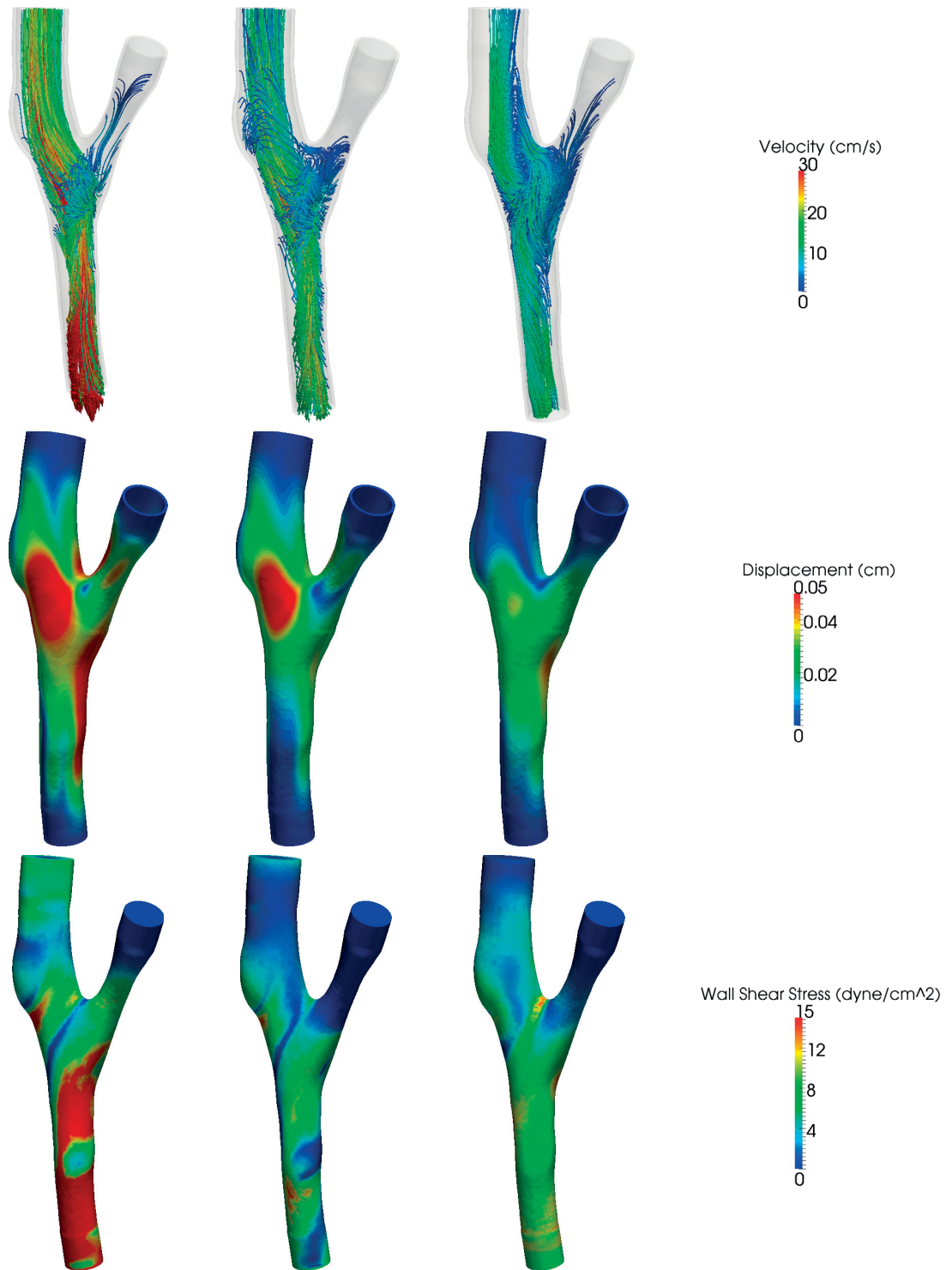
Figure 3.12: Post-processing of the results at time $t = 1.8$ s (left), 1.9 s (middle) and 2.0 s (right). Time $t = 1.8$ s coincides with the systolic peak of the third heart beat simulated. In the top row we show the streamlines of the fluid flow, in the middle row the magnitude of the structural displacement while in the bottom row the Wall Shear Stress.

As shown in Figure 3.11, we observe the robustness of FaCSI with respect to both the mesh size and the number of cores utilized. Indeed, on the smaller mesh (Mesh # 1) the number of linear solver iterations ranges from roughly 30 (with 128 cores) to 40 iterations (with 2'048 cores). On the larger mesh (Mesh # 2) the GMRES iterations increase from roughly 40 (using 512 cores) to 70 (with 16'384 cores). On the smaller mesh the strong scalability of the time to compute a single time step is close to the ideal scaling up to 512 cores while on the larger mesh is close to the be linear until 4'096 cores. We observe that on both Mesh # 1 and Mesh # 2, FaCSI scales almost linearly until the local number of degrees of freedom per core is roughly 40'000. For instance, on Mesh # 1 using 512 cores and on Mesh # 2 using 4'096 cores the single core workload is approximately 40'000. When the number of degrees of freedom per core is lower than 40'000 the communication occurring for the construction of the preconditioner and the solution of the linear system (as shown in Figure 3.11) dominates the relatively small amount of computational work performed by each single core. This behavior is in line with the weak scalability results reported in Figure 3.6, where we observed that FaCSI (configured by set C) was weakly scalable up to 40'000 degrees of freedom per core.

We recall that in [Grandperrin, 2013] a similar factorization as in Eq. (3.20) was used, and a SIMPLE preconditioner was exploited to directly approximate the factor $P_{\mathcal{F}}^{(3)}$. However, no static condensation was used to eliminate the interface fluid variables, yielding therefore to a different preconditioner (that in [Grandperrin, 2013] is called FSI-SIMPLE).

For the sake of illustration, in Figure 3.13 we show the number of linear solver iterations reported in [Grandperrin, 2013] to solve the femoropopliteal bypass example, with the same fluid and solid geometries and the same boundary conditions adopted here. The results of Figure 3.13 refer to a discretization of the FSI problem using 8'142'612 degrees of freedom, hence coarser than Mesh # 1 used in our Table 3.11. Moreover, we notice that the results of Figure 3.13 were obtained using subiterations for the application of the preconditioner FSI-SIMPLE. Subiterations allow to impose more accurately the preconditioner and in general ensure that the number of iterations remains almost constant as the number of cores utilized increases. We remark that the FaCSI preconditioner does not require subiterations.

By comparing the results of Figure 3.13 with the number of linear solver iterations associated to Mesh # 1 reported in Figure 3.11, we notice that the performance of FaCSI is much better than that of FSI-SIMPLE [Grandperrin, 2013] (without static condensation). In particular, it is noteworthy that the number of linear solver iterations of FaCSI (which ranges from roughly 30 to 40 on Mesh # 1) is remarkably smaller that those of FSI-SIMPLE (roughly 220) when 20 or 40 subiterations are used for the latter.
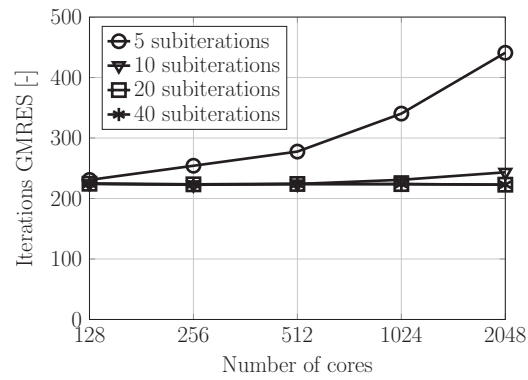
Figure 3.13: Femoropopliteal bypass example: number of linear solver iterations reported in [Grandperrin, 2013], Figure 5.18(c). The FSI problem is discretized using 8'142'612 degrees of freedom.

4 Benchmark problem for FSI in hemodynamics with complex nonlinear material models

In this Chapter, we consider a benchmark problem for blood flowing through a vessel wall representing an idealized coronary artery which includes fluid-structure interaction. This benchmark was proposed in [Balzani et al., 2015]. It has been designed to provide a useful testbed for fluid-structure interaction simulations in biomechanics featuring nonlinear structural models. Although being set on a simple geometry it still captures all numerical difficulties arising in realistic simulations and it is fully reproducible. We provide measures that may be useful for comparisons with future simulations and experiments or for code validation.

The geometry consists of a curved pipe that mimicks a tract of an artery. Physiologically-based inflow and outflow boundary conditions suited for blood flow in coronaries are considered. The simulation consists in a first initialization phase, followed by the simulation of several heartbeats. The initialization phase is carried out in order to raise the fluid pressure and the flowrate up to physiological reference values. It is crucial because the resulting prestretch in the structure strongly influences the fluid-structure interaction during the second phase. After describing the geometry, the boundary conditions and the physical parameters used for the fluid and the structure, we discuss both space discretizations, mesh convergence, sensitivity of the results w.r.t. the boundary conditions and thw material models used.

The content of this Chapter represents a revisitation of the results published in [Balzani et al., 2015].

4.1 Benchmark setup

The geometry of our benchmark problem shown in Figure 4.1 consists of a pipe in which a first curved part is followed by a straight one.

Inner radius of the structure	0.15cm
Outer radius of the structure	0.21cm
R, radius of curved part	1.0cm
L, length of straight part	1.0cm
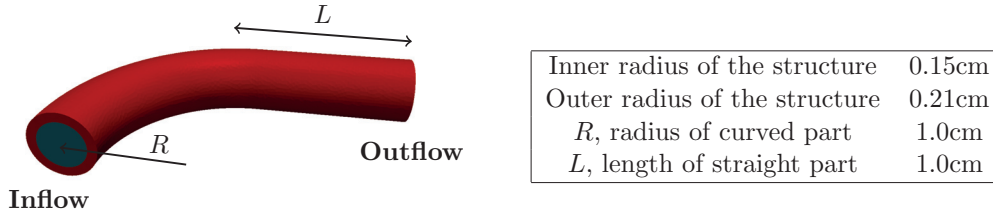
Figure 4.1: Geometry of the benchmark problem.

The wall thickness is chosen accordingly to realistic coronary arteries. We remark that the structural domain represents only the layer corresponding to the media of the artery. This choice represents a simplification w.r.t. the actual histology of human arteries: indeed, healthy arteries consist of mainly three layers, the intima, the media, and the adventitia, cf. [Holzapfel et al., 2000, Formaggia et al., 2009]. However, since we are interested in the set up of an easily reproducible benchmark problem, here focus on the mechanically most relevant layer, i.e. the media.

We model the mechanical response of the media using an anisotropic hyperelastic (see Chapter 2) and an anisotropic viscoelastic (see [Balzani et al., 2015], Section 2) material law. The material parameters used for the hyperelastic material model are taken from [Brands et al., 2008, Balzani et al., 2012, (Ψ_A Set 2)], see Table 4.1. These parameters are fitted to the material response of the media of a human abdominal aorta. As for the viscoelastic material model, we use two different sets of parameters, see Table 4.2. In Table 4.2 we denote by τ_1 the relaxation time while by β_1 the viscoelastic intensity [Balzani et al., 2015]. We remark that in Table 4.2, the parameters of Set 2 induce a short relaxation time in the structure such that the viscoelastic effects are more evident.

c_1 [kPa]	ε_1 [kPa]	ε_2	α_1 [kPa]	α_2
17.5	499.8	2.4	30 001.9	5.1

Table 4.1: Parameters used for the hyperelastic material model.

Set	c_1 [kPa]	ε_1 [kPa]	ε_2	α_1 [kPa]	α_2	τ_1	β_1
1	17.5	499.8	2.4	30 001.9	5.1	2.0	1.0
2	17.5	499.8	2.4	30 001.9	5.1	0.3	1.8

Table 4.2: Parameters used for the viscoelastic material model: long relaxation time (Set 1), and short relaxation time (Set 2).

Eight different meshes of increasing refinement are generated to carry out a mesh convergence study of the numerical results obtained, see Table 4.4. In our analysis we

consider three different spatial discretizations of the FSI problem, that we shortly name P1, P2 and $\bar{F}$, see Table 4.3. In the $\bar{F}$ discretization (see Remark 4.1, for the structure we use a a three-field (mixed) formulation which aims at avoiding locking effects in the finite element solution due to the almost incompressibility (see [Simo, 1998]).

Discretization	Fluid velocity	Fluid pressure	Structure displacement	ALE
P1	$\mathbb{P}1$	$\mathbb{P}1$	$\mathbb{P}1$	$\mathbb{P}1$
P2	$\mathbb{P}2$	$\mathbb{P}1$	$\mathbb{P}2$	$\mathbb{P}2$
$\bar{F}$	$\mathbb{P}2$	$\mathbb{P}1$	$\bar{F}$	$\mathbb{P}2$

Table 4.3: Discretizations used for the mesh convergence study.

When using the P1 discretization, the mesh convergence study will be carried out using meshes from #1 up to #7; for P2 and $\bar{F}$ discretizations, we make use only of meshes from #0 up to #4. In Tables 4.5 and 4.6 we report the number of degrees of freedom associated to the discretizations used. Note that, if we are only interested in fluid quantities, $\mathbb{P}1$ elements for the structure can suffice if a comparatively high number of degrees of freedom is considered. Conversely, $\mathbb{P}2$ or even better $\bar{F}$ elements for the structure are necessary for an accurate analysis of the structural stress distributions at a lower number of degrees of freedom.

Mesh	# Tetrahedra mesh fluid	# Tetrahedra mesh structure
#0	2'404	12'348
#1	6'549	21'636
#2	8'187	45'360
#3	12'670	98'742
#4	19'978	183'420
#5	40'011	274'500
#6	78'318	517'464
#7	179'513	1'036'800

Table 4.4: Details of the computational meshes used in our analysis.

Mesh	Fluid DoF	Structure DoF	Coupling DoF	Geometry DoF	Total
#1	7'240	14'664	3'546	5'430	30'880
#2	9'076	27'648	4'464	6'807	47995
#3	14'060	57'096	6'969	10'545	88'670
#4	20'460	101'937	9'075	15'345	146'817
#5	37'036	152'295	13'605	27'777	230'713
#6	68'544	282'165	21'417	51'408	423'534
#7	150'900	564'252	42'996	113'175	871'323

Table 4.5: Degrees of freedom associated to the P1 discretization.

Mesh	Fluid DoF	Structure DoF	Coupling DoF	Geometry DoF	Total
#0	15348	58'296	8'136	14'505	96'285
#1	36178	101'808	14'304	34'368	186'658
#2	45340	201'168	18'000	43'071	307'579
#3	70163	425'700	28'044	66'648	590'555
#4	105570	774'396	36'492	100'455	1'016'913

Table 4.6: Degrees of freedom associated to the P2 and $\bar{F}$ discretizations. The internal degrees of freedom in the $\bar{F}$ approach are statically condensated and are thus not considered (see Remark 4.1).

In the initialization phase we raise the fluid pressure and flowrate up to physiological reference values: this is crucial because the resulting prestretch in the structure will strongly influence the fluid-structure interaction during the subsequent simulation of the heartbeats.

In Sections 4.2 and 4.3 we describe the boundary conditions used and we discuss the numerical results obtained by solving part 1 and part 2, repectively, of the benchmark problem proposed.

The $\bar{\mathbf{F}}$ element

As shown in Table 4.3, different spatial approximations for the structure subproblem are considered. Besides the use of $\mathbb{P}1$ and $\mathbb{P}2$ finite elements, we will also make use the $\bar{\mathrm{F}}$ element type. The $\bar{\mathrm{F}}$ element stems from a three-field (mixed) formulation adopted for the structure problem; it was introduced to avoid locking effects in the finite element solution due to the almost incompressibility. Let $J = J(\boldsymbol{\varphi}) = \det(\mathbf{F})$, then we have

$$\mathbf{F} = J^{1/3}\tilde{\mathbf{F}}, \ \ \tilde{\mathbf{F}} = J^{-1/3}\mathbf{F}.$$

We introduce a new scalar variable θ, satisfying $\theta = J$ in a weak sense, and we define

$$\bar{\mathbf{F}} := \theta^{1/3}\tilde{\mathbf{F}}, \ \ \bar{\mathbf{C}} := \bar{\mathbf{F}}^T\bar{\mathbf{F}}$$

with $\bar{\mathbf{F}} = \bar{\mathbf{F}}(\boldsymbol{\varphi}, \theta)$, $\bar{\mathbf{C}} = \bar{\mathbf{C}}(\boldsymbol{\varphi}, \theta)$. We consider the following three-field Lagrangian

$$\mathcal{L}(\boldsymbol{\varphi}, \theta, \pi) = \int_\Omega W(\bar{\mathbf{C}}(\boldsymbol{\varphi}, \theta)) + \pi(J(\boldsymbol{\varphi}) - \theta)dx - V_{\text{ext}}(\boldsymbol{\varphi}),$$

where $V_{\text{ext}}(\boldsymbol{\varphi})$ is the potential energy of external forces; for more details, see [Simo, 1998, Section 45]. Hereafter, we understand by $\bar{\mathrm{F}}$ element a $\mathbb{P}2$-$\mathbb{P}0$-$\mathbb{P}0$ mixed finite element discretization, i.e., piecewise quadratic elements for the deformation field $\boldsymbol{\varphi}$ and piecewise constant elements for the scalar fields θ and π. In our formulation we perform static condensation of the degrees of freedom θ and π on each finite element.

4.2 Part 1: the initialization phase

4.2.1 Boundary conditions

At the inlet and outlet sections of the structure we apply homogeneous Dirichlet boundary conditions to the components of the structural displacement that are perpendicular to the respective faces. Specifically, we set $\hat{d}_z = 0$ and $\hat{d}_x = 0$ at the inlet and outlet sections of the structure, respectively. Additionally, to statically determine the artery, we impose zero displacement in y-direction for all degrees of freedom at the inlet and outlet of the structure located at $y = 0$, i.e. those on the red lines of Figure 4.2.
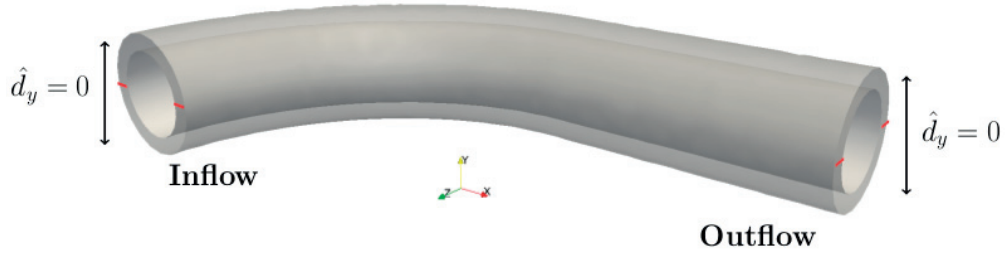
Figure 4.2: Dirichlet boundary condition at the inlet and outlet of the structure: y component of the displacement fixed at the red colored lines.

In the initialization phase, at the fluid inflow and outflow sections we apply an increasing inflow flow rate and an absorbing boundary condition, respectively. These boundary conditions allow the physical system to reach a steady condition at the end of the initialization phase in which the outflow pressure is $p_{\text{steady}} = 80\text{mmHg}$ and the inflow flow rate is $Q_{\text{steady}} = 3\text{cm}^3/\text{s}$ [Spiller et al., 1983]. In this way a prestretch of the arterial wall is generated and serves as a starting configuration for the subsequent simulation of several heart beats.

At the fluid inflow we prescribe a flow rate $Q_{\text{in}}(t)$ using a Dirichlet boundary condition, i.e., mapping $Q_{\text{in}}(t)$ through a parabolic inflow velocity profile. Specifically, at each dicrete time instance t^{n+1}, the value of $Q_{\text{in}}^{n+1} = Q_{\text{in}}(t^{n+1})$ is imposed at the inflow section of the fluid domain $\Gamma_{t,in}^{f}$ by a Dirichlet boundary condition on the velocity, namely $\mathbf{u}^{n+1}(\mathbf{x})\big|_{\Gamma_{t,in}^{f}} = (0,\, 0,\, u_z(\mathbf{x}))$ with

$$u_z^{n+1}(\mathbf{x}) = \alpha^{n+1}\, \hat{u}_z \circ \mathcal{A}_t^{-1}(\mathbf{x}), \tag{4.1}$$

where

$$\hat{u}_z(\hat{\mathbf{x}}) = \frac{R_{in}^2 - \|\hat{\mathbf{x}} - \hat{\mathbf{x}}_c\|^2}{R_{in}^2}. \tag{4.2}$$

$\hat{u}_z$ is a parabolic profile defined on $\widehat{\Gamma}_{in}^{f}$, which is the inflow section of the fluid domain at time $t_0 = 0$ s. R_{in} and $\hat{\mathbf{x}}_c$ are the radius and the barycenter of $\widehat{\Gamma}_{in}^{f}$, respectively, while

91

α^{n+1} reads

$$\alpha^{n+1} = \frac{Q_{\text{in}}^{n+1}}{\widehat{Q}_{\text{in}}^{n+1}}, \quad \text{being} \quad \widehat{Q}_{\text{in}}^{n+1} = \int_{\Gamma_{t,in}^f} \hat{u}_z \circ \mathcal{A}_t^{-1}(\mathbf{x}) \cdot \mathbf{n}_f \, d\gamma. \tag{4.3}$$

Indeed, this choice ensures that

$$\int_{\Gamma_{t,in}^f} \mathbf{u}^{n+1} \cdot \mathbf{n} = Q_{\text{in}}^{n+1}. \tag{4.4}$$

We raise the inflow flowrate Q_{in} from $0\text{cm}^3/\text{s}$ up to the physiological value of $3\text{cm}^3/\text{s}$ by means of a ramp function. There are many possible choices for the ramp function; here we consider both linear and cosine-type ramps. When using a linear ramp, the flow rate at the fluid inflow is raised according to:

$$Q_{\text{in}}(t) = \begin{cases} Q_{\text{steady}} \dfrac{t}{T_{ramp}} & \text{for } t_0 \le t \le T_{ramp}, \\ Q_{\text{steady}} & \text{for } T_{ramp} \le t \le T_{\text{steady}}, \end{cases} \tag{4.5}$$

where T_{ramp} denotes the time until the inflow flow rate reaches Q_{steady} and T_{steady} is the time at which the physical system reaches the steady state. Similarly, the use of a cosine-type ramp reads:

$$Q_{\text{in}}(t) = \begin{cases} \dfrac{1}{2} Q_{\text{steady}} \left(1 - \cos\left(\pi \dfrac{t}{T_{ramp}}\right)\right) & \text{for } t_0 \le t \le T_{ramp}, \\ Q_{\text{steady}} & \text{for } T_{ramp} \le t \le T_{\text{steady}}. \end{cases} \tag{4.6}$$

As we will see in Section 4.2.2, the time T_{steady} strongly depends on the choice of both T_{ramp} and the type of ramp function used. In Figure 4.3 we report an example of linear and cosine-type ramps used for our analysis. In the initialization phase, to prescribe
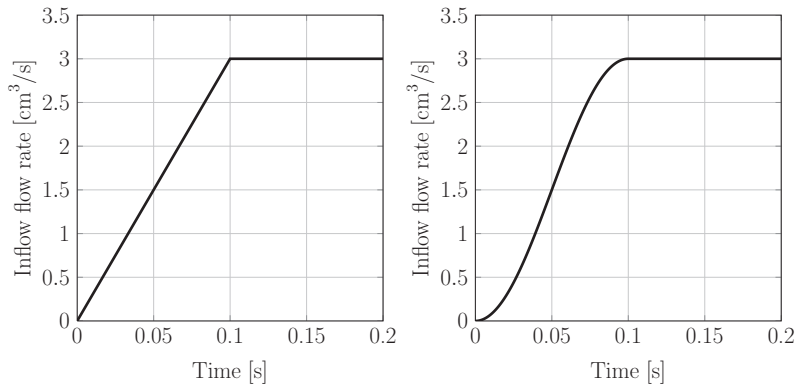
Figure 4.3: Linear (left) and cosine (right) type ramp with $T_{ramp} = 0.1$ s.

a desired physiological outflow fluid pressure at steady state, we consider a modified version of the absorbing boundary condition proposed in [Nobile and Vergara, 2008]. We recall that the absorbing boundary condition internally builds on a lower dimensional

linear elastic material model. In our nonlinear setting, in general, we can not expect this absorbing boundary condition to completely remove wave reflections. At time t^{n+1}, the following absorbing boundary condition is used:

$$\boldsymbol{\sigma}_f^{n+1} \cdot \mathbf{n}_f|_{\Gamma_{\text{out}}} = p_{f\text{out}}^{n+1} \mathbf{n}_f|_{\Gamma_{\text{out}}} \tag{4.7}$$

where

$$p_{\text{out}}^{n+1} = \left(\frac{\sqrt{\rho_F}}{2\sqrt{2}} \frac{Q_{\text{out}}^n}{\overline{A}} + \sqrt{\frac{tE}{1-\nu^2} \frac{\pi}{A^0} \sqrt{A^0}} \right)^2 - \frac{tE}{1-\nu^2} \frac{\pi}{A^0} \sqrt{A^0} + p_{\text{ref}}. \tag{4.8}$$

In (4.8), E, ν and t are Young's modulus, Poisson's ratio and the thickness of the structure, respectively, p_{ref} is a reference fluid pressure, Q_{out}^n is the outflow flow rate at the discrete time t^n, while A^0 is the area of the outflow section of the fluid domain in its reference configuration. In our setting, $\overline{A}$ is computed from (4.8) by imposing the steady state conditions, i.e., $p_{\text{out}}^{n+1} = p_{\text{steady}} = 80\text{mmHg}$ when $Q_{\text{out}}^n = Q_{\text{steady}} = 3\text{cm}^3/\text{s}$.

We remark that the values of Young's modulus E and Poisson's ratio ν are adjusted to the response of the nonlinear anisotropic hyperelastic material model described in Section 2.4.2. Here, only the material behavior in circumferential direction is considered for the adjustment of the linear elastic absorbing boundary condition, resulting in a Young's modulus of 120kPa and a Poisson's ratio of 0.49.

For the sake of visualization, in Figure 4.4 we show the prestreching obtained for the structure domain at the end of the intialization phase.
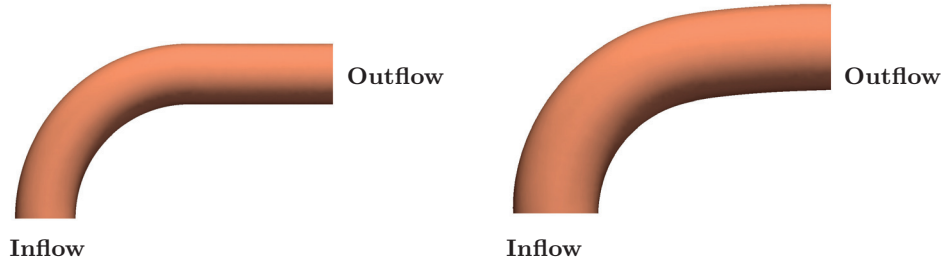
Figure 4.4: Geometry at a pressure of 0mmHg (left) and 80mmHg (right); displacement amplified by a factor of 3.0.

4.2.2 Sensitivity of the results to the choice of the ramp function

Linear ramp

In this Section we show the results obtained using the linear ramp (4.5) using the P1 discretization. We measure the flow rate, the average pressure, and the cross sectional area at the inflow and the outflow of the fluid domain, see Figure 4.1. The results of our

simulations are presented in Figure 4.5.
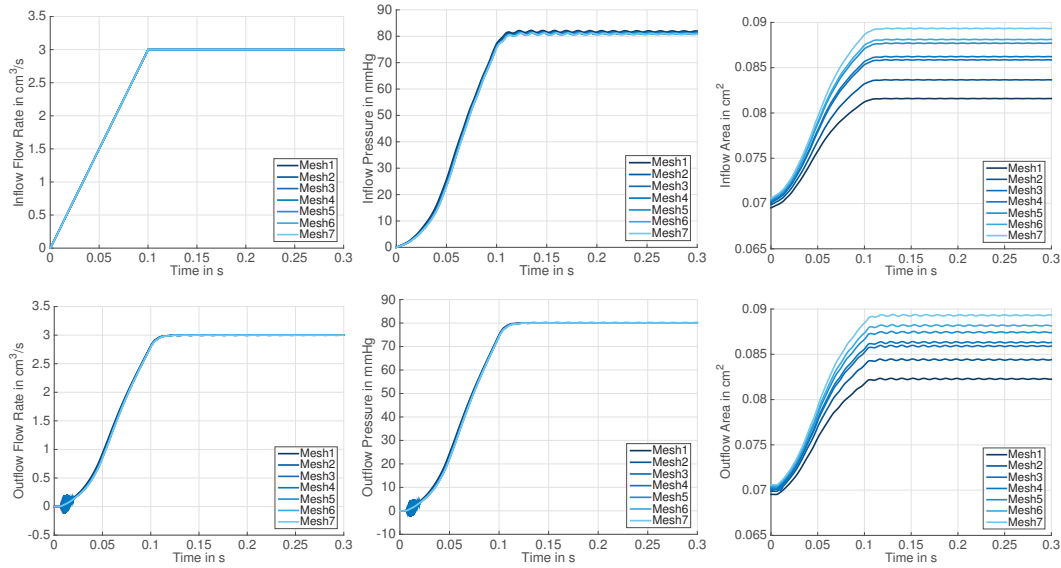
Figure 4.5: P1 mesh convergence study for the hyperelastic material using the linear ramp with $T_R = 0.1$s. Flow rate (left), average pressure (middle), lumen cross sectional area (right), over time at the inlet (top) and outlet (bottom).

As expected, the pressure at the inflow, see Figure 4.5 (top, middle), is slightly higher than the outflow pressure, cf. Figure 4.6. Furthermore, in Figure 4.6, we also notice that after T_{ramp}, small oscillations are still present and both their frequency and amplitude seem to be independent of the mesh size.

Regarding the outflow flow rate and pressure, see Figure 4.5 (bottom), small perturbations at the beginning of the ramp phase can be observed for the Meshes #2, #3, and #4. At the first glance, they could be attributed to the steep slope of the linear ramp, and thus the first time steps are very hard to solve. As we will discuss in Section 4.2.2, they are in fact due to the use of the P1 discretization. Within the simulation time of 0.3s, which corresponds to 3'000 time steps, the oscillations occuring after T_{ramp} decrease but do not vanish. Since we want to start the heartbeat from a steady state configuration, the use of a linear ramp requires the simulation to be continued until the oscillations decrease further.

Cosine-type ramp

We focus now on the results obtained by using the cosine ramp (4.6). We remark that this ramp is a $\mathcal{C}^1$-function which satisfies $\dot{Q}_{ramp}(t_0) = 0$, meaning that the transition between the increasing and the flat part of the ramps is smooth and therefore the difficulty of solving the first time steps is expected to decrease.
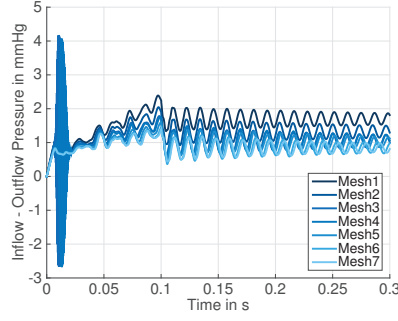
Figure 4.6: Inflow minus outflow pressure for the hyperelastic material using the linear ramp with $T_{ramp} = 0.1$ s.
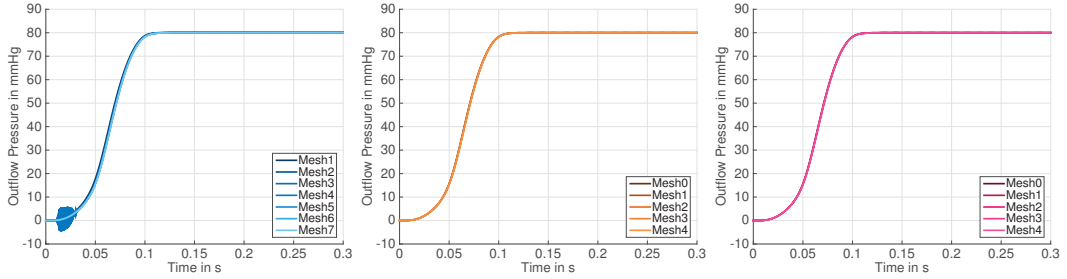
Figure 4.7: Outflow pressure for the hyperelastic material using the cosine-type ramp with $T_{ramp} = 0.1$ s for P1 (left), P2 (middle) and $\bar{F}$ discretizations.

Let us first discuss the perturbations in the outflow quantities (e.g., see bottom-left plot of Figure 4.5). We consider Meshes #1 to #7 for the P1 discretization, and Mesh #0 to Mesh #4 for both P2 and $\bar{F}$, see Table 4.4 and Table 4.6. In Figure 4.7, the corresponding outflow pressure is shown and we can see that the perturbations remain also for this smoother ramp. However, for P2 (middle) and $\bar{F}$ (right) discretizations, the perturbations at the beginning of the ramp vanish.

Mesh	Linear ramp P1	Cosine ramp P1	Cosine ramp P2	Cosine ramp $\bar{F}$
#0	-	-	$2.7 \cdot 10^{-5}$	$2.7 \cdot 10^{-5}$
#1	$1.1 \cdot 10^{-4}$	$3.6 \cdot 10^{-6}$	$2.8 \cdot 10^{-5}$	$2.8 \cdot 10^{-5}$
#2	$1.2 \cdot 10^{-4}$	$8.6 \cdot 10^{-6}$	$2.7 \cdot 10^{-5}$	$2.7 \cdot 10^{-5}$
#3	$1.3 \cdot 10^{-4}$	$1.1 \cdot 10^{-5}$	$2.7 \cdot 10^{-5}$	$2.7 \cdot 10^{-5}$
#4	$1.3 \cdot 10^{-4}$	$1.3 \cdot 10^{-5}$	$2.7 \cdot 10^{-5}$	$2.7 \cdot 10^{-5}$
#5	$1.4 \cdot 10^{-4}$	$1.6 \cdot 10^{-5}$	-	-
#6	$1.2 \cdot 10^{-4}$	$1.9 \cdot 10^{-5}$	-	-
#7	$1.2 \cdot 10^{-4}$	$2.0 \cdot 10^{-5}$	-	-

Table 4.7: Amplitude of the oscillations of the outflow cross sectional area at $t = 0.2$ s.

Another reason for using the cosine ramp is to try to reduce the oscillations occuring after T_{ramp}, hence in the constant part of the ramp function. In Figure 4.8, the outflow cross sectional area for the P1, P2, and $\bar{F}$ discretizations is reported for the different
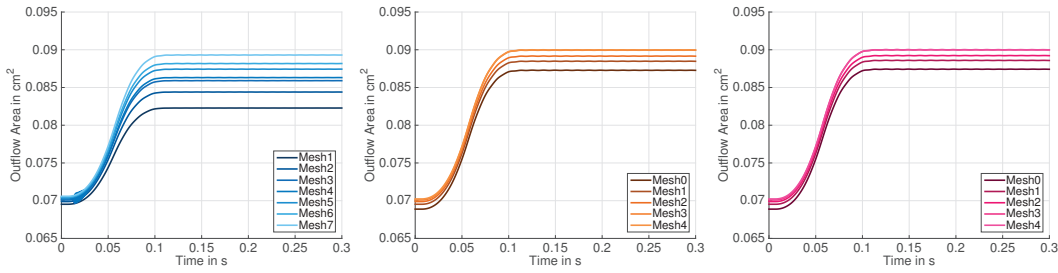
Figure 4.8: Mesh convergence study of the outflow cross sectional area for the hyperelastic material using the cosine-type ramp with $T_{ramp} = 0.1$ s for P1 (left), P2 (middle) and $\bar{F}$ discretizations. In this diagram, the graphs for Mesh #3 and Mesh #4 completely overlap for P2 and $\bar{F}$ discretizations.

meshes and discretizations considered. Comparing these results to those of Figure 4.5, on the visible scale we appreciate a substantial reduction of the amplitude of the oscillations. More precisely, the amplitude is reduced by one order of magnitude, see Table 4.7, using the cosine ramp instead of the linear one.

In order to investigate grid convergence, we foucus on the numerical results shown in Figure 4.8. As in Figure 4.5, grid convergence can not yet be observed for P1 elements (left). On the other hand, the results for P2 (middle) and $\bar{F}$ (right) discretizations do suggest mesh convergence. From the results presented here, from now on, we will use a cosine ramp because it yields to imperceptible oscillations in the output of interest after T_{ramp}. In the next Section we investigate whether we can further decrease T_{ramp}.

4.2.3 Sensitivity to the steepness of the ramp

In this Section we focus on the use of the cosine ramp and we consider three different values of T_{ramp}, namely $T_{ramp} \in \{0.05 \text{ s}, 0.1 \text{ s}, 0.2 \text{ s}\}$. We investigate how the choice of T_{ramp} affects the behavior of the outflow cross sectional area in time. In this regard, we restrict ourselves to the use of Mesh #1 for the P2 discretization. Furthermore, in addition to the hyperelastic material model, here we also consider a viscoelastic one (see [Balzani et al., 2015]). For the parameter Set 1 of Table 4.2, which has been used for the simulation, the overstresses are small and the relaxation time is long. Specifically, the relaxation time of the viscoelastic material model used here is longer than 2 s, and thus the system cannot reach the steady state before 2 s. Thus, viscoelastic effects are difficult to observe.

In Figure 4.9, oscillations are visible only for the steepest ramp considered, i.e. with $T_{ramp} = 0.05$ s. For both the longer ramps, namely for $T_{ramp} = 0.1$ s and $T_{ramp} = 0.2$ s, the oscillations are not visible at the scale presented, and thus are considered as acceptable. The qualitative behavior of the hyperelastic and the viscoelastic material is similar, however, we can observe that the cross sectional area is lower for the viscoelastic material

and slowly increases due to creep behavior. We will not focus on the differences between the material models now, but refer to Section 4.2.5, for a discussion on the influence of viscoelasticity in the fluid-structure interaction simulations with regard to the chosen space discretization.

Based on the conclusions reached so far we will use a cosine ramp of lenght $T_{ramp} = 0.1$ s. After another 0.2 s of constant inflow flow rate we consider the system to be at steady state, i.e., $T_{steady} = 0.3$ s, and ready for the subsequent simulation of the heart beats.
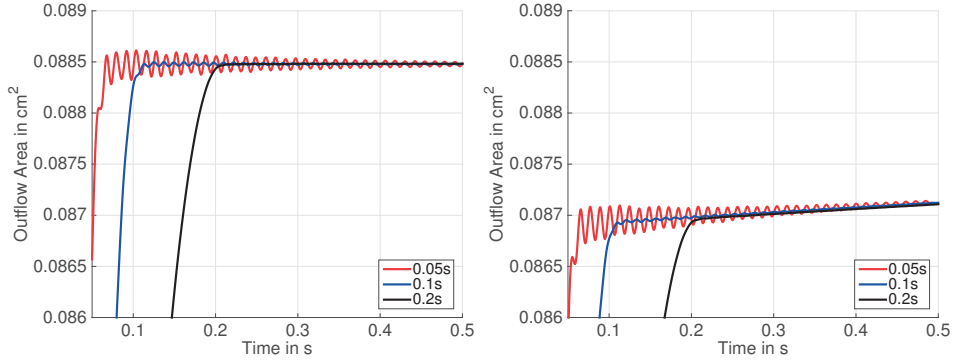
Figure 4.9: Outflow cross sectional area using the P2 discretization on Mesh #1. Hyperelastic (left), and viscoelastic (right) material models using, for the latter, parameter Set 1 of Table 4.2.

4.2.4 Sensitivity to parameters of the absorbing boundary conditions

In this Section we further investigate on the oscillations observed in the numerical results reported so far after T_{ramp}: in particular, we are interested in assessing whether the reason could be the absorbing boundary condition that we prescribe at the fluid outflow to remove wave reflections. We recall that the absorbing boundary condition is based on the assumpion that a one dimensional linear elastic model is appended at the outlet boundary section. Since here we use highly nonlinear material models, it is not clear if the absorbing boundary condition will be able to completely remove wave reflections at the outlet, especially if the corresponding linear elastic material parameters are not chosen appropriately.

We investigate the influence of Young's modulus E in the absorbing boundary condition. In order to minimize the computational effort, for these simulations we used the P1 discretization on Mesh #1.

As can be seen in Figure 4.10, neither the inflow pressure (left) nor the outflow cross sectional area (right) are influenced strongly by the varying Young's modulus. These measured quantities showed the strongest oscillations in the previous sections, which are however relatively small due to the particular choice of the ramp. This suggests that the
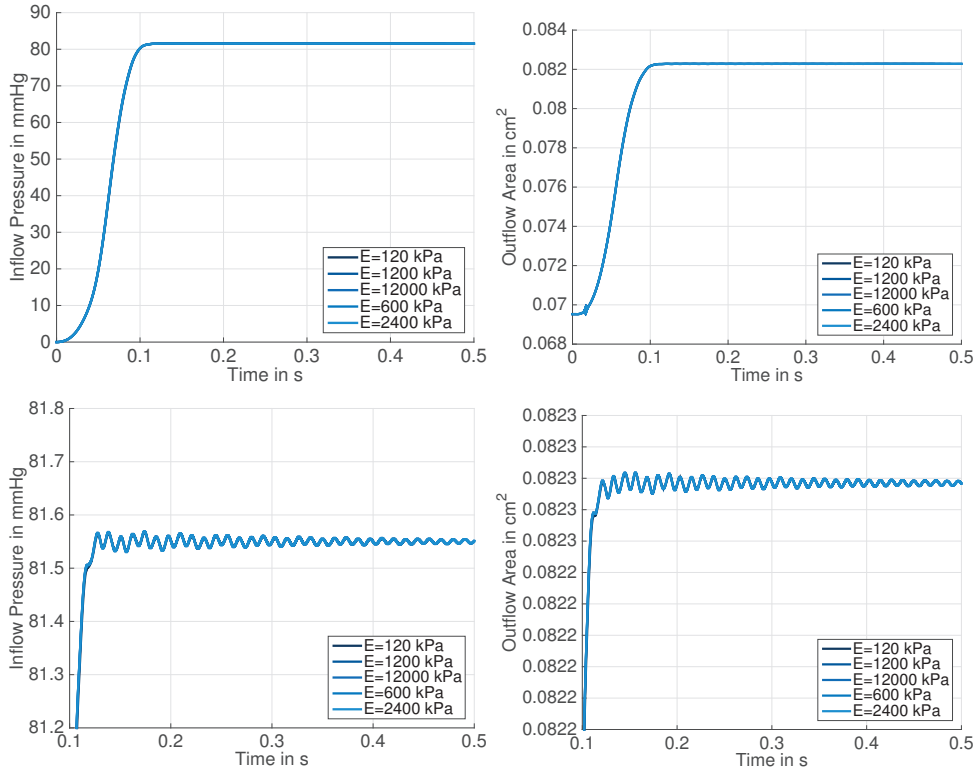
Figure 4.10: Sensitivity analysis for the absorbing boundary conditions performed using the P1 discretization on Mesh #1: inflow average pressure (left), and outflow lumen cross sectional area (right). All curves overlap completely. Global view (top), and zoom (bottom).

remaining oscillations in the constant part of the ramp are not caused by the absorbing boundary condition used.

4.2.5   Influence of viscoelasticity

As already mentioned in Section 4.2.2, our results suggest to favor P2 and $\bar{F}$ with respect to P1. In this Section, we compare the different space discretizations in detail with the focus being on the influence of viscoelasticity on the numerical results. As a result of our analysis we will find that the P1 discretization does not only show disadvantageous approximation properties with respect to P2 and $\bar{F}$, but it also yields a qualitatively incorrect behavior.

In Figure 4.11 we compare the results obtained by simulating the initialization phase of the benchmark problem using the viscoelastic and the hyperelastic material models. To better highlight the viscoelasticity effects we use parameter Set 2 from Table 4.2, which has a much shorter relaxation time compared to the one of Table 4.2. In Figure 4.11, the expected behavior can be observed: when we impose the same pressure (left) as for the
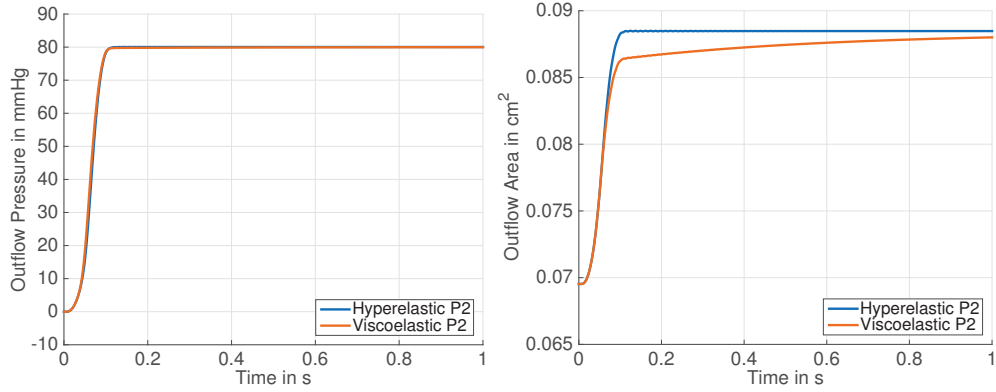
Figure 4.11: Comparison of the hyperelastic and the viscoelastic material models using the P2 discretization, the cosine ramp and parameter Set 2 (for the viscoelastic material) from Table 4.2 on Mesh #1. Outflow average pressure (left), outflow lumen cross sectional area (right).

hyperelastic material model, the displacement is lower in the beginning and converges to the displacement of the hyperelastic material model over time and this is due by the creep behavior introduced in fiber direction.

Differently than P2 discretization, the use of P1 leads to a qualitatively wrong behavior, as can be observed in Figure 4.12: for a constant pressure (left), the displacement (right) decreases using the P1 discretization, while the use of $\bar{F}$ yields the same (correct) results as P2. Moreover, we notice that the P2 discretization yields the expected asymptotic behavior of the viscoelastic material model; conversely, using P1, such expected asymptotic behavior is not observed.
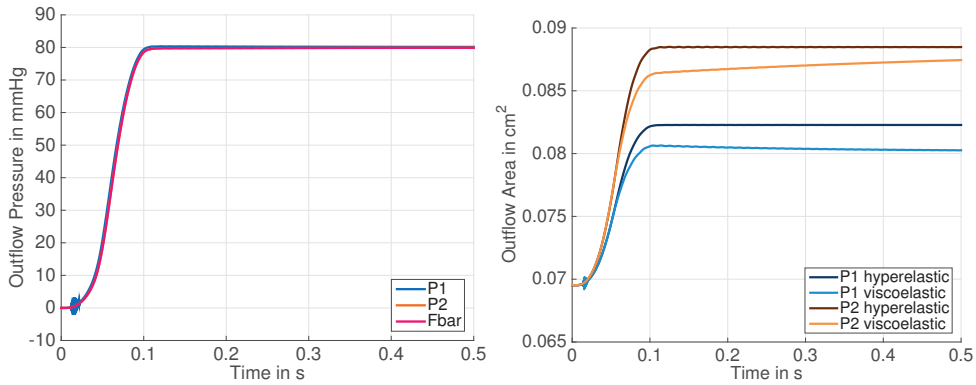
Figure 4.12: On the left we show the outflow pressure obtained using the viscoelastic material model on Mesh #1 for different space discretizations. On the right, comparison of the hyperelastic and the viscoelastic material model using P1 and P2 discretizations. We use parameter Set 2 from Table 4.2 for the viscoelastic material.

It is noteworthy that P1 discretization leads to a much smaller displacement than P2 or $\bar{F}$ elements for the same mesh. This can be seen for the hyperelastic and also the

viscoelastic material model, see Figure 4.12 (right). We understand this behavior as the property of P1 discretization which tends to feature locking effects and to be mechanically stiffer compared to P2 and $\bar{F}$.

These observations, in combination with the discussion addressed in Section 4.2.2 about the perturbations which arise in the beginning of the ramp phase for the P1 discretization, are convincing arguments that P1 discretization is not sufficient to describe accurately the structural behavior. However, it may be sufficient to use $\mathbb{P}1$ elements for the structure if one consider hyperelastic material models and provided that a very fine mesh is used.

4.2.6   Further investigations on the oscillations

In this Section we investigate whether the oscillations which occur after T_{ramp} may be due to the geometry considered: in particular, if they are due to the length of the straight part of the pipe. Therefore, here we consider a modified geometry which features a longer straight part, namely we consider $L = 4$ cm, see Figure 4.13. The details of the mesh generated are reported in Tables 4.8 and 4.9. For the numerical simulation we use a cosine ramp with $T_R = 0.05$ s.

Figure 4.13: Geometry of the problem with a longer straight part, $L = 4$ cm.

#Elements fluid mesh	#Elements structure mesh	#DoF P1	#DoF P2	#DoF $\bar{F}$
2'404	12'348	64'999	391'693	391'693

Table 4.8: Number of elements of the meshes generated for the new geometry and total number of degrees of freedomm for the P1, P2 and $\bar{F}$ discretizations.

Discretization	Fluid DoF	Structure DoF	Coupling DoF	Geometry DoF	Total
P1	14'188	32'232	7'938	10'641	64'999
P2	69'292	224'784	31'872	65'745	391'693
$\bar{F}$	69'292	224'784	31'872	65'745	391'693

Table 4.9: Number of degrees of freedom associated to the P1, P2 and $\bar{F}$ discretizations.

In Figure 4.14, the outflow flow rate (left), inflow average pressure (middle), and outflow lumen cross sectional area (right) are shown for the P1 and P2 discretizations, comparing the geometry described in Figure 4.1 with the new one with a longer straight part. As
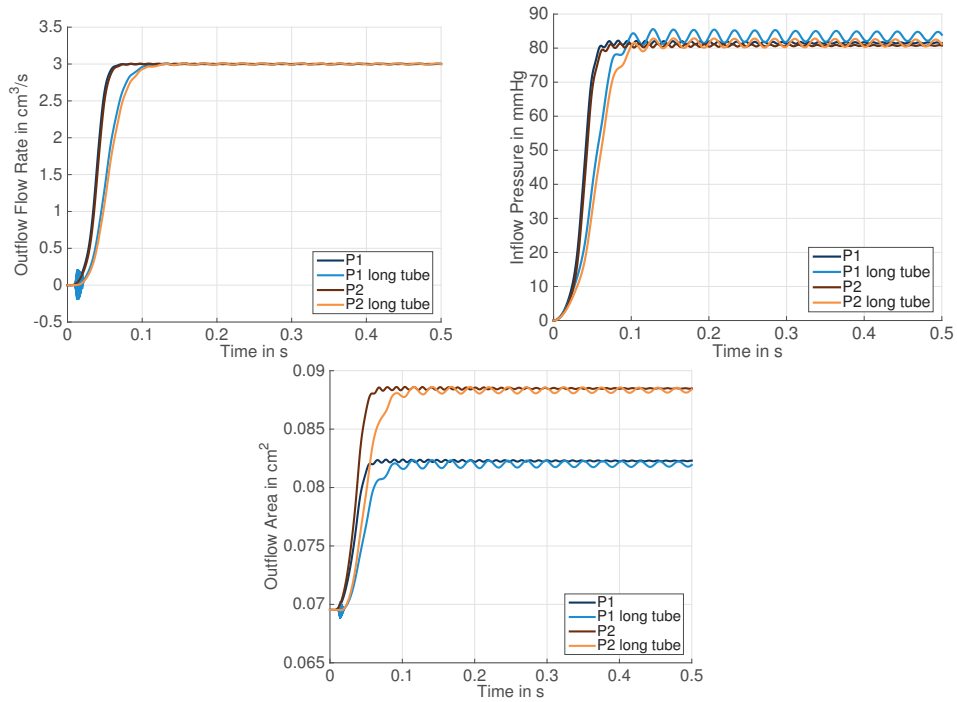
Figure 4.14: Comparison of the numerical results obtained with P1 and P2 discretizations using the new geometry (denoted in the legend as "long tube") and the one shown in Figure 4.1.

expected, the outflow flow rate of the long tube has a delay compared to the standard geometry, because it takes longer for the fluid wave to reach the outflow of the tube. The oscillations arising in the inflow pressure and the outflow cross sectional lumen area show a much larger amplitude and also a frequency which is roughly smaller by a factor of 1/4. Thus, the oscillations may depend on the length of the geometry. In Figure 4.15 we finally report the structure displacement at different time instances of the simulation using the new geometry.
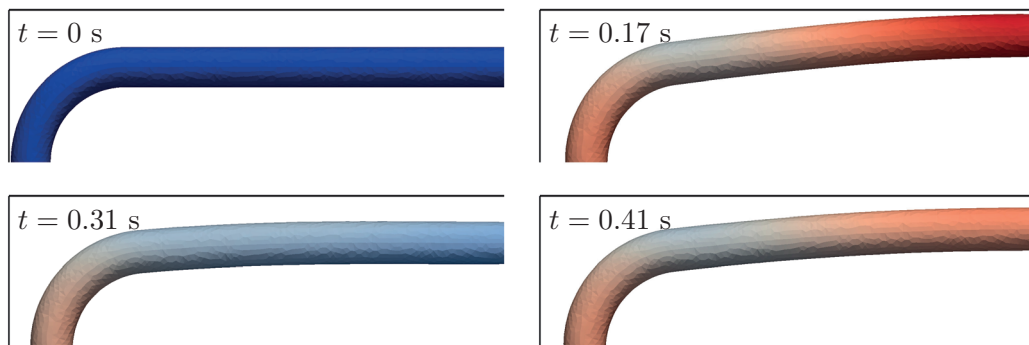
Figure 4.15: Structure displacement of the new geometry.

Based on the analyses carried out so far, we may conclude that the best setting to be adopted for the numerical simulation of the intialization phase consists in using:

- cosine ramp with $T_{ramp} = 0.1$ s and $T_{steady} = 0.3$ s for the inflow flow rate;

- P2 and $\bar{F}$ space discretizations;

- $L = 1$ cm as lenght for the straight part of the geometry.

Once the initiliazation phase is completed, in Section 4.3 we focus on the set up and numerical simulation of several heart beats.

4.3 Part 2: simulation of several heart beats

In this Section we present the settings and discuss the results of part 2 of the benchmark problem proposed: it consists in the numerical simulation of several heart beats. In the former initialization phase, the artery has been prestretched up to a physiological pressure of 80 mmHg and the flow rate has been raised up to a physiological value of 3 cm^3/s by using a cosine ramp of steepness $T_{ramp} = 0.1$ s. As already mentioned in the previous sections, after T_{ramp} we continue the simulation of part 1 of the benchmark until the system reaches a steady state at time T_{steady}. After the system has reached the steady state, we perform the simulation of several heart beats.

4.3.1 Boundary conditions

During the heart beats phase, at the fluid inflow we prescribe the flow rate profile over time $Q_{\text{in}}(t)$ shown in Figure 4.16. A typical pressure profile in coronaries is provided
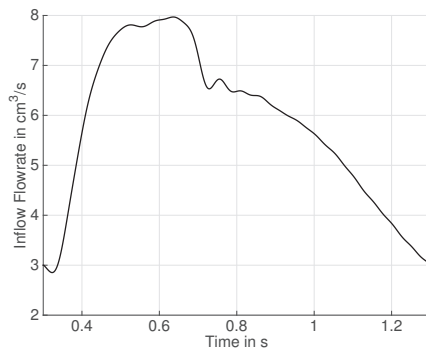
Figure 4.16: Inflow flow rate for the heart beat phase.

by [hem, 2014]. However, imposing a pressure or, better, a normal stress at inflow, can lead to instabilities (see [Nobile., 2001], Section 3.2), which we indeed observed using

fine meshes. These instabilities did not occur when using Mesh #1. Therefore, from a full heartbeat simulation performed using Mesh #1, the resulting inflow flow rate over time was then approximated by means of a Fourier series of order 20, and thus a periodic function Q_{in} was obtained.

We remark that, in this way, the inflow flow rate results in a pressure (which mainly influences the stress distribution through the arterial wall) which follows a typical profile for a coronary. The reason why the pressure and flow rate profiles used in our simulations are not significantly different is due to the fact that, in our model, we do not take into account the forces exerted by the heart muscle on the coronary vessels. Nevertheless, the flow rate reported in Figure 4.16 is in rough accordance to the one of a right coronary artery, for which the systolic heart compression through the right ventricular myocardium has much smaller effect on the flow, compared to the influence which the left ventricular myocardium has on the left coronary [Mohrman and Heller, 2013, Chandramouli, 2010].

The function Q_h describes the inflow flow rate over time during each heartbeat, see Figure 4.16. Analogously to the inflow flow rate profile used in the initialization phase, here $Q_{\text{in}}(t)$ is prescribed as a Dirichlet boundary condition at the inflow section of the fluid domain.

At the fluid outflow, during the heart beats phase, we use a standard absorbing boundary condition [Nobile and Vergara, 2008]. For the structure, we use the same boundary conditions adopted for the initialization phase.

4.3.2   Numerical results

During the simulation of the heart beats, we use a time step $\Delta t = 10^{-3}$ s that is larger with respect to the one used for the initialization phase. In Figure 4.17, the average inflow pressure (left) and outflow cross sectional lumen area (right) for P2 and $\bar{F}$ discretizations are presented. Similarly to what we observed during the initialization phase, also during all three heartbeats we notice a very similar behavior for both the discretizations considered.

In Figure 4.18 and 4.19, the deformation and flow rate profile over time is depicted. The largest structural deformations are observed at the inner part of the curvature towards the inlet section. Here, we notice that the structure undergoes large deformations mostly because it is close to the inflow section of the fluid domain.

Mesh convergence study

In analogy to studies carried out in Section 4.2.2, here we address a mesh convergence study for the heart beats phase of the benchmark problem. In Figure 4.20, mesh
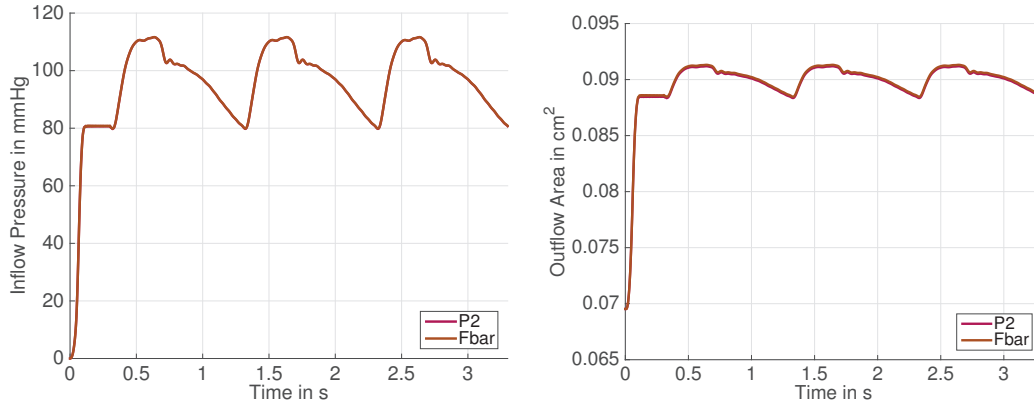
Figure 4.17: Simulation of 3 heart beats using Mesh #1 and the hyperelastic material model: inflow pressure (left), and outflow cross sectional lumen area (right).
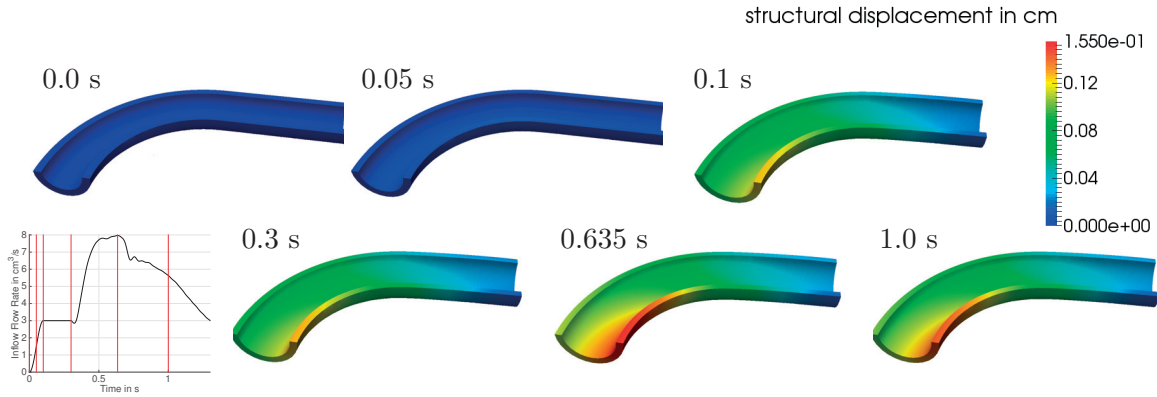
Figure 4.18: Evolution of the structure displacement at times 0.0s (top left), 0.05 s (top middle), 0.1 s (top right), 0.3 s (bottom left), 0.635 s (bottom middle), and 1.0 s (bottom right). Simulation performed using Mesh #3 and the $\bar{F}$ discretization. Displacement is magnified by a factor 2.0.

convergence plots for P1 (left), P2 (middle), and $\bar{F}$ (right) elements are shown. We considered Meshes #1 to #7 for P1 and Mesh #0 to #4 for P2 and $\bar{F}$ discretizations, respectively. When using the P1 discretization, we notice that the outflow area does not feature mesh convergence; conversely, for both P2 and $\bar{F}$ discretizations this is the case. In terms of inflow pressure (top row of Figure 4.20), for all the discretizations considered, there are only mild differences in the results obtained using the different discretizations. However, we notice that the pressure of the coarsest mesh obtained using the P1 discretization is significantly higher than the maximal pressure of the coarsest P2 or $\bar{F}$ mesh. We conclude that for P1 elements, we are still far away from asymptotics, while for P2 and $\bar{F}$ elements, we have indication of mesh convergence: indeed, the graphs for Mesh #3 and Mesh #4 completely overlap for all quantities.
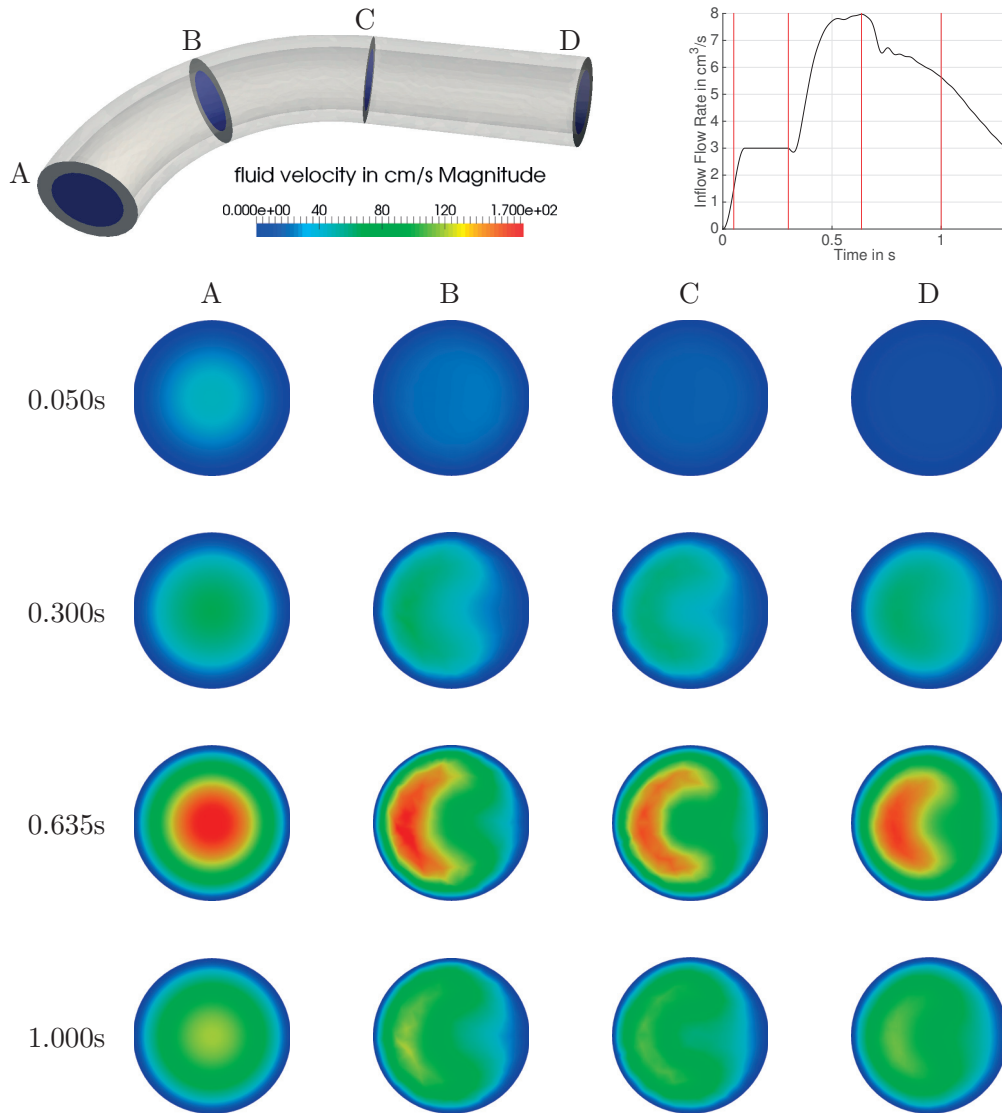
Figure 4.19: Evolution of the fluid velocity at different cross sections of the fluid domain. Simulation performed using Mesh #7 and the P1 discretization.

Analysis of Stresses

In this section, the transmural stress distribution inside the arterial wall is investigated. Therefore, a simulation including a cosine ramp with $T_{ramp} = 0.1$ s followed by a heartbeat starting at time $t = 0.3$ s is considered. For the structural response our polyconvex, anisotropic hyperelastic material model is used. To analyze the quality of the approximated stress quantities, all different discretizations, i.e. P1, P2 and $\bar{F}$, are considered and compared one to each other. This comparative analysis is carried out using Mesh #7 for the P1 discretization, whereas for the P2 and $\bar{F}$ simulations Mesh #3 is considered: indeed, following the findings reported in Section 4.3.2 these meshes are
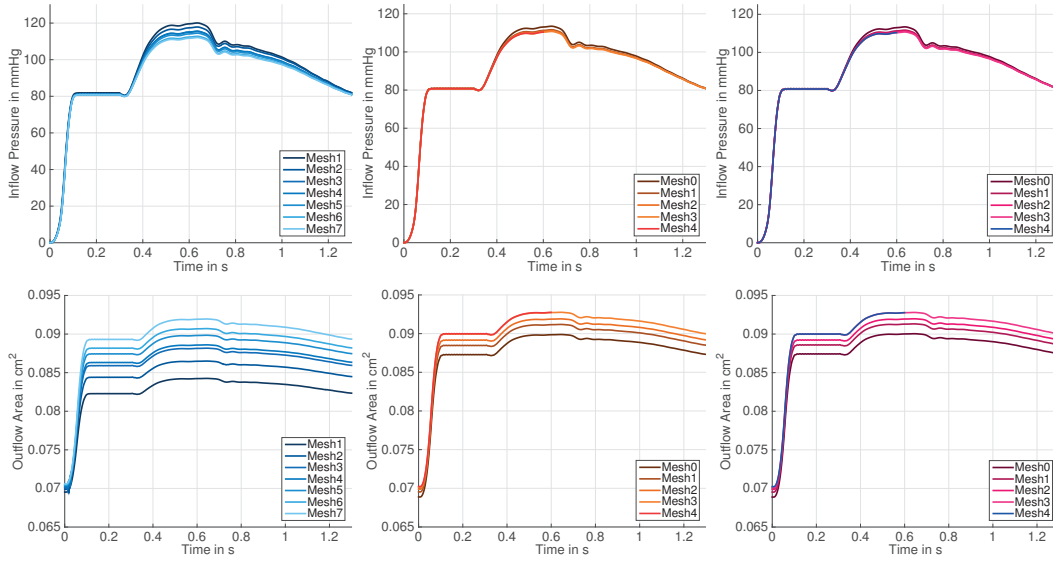
Figure 4.20: Mesh convergence of the inflow pressure (top) and outflow cross sectional lumen area (bottom) during the heartbeat phase: P1 (left), P2 (middle) and $\bar{F}$ (right) discretizations.
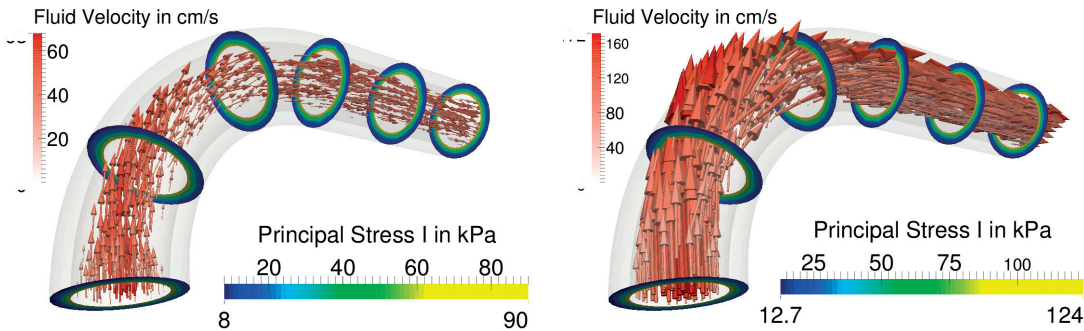
Figure 4.21: Fluid velocity and first principal Cauchy stress at $t = 0.3$s (left) and at $t = 0.635$s (right).

considered to yield sufficiently accurate solutions in the sense of mesh convergence. The stress quantities are evaluated at two different times during the simulation, i.e., $t = 0.3$ s and $t = 0.635$ s. These correlate with the steady state right before the beginning of the heart beat representing a diastolic blood pressure of 80mmHg, and with the peak value of the inflow flow rate for the heartbeat phase, where a systolic blood pressure of approximately 120mmHg is reached. An illustration of the evaluation points and the associated fluid velocity and transmural distribution of the first principal Cauchy stresses, at different slices of the geometry, is shown in Figure 4.21.
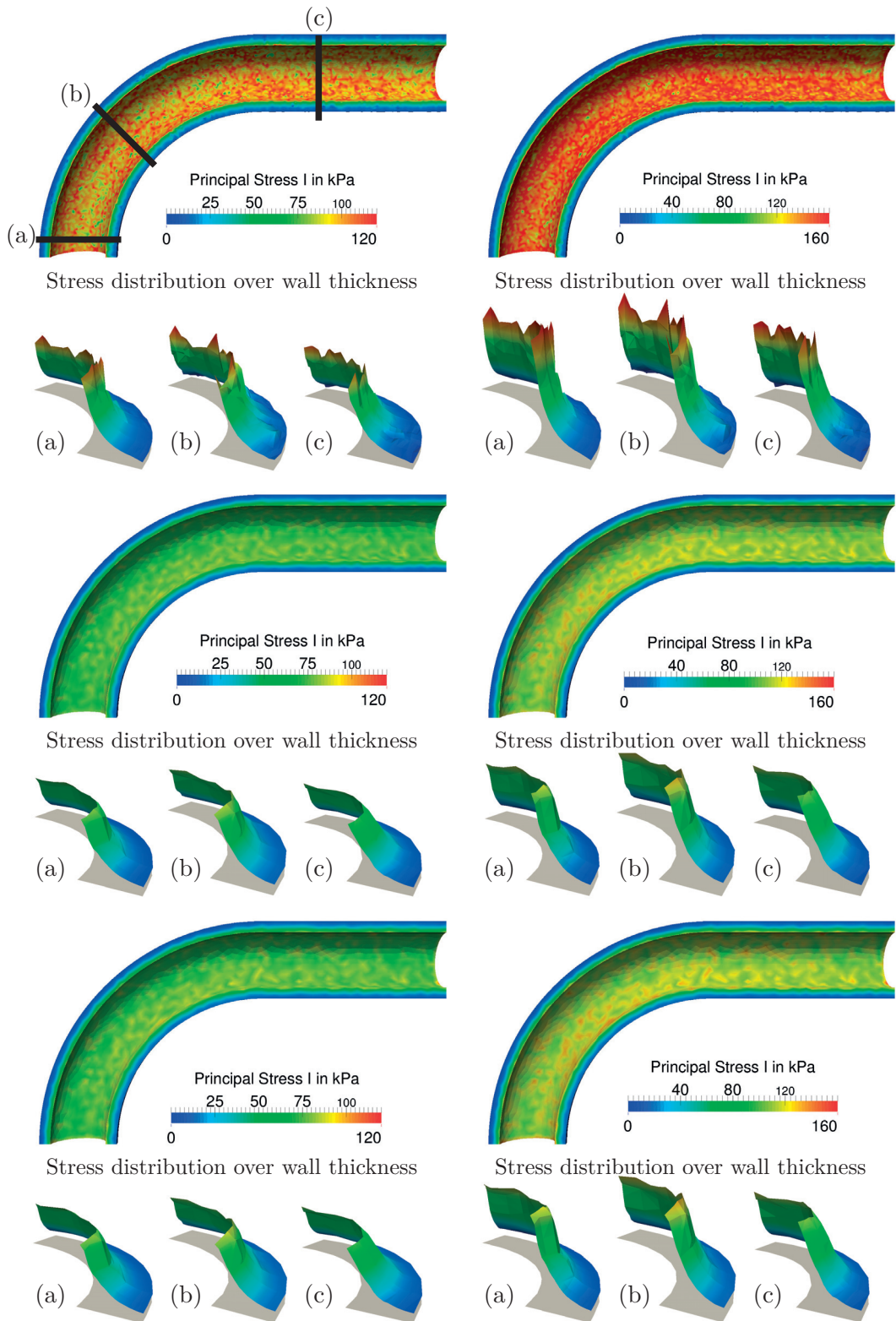
Figure 4.22: Comparison of the first principal Cauchy stress for P1, P2 and $\bar{\mathrm{F}}$ discretizations at the inner surface and over the wall thickness: P1 at $t = 0.3$ s (top left), P1 at $t = 0.635$ s (top right), P2 at $t = 0.3$ s (middle left), P2 at $t = 0.635$ s (middle right), $\bar{F}$ at $t = 0.3$ s (bottom left), $\bar{F}$ at $t = 0.635$ s (bottom right).
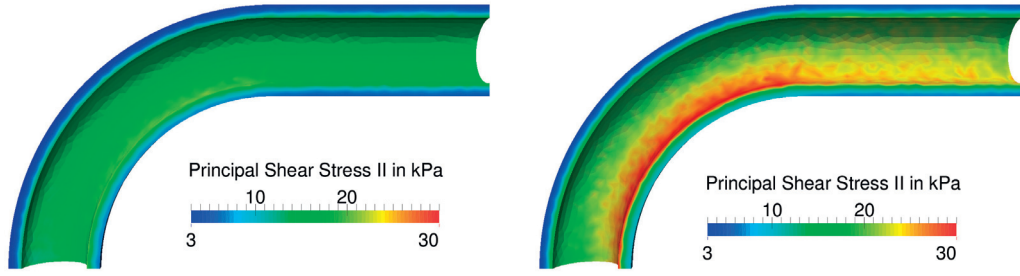
Figure 4.23: The principal Cauchy shear stress using the $\bar{F}$ discretization at $t = 0.3$ s (left) and $t = 0.635$ s (right).

In Figure 4.21 the results obtained from a simulation with the P2 discretization are shown. Even though the given geometry in the reference configuration is rotationally symmetric with respect to the axis orthogonal to the respective cross section, the evaluation of circumferential, axial and radial stresses in the current configuration may not be straightforward due to the deformation induced by the blood flow. However, the first, second, and third principal normal stresses coincide almost perfectly with the normal stresses in circumferential, axial and radial direction, respectively. Figure 4.22 shows the first principal Cauchy stresses, where the geometry has been clipped in the x-z plane such that the inner surface as well as the stress distribution over the wall thickness, at three representative cross-sections denoted by (a), (b) and (c), is displayed. The P1 discretization shows clearly higher stress values, which strongly oscillate on the inner surface of the tube. This observation highlights the stiffness of $\mathbb{P}1$ finite elements and their sensitivity with respect to locking effects.

On the other hand the $\bar{F}$ and P2 discretizations show a smoother stress distribution. This significant difference in the stresses and also the heavy checker-boarding of P1 emphasizes to not use linear elements but at least quadratic ones. The non-symmetric flow profiles visible in Figure 4.19 are however hardly reflected by the principal stress distributions. This is most probably due to a pressure-dominated response reflected by these stresses. Figure 4.23 presents the maximal shear stresses in the fluid-solid interface plane, which are obtained by rotating the local principle stress directions by 45° around the radial axis. As can be seen, these shear stresses are higher at the inner curve and represent therefore a non-rotationally symmetric stress distribution. These observations correspond well with common hypotheses stating that the plaque evolves where low flow rates and high shear stresses are found in domains close to the endothelial cells, which is mostly at the inner curves of vessel walls.

The non-conforming case Part II

5 A new interpolation-based method for the numerical solution of PDEs on subdomains featuring nonconforming interfaces

In Chapters 3 and 4 we have focused on efficient discretizations and parallel algorithms for the numerical solution of fluid-structure interaction problems assuming conforming fluid-structure discretizations at their interface. Here, we extend the algorithms presented so far to the nonconforming case: the nonconformity may be due to different meshes and/or different polynomial degrees used from the two sides of the interface, or even to a geometrical mismatch. Indeed, in fluid-structure interaction problems the different resolution requirements in the fluid and structure physical domains, as well as the presence of complex interface geometries make the use of matching fluid and structure meshes problematic. In such situations, it might be natural to deal with discretizations that are nonconforming at the interface, provided however that the matching conditions at the interface are properly fulfilled.

Part 2 of this thesis focuses on the case in which the fluid and structure domains are discretized arbitrarily and may not necessarily agree on the interface. To deal with nonconforming fluid-structure discretizations we use a new method called INTERNODES (INTERpolation for NOnconforming DEcompositionS) that was recently introduced in [Deparis et al., 2015a]. INTERNODES is a general strategy that allows for the approximation of partial differential equations on domains decomposed into two (or several) subdomains featuring nonconforming interfaces.

In this Chapter we entirely report the submitted paper [Deparis et al., 2015a].

5.1   Preliminaries

In this Chapter we are interested in the approximation of partial differential equations on domains decomposed into two (or several) subdomains featuring "nonconforming interfaces". By this we mean that either a priori independent grids and/or local polynomial degrees are used to discretize each subdomain. More in particular, we refer to these two cases as "grid nonconformity" and "polynomial nonconformity", respectively. A third possible case of nonconforming interfaces that our approach can cover is that of subdomains that face each other through two interfaces that geometrically do not fully agree one another, meaning that the two subdomains may either slightly overlap and/or featuring tiny holes between them (see Figure 5.2). We name this latter situation of geometrical mismatch as "geometric nonconformity". It may arise when using CAD to generate the geometries of the subdomains, e.g. in fluid-structure interaction problems in hydrodynamics or aerodynamics [Parolini and Quarteroni, 2005, Lombardi et al., 2012], or else when generating the computational geometries of lumen and vessel walls from DYCOM images for arterial blood flow dynamics [Formaggia et al., 2009, Reymond et al., 2013].

To deal with nonconforming discretizations, in this Chapter we describe *INTERNODES*, formerly proposed in [Deparis et al., 2015a]. Across each interface, one subdomain is identified as master and the other as slave. We consider Galerkin methods for the discretization (such as finite element or spectral element methods) that make use of two interpolants for transferring information across the interface: one from master to slave and another one from slave to master. The former is used to ensure continuity of the primal variable (the problem solution), while the latter the continuity of the dual variable (the normal flux). In particular, since the dual variable is expressed in weak form, we first compute a strong representation of the dual variable from the slave side, interpolate it, transform the interpolated quantity back into weak form and assign it to the master side. In case of slightly nonmatching geometries, we use a Rescaled Localized-Radial Basis Function (RL-RBF) interpolation [Deparis et al., 2014a] instead of the Lagrange interpolant.

The INTERNODES method, being based on interpolation rather than on L^2 projection at interfaces, is in general simpler to implement than the mortar method: it only requires separate mass matrices and not the cross mass matrix that connects interface basis functions from both sides. It does not require any ad hoc numerical quadrature, neither special treatment of cross-points where more than two subdomains meet. These issues will be further elaborated in Sect. 5.6. INTERNODES with RBF interpolants is also very well suited to address geometric nonconformity [Deparis et al., 2014a].

This Chapter is organized as follows. After introducing the elliptic boundary value problem in Section 5.2, we formulate in Section 5.3 its Galerkin discretization based on either the Finite Element Method (FEM) or the Spectral Element Method (SEM),

using nonconforming interfaces. In Section 5.4 we build the slave-to-master and master-to-slave interface intergrid operators (either Lagrangian or RBF based). In Section 5.5 we formulate the INTERNODES method: we first state it in algebraic terms, then we provide a variational interpretation as a non conforming generalized Galerkin approximation to the original elliptic boundary-value problem. Section 5.6 is devoted to an analysis of similarities and differences between INTERNODES and the mortar method (both theoretical properties and algorithmic aspects). In Section 5.7 we perform a systematic comparison of the numerical results that are obtained for FEM-FEM, FEM-SEM and SEM-SEM couplings, when approximating the Dirichlet problem in a 2D domain. The same problem is addressed in Section 5.8 for the case of geometric nonconformity. A more realistic application is considered in Section 5.9 where we treat a severe mesh nonconformity for the simulation of the external flow in three dimensions. In particular, the latter simulation concerns the incompressible Navier-Stokes equations: the INTERNODES method has been easily extended to this case by simply replacing normal fluxes with normal Cauchy stresses in the new context.

5.2 Problem setting

Let $\Omega \subset \mathbb{R}^d$, with $d = 2,\ 3$, be an open domain with Lipschitz boundary $\partial\Omega$. $\partial\Omega_N$ and $\partial\Omega_D$ are suitable disjoint subsets of $\partial\Omega$ such that $\overline{\partial\Omega_D} \cup \overline{\partial\Omega_N} = \partial\Omega$. Given $f \in L^2(\Omega)$, $g_D \in H^{1/2}(\partial\Omega_D)$, $g_N \in H^{-1/2}(\partial\Omega_N)$, $\mu,\ \alpha \in L^\infty(\Omega)$ such that $\exists \mu_0 > 0,\ \mu \geq \mu_0,\ \alpha \geq 0$, and $\mathbf{b} \in W^{1,\infty}(\Omega)$ s.t. $\alpha - \frac{1}{2}\nabla \cdot \mathbf{b} \geq 0$ we look for the solution u of the second order elliptic equation

$$\begin{cases} Lu \equiv -\nabla \cdot (\mu\nabla u) + \mathbf{b} \cdot \nabla u + \alpha u = f & \text{in } \Omega, \\ u = g_D & \text{on } \partial\Omega_D, \\ \mu\dfrac{\partial u}{\partial n} = g_N & \text{on } \partial\Omega_N, \end{cases} \tag{5.1}$$

being n the outward unit normal vector to $\partial\Omega$.

By setting $V = H^1_{\partial\Omega_D}(\Omega) = \{v \in H^1(\Omega) : \ v|_{\partial\Omega_D} = 0\}$, the weak form of problem (5.1) reads: find $u \in H^1(\Omega)$, with $u = g_D$ on $\partial\Omega_D$, such that

$$a(u,v) = (f,v)_\Omega + \langle g_N, v\rangle_{\partial\Omega_N} \qquad \forall v \in V, \tag{5.2}$$

where

$$a(u,v) = \int_\Omega (\mu\nabla u \cdot \nabla v + (\mathbf{b} \cdot \nabla u)v + \alpha uv)d\Omega, \tag{5.3}$$

while $(\cdot,\cdot)_\Omega$ and $\langle\cdot,\cdot\rangle_{\partial\Omega_N}$ denote the inner product in $L^2(\Omega)$ and the duality pairing between $H^{1/2}(\partial\Omega_N)$ and $H^{-1/2}(\partial\Omega_N)$, respectively.
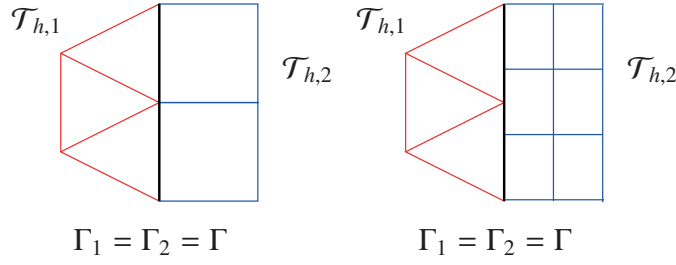
Figure 5.1: Conforming (at left) and nonconforming (at right) grids at the interface when $d = 2$.

For the sake of exposition we partition Ω into two non-overlapping subdomains Ω_1 and Ω_2 such that $\overline{\Omega} = \overline{\Omega_1 \cup \Omega_2}$; we call one *master* (say Ω_1) and the other *slave* (say Ω_2), and we set $\partial\Omega_{D,k} = \partial\Omega_D \cap \partial\Omega_k$ and $\partial\Omega_{N,k} = \partial\Omega_N \cap \partial\Omega_k$, for $k = 1, 2$.

5.3 Discretization

A-priori independent discretizations of either finite element type (FEM) or spectral element type (SEM) are designed in Ω_1 and Ω_2 [Quarteroni and Valli, 1994, Canuto et al., 2007]. SEM will be equivalently named $hp-$FEM (see [Sherwin and Karniadakis, 1995]).

We denote by $\mathcal{T}_{h,k}$ (for $k = 1, 2$) the meshes induced by the discretization in Ω_k and we assume that they satisfy standard regularity requirements (see [Quarteroni and Valli, 1994]). In both Ω_k ($k = 1, 2$) we introduce the finite elements approximation spaces

$$X_{h_k}^{p_k} = \{v \in C^0(\overline{\Omega}_k) : v_{|T} \in Q_{p_k}, \forall T \in \mathcal{T}_{h,k}\}, \tag{5.4}$$

where $Q_{p_k} = \mathbb{P}_{p_k}$ in the simplicial case and $Q_{p_k} = \mathbb{Q}_{p_k} \circ \mathbf{F}_T^{-1}$ for quads, being $\mathbf{F}_T$ the C^1 diffeomorphism that maps the reference element $\hat{T}$ into the generic element $T \in \mathcal{T}_{h,k}$ ([Quarteroni and Valli, 1994]). For any $T \in \mathcal{T}_{h,k}$, we assume that $\partial T \cap \partial\Omega$ fully belongs to either $\partial\Omega_D$ or $\partial\Omega_N$.

For $k = 1, 2$, we introduce the finite dimensional subspaces $V_{k,\delta}$ of $V_k = H^1_{\partial\Omega_{D,k}}(\Omega_k)$, where δ stands for discretization, more precisely

$$V_{k,\delta} = X_{h_k}^{p_k} \cap V_k, \qquad V_{k,\delta}^0 = \{v \in V_{k,\delta}, v|_\Gamma = 0\}. \tag{5.5}$$

On the interface Γ, we allow the meshes $\mathcal{T}_{h,1}$ and $\mathcal{T}_{h,2}$ to induce either *conforming grids* (like in Figure 5.1, left) or *nonconforming grids* (as in Figure 5.1, right). More precisely, the meshes are conforming if their restrictions to Γ coincide; otherwise they are nonconforming.

114
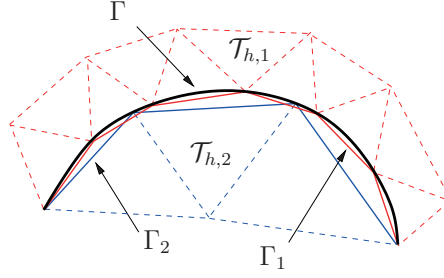
Figure 5.2: A situation with nonmatching interfaces Γ_1 and Γ_2 in the case $d = 2$.

Another situation we would like to address is the one when different polynomial degrees are used on the two subdomains (called *polynomial nonconformity*), or again the case in which FEM on simplicials from one side is coupled with SEM on quads from the other side, with different polynomial degrees. For example, we reference to Figure 5.1, left, using FEM in Ω_1 and SEM in Ω_2.

Finally, in some situations, while discretizing Γ, we could even end up with two non-matching interfaces, that is $\Gamma_1 \neq \Gamma_2$. We refer to this last situation as *nonmatching interfaces* or *geometrically nonconforming partitions*. A possible instance is when Γ is a curved line that is discretized by piecewise straight segments, see Figure 5.2. Another instance may occur when using isogeometric analysis (see, e.g., [Cottrell et al., 2009]).

In order to unify our theory for both the cases of matching and nonmatching interfaces, from now on we will refer to Γ_1 and Γ_2 separately, understanding that $\Gamma_1 = \Gamma_2 = \Gamma$ in the geometrically conforming case.

Generally speaking, we call *nonconforming* a situation where one (or several) of the previous cases (nonconforming grids, polynomial nonconformity, nonmatching interfaces) arises.

5.4 Intergrid operators

For $k = 1, 2$, let us introduce the discrete trace functional spaces

$$\Lambda_{k,\delta} = \{\varphi = v|_{\Gamma_k}, \ v \in X_{h_k}^{p_k}\}, \quad n_k = \dim(\Lambda_{k,\delta}), \tag{5.6}$$

$$\Lambda_{k,\delta}^0 = \{\varphi \in \Lambda_{k,\delta} : \ \varphi|_{\partial\Gamma} = 0\} \subseteq \Lambda_{k,\delta}, \quad n_k^0 = \dim(\Lambda_{k,\delta}^0), \tag{5.7}$$

and denote by $\{\lambda_j^{(k)}\}_{j=1}^{n_k}$ the Lagrange basis of $\Lambda_{k,\delta}$ associated with the nodes $\mathbf{x}_i^{(\Gamma_k)} \in \Gamma_k$ (for $i = 1, \ldots, n_k$) induced by the mesh $\mathcal{T}_{h,k}$. Notice that $\Lambda_{k,\delta}^0 = \Lambda_{k,\delta}$ when $dist(\Gamma, \partial\Omega_D) > 0$. As a matter of fact, $\Lambda_{k,\delta}^0$ does not include the Lagrange basis functions of $\Lambda_{k,\delta}$ associated with the nodes of $\Gamma_k \cap \partial\Omega_D$.

For ease of notation, we suppose that the n_k^0 basis functions of $\Lambda_{k,\delta}^0$ coincide with the first n_k^0 basis functions of $\Lambda_{k,\delta}$, thus the functions $\lambda_i^{(k)}$, for $i = n_k^0 + 1, \ldots, n_k$, are those associated with the nodes of $\Gamma_k \cap \partial\Omega_D$.

To define our method we need to introduce intergrid transfer operators, extension operators, and an interface space.

We introduce two linear operators

$$\Pi_{12} : \Lambda_{2,\delta} \to \Lambda_{1,\delta}, \qquad \Pi_{21} : \Lambda_{1,\delta} \to \Lambda_{2,\delta} \tag{5.8}$$

that realize the *intergrid transfer*. We consider two different instances:

1. Lagrange interpolation,

2. Radial Basis Function (RBF) interpolation [Buhmann, 2003, Wendland, 1995], in particular RL-RBF [Deparis et al., 2014a].

For readers' convenience, we define here the interpolation operators. The Lagrange interpolation operator Π_{21} is characterized as follows. Let us consider a function $\eta_{1,\delta} \in \Lambda_{1,\delta}$, then $\Pi_{21}\eta_{1,\delta}$ can be written w.r.t. the basis $\{\lambda_i^{(2)}\}$ of $\Lambda_{2,\delta}$ as

$$(\Pi_{21}\eta_{1,\delta})(\mathbf{x}) = \sum_{i=1}^{n_2} (\Pi_{21}\eta_{1,\delta})(\mathbf{x}_i^{(\Gamma_2)})\lambda_i^{(2)}(\mathbf{x}), \quad \forall \mathbf{x} \in \Gamma_2. \tag{5.9}$$

By expanding $\eta_{1,\delta}$ with respect to the basis functions $\lambda_j^{(1)}$ of $\Lambda_{1,\delta}$ we have

$$\eta_{1,\delta}(\mathbf{x}) = \sum_{j=1}^{n_1} \eta_{1,\delta}(\mathbf{x}_j^{(\Gamma_1)})\lambda_j^{(1)}(\mathbf{x}) \qquad \forall \mathbf{x} \in \Gamma_1,$$

and then, for any $\mathbf{x} \in \Gamma_2$,

$$(\Pi_{21}\eta_{1,\delta})(\mathbf{x}) = \sum_{i=1}^{n_2} \left(\sum_{j=1}^{n_1} \eta_{1,\delta}(\mathbf{x}_j^{(\Gamma_1)})(\Pi_{21}\lambda_j^{(1)})(\mathbf{x}_i^{(\Gamma_2)}) \right) \lambda_i^{(2)}(\mathbf{x}).$$

Finally, denoting by $\boldsymbol{\eta}_1$ the array in $\mathbb{R}^{n_1}$ whose components are the nodal values $\eta_{1,\delta}(\mathbf{x}_i^{(\Gamma_1)})$, for $i = 1, \ldots, n_1$, and by

$$(R_{21})_{ij} = (\Pi_{21}\lambda_j^{(1)})(\mathbf{x}_i^{(\Gamma_2)}), \quad i = 1, \ldots, n_2, \ j = 1, \ldots, n_1, \tag{5.10}$$

the entries of the matrix associated with the operator Π_{21}, we can write

$$(\Pi_{21}\eta_{1,\delta})(\mathbf{x}_i^{(\Gamma_2)}) = (R_{21}\boldsymbol{\eta}_1)_i, \quad i = 1, \ldots, n_2.$$

By proceeding in a similar way for Π_{12}, we denote the entries of the matrix associated with the operator Π_{12} by

$$(R_{12})_{ij} = (\Pi_{12}\lambda_j^{(2)})(\mathbf{x}_i^{(\Gamma_1)}), \quad i = 1, \ldots, n_1, \ j = 1, \ldots, n_2, \tag{5.11}$$

so that

$$(\Pi_{12}\eta_{2,\delta})(\mathbf{x}_i^{(\Gamma_1)}) = (R_{12}\boldsymbol{\eta}_{2,\delta})_i, \quad i = 1, \ldots, n_1.$$

The RL-RBF interpolation operators are defined as in [Deparis et al., 2014a] and they read

$$(\Pi_{21}\eta_{1,\delta})(\mathbf{x}) = \frac{\sum_{i=1}^{n_1} \gamma_i^{\eta_{1,\delta}} \phi(\|\mathbf{x} - \mathbf{x}_i^{(\Gamma_1)}\|, r_i)}{\sum_{i=1}^{n_1} \gamma_i^1 \phi(\|\mathbf{x} - \mathbf{x}_i^{(\Gamma_1)}\|, r_i)}, \tag{5.12}$$

$$(\Pi_{12}\eta_{2,\delta})(\mathbf{x}) = \frac{\sum_{i=1}^{n_2} \gamma_i^{\eta_{2,\delta}} \phi(\|\mathbf{x} - \mathbf{x}_i^{(\Gamma_2)}\|, r_i)}{\sum_{i=1}^{n_2} \gamma_i^1 \phi(\|\mathbf{x} - \mathbf{x}_i^{(\Gamma_2)}\|, r_i)}, \tag{5.13}$$

where

$$\phi(z, r) = \left(1 - \frac{z}{r}\right)_+^4 \left(1 - 4\frac{z}{r}\right) \tag{5.14}$$

is the locally supported Wendland C^2 radial basis function [Wendland, 1995], $r_i \in \mathbb{R}$ is the local support of the basis function, and γ_i^f are the weights of the interpolant of the function f ($f \equiv 1$ denotes the constant function $f(x) = 1$) and they are determined by imposing the interpolation constraints at either the nodes $\mathbf{x}_i^{(\Gamma_2)}$ ($i = 1, \ldots, n_2$) for Π_{21}, or at $\mathbf{x}_i^{(\Gamma_1)}$ ($i = 1, \ldots, n_1$) for Π_{12}.

Then, for $k = 1, 2$ we define two linear and continuous *extension operators*

$$E_k : \Lambda_{k,\delta} \to X_{h_k}^{p_k}, \quad s.t. \quad (E_k\lambda^{(k)})|_{\Gamma_k} = \lambda^{(k)}, \tag{5.15}$$

that extend any $\lambda^{(k)} \in \Lambda_{k,\delta}$ by setting to zero the values of $E_k\lambda^{(k)}$ at all nodes of $\mathcal{T}_{h,k}$ not belonging to Γ_k. In particular, for any Lagrange basis function $\lambda_j^{(k)}$ of $\Lambda_{k,\delta}$, $E_k\lambda_j^{(k)}$ is the Lagrange basis function of $X_{h_k}^{p_k}$ (associated with the nodes of the mesh $\mathcal{T}_{h,k}$) whose restriction on Γ_k coincides with $\lambda_j^{(k)}$. It follows that $E_k\lambda_j^{(k)} \in V_{k,\delta}$ (i.e., it satisfies homogeneous Dirichlet boundary conditions) only if $\lambda_j^{(k)} \in \Lambda_{k,\delta}^0$, or equivalently, when $j = 1, \ldots, n_k^0$.

The *interface* space is a space of functions defined in the whole $\overline{\Omega}$ as follows

$$V_{\Gamma_1} = \{\varphi \in L^2(\Omega) : \exists \lambda_1 \in \Lambda^0_{1,\delta} : \varphi|_{\Omega_1} = E_1\lambda_1, \ \varphi|_{\Omega_2} = E_2(\Pi_{21}\lambda_1)\}. \tag{5.16}$$

Note that its definition depends on the choice of the master Ω_1 and slave Ω_2 domain. We denote a basis of V_{Γ_1} as $\{\lambda^e_j\}^{n^0_1}_{j=1}$, where "$e$" stands for "extension". There is a one-to-one map between $\lambda^{(1)}_j$ (the jth basis function of $\Lambda^0_{1,\delta}$) and λ^e_j (i.e., $\lambda^e_j|_{\Gamma_1} = \lambda^{(1)}_j$), and λ^e_j satisfies $\lambda^e_j|_{\Omega_1} = E_1\lambda^{(1)}_j$ and $\lambda^e_j|_{\Omega_2} = E_2(\Pi_{21}\lambda^{(1)}_j)$.

Then, we define the subspaces of V

$$\widetilde{V}_{k,\delta} = \{v \in V : v|_{\Omega_k} \in V^0_{k,\delta} \text{ and } v|_{\Omega\setminus\Omega_k} = 0\}, \quad N^0_k = \dim(\widetilde{V}_{k,\delta}) \tag{5.17}$$

and we indicate their Lagrange basis as $\{\Phi^{(k)}_i\}$ for $i = 1, \ldots, N^0_k$ and for $k = 1, 2$.

Thus we set

$$V_\delta = \widetilde{V}_{1,\delta} \oplus \widetilde{V}_{2,\delta} \oplus V_{\Gamma_1}. \tag{5.18}$$

Notice that $V_\delta \not\subset V$ in general.

5.5 Formulation of the nonconforming problem

We define the bilinear forms $a_k : H^1(\Omega_k) \times H^1(\Omega_k) \to \mathbb{R}$:

$$\begin{aligned}
a_1(u,v) &= \int_{\Omega_1} (\mu\nabla u \cdot \nabla v + (\mathbf{b} \cdot \nabla u)v + \alpha uv)d\Omega\,, \\
a_2(u,v) &= \int_{\Omega_2} (\mu\nabla u \cdot \nabla v + (\mathbf{b} \cdot \nabla u)v + \alpha uv)d\Omega - \int_{\partial\Omega_{D,2}} \mu\frac{\partial u}{\partial n}v \ d\partial\Omega\,;
\end{aligned} \tag{5.19}$$

The presence of the boundary integral in a_2 will be justified later, see Remark 5.5.2. If we assume that $g_D \in C^0(\overline{\partial\Omega_D})$, its liftings $R_k g_D \in X^{p_k}_{h_k}$ are

$$\begin{aligned}
R_1 g_D(\mathbf{x}) &= \sum^{N^D_1}_{i=1} g(\mathbf{x}^{(1)}_{i,D})\Phi^{(1)}_{i,D}(\mathbf{x}) + \sum^{n_1}_{i=n^0_1+1} g(\mathbf{x}^{(\Gamma_1)}_i)E_1\lambda^{(1)}_i(\mathbf{x}), &\forall \mathbf{x} \in \overline{\Omega}_1\,, \\
R_2 g_D(\mathbf{x}) &= \sum^{N^D_2}_{i=1} g(\mathbf{x}^{(2)}_{i,D})\Phi^{(2)}_{i,D}(\mathbf{x}) + \sum^{n_1}_{i=n^0_1+1} g(\mathbf{x}^{(\Gamma_1)}_i)E_2(\Pi_{21}\lambda^{(1)}_i(\mathbf{x})), &\forall \mathbf{x} \in \overline{\Omega}_2\,,
\end{aligned} \tag{5.20}$$

where $\Phi_{i,D}^{(k)} \in X_{h_k}^{p_k}$ (for $i = 1, \ldots, N_k^D$) denote the Lagrange basis functions associated with the nodes $\mathbf{x}_{i,D}^{(k)} \in \mathcal{T}_{h,k} \cap (\partial\Omega_{D,k} \setminus \Gamma_k)$, while $\lambda_1^{(1)}$ for $i = n_1^0 + 1, \ldots, n_1$ are the Lagrange basis functions associated with the nodes in $\mathcal{T}_{h,1} \cap (\Gamma_1 \cap \partial\Omega_{D,1})$. Finally we define the linear functionals as follows

$$\mathcal{F}_k(v) = (f, v)_{\Omega_k} + \langle g_N, v \rangle_{\partial\Omega_{N,k}} - a_k(R_k g_D, v), \quad \forall v \in H^1(\Omega_k). \tag{5.21}$$

Then, we set the matrices

$$
\begin{aligned}
(A_{kk})_{ij} &= a_k(\Phi_j^{(k)}, \Phi_i^{(k)}), & i, j &= 1, \ldots, N_k^0, \\
(A_{k,\Gamma_k})_{ij} &= a_k(E_k \lambda_j^{(k)}, \Phi_i^{(k)}), & i &= 1, \ldots, N_k^0, \ j = 1, \ldots, n_k, \\
A_{k,\Gamma_k}^0 &= [A_{k,\Gamma_k}]_{i=1,\ldots,N_k^0, \ j=1,\ldots,n_k^0} \\
(A_{\Gamma_k,k})_{ij} &= a_k(\Phi_j^{(k)}, E_k \lambda_i^{(k)}), & i &= 1, \ldots, n_k, \ j = 1, \ldots, N_k^0, \\
A_{\Gamma_k,k}^0 &= [A_{\Gamma_k,k}]_{i=1,\ldots,n_k^0, \ j=1,\ldots,N_k^0} \\
(A_{\Gamma_k,\Gamma_k})_{ij} &= a_k(E_k \lambda_j^{(k)}, E_k \lambda_i^{(k)}), & i, j &= 1, \ldots, n_k, \\
A_{\Gamma_k,\Gamma_k}^0 &= [A_{\Gamma_k,\Gamma_k}]_{i,j=1,\ldots,n_k^0}
\end{aligned}
\tag{5.22}
$$

and the vectors

$$
\begin{aligned}
\mathbf{f}_k^0 &= \mathcal{F}_k(\Phi_i^{(k)}), & i &= 1, \ldots, N_k^0, \\
\mathbf{f}_{\Gamma_k} &= \mathcal{F}_k(E_k \lambda_i^{(k)}), & i &= 1, \ldots, n_k, \\
\mathbf{f}_{\Gamma_k}^0 &= [\mathbf{f}_{\Gamma_k}]_{i=1,\ldots,n_k^0}.
\end{aligned}
\tag{5.23}
$$

In the special case of fully conforming discretizations (that is both grid and polynomial conformity, with $\Gamma_1 = \Gamma_2 = \Gamma$ and $n_1 = n_2$), by defining

$$R_\delta g_D = \begin{cases} R_1 g_D & \text{in } \Omega_1 \\ R_2 g_D & \text{in } \Omega_2, \end{cases} \tag{5.24}$$

We recall that the classical Galerkin approximation is defined as follows: find $u_\delta \in H^1(\Omega)$, such that $(u_\delta - R_\delta g_D) \in V_\delta \subset V$, solution of the conforming Galerkin problem

$$a(u_\delta, v_\delta) = (f, v_\delta)_\Omega + \langle g_N, v_\delta \rangle_{\partial\Omega_N} \quad \forall v_\delta \in V_\delta. \tag{5.25}$$

The well-known algebraic domain decomposition form of (5.25) reads ([Quarteroni and

Valli, 1999])

$$
\begin{pmatrix}
A_{1,1} & 0 & A^0_{1,\Gamma_1} \\
0 & A_{2,2} & A^0_{2,\Gamma_2} \\
A^0_{\Gamma_1,1} & A^0_{\Gamma_2,2} & A^0_{\Gamma_1,\Gamma_1} + A^0_{\Gamma_2,\Gamma_2}
\end{pmatrix}
\begin{pmatrix}
\mathbf{u}^0_1 \\
\mathbf{u}^0_2 \\
\mathbf{u}^0_{\Gamma_1}
\end{pmatrix}
=
\begin{pmatrix}
\mathbf{f}^0_1 \\
\mathbf{f}^0_2 \\
\mathbf{f}^0_{\Gamma_1} + \mathbf{f}^0_{\Gamma_2}
\end{pmatrix}.
\tag{5.26}
$$

5.5.1   Algebraic formulation of the INTERNODES method

For $k = 1, 2$, let

$$
\mathbf{u}^0_k = [u_{k,\delta}(\mathbf{x}^{(k)}_j)]^{N^0_k}_{j=1} \ (k = 1, 2), \quad \text{and} \quad \mathbf{u}^0_{\Gamma_1} = [u_{1,\delta}(\mathbf{x}^{(\Gamma_1)}_j)]^{n^0_1}_{j=1},
\tag{5.27}
$$

be the array of the nodal values of $u_{k,\delta} = u_\delta|_{\Omega_k}$ at the nodes of $\overline{\Omega}_k \setminus (\Gamma_k \cup \partial\Omega_{D,k})$, and the array of the nodal values of $u_\delta|_{\Gamma_1}$ at the nodes of $\Gamma_1 \setminus \partial\Omega_D$, respectively.

Denoting by $\mathbf{g}_k$ and $\mathbf{g}_{\Gamma_k}$ the arrays of the nodal values $g_D(\mathbf{x}^{(k)}_{i,D})$ for $i = 1, \dots, N^D_k$ and $g_D(\mathbf{x}^{(\Gamma_k)}_i)$ for $i = n^0_k + 1, \dots, n_k$, respectively, the solutions arrays including the Dirichlet nodal values are

$$
\mathbf{u}_k = \begin{pmatrix} \mathbf{u}^0_k \\ \mathbf{g}_k \end{pmatrix}, \qquad \mathbf{u}_{\Gamma_k} = \begin{pmatrix} \mathbf{u}^0_{\Gamma_k} \\ \mathbf{g}_{\Gamma_k} \end{pmatrix}.
$$

In the nonconforming case we need further matrices: the local mass matrices associated with the interfaces, that is

$$
(M_{\Gamma_k})_{ij} = (\lambda^{(k)}_i, \lambda^{(k)}_j)_{L^2(\Gamma_k)}, \qquad i, j = 1, \dots, n_k, \quad k = 1, 2
\tag{5.28}
$$

and the matrices $R_{12} \in \mathbb{R}^{n_1 \times n_2}$ and $R_{21} \in \mathbb{R}^{n_2 \times n_1}$ defined in (5.10) and (5.11), respectively. Finally, by setting

$$
Q_{21} = R_{21}, \qquad Q_{12} = M_{\Gamma_1} R_{12} M^{-1}_{\Gamma_2},
\tag{5.29}
$$

and denoting by $Q^0_{12} \in \mathbb{R}^{n^0_1 \times n_2}$ the submatrix of Q_{12} of its first n^0_1 rows, and by $Q^0_{21} \in \mathbb{R}^{n_2 \times n^0_1}$ the submatrix of Q_{21} of its first n^0_1 columns, our *nonconforming* generalization of (5.26) reads

$$
\begin{pmatrix}
A_{1,1} & 0 & A^0_{1,\Gamma_1} \\
0 & A_{2,2} & A_{2,\Gamma_2} Q^0_{21} \\
A_{\Gamma_1,1} & Q^0_{12} A_{\Gamma_2,2} & A^0_{\Gamma_1,\Gamma_1} + Q^0_{12} A_{\Gamma_2,\Gamma_2} Q^0_{21}
\end{pmatrix}
\begin{pmatrix}
\mathbf{u}^0_1 \\
\mathbf{u}^0_2 \\
\mathbf{u}^0_{\Gamma_1}
\end{pmatrix}
=
\begin{pmatrix}
\mathbf{f}^0_1 \\
\mathbf{f}^0_2 \\
\mathbf{f}^0_{\Gamma_1} + Q^0_{12}\mathbf{f}_{\Gamma_2}
\end{pmatrix}.
\tag{5.30}
$$

Notice that, in the fully conforming case, Q_{12} and Q_{21} coincide with the identity matrix of size $n_1 = n_2$, thus $A_{2,\Gamma_2} Q_{21}^0 = A_{2,\Gamma_2}^0$, $Q_{12}^0 A_{\Gamma_2,2} = A_{\Gamma_2,2}^0$, and $Q_{12}^0 A_{\Gamma_2,\Gamma_2} Q_{21}^0 = A_{\Gamma_2,\Gamma_2}^0$ (and (5.30) returns (5.26)).

The sketch of the algorithm is reported for reader's convenience in Algorithm 1.

Algorithm 1 INTERNODES algorithm

1: Build the local stiffness matrices $A_{k,k}$, A_{k,Γ_k}, and $A_{\Gamma_k,k}$ (formula (5.22)),
2: Build the right hand sides $\mathbf{f}_k$ and $\mathbf{f}_{\Gamma_k}$ for $k = 1, 2$ (formula (5.23)),
3: Build the local interface mass matrices M_{Γ_k}, for $k = 1, 2$, (formula (5.28)),
4: Build the interpolation matrices R_{21} and R_{12} (formulas (5.10) and (5.11)) and Q_{21} and Q_{12} (formula (5.29)) (only the nodes coordinates on the interfaces are needed in this step),
5: Solve system (5.30)

5.5.2 Variational formulation of the INTERNODES method

System (5.30) represents the algebraic counterpart of the following variational problem: find $u_{1,\delta} \in X_{h_1}^{p_1} : (u_{1,\delta} - R_1 g_D) \in V_{1,\delta}$ and $u_{2,\delta} \in X_{h_2}^{p_2} : (u_{2,\delta} - R_2 g_D) \in V_{2,\delta}$ such that

$$
\begin{aligned}
a_1(u_{1,\delta}, v_{1,\delta}) &= (f, v_{1,\delta})_{\Omega_1} + \langle g_N, v_{1,\delta}\rangle_{\partial\Omega_{N,1}} && \forall v_{1,\delta} \in \widetilde{V}_{1,\delta}, \\
a_2(u_{2,\delta}, v_{2,\delta}) &= (f, v_{2,\delta})_{\Omega_2} + \langle g_N, v_{2,\delta}\rangle_{\partial\Omega_{N,2}} && \forall v_{2,\delta} \in \widetilde{V}_{2,\delta}, \\
u_{2,\delta}|_{\Gamma_2} &= \Pi_{21}(u_{1,\delta}|_{\Gamma_1}) \\
a_1(u_{1,\delta}, w_\delta) + a_2(u_{2,\delta}, \tilde{w}_\delta) &= (f, w_\delta)_{\Omega_1} + (f, \tilde{w}_\delta)_{\Omega_2} \\
&\quad + \langle g_N, w_\delta\rangle_{\partial\Omega_{N,1}} + \langle g_N, \tilde{w}_\delta\rangle_{\partial\Omega_{N,2}} \\
&\qquad \forall w_\delta \in V_{\Gamma_1}, \text{with } \tilde{w}_\delta = E_2(\Pi_{12}^* w_\delta|_{\Gamma_1}).
\end{aligned}
\tag{5.31}
$$

Here $\Pi_{12}^* : \Lambda_{1,\delta} \to \Lambda_{2,\delta}$ is the adjoint operator of Π_{12} w.r.t. the L^2 product, i.e., for any $\eta_{1,\delta} \in \Lambda_{1,\delta}$ and $\eta_{2,\delta} \in \Lambda_{2,\delta}$, it satisfies

$$
(\Pi_{12}^* \eta_{1,\delta}, \eta_{2,\delta})_{L^2(\Gamma_2)} = (\eta_{1,\delta}, \Pi_{12}\eta_{2,\delta})_{L^2(\Gamma_1)}.
\tag{5.32}
$$

Remark: Notice that, even if $\eta_{1,\delta} \in \Lambda_{1,\delta}^0$, in general $(\Pi_{12}^*\eta_{1,\delta})|_{\partial\Gamma}$ is not null and by taking $v = E_2(\Pi_{12}^*\eta_{1,\delta})$ in $(5.19)_2$, it holds $v|_{\partial\Omega_{D,2}} \neq 0$ and the last integral in $(5.19)_2$ is non-zero.

Remark: in the conforming case, by setting $\Pi_{12} = \Pi_{21} = I$, Eq. (5.31) returns the well known two-domain formulation associated with the Galerkin finite element method, see [Quarteroni and Valli, 1999].

We prove now the equivalence between (5.30) and (5.31). Equations $(5.31)_{1,2}$ correspond to the first two equations of the system (5.30); $(5.31)_3$ follows directly by the definition of the space V_{Γ_1} and yields $\mathbf{u}_{\Gamma_2} = Q_{21}\mathbf{u}_{\Gamma_1}$. Finally, $(5.31)_4$ corresponds to the last equation of system (5.30). To prove this statement, let us choose $\eta_{2,\delta} = \lambda_j^{(2)}$ (for any $j = 1, \ldots, n_2$) and $\eta_{1,\delta} = \lambda_i^{(1)}$ (for any $i = 1, \ldots, n_1$) in (5.32), thus by (5.9) it holds

$$(\Pi_{12}\lambda_j^{(2)})(\mathbf{x}) = \sum_{\ell=1}^{n_1}(\Pi_{12}\lambda_j^{(2)})(\mathbf{x}_\ell^{(\Gamma_1)})\lambda_\ell^{(1)}(\mathbf{x}) \quad \forall \mathbf{x} \in \Gamma_1,$$

and

$$
\begin{aligned}
(\Pi_{12}\lambda_j^{(2)}, \lambda_i^{(1)})_{L^2(\Gamma_1)} &= \int_{\Gamma_1}\sum_{\ell=1}^{n_1}(\Pi_{12}\lambda_j^{(2)})(\mathbf{x}_\ell^{(\Gamma_1)})\lambda_\ell^{(1)}(\mathbf{x})\lambda_i^{(1)}(\mathbf{x})d\Gamma \\
&= \sum_{\ell=1}^{n_1}(\Pi_{12}\lambda_j^{(2)})(\mathbf{x}_\ell^{(\Gamma_1)})\int_{\Gamma_1}\lambda_\ell^{(1)}(\mathbf{x})\lambda_i^{(1)}(\mathbf{x})d\Gamma \\
&= \sum_{\ell=1}^{n_1}(R_{12})_{\ell j}(M_{\Gamma_1})_{i\ell} = (M_{\Gamma_1}R_{12})_{ij}.
\end{aligned}
$$

At the same time, if we expand $\Pi_{12}^*\lambda_i^{(1)}$ w.r.t. the basis function in $\Lambda_{2,\delta}$ as

$$(\Pi_{12}^*\lambda_i^{(1)})(\mathbf{x}) = \sum_{k=1}^{n_2}(\Pi_{12}^*\lambda_i^{(1)})(\mathbf{x}_k^{(2)})\lambda_k^{(\Gamma_2)}(\mathbf{x}) \quad \forall \mathbf{x} \in \Gamma_2, \tag{5.33}$$

and we denote by P the associated matrix such that $P_{ji} = (\Pi_{12}^*\lambda_i^{(1)})(\mathbf{x}_j^{(\Gamma_2)})$, we have

$$
\begin{aligned}
(\Pi_{12}^*\lambda_i^{(1)}, \lambda_j^{(2)})_{L^2(\Gamma_2)} &= \int_{\Gamma_2}\sum_{k=1}^{n_2}(\Pi_{12}^*\lambda_i^{(1)})(\mathbf{x}_k^{(\Gamma_2)})\lambda_k^{(2)}(\mathbf{x})\lambda_j^{(2)}(\mathbf{x})d\Gamma \\
&= \sum_{k=1}^{n_2}(\Pi_{12}^*\lambda_i^{(1)})(\mathbf{x}_k^{(\Gamma_2)})\int_{\Gamma_2}\lambda_k^{(2)}(\mathbf{x})\lambda_j^{(2)}(\mathbf{x})d\Gamma \\
&= \sum_{k=1}^{n_2}P_{ki}(M_{\Gamma_2})_{jk} = (M_{\Gamma_2}P)_{ji}.
\end{aligned}
$$

Then, the algebraic counterpart of (5.32) reads

$$(M_{\Gamma_1}R_{12})_{ij} = (M_{\Gamma_2}P)_{ji} = (P^T M_{\Gamma_2})_{ij},$$

for any $i = 1, \ldots, n_1$ and $j = 1, \ldots, n_2$, or equivalently

$$P^T = M_{\Gamma_1} R_{12} M_{\Gamma_2}^{-1} \quad (= Q_{12} \text{ by } (5.29)).$$

This means that the matrix associated with Π_{12}^* is $P = Q_{12}^T$.

Now, let us write

$$
\begin{aligned}
u_{1,\delta}(\mathbf{x}) =\ & \sum_{j=1}^{N_1^0} u_{1,\delta}(\mathbf{x}_j^{(1)}) \Phi_j^{(1)}(\mathbf{x}) + \sum_{j=1}^{n_1^0} u_{1,\delta}(\mathbf{x}_j^{(\Gamma_1)}) E_1 \lambda_j^{(1)}(\mathbf{x}) \\
& + R_1 g_D(\mathbf{x}) && \forall \mathbf{x} \in \overline{\Omega}_1, \\
u_{2,\delta}(\mathbf{x}) =\ & \sum_{j=1}^{N_2^0} u_{2,\delta}(\mathbf{x}_j^{(2)}) \Phi_j^{(2)}(\mathbf{x}) + \sum_{j=1}^{n_1^0} u_{1,\delta}(\mathbf{x}_j^{(\Gamma_1)}) E_2 (\Pi_{21} \lambda_j^{(1)})(\mathbf{x}) \\
& + R_2 g_D(\mathbf{x}) && \forall \mathbf{x} \in \overline{\Omega}_2,
\end{aligned}
$$

and choose $w_\delta = \lambda_i^e$, (for $i = 1, \ldots, n_1^0$) in $(5.31)_4$.

Recalling that $\lambda_i^e|_{\Gamma_1} = \lambda_i^{(1)}$ and by (5.20) and (5.27), $(5.31)_4$ reads for $i = 1, \ldots, n_1^0$:

$$
\begin{aligned}
& \sum_{j=1}^{N_1^0} \mathbf{u}_{1j} a_1(\Phi_j^{(1)}, E_1 \lambda_i^{(1)}) + \sum_{j=1}^{N_2^0} \mathbf{u}_{2j}\ a_2(\Phi_j^{(2)}, E_2(\Pi_{12}^* \lambda_i^{(1)})) \\
& + \sum_{j=1}^{n_1^0} \mathbf{u}_{\Gamma_1 j} [a_1(E_1 \lambda_j^{(1)}, E_1 \lambda_i^{(1)}) + a_2(E_2(\Pi_{21} \lambda_j^{(1)}), E_2(\Pi_{12}^* \lambda_i^{(1)})) \\
& \qquad = \mathcal{F}_1(E_1 \lambda_i^{(1)}) + \mathcal{F}_2(E_2(\Pi_{12}^* \lambda_i^{(1)})),
\end{aligned}
$$

and thanks to both (5.22) and (5.33), it holds

$$
\begin{aligned}
a_2(\Phi_j^{(2)}, E_2(\Pi_{12}^* \lambda_i^{(1)})) \ &= \sum_{k=1}^{n_2} (\Pi_{12}^* \lambda_i^{(1)})(\mathbf{x}_k^{(\Gamma_2)})\ a_2(\Phi_j^{(2)}, E_2 \lambda_k^{(2)}) \\
&= \sum_{k=1}^{n_2} (Q_{12}^T)_{ki} (A_{\Gamma_2,2})_{kj} = (Q_{12} A_{\Gamma_2,2})_{ij}, \quad \begin{aligned} i &= 1, \ldots, n_1^0, \\ j &= 1, \ldots, N_2^0, \end{aligned}
\end{aligned}
$$

$$
\begin{aligned}
a_2(E_2(\Pi_{21}\lambda_j^{(1)}), E_2(\Pi_{12}^*\lambda_i^{(1)})) &= \\
&= \sum_{k=1}^{n_2}(\Pi_{12}^*\lambda_i^{(1)})(\mathbf{x}_k^{(\Gamma_2)}) \sum_{\ell=1}^{n_2}(\Pi_{21}\lambda_j^{(1)})(\mathbf{x}_\ell^{(\Gamma_2)})\, a_2(E_2\lambda_\ell^{(2)}, E_2\lambda_k^{(2)}) \\
&= \sum_{k=1}^{n_2}\sum_{\ell=1}^{n_2}(Q_{12}^T)_{ki}(A_{\Gamma_2,\Gamma_2})_{k\ell}(Q_{21})_{\ell j} = (Q_{12}A_{\Gamma_2,\Gamma_2}Q_{21})_{ij}, \qquad
\begin{aligned}
i &= 1,\ldots,n_1^0 \\
j &= 1,\ldots,n_1^0,
\end{aligned}
\end{aligned}
$$

and

$$
\mathcal{F}_2(E_2(\Pi_{12}^*\lambda_i^{(1)})) = (Q_{12}\mathbf{f}_{\Gamma_2})_i, \quad i = 1,\ldots,n_1^0,
$$

thus $(5.30)_3$ is the algebraic counterpart of $(5.31)_4$.

Equation $(5.31)_4$ (or equivalently $(5.30)_3$) expresses the balance of residuals in strong form. Algebraically, this becomes more evident once we reformulate $(5.30)_3$ as

$$
-(Q_{12}\mathbf{r}_2)_i = -(M_{\Gamma_1}R_{12}M_{\Gamma_2}^{-1}\mathbf{r}_2)_i = (\mathbf{r}_1^0)_i, \qquad i = 1,\ldots,n_1^0 \tag{5.34}
$$

where

$$
\mathbf{r}_1^0 = \mathbf{f}_{\Gamma_1}^0 - A_{\Gamma_1,1}^0\mathbf{u}_1^0 - A_{\Gamma_1,\Gamma_1}^0\mathbf{u}_{\Gamma_1}^0, \quad \mathbf{r}_2 = \mathbf{f}_{\Gamma_2} - A_{\Gamma_2,2}\mathbf{u}_2^0 - A_{\Gamma_2,\Gamma_2}Q_{21}^0\mathbf{u}_{\Gamma_1}^0. \tag{5.35}
$$

In eq. (5.34), we notice that $M_{\Gamma_2}^{-1}\mathbf{r}_2$ is an approximation of the strong form of the normal stresses on Γ_2; $R_{12}M_{\Gamma_2}^{-1}\mathbf{r}_2$ is an interpolation of the normal stresses on Γ_1, still in strong form, and $M_{\Gamma_1}R_{12}M_{\Gamma_2}^{-1}\mathbf{r}_2$ returns the weak form of the normal stresses but now on Γ_1. Note that the order of magnitude of the entries of $\mathbf{r}_2$ depend on the mesh size used to discretize Ω_2, that of the entries of $\mathbf{r}_1$ depend on the mesh size of Ω_1, while the order of magnitude of those of both $M_{\Gamma_2}^{-1}\mathbf{r}_2$ and $R_{12}M_{\Gamma_2}^{-1}\mathbf{r}_2$ are independent of the mesh size.

Equation $(5.31)_4$ is the weak realization of the property

$$
\mu\frac{\partial u_{1,\delta}}{\partial n_1} = -\Pi_{12}\left(\mu\frac{\partial u_{2,\delta}}{\partial n_2}\right) \qquad \text{on } \Gamma_1, \tag{5.36}
$$

that enforces the discrete continuity of the normal fluxes across Γ_1.

5.5.3   Nonconforming Petrov-Galerkin formulation of the INTERN-ODES method

By defining the spaces

$$
\begin{aligned}
V_{\Gamma_1}^* = \{\varphi^* \in L^2(\Omega) : \exists \lambda_1 \in \Lambda_{1,\delta}^0 : \quad &\varphi^*|_{\Omega_1} = E_1\lambda_1, \\
&\varphi^*|_{\Omega_2} = E_2(\Pi_{12}^*\lambda_1)\}.
\end{aligned} \tag{5.37}
$$

and

$$V_\delta^* = \widetilde{V}_{1,\delta} \oplus \widetilde{V}_{2,\delta} \oplus V_{\Gamma_1}^*, \tag{5.38}$$

the variational statement (5.31) can be written in compact form as a *nonconforming Petrov-Galerkin* problem: find $u_\delta \in X_{h_1}^{p_1} \times X_{h_2}^{p_2}$ with $(u_\delta - R_\delta g_D) \in V_\delta$:

$$a_1(u_\delta, v_\delta^*) + a_2(u_\delta, v_\delta^*) = \sum_{k=1}^{2} \left[(f, v_\delta^*)_{\Omega_k} + \langle g_N, v_\delta^* \rangle_{\partial\Omega_{N,k}} \right], \quad \forall v_\delta^* \in V_\delta^*. \tag{5.39}$$

5.5.4 Nonconforming generalized Galerkin formulation of the INTERN-ODES method

The finite element assembly of problem (5.39) would be rather involved as it requires to generate a set of basis functions for V_δ^*. For this reason we reformulate (5.39) as a more convenient *nonconforming generalized Galerkin* problem. With this aim for any $w_\delta \in V_\delta$ we define

$$a_{2,\delta}(w_\delta, v_\delta) = \begin{cases} a_2(w_\delta, v_\delta), & \text{if } v_\delta \in \widetilde{V}_{1,\delta} \oplus \widetilde{V}_{2,\delta} \\ a_2(w_\delta, E_2(\Pi_{12}^* v_\delta|_{\Gamma_1})), & \text{if } v_\delta \in V_{\Gamma_1} \end{cases}$$

$$(f, v_\delta)_{2,\delta} = \begin{cases} (f, v_\delta)_{\Omega_2}, & \text{if } v_\delta \in \widetilde{V}_{1,\delta} \oplus \widetilde{V}_{2,\delta} \\ (f, E_2(\Pi_{12}^* v_\delta|_{\Gamma_1}))_{\Omega_2}, & \text{if } v_\delta \in V_{\Gamma_1} \end{cases} \tag{5.40}$$

$$\langle g_N, v_\delta \rangle_{2,\delta} = \begin{cases} \langle g_N, v_\delta \rangle_{\Omega_2}, & \text{if } v_\delta \in \widetilde{V}_{1,\delta} \oplus \widetilde{V}_{2,\delta} \\ \langle g_N, E_2(\Pi_{12}^* v_\delta|_{\Gamma_1}) \rangle_{\Omega_2}, & \text{if } v_\delta \in V_{\Gamma_1} \end{cases}$$

We can therefore conclude that problem (5.31) can be equivalently reformulated as a nonconforming generalized Galerkin problem:

Find $u_\delta \in X_{h_1}^{p_1} \times X_{h_2}^{p_2}$, with $(u_\delta - R_\delta g_D) \in V_\delta$:

$$\begin{aligned} a_1(u_\delta, v_\delta) + a_{2,\delta}(u_\delta, v_\delta) = \ & (f, v_\delta)_{\Omega_1} + (f, v_\delta)_{2,\delta} \\ & + \langle g_N, v_\delta \rangle_{\partial\Omega_{N,1}} + \langle g_N, v_\delta \rangle_{2,\delta}, \quad \forall v_\delta \in V_\delta. \end{aligned} \tag{5.41}$$

5.6   On the mortar method and its relationship with INTERNODES

As already pointed out in Section 5.1, the mortar method represents nowadays a well established approach for the solution of PDEs using nonconforming discretizations. A big deal of attention has been devoted to the theoretical analysis [Maday et al., 1988, Bernardi et al., 1994, Wohlmuth, 2000, Belgacem, 1999, Lamichhane and Wohlmuth, 2004, Brivadis et al., 2015, Bernardi et al., 2004] as well as to the algorithmic developments [Ben Belgacem et al., 1999, Popp, 2012, Puso and Laursen, 2003, Puso and Laursen, 2004, Ben Belgacem et al., 2003, Bernardi and Maday, 2000] of this method, in connection with a broad variety of applications. Notable examples concern problems in structural mechanics [Puso, 2004, Puso and Laursen, 2004, Flemisch et al., 2005], fluid dynamics [Ehrl et al., 2014], structural dynamics [Faucher and Combescure, 2003], electromagnetism [Ben Belgacem et al., 2001, Rapetti et al., 2000, Buffa et al., 2001, Bouillault et al., 2003], contact problems [Fischer and Wriggers, 2005, De Lorenzis et al., 2012, Popp et al., 2012, Popp et al., 2009, Popp et al., 2010], multiphysics [Klöppel et al., 2011, Popp, 2012, Baaijens, 2001, Mayer et al., 2010], etc.

Although the mortar method is a projection (rather than an interpolation-based) method, we can still represent it by the general algebraic form (5.30), provided we replace Q_{21}^0 with the matrix associated with the mortar projection (named Ξ in [Quarteroni, 2013, Sect. 11.4] or P in [Klöppel et al., 2011, eq. (46)]) and Q_{12}^0 with Ξ^T. Similarly, the variational formulation of the mortar method (see [Bernardi et al., 1994]) can be retrieved from (5.41) by replacing V_δ with the mortar space

$$
\begin{aligned}
V_\delta^M = \{ v_\delta \in L^2(\Omega), v_{k,\delta} = v_\delta|_{\Omega_k} \in V_{k,\delta} \text{for } k = 1, 2 \text{ and} \\
v_{2,\delta} = \Pi_{21}^M v_{1,\delta} \text{on } \Gamma \},
\end{aligned}
\tag{5.42}
$$

where Π_{21}^M is the L^2-projection from master to slave on the interface, and by replacing Π_{12}^* with Π_{21}^M in (5.40). Note in particular that the mortar method requires a single intergrid operator, Π_{21}^M, rather than two operators Π_{12} and Π_{21} in INTERNODES.

On the other hand, we warn the reader that INTERNODES, even though being interpolatory, *does not* coincide with the so-called *pointwise matching* method that was presented in the seminal mortar paper [Bernardi et al., 1994, eqs. (3.5)-(3.7)]. The pointwise matching is notoriously sub-optimal, as proven in [Bernardi et al., 1994, Sect. 3.2] and numerically corroborated in [Bègue et al., 1989] for spectral elements discretizations.

The algorithmic and implementation aspects of both methods deserve some further consideration. Most oftern mortar method is formulated as a saddle point problem by introducing an extra field, the Lagrange multiplier. This yields an inf-sup compatibility condition to be fulfilled in order to ensure well-posedness. Many algorithms exist aimed

	INTERNODES			mortar		
k	$\mathcal{K}$	$\max_i |\lambda_i|$	$\min_i |\lambda_i|$	$\mathcal{K}$	$\max_i |\lambda_i|$	$\min_i |\lambda_i|$
16	511.65	7.98	1.56e-2	518.63	7.98	1.54e-2
32	2081.39	7.99	3.84e-3	2093.80	7.99	3.82e-3
64	8386.54	7.99	9.54e-4	8410.09	7.99	9.51e-4

Table 5.1: Iterative condition number and extreme eigenvalues.

at condensing the system by eliminating the Lagrange multipliers, in particular the one using dual spaces for Lagrange multipliers [Wohlmuth, 2000, Ehrl et al., 2014].

When mortar methods are formulated as a single field problem, the corresponding algebraic system (5.30) (with Π_{12} and Π_{21} replaced by Π_{21}^M as indicated above) is symmetric, provided the original differential operator is self-adjoint. This property is not fulfilled by INTERNODES due to the two a-priori different inter-grid operators.

The two stiffness matrices feature similar condition numbers. For example, on a piecewise linear finite element approximation of the Dirichlet problem for the Laplacian in the rectangle $(0, 2) \times (0, 1)$, we report in Figure 5.3 the spectra for both INTERNODES and the mortar method relatively to structured triangulations of variable step size (precisely, we are using Set D of Table 5.2 for $k = \{16,\ 32,\ 64\}$). The eigenvalues of the mortar matrix are positive real whereas those of INTERNODES feature tiny imaginary parts that vanish as the step size does. The *iterative condition number* $\mathcal{K} = \max_i |\lambda_i| / \min_i |\lambda_i|$ behaves right the same way (and scales with h^{-2}), as reported in Table 5.1.

Concerning more specifically the implementation issues, INTERNODES simply requires local mass matrices at the interface and not the cross mass matrix connecting interface basis functions from both sides as in the mortar method. Moreover, it does not require numerical quadratures, neither a special treatment of cross-points where more than two subdomains meet. An in-depth analysis of these and other subtle implementation issues is carried out in [Ehrl et al., 2014, Maday et al., 2002, Popp, 2012, Wohlmuth, 2000, Flemisch et al., 2005, Puso and Laursen, 2003]. The implementation of mortar method for geometric nonconforming interfaces is also far from trivial (INTERNODES instead does not feature any additional difficulty with respect to the case of geometric matching interfaces): as a matter of fact, it requires several steps such as projection, intersection, local meshing and numerical quadrature to build up the mortar interface coupling operator. These aspects are carefully addressed in [Popp, 2012] (see in particular Algorithm 1, Section 3.2.3).
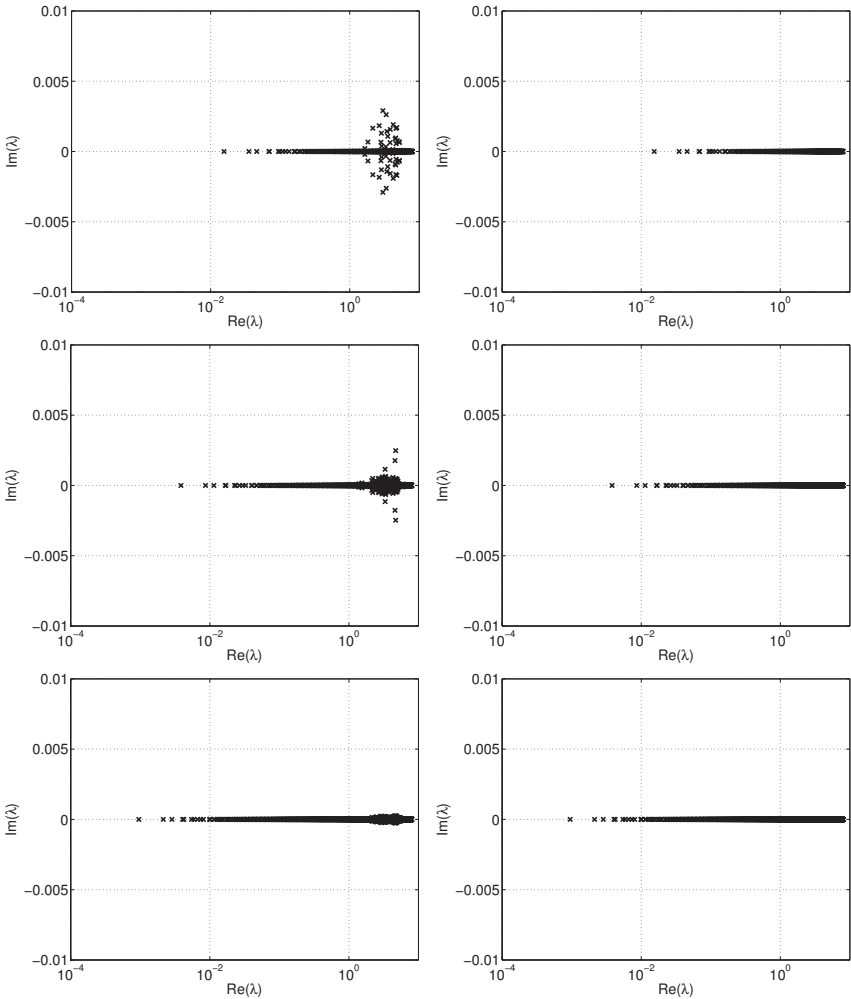
Figure 5.3: The spectra of the Dirichlet stiffness matrix for INTERNODES (left) and mortar (right), corresponding to three different structured triangulations (Set D of Table 5.2, $k = 16$ (top), 32 (middle), 64 (bottom)).
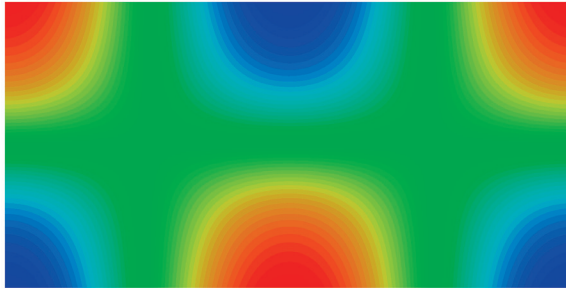
Figure 5.4: Solution $u(x,y) = \arctan(4(y-0.5))\cos(\pi x)$ of problem (5.43).

5.7 Numerical solution of an elliptic problem

In the first preliminary test, we consider the numerical solution of the Poisson problem

$$
\begin{aligned}
-\Delta u(x,y) &= f(x,y) &&\text{in} &&\Omega = (0,2) \times (0,1), \\
u(x,y) &= g_D(x,y) &&\text{on} &&\partial\Omega_D = \partial\Omega,
\end{aligned}
\tag{5.43}
$$

and we show the orders of convergence of INTERNODES when nonconforming meshes and/or nonconforming discretizations (based on the coupling of finite elements with spectral elements) are used.

In (5.43) the functions $f(x,y)$ and $g(x,y)$ are chosen in such a way that $u(x,y) = \arctan(4(y-0.5))\cos(\pi x)$ (see Figure 5.4). We decompose the domain Ω in two subdomains: $\Omega_1 = (0,1) \times (0,1)$ and $\Omega_2 = (1,2) \times (0,1)$.

5.7.1 Coupling of nonconforming FEM-FEM discretizations

In this Section we solve problem (5.43) by considering nonconforming finite elements discretizations at the subdomains interface Γ. The nonconformity may come from the use of different mesh-sizes and/or different polynomial degree of the finite elements basis functions between the master and slave domains. In our numerical experiments we considered $\mathbb{P}1, \mathbb{P}2$ and $\mathbb{P}3$ finite elements, using structured grids that feature an aspect ratio of 1 or 2 across the interface. The details of the meshes used in our simulations are reported in Table 5.2, wherein $k = \{8, 16, 32, 64\}$ denotes the number of grid points along each coordinate of the master and slave domains. Furthermore, the method proposed is tested using both the Lagrange and the RL-RBF interpolants as intergrid operator.

In Figure 5.5 we show the rate of convergence obtained by INTERNODES for some of the simulations performed using the Lagrange interpolant and for set C (left column) and set D (right column). The results reported are the H^1-norms of the errors computed in each individual subdomain, i.e., $\|u - u_{1,\delta}\|_{H^1(\Omega_1)}$ and $\|u - u_{2,\delta}\|_{H^1(\Omega_2)}$.

129
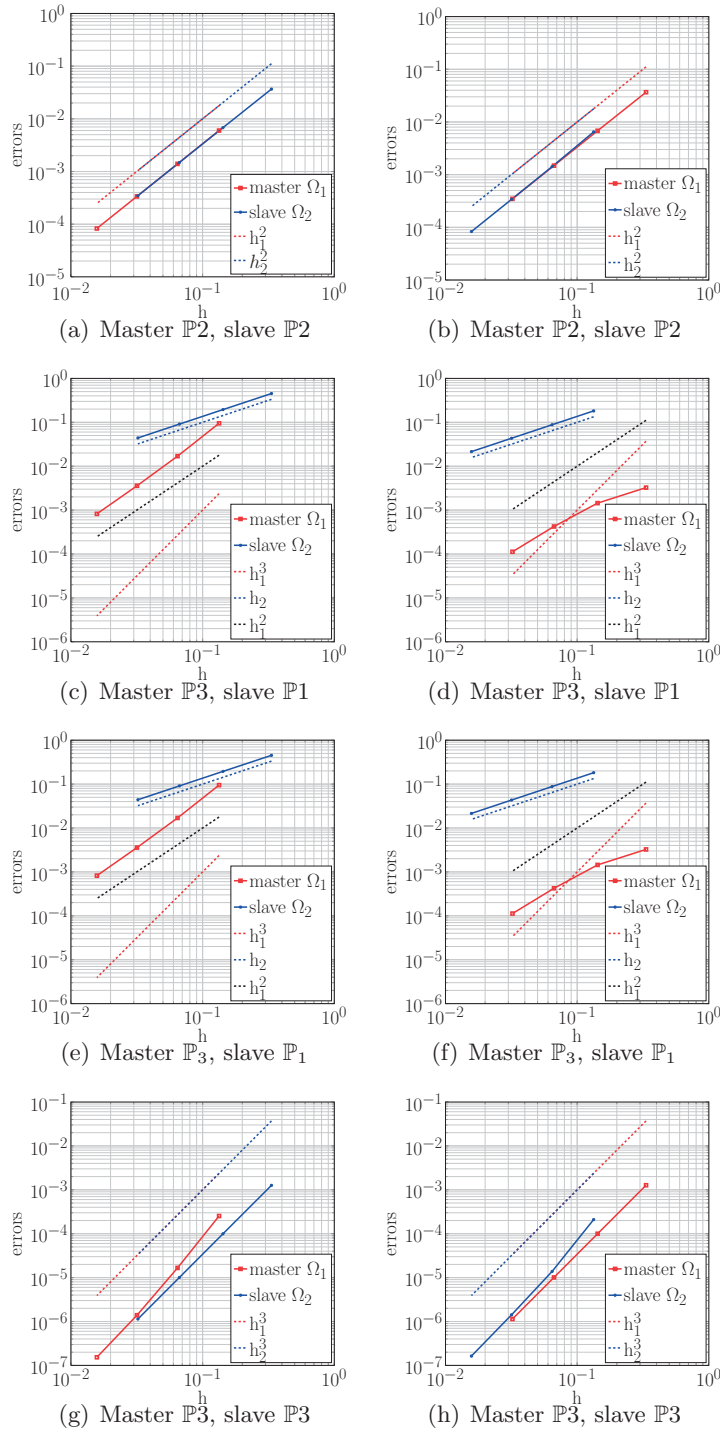
Figure 5.5: FEM-FEM coupling: orders of convergence obtained using Lagrangian interpolants and nonconforming meshes with aspect ratio 2. Left column using Set C, right column using Set D (see Table 5.2).

	Master domain	Slave domain	Aspect ratio
Set A	$(k+1) \times (k+1)$	$(k-1) \times (k-1)$	≈ 1
Set B	$(k-1) \times (k-1)$	$(k+1) \times (k+1)$	≈ 1
Set C	$(2k+1) \times (2k+1)$	$(k-1) \times (k-1)$	≈ 2
Set D	$(k-1) \times (k-1)$	$(2k+1) \times (2k+1)$	≈ 2

Table 5.2: Details of the meshes used for the numerical simulations.

Master \ Slave	$\mathbb{P}1$		$\mathbb{P}2$		$\mathbb{P}3$	
$\mathbb{P}1$	1-1	1-1	1-2	1-2	1-1	1-1
	1-1	1-1	1-2	1-2	1-1	1-1
$\mathbb{P}2$	2-1	2-1	2-2	2-2	2-3	2-3
	2-1	2-1	2-2	2-2	2-3	2-3
$\mathbb{P}3$	2-1	2-1	3-2	3-2	3-3	3-3
	2-1	2-1	3-2	3-2	3-3	3-3

Table 5.3: Orders of convergence in H^1 norm obtained using nonconforming meshes and the Lagrange interpolation. In the top row we report the results obtained using Set A (left) and Set B (right) while in the bottom those with Set C (left) and Set D (right).

By comparing the left and right plots in the first and fourth rows of Figure 5.5 (obtained with nonconforming meshes but same polynomial degree in the master and slave domains) we observe that, as expected, the most accurate results are always obtained on the subdomain triangulated with the finer mesh, independently whether this is a master or a slave. When the master domain is discretized using a polynomial degree lower than the one of the slave (compare the left and right plots of the second row in Figure 5.5) we notice that it is better, in terms of accuracy, to use the finer mesh on the master domain. In the opposite case, i.e. when the master domain is discretized using a polynomial degree that is higher than the one of the slave (compare the left and right plots of the third row in Figure 5.5) we observe that more precise results are obtained using the finer mesh on the slave domain.

M \ S	$\mathbb{P}1$		$\mathbb{P}2$		$\mathbb{P}3$	
	Lagr.	RL-RBF	Lagr.	RL-RBF	Lagr.	RL-RBF
$\mathbb{P}1$	1-1	1-1	1-2	1-2	1-2	1-2
$\mathbb{P}2$	2-1	2-1	2-2	2-2	2-3	2-3
$\mathbb{P}3$	2-1	2-1	3-2	3-2	3-3	3-3

Table 5.4: Orders of convergence in H^1 norm obtained in our numerical simulations using conforming meshes but nonconforming polynomial degrees. In each cell of the table, on the left column we report the results computed using the Lagrange interpolation, on the right those by the RL-RBF interpolation. M stands for master while S for slave domain.

In Table 5.3 we summarize the orders of convergence obtained by INTERNODES using nonconforming meshes and the Lagrange interpolant, while in Table 5.4 those using matching grids but nonconforming polynomial degrees. Let us denote by p_1 and p_2 the polynomial degrees used in Ω_1 and Ω_2, respectively. As shown in Table 5.3, if $|p_1 - p_2| \leq 1$, the use of the Lagrange interpolant yields rates of convergence that are optimal in each individual subdomain, in fact they behave as $h_i^{p_i}$, independently of the choice of which domain plays the role of the master or slave. In the case where $p_1 - p_2 > 1$, for instance using $\mathbb{P}3$-$\mathbb{P}1$ finite elements, the rate of convergence behaves like $h_1^{p_1-1}$ in Ω_1 and like $h_2^{p_2}$ in Ω_2 (or, if $p_2 - p_1 > 1$, as $h_1^{p_1}$ in Ω_1 and as $h_2^{p_1+1}$ in Ω_2).

These results can be summarized by the help of the following empirical formula, holding for Lagrange interpolants: if both h_1, $h_2 \to 0$,

$$\|u - u_{i,\delta}\|_{H^1(\Omega_i)} \leq C_i(p_1, p_2) h_i^{\min(q_i, s_i - 1)} \|u\|_{H^{s_i}(\Omega_i)} \quad \text{for } i = 1, 2, \tag{5.44}$$

where

$$
\begin{aligned}
q_1 &= \min(p_1, p_2 + 1), \\
q_2 &= \begin{cases} p_2 & \text{if } p_2 \leq p_1 + 1 \\ p_1 & \text{if } p_2 > p_1 + 1. \end{cases}
\end{aligned}
$$

In (5.44), C_i are positive constants independent of h_i, while $s_i > 1$ is the order of the Sobolev regularity of the exact solution in Ω_i.

Master \ Slave	$\mathbb{P}1$		$\mathbb{P}2$		$\mathbb{P}3$	
$\mathbb{P}1$	1-1	1-1	1-2	1-2	1-2	1-2
	1-1	1-1	1-2	1-2	1-2	1-2
$\mathbb{P}2$	2-1	2-1	2-2	2-2	2-3	2-3
	2-1	2-1	2-2	2-2	2-3	2-3
$\mathbb{P}3$	2-1	2-1	3-2	3-2	3-3	3-3
	2-1	2-1	3-2	3-2	3-3	2-2

Table 5.5: Orders of convergence in H^1 norm obtained using nonconforming meshes and the RL-RBF interpolation. The cells are organized as in Table 5.3.

The results obtained on nonconforming meshes using the RL-RBF interpolant are reported both in Tables 5.4 and 5.5. We notice that, if $|p_1 - p_2| \leq 1$, the method leads to optimal rates of convergence in all the numerical experiments performed, apart from the case of the $\mathbb{P}3$-$\mathbb{P}3$ discretization with grids of Set D. This may be due to the fact that, as shown in Eq. (5.12), the construction of the RL-RBF interpolant does not take into account the polynomial degree of the trace of the finite element basis functions at the interface since it only requires the nodal coordinates and corresponding nodal values at the two

interfaces, separately.

However, this same feature makes RL-RBF a flexible interpolation tool to deal with problems with geometrically nonconforming interfaces (as in the case of Figure 5.2). The treatment of nonmatching interfaces in the mortar setting is instead more involved as it requires, in particular, an ad-hoc projection to retrieve a yet another (virtual) common interface, cf. [Dickopf and Krause, 2009, Klöppel et al., 2011].

In Figure 5.6 we report the PDE's approximation errors in broken norm (see [Quarteroni, 2013, Sect. 11.3]) and the pure interpolation errors for both Lagrange and RL-RBF interpolants versus the polynomial degree p when non-conforming meshes are used (Set D, $k = 64$). We notice that the approximation error and the interpolation error feature almost the same rate of decay with respect to p. In particular, for $p = 1$ the RL-RBF interpolation leads to more accurate results w.r.t. the Lagrange one; for $p = 2$ both interpolants yield the same accuracy while for $p = 3$ the Lagrange interpolation is more accurate. This justifies the sub-optimal orders of the block $\mathbb{P}_1 - \mathbb{P}_3$ of Table 5.3 w.r.t. the corresponding block of Table 5.5, as well as those of the $\mathbb{P}_3 - \mathbb{P}_3$ simulation with Set D in Table 5.5.
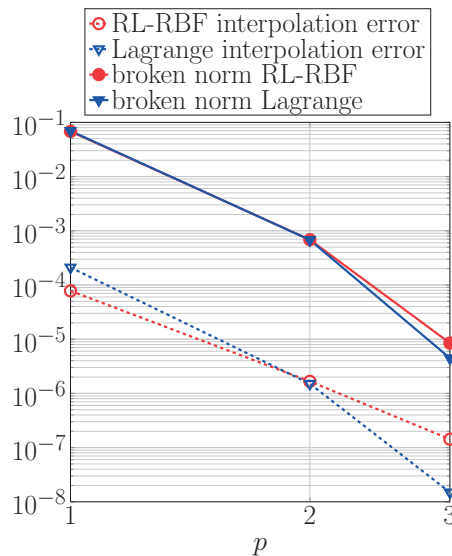
Figure 5.6: Comparison between PDE approximation errors and interpolation errors for $\mathbb{P}_p - \mathbb{P}_p$ FEM, and non-conforming meshes (set D of Table 5.2 and $k = 64$).

5.7.2 Coupling of nonconforming SEM-SEM discretizations

In this Section we consider SEM discretization in both master and slave domains and we compare the errors obtained by INTERNODES (using the Lagrange intergrid operator) with those generated by the mortar approach. As in the previous subsection, we plot the

errors in H^1-norm, i.e., $\|u - u_{1,\delta}\|_{H^1(\Omega_1)}$ and $\|u - u_{2,\delta}\|_{H^1(\Omega_2)}$.

Pictures in the left column of Figure 5.7 refer to INTERNODES, while those in the right column to the mortar approach.

Let p_1 and p_2 denote the polynomial degrees used in Ω_1 and Ω_2, respectively. The errors displayed by the two methods are comparable; moreover, for $i = 1, 2$, they decay as $h_i^{p_i}$ if $|p_1 - p_2| \leq 1$, while the order of convergence is downgraded when $|p_1 - p_2| > 1$, as we can see in the last row of Figure 5.7, where $p_1 = 5$ and $p_2 = 2$. In fact, in the latter case, the error in the master domain behaves like h_1^3 for both the methods and not as h_1^5.

More precisely, the plot in the first row refers to a test case with polynomial conformity and mesh nonconformity; the one in the second row to a case with both polynomial and mesh nonconformity, with and $p_1 = p_2 + 1$; that in the third row again to a case with both polynomial and mesh nonconformity, with and $p_1 = p_2 - 1$; finally the last row to a situation with $p_1 - p_2 > 1$.

In Tables 5.6 and 5.7 we show the rates of convergence with respect to h both for INTERNODES and the mortar approach, respectively, when considering different nonconforming situations, as those in Tables 5.3 and 5.5.

First of all we notice that INTERNODES is accurate as well as the mortar method. Furthermore, the trend observed for the FEM discretization (and anticipated by the convergence curves of Figure 5.7) holds also for SEM case.

M \ S	Q2		Q3		Q4		Q5	
Q2	2-2	2-2	2-3	2-3	2-2	2-3	2-2	2-3
	2-2	2-2	2-3	2-3	2-2	2-3	2-2	2-3
Q3	3-2	3-2	3-3	3-3	3-4	3-4	3-3	3-4
	3-2	3-2	3-3	3-3	3-4	3-4	3-4	3-4
Q4	4-2	3-2	4-3	4-3	4-4	4-4	4-5	4-5
	3-2	3-2	4-3	4-3	4-4	4-4	4-5	4-5
Q5	4-2	3-2	5-3	4-3	5-4	5-4	5-5	5-5
	3-2	3-2	5-3	5-3	5-4	5-4	5-5	5-5

Table 5.6: SEM-SEM coupling: orders of convergence with respect to the mesh sizes h_1 and h_2 of INTERNODES using nonconforming meshes. M stands for master domain while S for slave domain. The cells are organized as in Table 5.3.

In Table 5.8 the orders of convergence in H^1 norm versus the mesh size h are shown in the case of conforming meshes and different (but also equal) polynomial degrees.

The convergence analysis w.r.t. the polynomial degrees p_i is more involved and it is currently under investigation. See however Figure 5.8 below where the error behavior
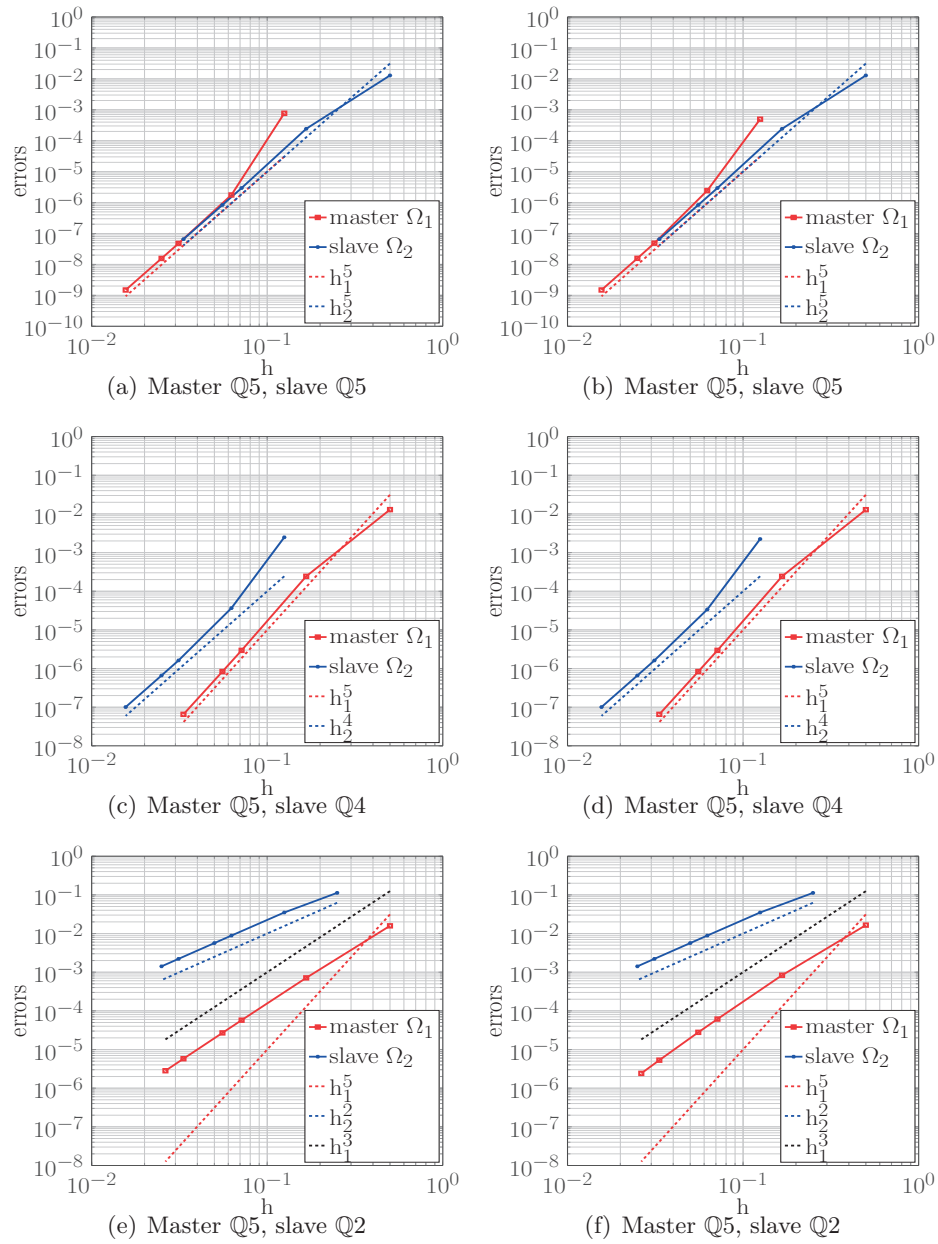
Figure 5.7: Convergence history with respect to the mesh sizes h_1 and h_2 for INTERN-ODES (left) and mortar (right) approaches. SEM discretization. Set C; second line: Set D; third line: Set A.

135

M \ S	Q2		Q3		Q4		Q5	
Q2	2-2	2-2	2-3	2-3	2-2	2-3	2-2	2-3
	2-2	2-2	2-3	2-3	2-2	2-3	2-2	2-3
Q3	3-2	3-2	3-3	3-3	3-4	3-4	3-3	3-4
	3-2	3-2	3-3	3-3	3-4	3-4	3-4	3-4
Q4	4-2	3-2	4-3	4-3	4-4	4-4	4-5	4-5
	3-2	3-2	4-3	4-3	4-4	4-4	4-5	4-5
Q5	4-2	3-2	5-3	4-3	5-4	5-4	5-5	5-5
	3-2	3-2	5-3	5-3	5-4	5-4	5-5	5-5

Table 5.7: SEM-SEM coupling: orders of convergence with respect to the mesh sizes h_1 and h_2 of the mortar approach using nonconforming meshes. M stands for master domain while S for slave domain. The cells are organized as in Table 5.3.

M \ S	Q2		Q3		Q4		Q5	
Q2	2-2	2-2	2-3	2-3	2-2	2-2	2-2	2-2
Q3	3-2	3-2	3-3	3-3	3-4	3-4	3-4	3-4
Q4	4-2	4-2	4-3	4-3	4-4	4-4	4-5	4-5
Q5	4-2	4-2	5-3	5-3	5-4	5-4	5-5	5-5

Table 5.8: SEM-SEM coupling: orders of convergence with respect to the mesh sizes h_1 and h_2, using conforming meshes. In each cell of the table, on the left and on the right we report the results computed using INTERNODES and mortar approach, respectively.

of both INTERNODES and the mortar methods vs the polynomial degree p are shown. The two curves are practically overlaid when using Lagrangian interpolation for IN-TERNODES. In the same figure we also plot the pure interpolation errors: as it can be appreciated, the approximation error and the interpolation error feature the same rate of decay with respect to p. Also reported are the RBF interpolation errors: for moderate polynomial degrees ($p \leq 5$) the rate of decay is the same as for Lagrangian interpolation, whereas (as expected) it flattens for larger values of p. Note that the better accuracy displayed for the RBF interpolation errors with respect to that of Table 5.5 is due to the fact that interpolation nodes now coincide with the (non-uniformly spaced) Gauss-Lobatto-Legendre nodes [Canuto et al., 2006].

5.7.3 Coupling of FEM-SEM discretizations

We consider now the coupling of FEM-SEM discretizations. We set $\Omega_1 = (0,1) \times (0,1)$, $\Omega_2 = (1,2) \times (0,1)$ and the function $u(x,y) = \arctan(4(y-0.5))\cos(\pi(x-0.1))$ as exact solution of the problem (5.43).
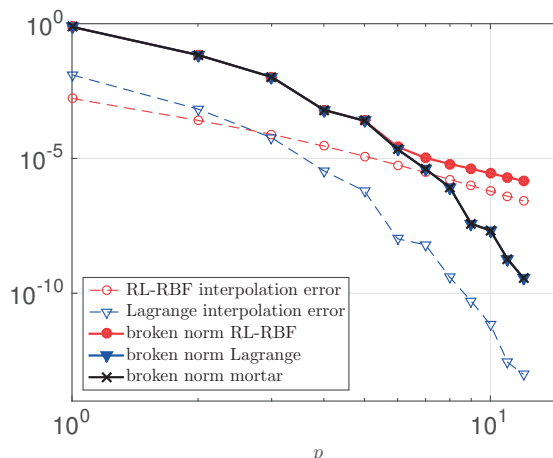
Figure 5.8: Comparison between PDE approximation errors and interpolation errors.

Polynomial nonconformity. In Table 5.9 we show the convergence orders w.r.t. the mesh size h when the master domain Ω_1 is discretized by $\mathbb{P}1$ finite elements and the slave domain Ω_2 by $\mathbb{Q}_p$ spectral elements with $p = 2, 3, 4$ and vice versa. h denotes the diameter of the structured and regular triangular mesh, that coincides with the diameter of the spectral elements. In this first test case we consider mesh conformity and interpolation by either Lagrange and RL-RBF. Finally we compare the results obtained by INTERNODES with those generated by the mortar method.

The advantage of using RL-RBF instead of Lagrange interpolation is clear when the master discrete space is the poorest one, i.e. when it is discretized by $\mathbb{P}1$. More precisely, when using Lagrange interpolation, the first order of convergence driven by $\mathbb{P}1$ in Ω_1 is observed in Ω_2 as well, even if in Ω_2 a higher degree, $p \geq 2$, is used. Conversely, when using RL-RBF, the order of convergence in the slave domain is equal to 2, thus reflecting the more accurate discretization used. In any case, even when $p > 2$ the order of convergence in Ω_2 is still 2.

When the master domain is discretized more finely by $\mathbb{Q}_p$ ($p \geq 2$) and $\mathbb{P}1$ are used in the slave, the rates of convergence are 2 and 1 in the master and the slave domain, respectively, for both the approaches.

Mesh nonconformity. We consider now nonconforming meshes and, as in the previous sections, four different situations, characterized by a varying aspect ratio between the mesh sizes h_1 and h_2, as well as by the refinements of the grids. In Tables 5.10 and 5.11 the convergence orders w.r.t. the mesh size h are shown. As for the mesh conforming case, when the master domain is discretized by $\mathbb{P}1$, the Lagrange interpolation downgrades the higher approximation degree of the slave domain, while the RL-RBF interpolation always provides convergence order 1 in the master domain and 2 in the slave one. On the contrary, when the master domain is discretized by SEM, the convergence orders w.r.t. h

Master - Slave	Lagrange	RL-RBF	mortar
$\mathbb{P}1-\mathbb{Q}2$	1-1	1-2	1-1.6
$\mathbb{P}1-\mathbb{Q}3$	1-1	1-2	1-1.7
$\mathbb{P}1-\mathbb{Q}4$	1-1	1-2	1-1.7
$\mathbb{Q}2-\mathbb{P}1$	2-1	2-1	2-1
$\mathbb{Q}3-\mathbb{P}1$	2-1	2-1	2-1
$\mathbb{Q}4-\mathbb{P}1$	2-1	2-1	2-1

Table 5.9: FEM-SEM coupling: orders of convergence with respect to the mesh sizes h_1 and h_2 when using conforming meshes.

are 2 in the master domain and 1 in the slave one for all the considered approaches.

Master - Slave	Lagrange		RL-RBF		mortar	
$\mathbb{P}1-\mathbb{Q}2$	1-1.5	1-2	1-2	1-2	1-2	1-2
	1-2	1-1.5	1-2	1-2	1-2	1-2
$\mathbb{P}1-\mathbb{Q}3$	1-1	1-2	1-2	1-2	1-1.5	1-2
	1-1	1-1.5	1-2	1-2	1-2	1-2
$\mathbb{P}1-\mathbb{Q}4$	1-1	1-2	1-2	1-2	1-1.5	1-2
	1-1	1-1	1-2	1-2	1-2	1-2

Table 5.10: FEM-SEM coupling: orders of convergence w.r.t. the mesh-sizes h_1 in Ω_1 and h_2 in Ω_2 when using nonconforming meshes. The cells are organized as in Table 5.3.

Master - Slave	Lagrange		RL-RBF		mortar	
$\mathbb{Q}2-\mathbb{P}1$	2-1	2-1	2-1	2-1	2-1	2-1
	2-1	2-1	2-1	2-1	2-1	2-1
$\mathbb{Q}3-\mathbb{P}1$	2-1	2-1	2-1	2-1	2-1	2-1
	2-1	2-1	2-1	2-1	2-1	2-1
$\mathbb{Q}4-\mathbb{P}1$	2-1	2-1	2-1	2-1	2-1	2-1
	2-1	2-1	2-1	2-1	2-1	2-1

Table 5.11: SEM-FEM coupling: orders of convergence w.r.t. the respective mesh-sizes h_1 in Ω_1 and h_2 in Ω_2 when using nonconforming meshes. The cells are organized as in Table 5.3.

The higher accuracy of the SEM discretization is downgraded by that of the $\mathbb{P}1$ FEM approximation. To verify this statement, we fix now the discretization in Ω_1 (master domain) by using 6×6 quads $\mathbb{Q}4$, while we refine the $\mathbb{P}1$ mesh in Ω_2 by choosing $h_2 = 1/8$, $1/16$, $1/32$, $1/64$, $1/128$. In Figure 5.9, the H^1 norm of the errors with respect to the exact solution are shown versus h_2. The error in Ω_1 decays as h_2^2 until the accuracy prescribed by global $\mathbb{Q}4$ discretization is reached, while the error in Ω_2 is $\mathcal{O}(h_2)$.
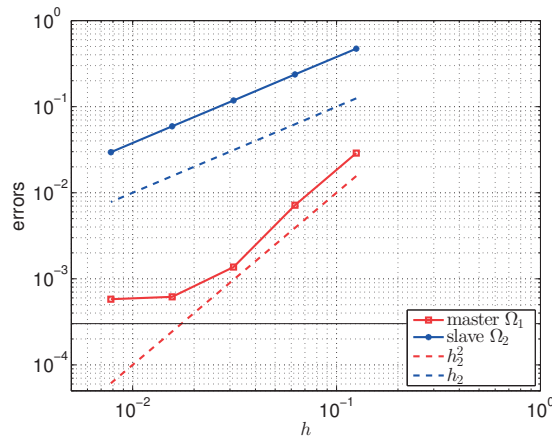
Figure 5.9: SEM-FEM coupling. H^1 norm errors vs. h_2 when $\mathbb{Q}4$ are used in Ω_1 (master) with fix $h_1 = 1/6$, and $\mathbb{P}1$ are used in Ω_2 (slave). The black line denotes the error obtained by discretizing the global domain by conforming $\mathbb{Q}4$ SEM.

5.8 Coupling of geometrically nonconforming subdomains

To assess the robustness of INTERNODES with respect to the geometrically nonconforming case, we solve problem (5.43) with exact solution $u(x,y) = \sin((x-1.2)(y-1.2)2\pi)+1$ in the domain $\Omega = (-0.5, 0.5) \times (-0.5, 0.5)$, decomposed as shown in Figure 5.10. The inner circle is centered at point $(0,0)$ and has radius $R = 0.35$.
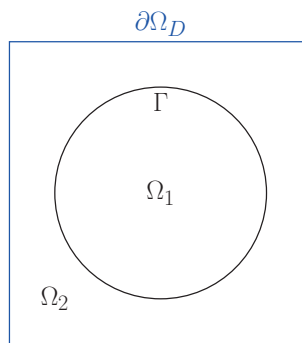
Figure 5.10: Domain decomposition considered for the example with geometrically nonconforming interfaces.

In Figure 5.11 we show the results obtained using $\mathbb{P}1$ finite elements in both the slave and the master domains. Although many gaps and overlaps are present at the interface between the subdomain grids (see bottom row in Figure 5.11), we observe that the quality of the numerical solutions obtained does not worsen. In Figure 5.12 the results obtained using first or second degree polynomials in the master and slave domains are reported. From Figure 5.12(a) we observe that when using linear basis functions, INTERNODES leads to first order rate of convergence in both the master and the slave subdomains. Finally, as shown in Figure 5.12(b), we notice that quadratic convergence is obtained
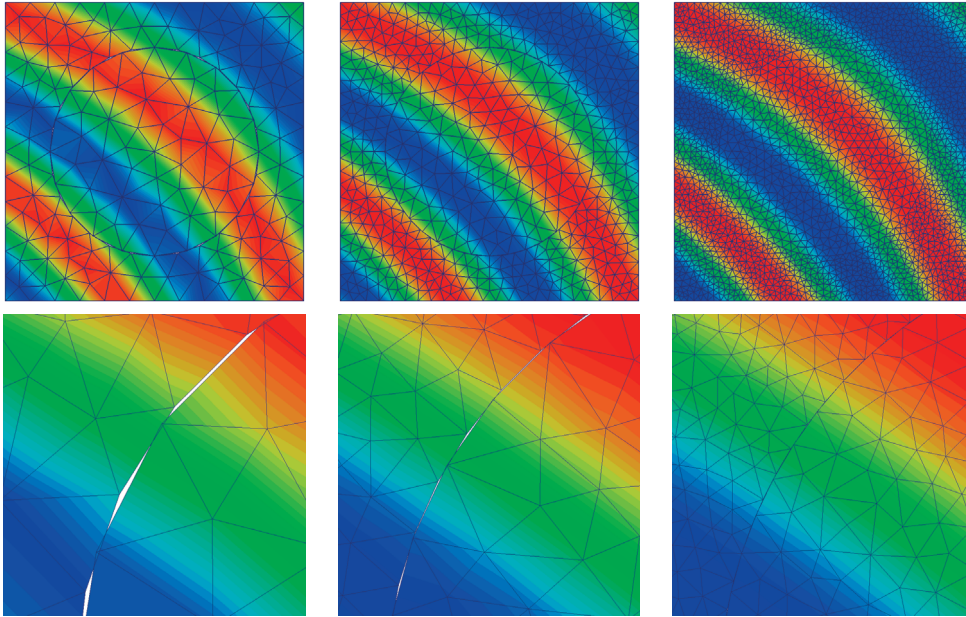
Figure 5.11: Solutions obtained by INTERNODES using $\mathbb{P}1$-$\mathbb{P}1$ finite elements for the master and slave domains using meshes of increasing refinement that are geometrically nonconforming. In the top row we show the numerical results on the whole domain while in the bottom row a zoom of the solution close to the interface.

(a) Master $\mathbb{P}1$ (finer grid), slave $\mathbb{P}1$.

(b) Master $\mathbb{P}2$ (finer grid), slave $\mathbb{P}2$.
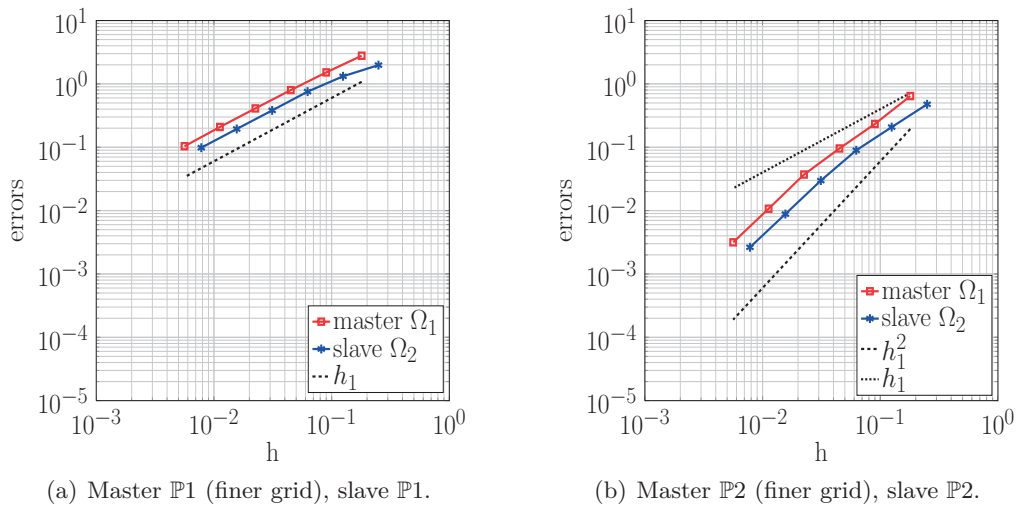
Figure 5.12: Rates of convergence in H^1 norm using geometrically nonconforming interfaces.

with $\mathbb{P}2$ finite elements only for sufficiently small mesh sizes for which the gaps and overlaps between the master and slave subdomains tend to become imperceptible (see bottom-right picture of Figure 5.11).

5.9 Numerical solution of a fluid flow past a cylinder

In this Section we consider the numerical simulation of a fluid flow past a 3D cylindrical obstacle at two different Reynolds numbers, that are $Re = 20$ and $Re = 100$, see [Schäfer and S.Turek, 1996].

We model the flow dynamics by the Navier-Stokes equations for an incompressible fluid. The equations are discretized in space by means of the Finite Element method and in time by Finite Differences. More specifically, we use $\mathbb{P}1$-$\mathbb{P}1$ finite elements for the spatial approximation of the fluid velocity and pressure variables (stabilized by SUPG), respectively, while a second order backward differentiation formula is used for the time discretization (see, e.g. [Quarteroni, 2013]). The nonlinear convective term in the fluid momentum equation is linearized by means of a second order temporal extrapolation [Forti and Dedè, 2015, Gervasio et al., 2006].

In order to compare the numerical results obtained by INTERNODES with those available in the literature we compute the drag and lift coefficients of the cylinder. To this end, we introduce a unit vector directed as the incoming flow $\hat{\mathbf{v}}_\infty = \dfrac{\mathbf{v}_\infty}{\|V_\infty\|}$, and a unit vector $\hat{\mathbf{n}}_\infty$ orthogonal to $\hat{\mathbf{v}}_\infty$. The aerodynamic drag and lift coefficients for the cylinder read:

$$C_D(\mathbf{u}_f, p_f) = -\frac{1}{q_\infty S} \oint_S (\boldsymbol{\sigma}_f(\mathbf{u}_f, p_f)\,\hat{\mathbf{n}}) \cdot \hat{\mathbf{v}}_\infty \, d\Gamma, \tag{5.45}$$

$$C_L(\mathbf{u}_f, p_f) = \frac{1}{q_\infty S} \oint_S (\boldsymbol{\sigma}_f(\mathbf{u}_f, p_f)\,\hat{\mathbf{n}}) \cdot \hat{\mathbf{n}}_\infty \, d\Gamma, \tag{5.46}$$

where $\mathbf{u}_f$ and p_f are the velocity and pressure variables, $\boldsymbol{\sigma}_f$ is the Cauchy stress tensor of the fluid, $q_\infty = \frac{1}{2}\rho_f V_\infty^2$ is the dynamic pressure, ρ_f is the density of the fluid and S is the surface area of the cylinder.

For an accurate estimation of the aerodynamic coefficients, the use of a boundary layer refinement of the computational mesh around the cylinder is mandatory (see, [Ghia et al., 1982]). A possible strategy to generate such a refinement consists in gradually decreasing the mesh element size in the domain while approaching the cylinder, as shown in Figure 5.13(a). An alternative strategy relies in splitting the computational fluid domain into two sub-domains with independent (nonconforming) meshes, see Figure 5.13(b): the finer mesh is used to represent the boundary layer around the cylinder while the coarse one for the far field. In the latter case, after space and time discretization of the Navier-Stokes equations, the algebraic form of the linear system to be solved assumes the form of Eq. (5.30) (in which the matrices $A_{i,j}$ and the right hand sides $\mathbf{f}_i$ are those associated with the fully-discretized Navier-Stokes equations).

The values of the physical parameters for the fluid as well as the boundary conditions used in our simulations are those described in [Schäfer and S.Turek, 1996]. The essential
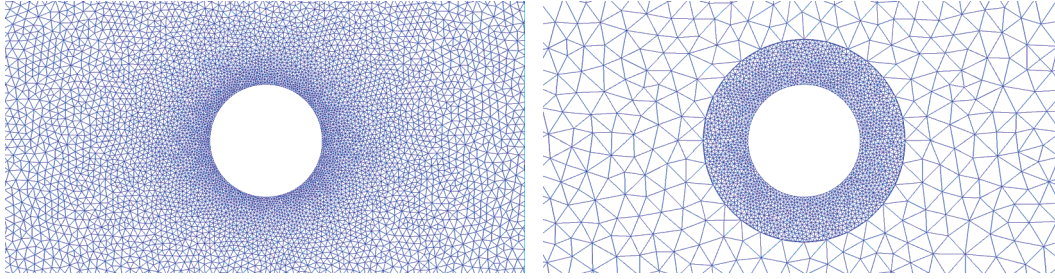
(a) Boundary layer refinement obtained by pro-gressive reduction of the mesh size (cross section).

(b) Independent meshes for the far field and the boundary layer zones (cross section).

Figure 5.13: Two different strategies to realize boundary layers mesh refinements.

boundary condition on the fluid velocity at the cylinder surface is imposed in weak form [Bazilevs and Hughes, 2007, Hsu et al., 2012]. In Table 5.12 we report the drag and lift coefficients of the cylinder obtained using different fluid meshes in which the boundary layer refinement was obtained as in Figure 5.13(a).

Mesh level	DOF	C_D	C_L	% error C_D	% error C_L
1	149'004	6.39269	0.003331	3.35	64.56
2	250'400	6.26037	0.005431	1.21	42.22
3	531'992	6.20392	0.006838	0.31	27.26
4	1'209'060	6.17584	0.009412	0.15	0.11

Table 5.12: Numerical results obtained for the benchmark problem at $Re = 20$. The reference drag and lift coefficients are $C_D = 6.18533$ and $C_L = 0.009401$, respectively.

When splitting the computational fluid domain into two sub-domains with nonconforming meshes, the coarser mesh is used to represent the far field while the finer one around the cylinder. In this example, the mesh-size used for the coarser mesh is the one of Mesh Level 1 while the one of the finer mesh coincides with the mesh-size of Mesh level 4 (see Table 5.12). Furthermore, the far field domain is considered as slave domain while the one around the cylinder is the master. In this way the interface degrees of freedom of the master (finer) domain are primal unknowns of the problem (see Eq. (5.30)). We used 373'068 degrees of freedom in the master domain and 103'768 in the slave. We remark that the ratio between the mesh size of the far field and the one in the boundary layer is approximately 6.

The numerical simulation performed using two nonconforming meshes yields a lift coefficient $C_L = 0.009487$ and a drag coefficient $C_D = 6.19713$. The errors with respect to reference values are 0.91% and 0.19% on the estimation of the lift and the drag coefficients, respectively. To analyze the computational costs, we compare the average time to complete a single time step and the number of linear solver iterations on the simulations with Mesh level 4 of Table 5.12 and the one by INTERNODES with
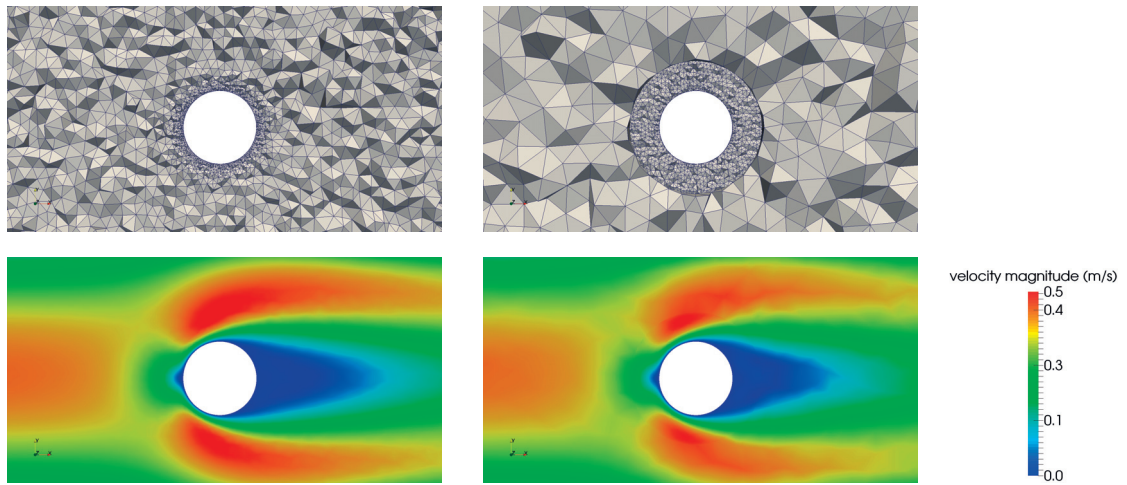
Figure 5.14: Zoom of the meshes and the velocity fields in the region close to the cylinder on a cut plane at $z = 0.205\,m$: in the first row we show the meshes used for the numerical simulations. In the second row we plot the velocity fields obtained.
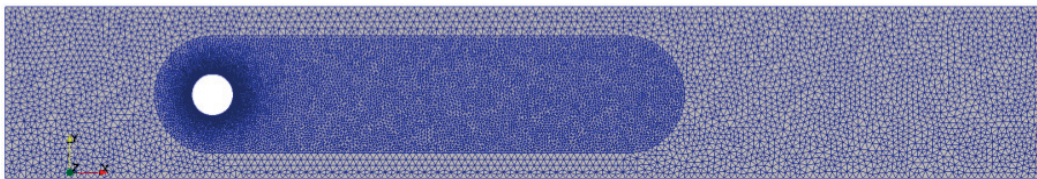
Figure 5.15: Horizontal view of the meshes used for the numerical example at $Re = 100$.

nonconforming meshes. The approach based on the use of nonconforming meshes leads to a reduction of the 50% of the time to perform a time step (thanks to the fact that the number of degrees with nonconforming meshes is roughly half of the one of Mesh level 4).

Finally, we report the results obtained for $Re = 100$. In Figure 5.15 we show the fluid meshes considered for the region close to the obstacle and the far field. In this unsteady case, the geometry in which we use a finer mesh is extended to embed also the wake region behind the cylinder. We consider the far field domain as the slave domain, while the one near the cylinder as master. The computational meshes yield 281'393 degrees of freedom in the slave domain and 844'179 in the master. The aspect ratio between the mesh sizes of the master and slave domains at their interface is approximately 3. The same problem of fluid flow past a cylinder has also been investigated in [Ehrl et al., 2014] by a dual mortar approach for nonconforming meshes tying a fine boundary layer grid in the near field with a coarser grid in the far field.

In Table 5.13, we compare the aerodynamic coefficients of the cylinder computed numerically with those available in literature.

	Maximum C_D	Maximum C_L	Minimum C_L
Computed	3.3017	0.0029	-0.011017
Reference	3.2978	0.0028	-0.010999

Table 5.13: Comparison of the aerodynamic coefficients computed with reference values available in literature [Schäfer and S.Turek, 1996].

In Figure 5.16 we show the numerical results computed at different times on a cut plane parallel to the z axis (located at at $z = 0.205\,m$): we notice that both the velocity and pressure solutions obtained in the master and slave domains are in very good agreement at their interface. In addition, we notice that the velocity field computed at time $t = 4$ s (shown in Figure 5.16) is in very good agreement w.r.t. the one reported in [Ehrl et al., 2014], Figure 16. Finally, to better assess the behavior of the solution across the interface, in Figure 5.17 we plot the fluid velocity along a vertical line passing through both the master and slave sub-domains.
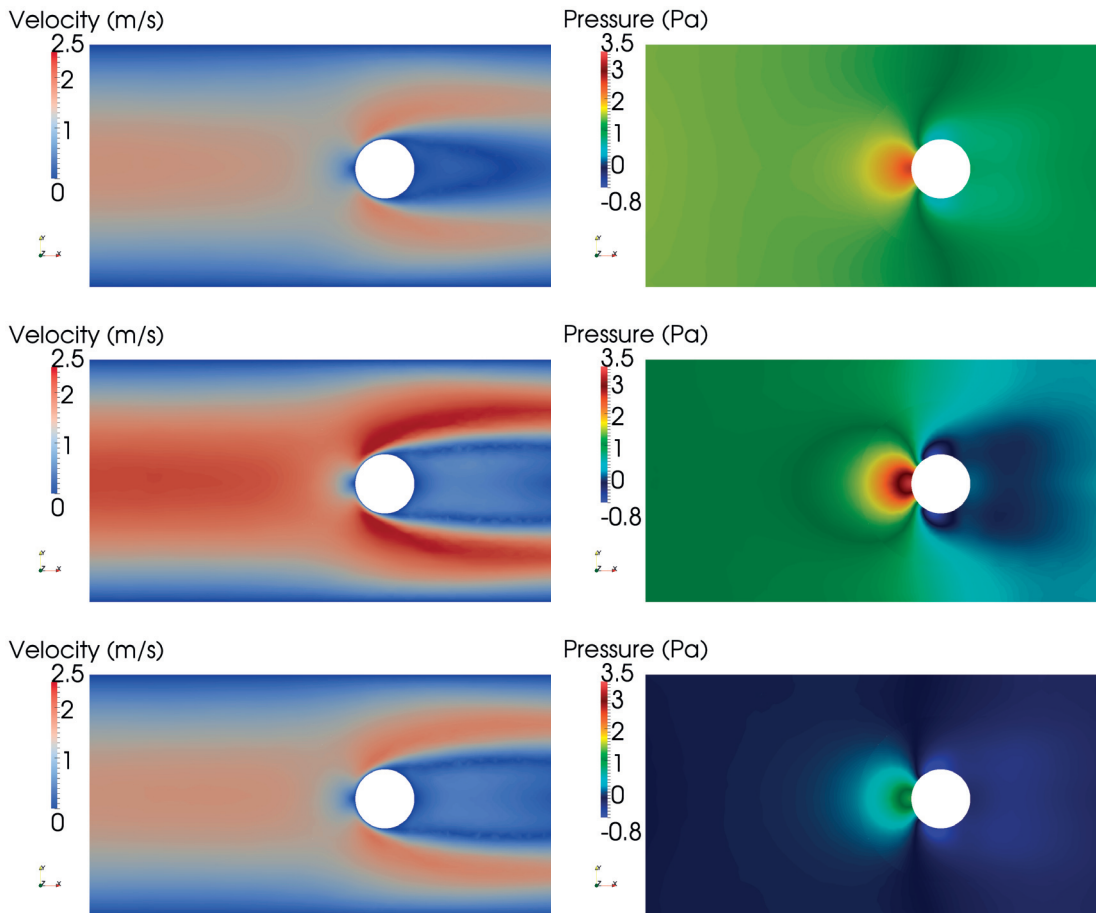
Figure 5.16: Visualization of the numerical solution obtained at times $t = 2\,s$ (top row), $t = 4\,s$ (middle row) and $t = 6\,s$ (bottom row).

(b) Time $t = 2\,s$.

(c) Time $t = 4\,s$.

(d) Time $t = 6\,s$.
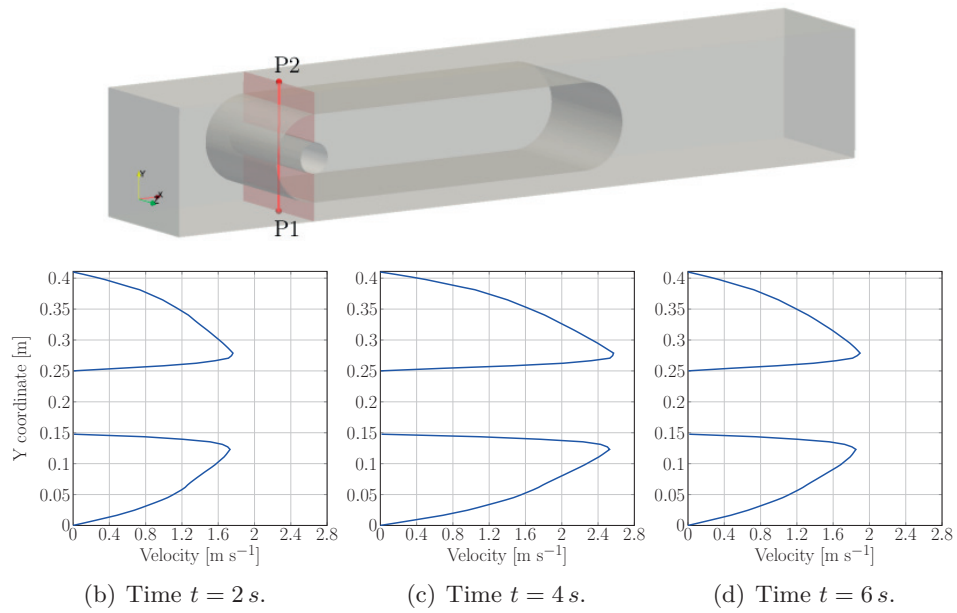
Figure 5.17: Plot over line, between points P1 = (0.5,0,0.205) and P2 = (0.5,0.41,0.205), of the flow velocity at different times.

6 Numerical solution of FSI problems featuring nonconforming interfaces

In this Chapter we address the numerical solution of fluid-structure interaction problems when nonconforming grids and/or nonconforming finite elements discretizations are used at the interface separating the computational domain of the fluid from the one of the structure. In order to deal with nonconforming fluid-structure discretizations we use the method INTERNODES presented in Chapter 5. After identifying a master domain (the structural domain) and a slave domain (the fluid domain), we build the two inter-grid operators based on Rescaled-Localized Radial Basis Functions (RL-RBF) interpolants: one Π_{fs} from solid to fluid, and the other Π_{sf} from fluid to solid. Then, we enforce the kinematic condition by equating the fluid velocity at the interface as the image through Π_{fs} of the temporal derivative of the structural displacement. On the other hand, the dynamic interface condition is fulfilled via a variational method where the strong form of the structural normal component of the Cauchy stress is obtained as the image through Π_{sf} of a strong representation of the normal component of the fluid stress. A numerical verification of the numerical results obtained in the nonconforming case is carried out for a straight cylinder and for a patient-specific arterial bypass geometry. Furthermore, we study the scalability performance of the FaCSI preconditioner considered in Chapter 3 by solving large-scale FSI problems in which nonconforming discretizations are used.

The contents of Sections 6.2 and 6.3 of this Chapter have been already published in [Deparis et al., 2015d].

(a) Conforming meshes. (b) Non-conforming meshes.
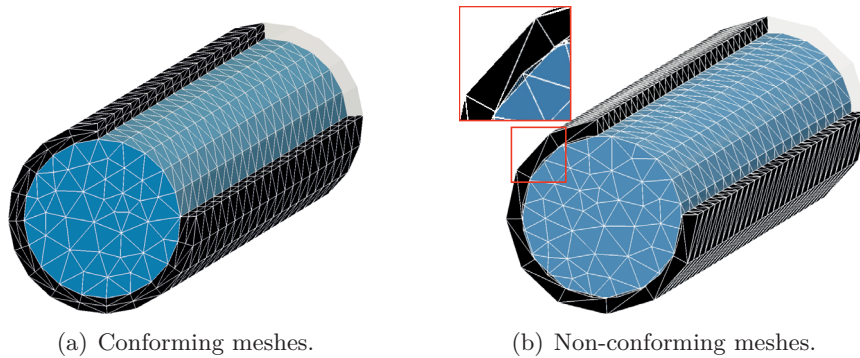
Figure 6.1: Conforming (left) and non-conforming (right) fluid–structure meshes.

6.1 Preliminaries

Solution algorithms for fluid-structure interaction problems are generally derived assuming conforming fluid-structure discretizations at their interface. In such cases, as in Chapter 3, the enforcement of the coupling conditions is straightforward. However, due to the different resolution requirements in the fluid and structure physical domains, as well as the presence of complex interface geometries make the use of matching fluid and structure meshes problematic. In such situations, it is much simpler to deal with discretizations that are nonconforming, provided however that the matching conditions at the interface are properly fulfilled.

The mortar element method is a well known technique commonly used to deal with nonconforming discretizations. In this Chapter, to deal with nonconforming discretizations at the discrete fluid-structure interface we use INTERNODES, that has been described in Chapter 5. In our spatial simulation settings we allow the fluid computational grid and/or the fluid finite element discretization to be nonconforming with the structural one at the interface, see Figure 6.1. Even worse, the two interfaces could be geometrically nonconforming, a situation that arises when the two subdomains are triangulated independently.

For readers' convenience, in Section 6.2, after briefly recalling the complete algebraic formulation in the conforming case, we treat the nonconforming case. In Section 6.3 we describe the solution algorithm used to solve the fully-coupled nonconforming FSI problems. In particular we extend FaCSI to the nonconforming case. Section 6.5 addresses the numerical verification of our approach on an FSI problem for a straight flexible cylinder. Finally, in Section 6.5.4, we address the case of a patient-specific geometry of a femoropopliteal bypass and we compare the results obtained with those shown in Section 3.7.2 with conforming discretizations.

148

6.2 Nonconforming fluid-structure interaction problem

In this Section we focus on the nonconforming formulation of the fluid-structure interaction problem obtained after spatial and temporal discretization. In order to compare the conforming and nonconforming FSI formulations, we begin by recalling the conforming case described in Chapter 3. We remark that the models adopted here for the fluid and the structure are those described in Section 3.2. Furthermore, as in Chapter 3, the time discretization for the fluid problem is carried out using a second order BDF scheme while for the structure we use the Newmark method.

To begin with, we assume that at the (common) interface Γ the fluid and solid discretizations are conforming, see Figure 6.1(a). At each time step, the resulting nonlinear fully-discrete FSI system to be solved reads:

$$
\begin{pmatrix}
S(\hat{\mathbf{d}}_s^{n+1}) & + & 0 & + & 0 & - I_{\Gamma s}^T \boldsymbol{\lambda}^{n+1} \\
-I_{\Gamma s}\hat{\mathbf{d}}_s^{n+1} & + G(\hat{\mathbf{d}}_f^{n+1}) + & 0 & + & 0 & \\
0 & + & 0 & + F(\mathbf{u}_f^{n+1}, p_f^{n+1}, \hat{\mathbf{d}}_f^{n+1}) + I_{\Gamma f}^T \boldsymbol{\lambda}^{n+1} \\
-\frac{\gamma}{\beta \Delta t} I_{\Gamma s}\hat{\mathbf{d}}_s^{n+1} + & 0 & + & I_{\Gamma f}\mathbf{u}_f^{n+1} & + & 0
\end{pmatrix}
=
\begin{pmatrix}
\mathbf{b}_s \\
0 \\
\mathbf{b}_f \\
\mathbf{b}_c
\end{pmatrix},
\quad (6.1)
$$

where in Eq. (6.1) we denoted by $\boldsymbol{\lambda}^{n+1}$ the vector of normal stresses (in weak form) at the fluid–structure interface. The matrices $I_{\Gamma f}$ and $I_{\Gamma s}$ are the restriction of fluid and structure vectors to the interface and account for the continuity of velocities and the geometry adherence on Γ, which are imposed strongly. Their transposes account for the continuity of the normal stresses, which is imposed weakly.

We address now the nonconforming case using INTERNODES: we assume the interface Γ discretized using two different meshes and/or finite element approximations depending on the side which is considered, see Figure 6.1(b). As for the mortar element method, we need to identify the so–called master and slave domains Ω_{slave} and Ω_{master}, respectively, that will play a different role. In particular, we assume the structure domain to be the master, $\hat{\Omega}^s \equiv \Omega_{master}$, while the fluid one represents the slave, $\Omega_t^f \equiv \Omega_{slave}$. In FSI problems, the normal component of the stresses in weak form at the interface are usually computed as residuals of the fluid and structure equations. In (6.1) they are represented by $\boldsymbol{\lambda}$. When dealing with nonconforming discretizations at the interface, they may be represented by two different vectors, $\boldsymbol{\lambda}_f$ on the fluid side and $\boldsymbol{\lambda}_s$ on the solid one.

Remark 6.1: as we have seen in Chapter 5, the choice of the master and slave domains in INTERNODES is arbitrary. Here, our choice is driven by the computational efficiency of the construction of the preconditioner FaCSI, as we will show in Section 6.4.

In the nonconforming case the interface coupling conditions become more involved with respect to the conforming case since an interpolation or a projection procedure has to

be performed to enable the transfer of physical information between two different grids. In this Chapter this procedure is carried out using the Rescaled Localized Radial Basis Functions (RL-RBF) interpolant proposed in [Deparis et al., 2014a]. We remark that other interpolants can be used as well (see, e.g., Section 5.4); however we choose RL-RBF since it allows to consider also slightly nonconforming geometries, i.e., those for which Γ^f and Γ^s do not exactly coincide. We define the two matrices representing the interpolation between the two sides of the interface and denote them by R_{sf}, from Γ^f to Γ^s, and R_{fs}, from Γ^s to Γ^f.

To better understand the way Eq. (6.1) is generalized to the nonconforming case, we reformulate it by introducing the redundant variables $\boldsymbol{\lambda}_f$ (the normal component of the stresses in weak form from the fluid side) and $\boldsymbol{\lambda}_s$ (the normal component of stresses in weak form from the structure side), and set $\boldsymbol{\lambda}_f = \boldsymbol{\lambda}_s(= \boldsymbol{\lambda})$. Then, Eq. (6.1) can be equivalently reformulated as:

$$
\begin{pmatrix}
S(\hat{\mathbf{d}}_s^{n+1}) & + & 0 & + & 0 & + & 0 & -I_{\Gamma^s}^T \boldsymbol{\lambda}_s^{n+1} \\
-I_{\Gamma^s}\hat{\mathbf{d}}_s^{n+1} & +G(\hat{\mathbf{d}}_f^{n+1})+ & & 0 & + & 0 & + & 0 \\
0 & + & 0 & + & 0 & -I_{\Gamma^f}^T \boldsymbol{\lambda}_f^{n+1} & +I_{\Gamma^s}^T \boldsymbol{\lambda}_s^{n+1} \\
0 & + & 0 & +F(\mathbf{u}_f^{n+1},p_f^{n+1},\hat{\mathbf{d}}_f^{n+1})+I_{\Gamma^f}^T \boldsymbol{\lambda}_f^{n+1}+ & & 0 \\
-\dfrac{\gamma}{\beta\Delta t}\,I_{\Gamma^s}\hat{\mathbf{d}}_s^{n+1}+ & & 0 & + & I_{\Gamma^f}\mathbf{u}_f^{n+1} & + & 0 & + & 0
\end{pmatrix}
=
\begin{pmatrix}
\mathbf{b}_s \\
0 \\
0 \\
\mathbf{b}_f \\
\mathbf{b}_c
\end{pmatrix}.
$$

$$\tag{6.2}$$

In the nonconforming case, the kinematic coupling condition at the fluid-structure interface becomes:

$$
\mathbf{u}_f \circ \mathcal{A}_t = \Pi_{fs}\frac{\partial \hat{\mathbf{d}}_s}{\partial t} \quad \text{on } \Gamma^f,
\tag{6.3}
$$

which, after discretization, reads

$$
\mathbf{u}_f^{n+1}|_{\Gamma^f} = R_{fs}\left(\frac{\gamma}{\beta\Delta t}\hat{\mathbf{d}}_s^{n+1}|_{\Gamma^s} + \mathbf{b}_c|_{\Gamma^s}\right),
\tag{6.4}
$$

where R_{fs} is the matrix associated with operator Π_{fs}. Eq. (6.4) represents the discrete form of the kinematic coupling condition in the nonconforming case and it replaces row 5 in Eq. (6.2).

We focus now on the coupling condition of the normal component of the stresses at the fluid-structure interface. Let us denote by $\boldsymbol{\lambda}_s^{n+1}$ the weak form of the normal component of the Cauchy stress (or normal traction) on Γ^s at time t^{n+1}, and by M_{Γ^s} and M_{Γ^f} the mass matrices associated to the structure and fluid sides of the interface, respectively. Thanks to INTERNODES (see Eq. (5.29)) the discrete form of the dynamic coupling

condition reads:

$$\boldsymbol{\lambda}_s^{n+1} = M_{\Gamma^s} R_{sf} M_{\Gamma^f}^{-1} \boldsymbol{\lambda}_f^{n+1}. \tag{6.5}$$

This equation replaces the third row in Eq. (6.2). In Eq. (6.5), we notice that $M_{\Gamma^f}^{-1}\boldsymbol{\lambda}_f^{n+1}$ is an approximation of the strong form of the normal component of the stresses on Γ^f; $R_{sf}(M_{\Gamma^f}^{-1}\boldsymbol{\lambda}_f^{n+1})$ is an interpolation of the normal component of the stresses on the side of Γ^s, still in strong form, and $M_{\Gamma^s}(\Pi_{sf}M_{\Gamma^f}^{-1}\boldsymbol{\lambda}_f^{n+1})$ is again in weak form but on Γ^s. Note that the order of magnitude of the entries of $\boldsymbol{\lambda}_f^{n+1}$ depend on the mesh size used to discretize Ω_t^f, that of the entries of $M_{\Gamma^s}(\Pi_{sf}M_{\Gamma^f}^{-1}\boldsymbol{\lambda}_f^{n+1})$ depend on the mesh size of $\hat{\Omega}^s$, while the order of magnitude of those of $M_{\Gamma^f}^{-1}\boldsymbol{\lambda}_f^{n+1}$ and $\Pi_{sf}(M_{\Gamma^f}^{-1}\boldsymbol{\lambda}_f^{n+1})$ are independent of the mesh sizes.

To summarize, in the nonconforming case Eq. (6.2) has to be replaced by:

$$\begin{pmatrix} S(\hat{\mathbf{d}}_s^{n+1}) & - I_{\Gamma^s}^T \boldsymbol{\lambda}_s^{n+1} \\ -R_{fs}I_{\Gamma^s}\hat{\mathbf{d}}_s^{n+1} & + G(\hat{\mathbf{d}}_f^{n+1}) \\ -R_{sf}M_{\Gamma^f}^{-1}\boldsymbol{\lambda}_f^{n+1} & + M_{\Gamma^s}^{-1}\boldsymbol{\lambda}_s^{n+1} \\ F(\mathbf{u}_f^{n+1}, p_f^{n+1}, \hat{\mathbf{d}}_f^{n+1}) + I_{\Gamma^f}^T \boldsymbol{\lambda}_f^{n+1} \\ -\dfrac{\gamma}{\beta \Delta t} R_{fs}I_{\Gamma^s}\hat{\mathbf{d}}_s^{n+1} & + I_{\Gamma^f}\mathbf{u}_f^{n+1} \end{pmatrix} = \begin{pmatrix} \mathbf{b}_s \\ 0 \\ 0 \\ \mathbf{b}_f \\ R_{fs}\mathbf{b}_c \end{pmatrix}. \tag{6.6}$$

Upon eliminating $\boldsymbol{\lambda}_s^{n+1}$ using Eq. (6.5), we end up with the reduced nonlinear FSI system

$$\begin{pmatrix} S(\hat{\mathbf{d}}_s^{n+1}) & + & 0 & + & 0 & - I_{\Gamma^s}^T M_{\Gamma^s} R_{sf} M_{\Gamma^f}^{-1}\boldsymbol{\lambda}_f^{n+1} \\ -R_{sf}I_{\Gamma^s}\hat{\mathbf{d}}^{n+1} & + G(\hat{\mathbf{d}}_f^{n+1}) + & 0 & + & 0 \\ 0 & + & 0 & + F(\mathbf{u}_f^{n+1}, p_f^{n+1}, \hat{\mathbf{d}}_f^{n+1}) + & I_{\Gamma^f}^T \boldsymbol{\lambda}_f^{n+1} \\ -\dfrac{\gamma}{\beta \Delta t} R_{fs}I_{\Gamma^s}\hat{\mathbf{d}}_s^{n+1} + & 0 & + & I_{\Gamma^f}\mathbf{u}_f^{n+1} & + & 0 \end{pmatrix} = \begin{pmatrix} \mathbf{b}_s \\ 0 \\ \mathbf{b}_f \\ R_{fs}\mathbf{b}_c \end{pmatrix} \tag{6.7}$$

which should be regarded as the generalization of Eq. (6.1) to the nonconforming case.

6.3 Numerical solution of the nonconforming FSI problem

We focus on solving Eq. (6.7) using the Newton method. The solution of (6.7) at time $t^n = n\,\Delta t$ is denoted by $\mathbf{X}^n = (\mathbf{d}_s^n, \mathbf{d}_f^n, \mathbf{u}_f^n, p_f^n, \boldsymbol{\lambda}_f^n)^T$. At each time step, we compute a sequence of approximations $\mathbf{X}_1^{n+1}$, $\mathbf{X}_2^{n+1}$, etc. until the numerical solution converges up to a prescribed tolerance. Starting from an approximation of $\mathbf{X}_k^{n+1}$, the generic $k+1$ iteration of the Newton method applied to (6.7) requires first to assemble the residual

$\mathbf{R}_{nc,k}^{n+1} = (\mathbf{r}_{\mathbf{d}_s,k}^{n+1}, \mathbf{r}_{\mathbf{d}_f,k}^{n+1}, \mathbf{r}_{u_f,k}^{n+1}, r_{p_f,k}^{n+1}, \mathbf{r}_{\lambda,k}^{n+1})^T$ (the pedex nc stands for nonconforming):

$$\mathbf{R}_{nc,k}^{n+1} = \begin{pmatrix} \mathbf{b}_s \\ 0 \\ \mathbf{b}_f \\ \Pi_{fs}\mathbf{b}_c \end{pmatrix} - \begin{pmatrix} S(\hat{\mathbf{d}}_{s,k}^{n+1}) \qquad - I_{\Gamma s}^T M_{\Gamma s} R_{sf} M_{\Gamma f}^{-1} \boldsymbol{\lambda}_{f,k}^{n+1} \\ -R_{fs}I_{\Gamma s}\hat{\mathbf{d}}_{s,k}^{n+1} \quad + \quad G(\hat{\mathbf{d}}_{f,k}^{n+1}) \\ F(\mathbf{u}_{f,k}^{n+1}, p_{f,k}^{n+1}, \hat{\mathbf{d}}_{f,k}^{n+1}) + \quad I_{\Gamma f}^T \boldsymbol{\lambda}_{f,k}^{n+1} \\ -\dfrac{\gamma}{\beta\Delta t} R_{fs}I_{\Gamma s}\hat{\mathbf{d}}_{s,k}^{n+1} \quad + \quad I_{\Gamma f}\mathbf{u}_{f,k}^{n+1} \end{pmatrix}. \tag{6.8}$$

Then, we compute the Newton correction vector $\delta\mathbf{X}_k^{n+1} = (\delta\mathbf{d}_{s,k}^{n+1}, \delta\mathbf{d}_{f,k}^{n+1}, \delta\mathbf{u}_{f,k}^{n+1}, \delta p_k^{n+1},$ $\delta\boldsymbol{\lambda}_k^{n+1})^T$ by solving

$$J_{ncFSI}\,\delta\mathbf{X}_k^{n+1} = -\mathbf{R}_{nc,k}^{n+1}, \tag{6.9}$$

being

$$J_{ncFSI} = \begin{pmatrix} \mathcal{S} & 0 & 0 & -I_{\Gamma s}^T M_{\Gamma s} R_{sf} M_{\Gamma f}^{-1} \\ -R_{fs}I_{\Gamma s} & \mathcal{G} & 0 & 0 \\ 0 & \mathcal{D} & \mathcal{F} & I_{\Gamma f}^T \\ -\dfrac{\gamma}{\beta\Delta t} R_{fs}I_{\Gamma s} & 0 & I_{\Gamma f} & 0 \end{pmatrix}, \tag{6.10}$$

where $\mathcal{S}$, $\mathcal{G}$ and $\mathcal{F}$ represents the linearized structure, geometry and fluid problems, respectively; $\mathcal{D}$ are the shape derivatives (for their exact computation see [Fernández and Moubachir, 2003]). Linear system (6.9) is solved by the preconditioned GMRES method. Finally, we update the solution, i.e. $\mathbf{X}_{k+1}^{n+1} = \mathbf{X}_k^{n+1} + \delta\mathbf{X}_k^{n+1}$. We stop the Newton iterations when $\|\mathbf{R}_{nc,k}^{n+1}\|_\infty / \|\mathbf{R}_{nc,0}^{n+1}\|_\infty \leq \epsilon$, being $\mathbf{R}_{nc,0}^{n+1}$ the residual at the first Newton iteration and ϵ a prescribed tolerance.

In the fully conforming case, R_{fs} and R_{sf} coincide with the identity matrix and Eqs. (6.8) and (6.10) return Eqs. (3.15) and (3.17), respectively. We remark that, with respect to the fully conforming case, at each Newton iteration the evaluation of the residual is more computational expensive. Indeed, to compute the residual of the structure subproblem, first we have to apply to $\boldsymbol{\lambda}_k^{n+1}$ the inverse of the fluid mass matrix at the interface, then interpolate it from the fluid to structure side of the interface and eventually multiply it by the interface mass matrix of the solid. The residual associated to the geometry subproblem requires to interpolate $\hat{\mathbf{d}}_{s,k}^{n+1}$ from the structure to the fluid side of the interface. The computation of $\mathbf{r}_{\lambda,k}^{n+1}$ involves interpolation of $\hat{\mathbf{d}}_{s,k}^{n+1}$ and $\mathbf{b}_c$ from the structure to the fluid side of the interface.

Similarly, we notice that with respect to the conforming case, at each GMRES iteration the application of the Jacobian matrix J_{ncFSI} to a given input vector becomes more slightly computational expensive, too.

6.4 FaCSI with nonconforming FSI discretizations

In this Section we describe how the preconditioner FaCSI applies to the linearized fluid-structure interaction problem obtained after spatial and temporal discretizations in the nonconforming case. When nonconforming fluid-structure discretizations are used at the interface, the preconditioner FaCSI devised in Section 3.6.1 reads:

$$P_{FaCSI} = P_{\mathcal{S}}^{ap} \cdot P_{\mathcal{G}}^{ap} \cdot P_{\mathcal{F}}^{ap}, \tag{6.11}$$

where:

$$P_{\mathcal{S}}^{ap} = \begin{pmatrix} \mathcal{H}_{\mathcal{S}} & 0 & 0 & 0 \\ 0 & I & 0 & 0 \\ 0 & 0 & I & 0 \\ 0 & 0 & 0 & I \end{pmatrix}, \quad P_{\mathcal{G}}^{ap} = \begin{pmatrix} I & 0 & 0 & 0 \\ -R_{fs}I_{\Gamma^s} & \mathcal{H}_{\mathcal{G}} & 0 & 0 \\ 0 & 0 & I & 0 \\ 0 & 0 & 0 & I \end{pmatrix}, \tag{6.12}$$

and

$$P_{\mathcal{F}}^{ap} = \begin{pmatrix} I & 0 & 0 & 0 \\ 0 & I & 0 & 0 \\ 0 & \mathcal{D} & \begin{pmatrix} I & 0 & 0 \\ 0 & I_{\Gamma} & 0 \\ 0 & 0 & I \end{pmatrix} & \begin{pmatrix} 0 \\ 0 \\ 0 \end{pmatrix} \\ -\frac{\gamma}{\beta\Delta t}R_{fs}I_{\Gamma^s} & 0 & \begin{pmatrix} 0 & 0 & 0 \end{pmatrix} & I \end{pmatrix} \begin{pmatrix} I & 0 & 0 & 0 \\ 0 & I & 0 & 0 \\ 0 & 0 & \begin{pmatrix} I & 0 & 0 \\ 0 & 0 & 0 \\ 0 & 0 & I \end{pmatrix} & \begin{pmatrix} 0 \\ I_{\Gamma} \\ 0 \end{pmatrix} \\ 0 & 0 & \begin{pmatrix} 0 & I_{\Gamma} & 0 \end{pmatrix} & I \end{pmatrix}$$

$$\begin{pmatrix} I & 0 & 0 & 0 \\ 0 & I & 0 & 0 \\ 0 & 0 & \begin{pmatrix} \mathcal{H}_{\mathcal{K}_{ii}} & \mathcal{K}_{i\Gamma} & 0 \\ 0 & I_{\Gamma} & 0 \\ \mathcal{B}_i & \mathcal{B}_{\Gamma} & -\mathcal{H}_{\widetilde{\mathcal{S}}} \end{pmatrix} & \begin{pmatrix} 0 \\ I_{\Gamma} \\ 0 \end{pmatrix} \\ 0 & 0 & \begin{pmatrix} 0 & 0 & 0 \end{pmatrix} & I \end{pmatrix} \begin{pmatrix} I & 0 & 0 & 0 \\ 0 & I & 0 & 0 \\ 0 & 0 & \begin{pmatrix} I & 0 & D^{-1}\mathcal{B}_i^T \\ 0 & I_{\Gamma} & 0 \\ 0 & 0 & I \end{pmatrix} & \begin{pmatrix} 0 \\ I_{\Gamma} \\ 0 \end{pmatrix} \\ 0 & 0 & \begin{pmatrix} 0 & 0 & 0 \end{pmatrix} & I \end{pmatrix}$$

$$\begin{pmatrix} I & 0 & 0 & 0 \\ 0 & I & 0 & 0 \\ 0 & 0 & \begin{pmatrix} I & 0 & 0 \\ 0 & I_{\Gamma} & 0 \\ 0 & 0 & I \end{pmatrix} & \begin{pmatrix} 0 \\ 0 \\ 0 \end{pmatrix} \\ 0 & 0 & \begin{pmatrix} \mathcal{K}_{\Gamma i} & \mathcal{K}_{\Gamma\Gamma} & \mathcal{B}_{\Gamma}^T \end{pmatrix} & I \end{pmatrix}. \tag{6.13}$$

In particular, we have dropped the off-diagonal block $-I_{\Gamma^s}^T M_{\Gamma^s} R_{sf} M_{\Gamma f}^{-1}$. As before we condense the interface degrees of freedom related to the Lagrange multiplier in step 3 of the following algorithm. For the sake of clarity, we point out that, for a given residual $\mathbf{r} = (\mathbf{r}_{\mathbf{d}_s}, \mathbf{r}_{\mathbf{d}_f}, \mathbf{r}_{\mathbf{u}_f}, \mathbf{r}_{p_f}, \mathbf{r}_{\boldsymbol{\lambda}})^T$, the application of our preconditioner amounts to solve $P_{FaCSI}\mathbf{w} = \mathbf{r}$, therefore involving the following steps:

1. Application of $(P_{\mathcal{S}}^{ap})^{-1}$: $\mathbf{w}_{\mathbf{d}_s} = \mathcal{H}_{\mathcal{S}}^{-1}\mathbf{r}_{\mathbf{d}_s}$.

2. Application of $(P_{\mathcal{G}}^{ap})^{-1}$: $\mathbf{w}_{\mathbf{d}_f} = \mathcal{H}_{\mathcal{G}}^{-1}(\mathbf{r}_{\mathbf{d}_f} + R_{fs}I_{\Gamma^s}\mathbf{w}_{\mathbf{d}_s})$.

3. Application of $(P_{\mathcal{F}}^{ap})^{-1}$: compute $\mathbf{z}_F = \mathbf{r}_F - \mathcal{D}\mathbf{w}_{\mathbf{d}_f}$ and $\mathbf{z}_\lambda = \mathbf{r}_\lambda + \frac{\gamma}{\beta\Delta t}R_{fs}I_{\Gamma^s}\mathbf{w}_{\mathbf{d}_s}$. Then, after denoting by $\mathbf{w}_{\mathbf{u}}$ and $\mathbf{w}_p$, $\mathbf{z}_{\mathbf{u}}$ and $\mathbf{z}_p$ the velocity and pressure components of $\mathbf{w}_F$ and $\mathbf{z}_F$, respectively, thanks to (3.25c) we set $\mathbf{z}_{\mathbf{u},\Gamma} = \mathbf{z}_\lambda$. The application of the SIMPLE preconditioner involves:

   a) $\mathbf{y}_{\mathbf{u},i} = \mathcal{H}_{\mathcal{K}_{ii}}^{-1}(\mathbf{z}_{\mathbf{u},i} - \mathcal{K}_{i\Gamma}\mathbf{z}_{\mathbf{u},\Gamma})$,

   b) $\mathbf{w}_p = \mathcal{H}_{\widetilde{S}}^{-1}(\mathcal{B}_i\mathbf{y}_{\mathbf{u},i} - \mathbf{z}_p + \mathcal{B}_\Gamma\mathbf{z}_{\mathbf{u},\Gamma})$,

   c) $\mathbf{w}_{\mathbf{u}} = (\mathbf{w}_{\mathbf{u},i}, \mathbf{w}_{\mathbf{u},\Gamma})^T = (\mathbf{y}_{\mathbf{u},i} - D^{-1}\mathcal{B}_i^T\mathbf{w}_p, \mathbf{z}_{\mathbf{u},\Gamma})^T$.

   Finally, we compute $\mathbf{w}_\lambda = I_{\Gamma^{u_f}}(\mathbf{z}_{\mathbf{u}} - \mathcal{K}\mathbf{w}_{\mathbf{u}} - \mathcal{B}^T\mathbf{w}_p)$.

We notice that, with respect to the conforming case, at each linear solver iteration the application of the preconditioner FaCSI to a given residual involves one interpolation of the vector $\mathbf{w}_{\mathbf{d}_s}$ from the structure to the fluid interface.

6.5 Numerical Examples

We test our FSI solver on two different test cases: the first is an FSI example in which we study the fluid flow in a straight flexible tube, the second consists in the simulation of the hemodynamics in a femoropopliteal bypass. In Section 6.5.1 we carry out a mesh convergence study where we address both the case of nonconforming polynomial degrees and nonconfrming meshes at the fluid-structure interface. In Section 6.5.2 we study the weak and strong scalability properties of FaCSI in the nonconforming case and we quantify how to deal with nonconforming discretizations increases the computational costs with respect to the conforming case. In Section 6.5.3 we compare the performance of our solver with those reported in [Klöppel et al., 2011], wherein a dual mortar approach for FSI was used. Finally, we test our solver on a large-scale simulation of the hemodynamics in a femoropopliteal bypass in which both nonconforming meshes and polynomial degrees are used at the fluid-structure interface. We point out that all the settings for the numerical examples solved in Sections 6.5.1 and 6.5.2 are the same of those described in Section 3.7.1 of Chapter 3. Similarly, the settings adopted for the simulation in Section 6.5.4 are those already described in Section 3.7.2 of Chapter 3.

6.5.1 Mesh convergence study

In this Section we carry out a mesh convergence study of the solver implemented using nonconforming discretizations at the fluid-structure interface. To this end, we consider

five meshes of increasing refinement: in Table 6.1 we report the information of the fluid-structure meshes used for the analysis. Two different types of nonconformity, idetified by Set A and Set B, are taken into account in the mesh convergence study. In Set A, see

| | Fluid | | Structure | |
	# Vertices	# Tetrahedra	# Vertices	# Tetrahedra
Mesh # 1	2'337	11'040	2'460	9'600
Mesh # 2	13'603	72'000	8'052	31'680
Mesh # 3	64'943	362'400	23'028	91'200
Mesh # 4	183'300	1'045'800	60'912	272'160
Mesh # 5	285'912	1'641'180	84'816	379'440

Table 6.1: Details of the meshes used for the straight cylinder example.

| Set A - nonconforming polynomial degree | | | | |
Fluid DoF	Structure DoF	Coupling DoF	Geometry DoF	Total
9'348	48'600	2'340	7'011	67'299
54'412	159'720	7'788	40'809	262'729
259'772	458'280	22'572	194'829	935'453
733'200	1'274'616	45'036	549'900	2'602'752
1'143'648	1'775'928	58986	857'736	3'836'298

Table 6.2: Number of Degrees of Freedom for the nonconforming polynomial degree case.

| Set B - nonconforming meshes | | | | |
Fluid DoF	Structure DoF	Coupling DoF	Geometry DoF	Total
52'152	48'600	3'160	49'815	153'727
320'338	159'720	10'472	306'735	797'265
1'568'222	458'280	30'248	1'503'279	3'560'029
4'473'327	1'274'616	60'264	4'290'027	10'098'234
6'997'815	1'775'928	84'072	6'711'903	15'569'718

Table 6.3: Number of Degrees of Freedom (DoF) for the nonconforming meshes case.

Table 6.2, at the fluid-structure interface we use conforming meshes but nonconforming polynomial degrees; in Set B, see Table 6.3, we address the case of nonconforming meshes. In Set A we use $\mathbb{P}1$-$\mathbb{P}1$ finite elements (stabilized by SUPG-VMS) for the fluid velocity and pressure, respectively, $\mathbb{P}2$ for the the structure displacement and $\mathbb{P}1$ for the ALE. In Set B we discretize the fluid velocity and pressure by $\mathbb{P}2$-$\mathbb{P}1$ finite elements, respectively, the structure displacement by $\mathbb{P}2$ and the ALE by $\mathbb{P}2$ as well. We point out that the nonconforming meshes used in Set B have been generated by rotating the conforming ones used in Set A such that the fluid and structure meshes overlap for roughly a third of an element length.

In Figure 6.2 we show a post-processing of the solutions obtained at time $t = 0.005$ s: from left to rigth we report the results obtained with Set A-Mesh # 3, Set B-Mesh # 3 and conforming meshes. The results corresponding to the conforming case have been generated using Mesh # 5 of Table 3.4 (using more than 15 millions DoFs in total). We notice the results obtained using nonconforming discretizations match almost exactly those obtained in the conforming case, even if in the conforming case we used a much bigger number of degrees of freedom.

(a) Set A, Mesh # 3.   (b) Set B, Mesh # 3.   (c) Conforming case.
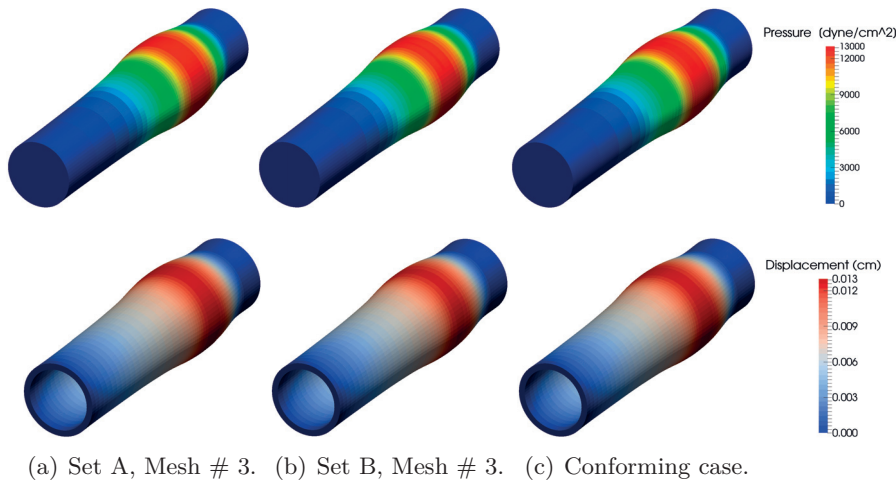
Figure 6.2: Post-processing of the results obtained at time $t = 0.005$ s. In the upper row we show the fluid pressure, while in the bottom one the magnitude of the structure displacement. The deformation of the fluid and structure domains is magnified by a factor 10 for visualization purposes.

Finally, in Figure 6.3 we compare the solutions obtained for Set A and Set B by plotting the values of the fluid velocity and pressure, and the radial component of the solid displacements versus time at two specific locations shown in Figure 6.3(a). Furthermore, in Figure 6.3, we also report the results obtained using conforming meshes (using Mesh # 5 of Table 3.4). The left most plots of Figure 6.3 show the mesh convergence of the structure displacements using Set A (top) and Set B (bottom). The use of quadratic finite elements in both Set A and Set B yields a very similar convergence behavior observed in both the cases. In the middle and right most plots of Figure 6.3 we report the mesh convergence results for the magnitude of the fluid velocity and the fluid pressure, respectively. In this regard, we notice the different convergence behavior between Set A and Set B. Indeed, as a consequence of using $\mathbb{P}1$-$\mathbb{P}1$ elements for the fluid velocity and pressure in Set A while $\mathbb{P}2$-$\mathbb{P}1$ in Set B, the curves associated to Set B converges much faster than those of Set A.
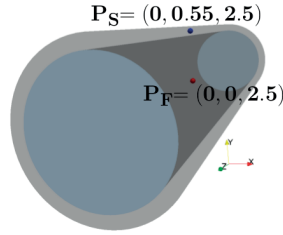
(a) Points of measure.
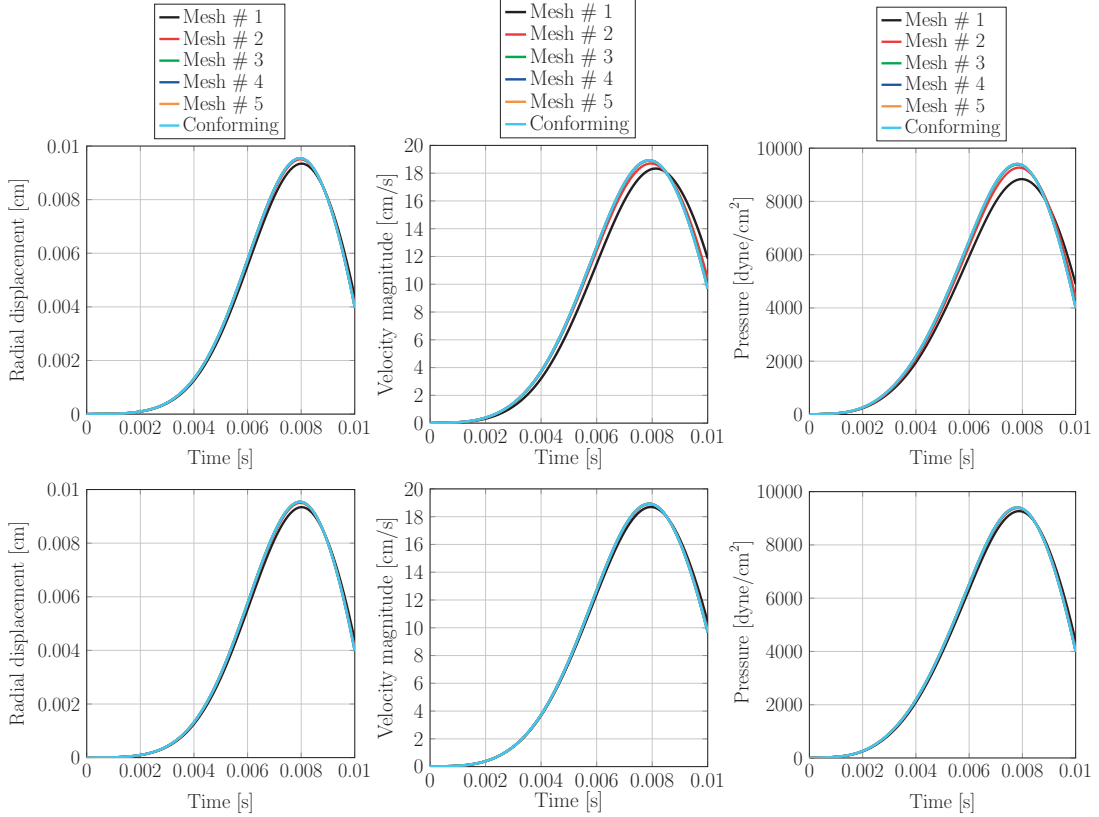
Figure 6.3: On the top we show the locations where results are taken in the fluid ($\mathbf{P_F}$) and the structure ($\mathbf{P_S}$). From left to right we report the evolution of the radial component of the structure displacement at $\mathbf{P_S}$, the magnitude of the fluid velocity and the fluid pressure at $\mathbf{P_F}$. In the mid row we report the results for Set A while in the bottom row those generated with Set B.

6.5.2 Weak and strong scalability study of FaCSI in the nonconforming case

In this Section we are interested in studying the weak and strong scalability performance of FaCSI when nonconforming meshes are used at interface separating the fluid and structure domains. In addition, we aim at comparing the performace obtained in the nonconforming case with those reported in Section 3.7.1, where matching fluid- structure grids were considered. As in Section 3.7.1, the strong and weak scalability performance

of FaCSI are tested by solving the straight flexible tube example using the three sets of fluid-structure meshes already adopted in Section 3.7.1. For readers' convenience, in Tables 6.4 and 6.5 we report the details of the meshes adopted and the corresponding number of degrees of freedom of the discretized FSI problem. We point out that the nonconforming meshes have obtained by rotating the conforming ones, see Figure 6.4.

	Fluid		Structure	
	# Vertices	# Tetrahedra	# Vertices	# Tetrahedra
Mesh # 1	210'090	1'202'040	65'424	292'320
Mesh # 2	559'471	3'228'960	191'080	913'920
Mesh # 3	841'341	4'880'640	300'456	1'497'600

Table 6.4: Details of the meshes used for the straight cylinder example.

	Fluid DoF	Structure DoF	Coupling DoF	Geometry DoF	Total
Mesh # 1	5'134'050	1'369'030	195'576	4'923'960	11'622'616
Mesh # 2	13'728'971	4'119'980	456'114	13'169'500	31'474'595
Mesh # 3	20'696'341	6'599'740	598'104	19'855'000	47'749'185

Table 6.5: Straight flexible tube test case: number of Degrees of Freedom (DoF).

(a) Mesh # 1, conforming case.

(b) Mesh # 1, nonconforming case.
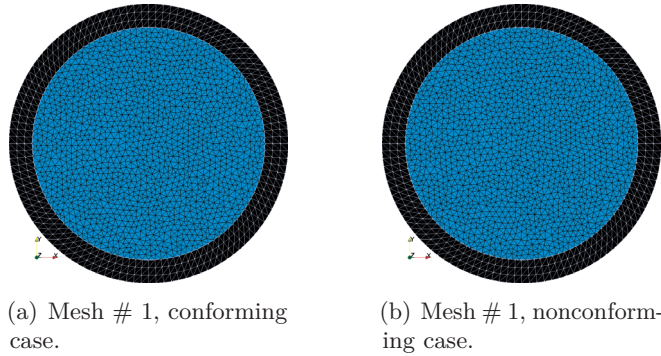
Figure 6.4: Front view of the conforming (left) and nonconforming (right) fluid–structure meshes used. With respect to the conforming case, in the nonconforming one we rotate the fluid meshes such that the fluid and structure interfaces are non-conforming.

Based on the scalability results reported in Section 3.7.1, here we configure FaCSI using SetC of Table 3.5. Specifically we make use of the AAS method for $\mathcal{H}_\mathcal{S}$, $\mathcal{H}_\mathcal{G}$, while the 3 level AMG method is used for $\mathcal{H}_{\mathcal{K}_{ii}}$ and $\mathcal{H}_{\widetilde{S}}$. We remark that the exact local subdomain solves for AAS as well as the exact coarse solve of the AMG preconditioner are carried out by LU factorization using the library MUMPS [Amestoy et al., 2001, Amestoy et al., 2006].

In Figure 6.5 and 6.6 we report the weak and strong scalability results obtained, respectively (consisting in average values over the first 10 time steps simulated). For the sake of

comparison, on the left column we report the weak scalability obtained in the conforming case while in the right column those with nonconforming discretizations.
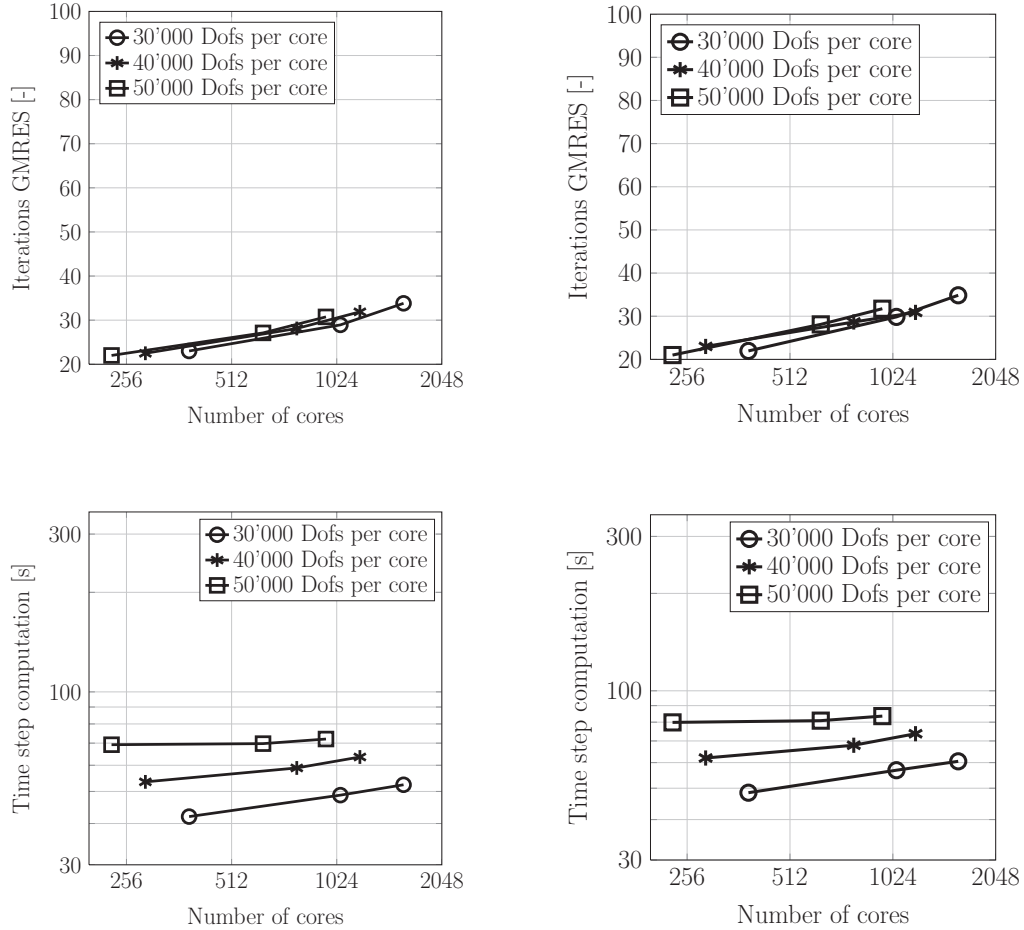
Figure 6.5: Weak scalability results: left column with conforming discretizations, right column using nonconforming discretizations.

By comparing the results with conforming and nonconforming fluid-structure interface discretizions, we notice that the weak scalability properties of FaCSI obtained in the nonconforming case are almost the same of those using conforming meshes. In particular, the iteration count only mildly depends on both the mesh size (along each curve the number of iterations vary from roughly 22 to 36 iterations) and the number of degrees of freedom per core since the three curves almost overlap. In terms of average time to complete a single time step, we notice that it is weakly scalable for a core workload of 50'000 Dofs while for 30'000 and 40'000 it increases with the cores count as the time spent by communication is larger than the actual one associated to the relatively small amount of computational work required on each individual core. We notice that dealing with nonconforming meshes yields an increase in computation time of approximately 15%. This is completely due, as already explained in Sections 6.3 and 6.4, to the intergrid interpolations which are carried out for both the application of the exact FSI jacobian
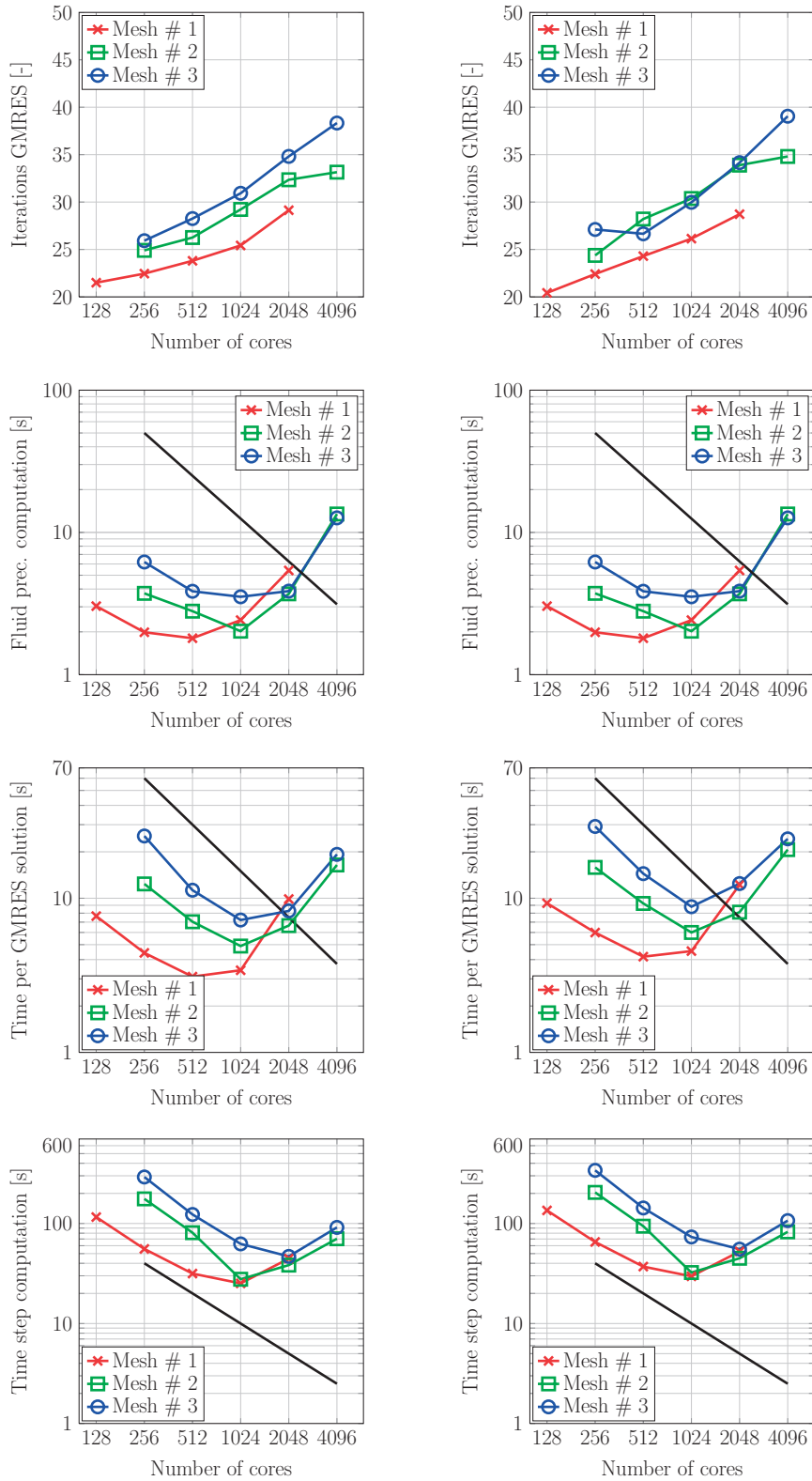
Figure 6.6: Strong scalability results: left column with conforming discretizations, right column using nonconforming discretizations.

matrix and the FaCSI preconditioner at each linear solver iteration.

We focus now on the strong scalability results reported in Figure 6.6. As already observed for the weak scalability study, the strong scalabity properties of FaCSI obtained with conforming discretizations are preserved in the nonconforming case. In particular, we notice that both the iterations count and the time to build the preconditioner are very similar in the conforming and nonconforming case. In terms of time to solve the linear system, we notice that dealing with nonconforming FSI discretizations increases the computational costs of about 15%. Finally, we notice that the time to complete a single time step increases of about the 15% too (as observed earlier in the weak scalability study) with respect to the conforming case as a consequence of the more computational expensive solution of the linear system.

6.5.3 Comparison with a dual mortar formulation for FSI with non-conforming interface discretizations

In this Section we compare the performance of the FSI solver implemented based on INTERNODES with those reported in [Klöppel et al., 2011], where the authors propose a dual mortar approach for fluid-structure interaction with non-conforming interface meshes. Specifically, they employ a dual mortar method [Wohlmuth, 2000, Puso, 2004, Lamichhane et al., 2005] with discrete Lagrange multipliers that are constructed based on a biorthogonality relation with the primal shape functions at the fluid-structure interface.

We compare the performance of our solver with the one used in [Klöppel et al., 2011] by numerically solving a fluid-structure interaction problem in a flexible tube. All the parameters used for setting-up the numerical example are those reported in [Klöppel et al., 2011]. In particular, the geometry of the fluid domain consists in a cylinder of length 10 cm and radius of 1cm. The fluid domain is sourrounded by a structure of constant thickness of 0.1 cm. The structure is modeled with a Neo-Hookean material law with Young's modulus $E = 10^6$ dyne/cm^2, Poisson's ratio $\nu = 0.3$ and density $\rho_s = 1.2$ g/cm^3. The fluid is characterized by a dynamic viscosity $\mu_f = 0.03$ g/(cm s) and density $\rho_f = 1.0$ g/cm^3. A normal stress of 10000 dyne/cm^2 is applied at the fluid inflow for $t < 0.003$ s.

To carry out the comparison with [Klöppel et al., 2011] (in which hexahedral elements were used, whereas we use tetrahedra) we solve the FSI problem using computational fluid and structure meshes which, after discretization, yield approximately the same number of degrees of freedom reported in [Klöppel et al., 2011]. In Tables 6.6 and 6.7 we report the number of degrees of freedom of the discretized FSI problem used in [Klöppel et al., 2011] and in this work, respectively. We notice that, as in [Klöppel et al., 2011], the fluid mesh is generated such that the fluid and structure meshes overlap for approximately a

third of an element length. The stopping criterion for the Newton method, as well as the one used for the GMRES linear solver, are the same of [Klöppel et al., 2011].

Mesh	Fluid DoF	Structure DoF	Geometry DoF	Total
1	9'612	2'400	7'209	19'221
2	71'444	14'688	53'583	139'715
3	189'916	44'352	142'437	376'705
4	540'956	96'960	405'717	1'043'633

Table 6.6: Degrees of freedom for different discretizations of the FSI problem, see Table 1 in [Klöppel et al., 2011].

Mesh	Fluid DoF	Structure DoF	Coupling DoF	Geometry DoF	Total
1	10'980	4'464	2'808	10'455	28'707
2	65'725	16'416	11'088	62'805	156'034
3	213'076	59'760	24'840	203'931	501'607
4	628'077	102'720	51'480	601'701	1'383'978

Table 6.7: Degrees of freedom for different discretizations of the FSI problem in our tests.

To compare the performance of INTERNODES with the ones reported in [Klöppel et al., 2011], computations are performed in parallel on up to 12 processors. The parallel performance are assessed by monitoring the average number of Newton iterations, of GMRES iterations and the average computation time per time step. The results obtained in [Klöppel et al., 2011] are reported in Table 6.8, while those generated using INTERNODES are shown in Table 6.9

By comparing the results reported in Table 6.8 and 6.9 we notice that the approach based on INTERNODES, for all the meshes used, leads to a number of linear solver iterations that is lower with respect to the dual mortar approach. As in [Klöppel et al., 2011], we point out that the preconditioner used here was simply carried over from the conforming case (see Section 6.4). Although in [Klöppel et al., 2011] no information are reported regarding the computing machines on which the simulations were run, we observe that the average computational time spent to complete a single time step is smaller using INTERNODES than the dual mortar technique by approximately a 15% (here the simulations were run on a single node of the PizDora supercomputer at CSCS, see Table 1.4).

Finally, for the sake of visualization, in Figure 6.7 we show the deformed configuration of the flexible tube at time $t = 0.01$ s: we notice that is in very good agreement with the result illustrated in Figure 8 of [Klöppel et al., 2011].

Mesh	# proc	Newton	GMRES	Time
1	4	2.97	36.1	6.09
2	8	2.98	32.8	27.1
3	12	2.97	37.1	50.68
4	12	2.78	42.7	121.68

Table 6.8: Performance of the FSI solver used in [Klöppel et al., 2011], see Table 2 rows marked with NC.

Mesh	# proc	Newton	GMRES	Time
1	4	2.86	20.7	4.55
2	8	2.86	20.8	17.62
3	12	2.88	20.9	43.43
4	12	2.91	23.3	101.85

Table 6.9: Performance of the FSI solver based on INTERNODES.
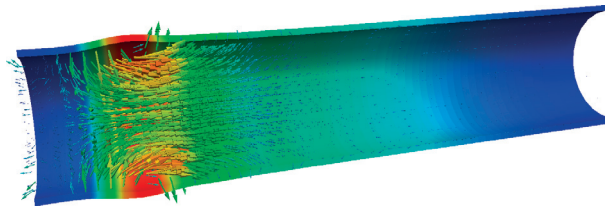
Figure 6.7: Deformed fluid-structure configuration at time $t =0.01$ s. Structure colored by the magnitude of the solid displacement; arrows are used to visualize the fluid velocity field.

6.5.4 FSI in a patient-specific femoropopliteal bypass

We consider a blood flow simulation in a patient–specific femoropopliteal bypass. To estimate accurately the Wall Shear Stress (WSS) distribution [Marchandise et al., 2012] in this example we consider a high-resolution fluid mesh which is much finer with respect to the structure grid. As a consequence, the structure mesh is nonconforming with respect to the one of the vessel wall, see Figure 6.8. The blood is characterized by a density $\rho_f = 1$ g/cm^3 and a dynamic viscosity $\mu_f = 0.0035$ $g/(cm\,s)$. The Young's modulus of the vessel wall is $E_s = 4 \times 10^6$ $dyne/cm^2$ and the Poisson's ratio is $\nu_s = 0.45$. The boundary conditions used for the simulation are the same described in Section 3.7.2, where conforming fluid-structure meshes were used. Based on the finding reported in Chapter 4, we discretize the solid displacement using $\mathbb{P}2$ finite elements. For the fluid, we use $\mathbb{P}1$-$\mathbb{P}1$ elements to approximated the velocity and pressure variables (stabilized by SUPG-VMS); $\mathbb{P}1$ elements are used for the ALE. Therefore, in this example we use both nonconforming meshes and nonconforming FE discretizations. The time step considered is $\Delta t = 0.001$ s. In Tables 6.10 and 6.11 we report the details of the meshes used and the number of degrees of freedom, respectively.

(a) Inlet (right) and occluded branch (left).   (b) Outlet.
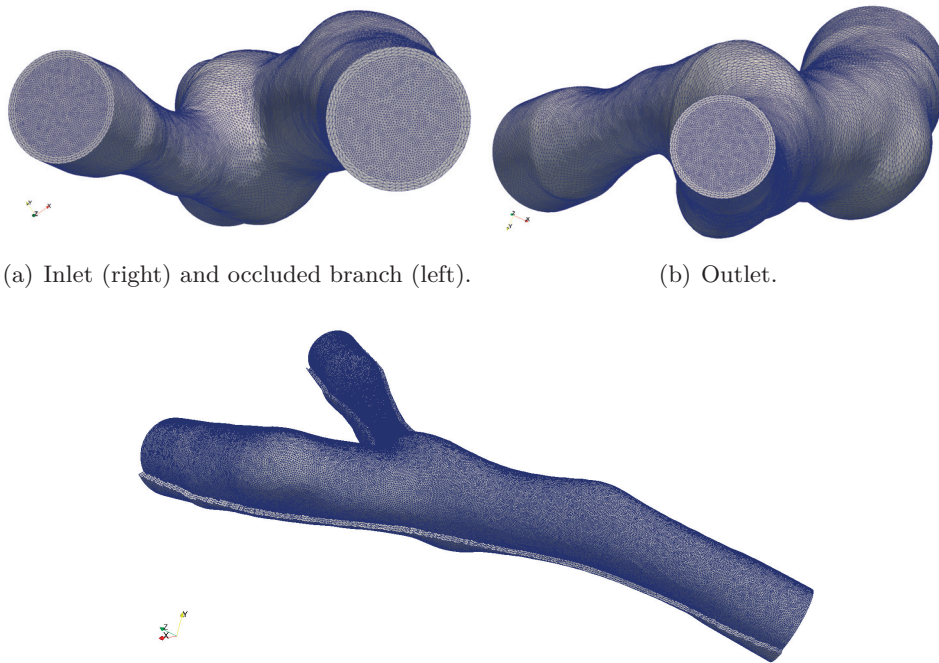
Figure 6.8: Meshes generated for the femoropopliteal bypass test case.

Fluid		Structure	
# Vertices	# Tetrahedra	# Vertices	# Tetrahedra
2'768'791	17'247'246	113'380	508'374

Table 6.10: Details of meshes used for the femoropopliteal bypass example in the nonconforming case.

Fluid DoF	Structure DoF	Coupling DoF	Geometry DoF	Total
11'075'164	9'481'350	943'170	8'306'373	29'806'057

Table 6.11: Number of degrees of freedom for femoropopliteal bypass test case in the nonconforming case.

In Figures 6.9, 6.10 and 6.11 we show the streamlines of the fluid flow, the structural displacement and the WSS distributions computed at three different time steps during the third heart-beat simulated. The results computed in the nonconforming case are also compared with those shown in Figure 3.12 generated using conforming interface discretizations. We notice that, although nonconforming meshes and discretizations are used here, both the WSS magnitude and distribution are in good agreement with the results obtained in Chapter 3 where conforming fluid-structure meshes were adopted.
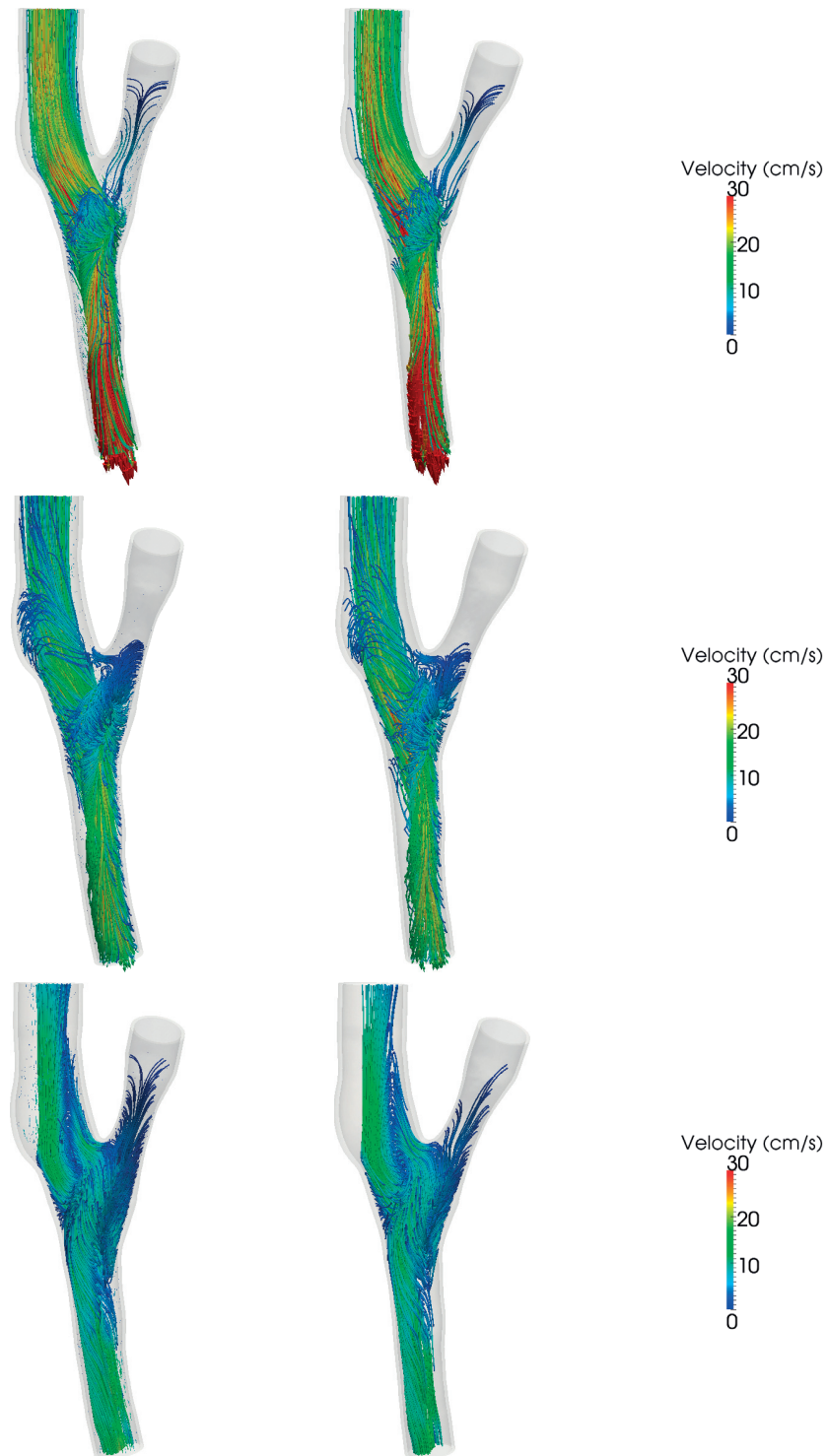
Figure 6.9: Streamlines of the fluid flow at time $t = 1.8$ s (top), 1.9 s (middle) and 2.0 s (bottom). In the left colums we report the results obtained in the conforming case (see Figure 3.12), on the right those generated using nonconforming discretizations.
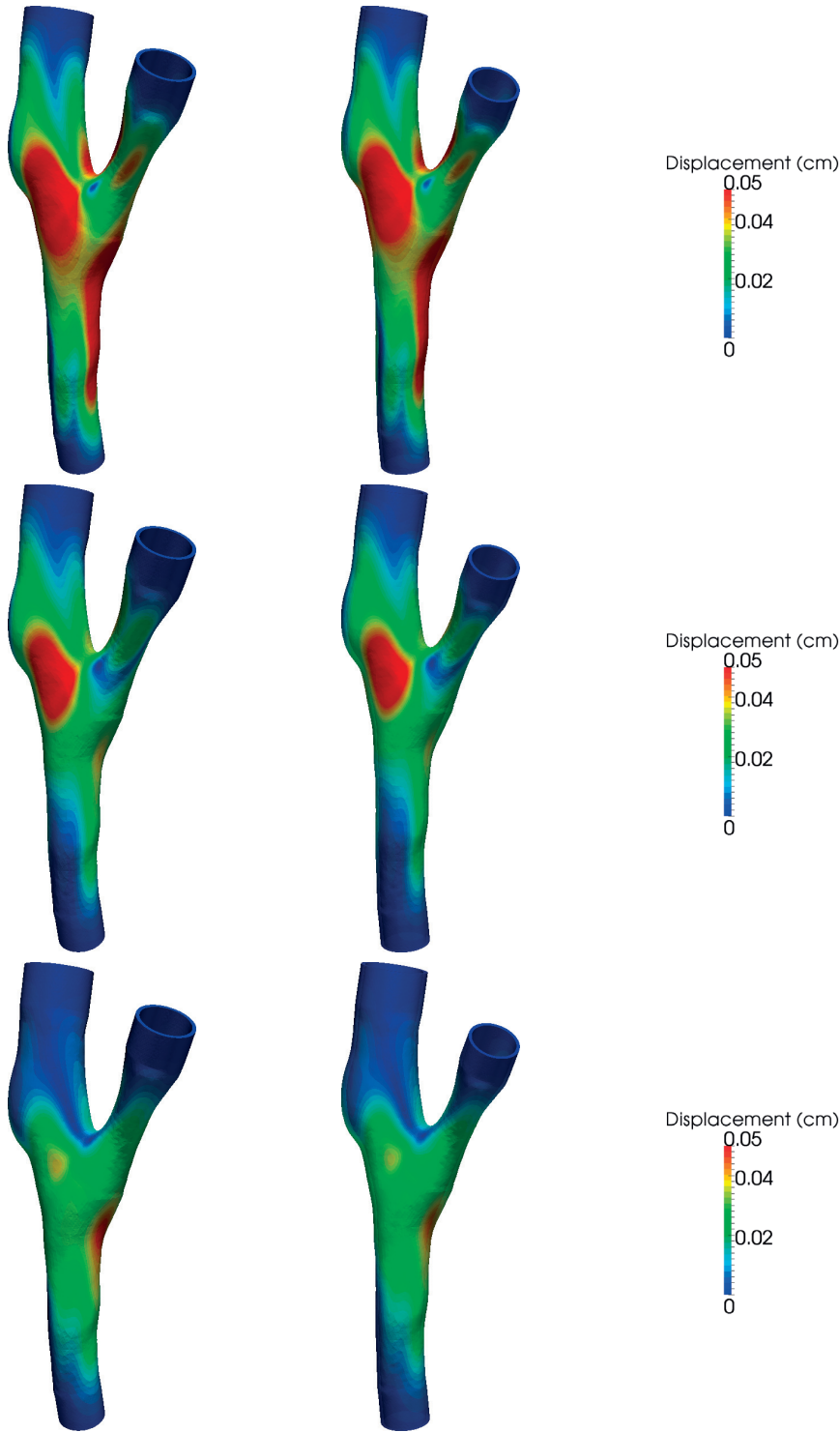
Figure 6.10: Magnitude of the structure displacement at time $t = 1.8$ s (top), 1.9 s (middle) and 2.0 s (bottom). In the left colums we report the results obtained in the conforming case (see Figure 3.12), on the right those generated using nonconforming discretizations.
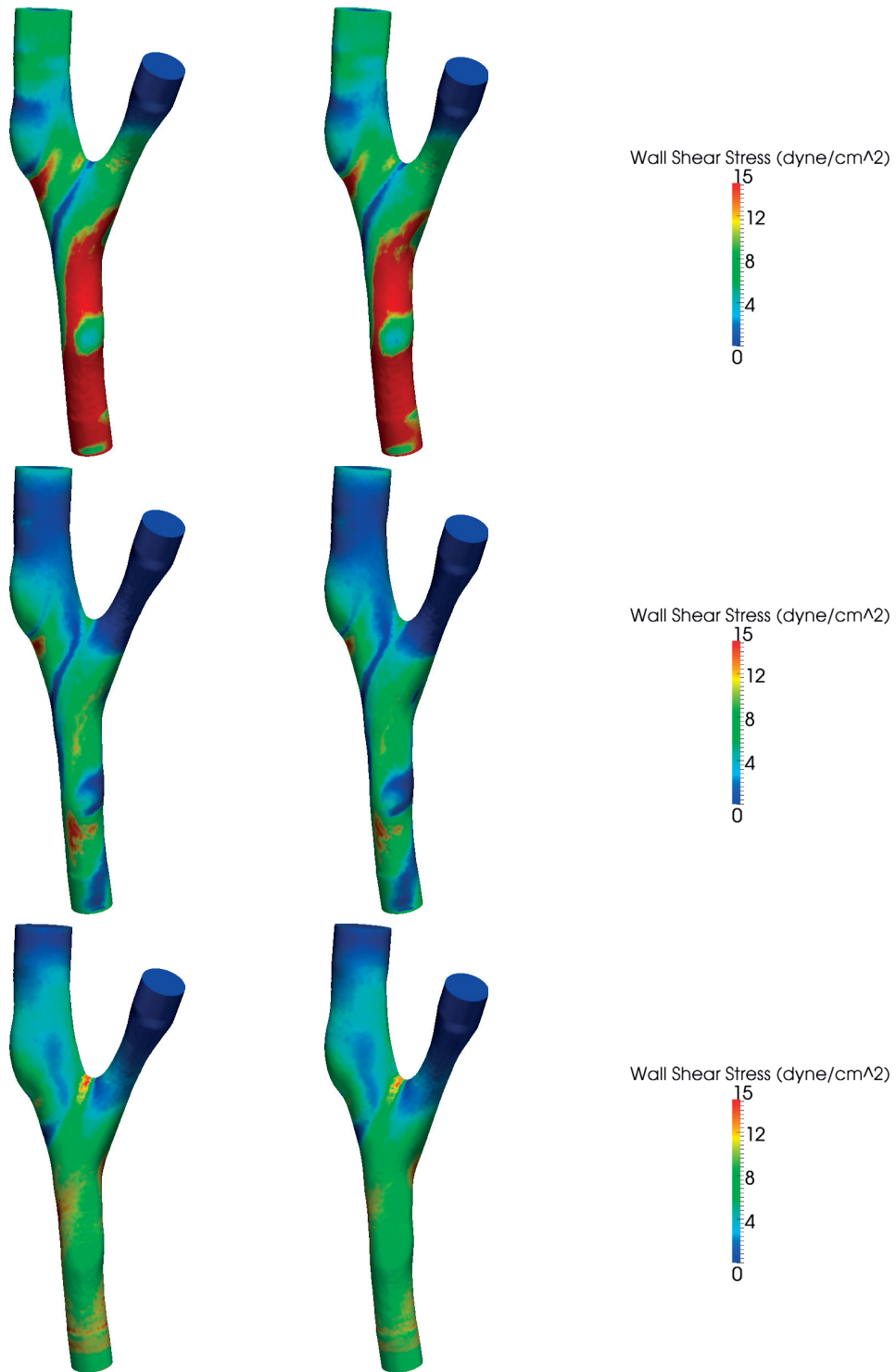
Figure 6.11: Wall Shear Stress at time $t = 1.8$ s (top), 1.9 s (middle) and 2.0 s (bottom). In the left colums we report the results obtained in the conforming case (see Figure 3.12), on the right those generated using nonconforming discretizations.
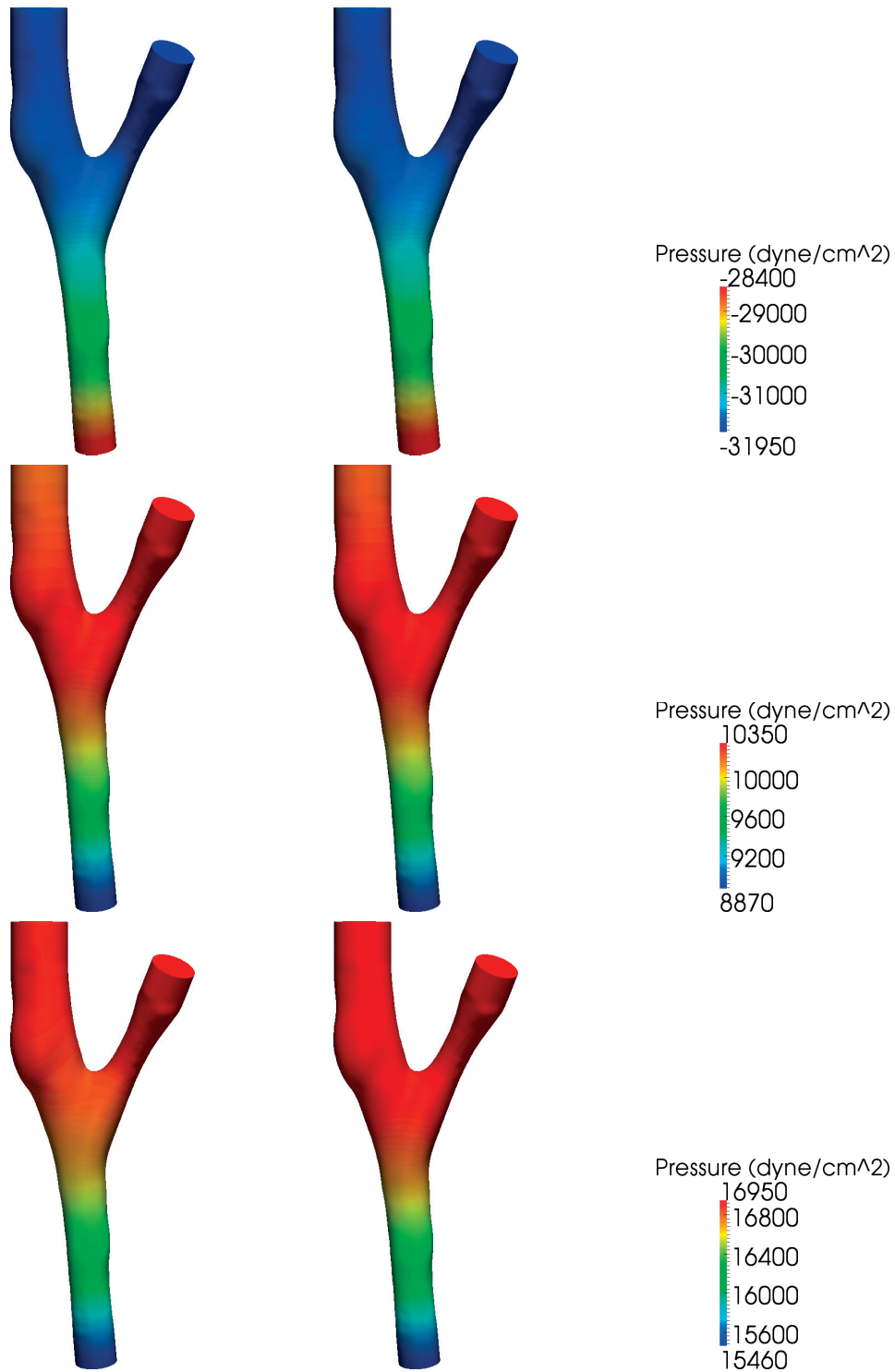
Figure 6.12: Fluid pressure at time $t = 1.8$ s (top), 1.9 s (middle) and 2.0 s (bottom). In the left colums we report the results obtained in the conforming case, on the right those generated using nonconforming discretizations.

7 Conclusions

In this thesis we addressed the development and implementation of efficient and parallel algorithms for the numerical simulation of large-scale fluid-structure interaction problems in hemodynamics. In the first Part we considered conforming fluid-structure discretizations at their common interface while in the second one we addressed the nonconforming case. The result is the development of a scalable fluid-structure interaction solver which can effectively be used to simulate complex problems in hemodynamics. This solver is *flexible and versatile* since it allows the use of nonconforming fluid-structure meshes with arbitrary discretizations. In addition, the algorithms devised allow for the *parallel* solution of FSI problems discretized with more than a hundred of millions degrees of freedom using thousands of cores on high performance computing machines. We report hereafter the main methodological contributions of this thesis.

- We proposed an efficient *semi-implicit time discretization* of the Navier-Stokes equations with Variational Multiscale-Large Eddy Simulation modeling. Thanks to linearization by Newton-Gregory backward polynomials, our approach yields only one linear system that has to be assembled and solved at each time step. In addition, to lower the computational costs of the numerical simulation, we developed a *parallel solver* based on the GMRES method preconditioned by an algebraic multigrid preconditioner.

- *INTERNODES*: we devise a new interpolation based method called INTERNODES for the numerical solution of partial differential equations on domains decomposed into several subdomains featuring nonconforming interfaces. The nonconforming problem was formulated in variational form as a generalized Galerkin problem

in which the intergrid operator for the data transfer across the nonconforming subdomain interfaces is based on interpolation. Two interpolants are used for transferring information across the interface: one from master to slave and another one from slave to master. The former is used to ensure continuity of the primal variable (the problem solution), while the latter for the dual variable (the normal flux). We extensively investigated the convergence properties of INTERNODES and we showed that the orders of convergence obtained by INTERNODES compare successfully with those generated by mortar.

- *FaCSI preconditioner*: we proposed a novel block preconditioner for fluid-structure interaction problems called FaCSI. It takes advantage of physics-specific ad-hoc preconditioners available for each subproblem (structure, geometry and fluid). An analysis of the strong and weak scalability properties of FaCSI was carried out by customizing it using different preconditioners (algebraic additive Schwarz and algebraic multigrid) for the structure, geometry and fluid problems. Our analysis showed that the most efficient choice consists in using the 1 level algebraic additive Schwarz preconditioners for the structure and geometry problems, together with the 3 level algebraic multigrid method for the fluid. In addition, we showed that the preconditioner FaCSI yields almost the same scalability performance regardless the use of conforming or nonconforming discretizations between the fluid and the structure at their interface.

High performance computing has maintained a central role in both the design and implementation of all the aforementioned techniques. All these methods have been instrumental to allow a very effective treatment of several benchmark cases and other more complex problems relevant for a wide range of engineering and physical applications in hemodynamics. In particular, the effectiveness of the solver implemented was demonstrated by tackling complex problems spanning different scenarios like the simulation of computational fluid dynamics at transitional and high Reynolds numbers in Chapter 1, and the simulation of fluid-structure interaction in patient-specific geometries using conforming (Chapter 3) and nonconforming interface discretizations (Chapter 6). In all these cases, our algorithms showed to be scalable up to thousands of cores utilized on high performance computing machines.

Perspectives and future work

The robust and parallel FSI solver developed in this thesis opens the way for studying more challenging hemodynamics problems in which more complex and detailed geometries may be taken in account. We plan to move towards the integration of our parallel solver in a geometrical multiscale framework, thus allowing the simulation of the arterial circulation throughout the whole arterial tree. In this regard, high-resolution 3D models will be used to numerically study the most critical zones while low dimensional models can be

exploited for the parts of the circulatory system which are not of primary interest.

One ongoing work focuses on extending algorithms developed to model the vessel wall as a composite multilayered structure. In [Bukac et al., 2016] we presented a monolithic computational model of FSI where the structure consists of two layers: a thin layer in direct contact with the fluid, and a thick layer sitting on top of the thin layer. The thin layer is treated using the membrane model proposed in [Figueroa et al., 2006, Colciago et al., 2014], while the thick layer is modeled using the equations of 3D linear elasticity. In addition to the composite structure described above, in this work we also varied the structure thickness and elasticity properties to capture the presence of atheroma, a fatty plaque tissue, associated with atherosclerosis. Furthermore in [Bukac et al., 2016] we addressed the numerical simulation of a diseased stented artery by allowing a change in the elastic properties of the thin structural layer where the stent struts are located.

From a numerical standpoint, the parallel algorithms for fluid-structure interaction devised in this thesis can be further extended, e.g., by exploiting adaptive time stepping as in [Mayr et al., 2015] in order to further reduce the computational effort of the simulations. Indeed, in this work the time discretization of the coupled FSI system was carried out by choosing a constant time step Δt throughout the whole simulation. In particular, the demanding high level of temporal accuracy forced the use of very small time step sizes. As a consequence, when the use of such small time steps is not required to maintain the desired level of accuracy throughout the entire simulation, this may lead to significant increase in computational costs. Conversely, an adaptive choice of the time step size may limit the overall computational time.

Bibliography

[hem, 2014] (2014). Hemolab. http://hemolab.lncc.br/adan-web.

[Akkerman et al., 2008] Akkerman, I., Bazilevs, Y., Calo, V. M., Hughes, T. J. R., and Hulshoff, S. (2008). The role of continuity in residual–based variational multiscale modeling of turbulence. *Computional Mechanics*, 41(3):371–378.

[Amestoy et al., 2001] Amestoy, P. R., Duff, I. S., Koster, J., and L'Excellent, J. Y. (2001). A fully asynchronous multifrontal solver using distributed dynamic scheduling. *SIAM Journal on Matrix Analysis and Applications*, 23(1):15–41.

[Amestoy et al., 2006] Amestoy, P. R., Guermouche, A., L'Excellent, J. Y., and Pralet, S. (2006). Hybrid scheduling for the parallel solution of linear systems. *Parallel Computing*, 32(2):136–156.

[Baaijens, 2001] Baaijens, F. P. T. (2001). A fictitious domain/mortar element method for fluid-structure interaction. *International Journal for Numerical Methods in Fluids*, 35(7):743–761.

[Badia et al., 2008a] Badia, S., Nobile, F., and Vergara, C. (2008a). Fluid-structure partitioned procedures based on Robin transmission conditions. *Journal of Computational Physics*, 227(14):7027–7051.

[Badia et al., 2009] Badia, S., Nobile, F., and Vergara, C. (2009). Robin-Robin preconditioned Krylov methods for fluid-structure interaction problems. *Computer Methods in Applied Mechanics and Engineering*, 198(33-36):2768–2784.

[Badia et al., 2008b] Badia, S., Quaini, A., and Quarteroni, A. (2008b). Modular vs. non-modular preconditioners for fluid-structure systems with large added-mass effect. *Computer Methods in Applied Mechanics and Engineering*, 197(49-50):4216–4232.

173

Bibliography

[Badia et al., 2008c] Badia, S., Quaini, A., and Quarteroni, A. (2008c). Splitting methods based on algebraic factorization for fluid-structure interaction. *SIAM Journal on Scientific Computing*, 30(4):1778–1805.

[Ball, 1977] Ball, J. (1977). Convexity conditions and existence theorems in non-linear elasticity. *Archive for Rational Mechanics and Analysis*, 63:337–403.

[Balzani, 2006] Balzani, D. (2006). *Polyconvex Anisotropic Energies and Modeling of Damage Applied to Arterial Walls*. Phd thesis, University Duisburg-Essen.

[Balzani et al., 2012] Balzani, D., Böse, D., Brands, D., Erbel, R., Klawonn, A., Rheinbach, O., and Schröder, J. (2012). Parallel simulation of patient-specific atherosclerotic arteries for the enhancement of intravascular ultrasound diagnostics. *Engineering Computations*, 29(8):888–906.

[Balzani et al., 2007a] Balzani, D., Brands, D., Klawonn, A., and Rheinbach, O. (2007a). Large-scale simulation of arterial walls: mechanical modeling. *Proceedings in Applied Mathematics and Mechanics*, 7(1):4020017–4020018. Special Issue: Sixth International Congress on Industrial Applied Mathematics (ICIAM07) and GAMM Annual Meeting, Zürich 2007.

[Balzani et al., 2010] Balzani, D., Brands, D., Klawonn, A., Rheinbach, O., and Schröder, J. (2010). On the mechanical modeling of anisotropic biological soft tissue and iterative parallel solution strategies. *Archive of Applied Mechanics*, 80(5):479–488.

[Balzani et al., 2015] Balzani, D., Deparis, S., Fausten, S., Forti, D., Heinlein, A., Klawonn, A., Quarteroni, A., Rheinbach, O., and Schröder, J. (2015). Numerical modeling of fluid-structure interaction in arteries with anisotropic polyconvex hyperelastic and anisotropic viscoelastic material models at finite strains. *International journal for Numerical Methods in Biomedical Engineering*. In press.

[Balzani et al., 2008] Balzani, D., Gruttmann, F., and Schröder, J. (2008). Analysis of thin shells using anisotropic polyconvex energy densities. *Computer Methods in Applied Mechanics and Engineering*, 197:1015–1032.

[Balzani et al., 2006a] Balzani, D., Neff, P., Schröder, J., and Holzapfel, G. A. (2006a). A polyconvex framework for soft biological tissues. Adjustment to experimental data. *International Journal of Solids and Structures*, 43(20):6052–6070.

[Balzani et al., 2007b] Balzani, D., Schröder, J., Brands, D., Klawonn, A., and Rheinbach, O. (2007b). Computer simulation of damage in overstretched atherosclerotic arteries. *Proceedings of ICCB 2007 - III. International Congress on Computational Bioengineering*, pages 209–214.

[Balzani et al., 2006b] Balzani, D., Schröder, J., and Gross, D. (2006b). Simulation of discontinuous damage incorporating residual stresses in circumferentially overstretched atherosclerotic arteries. *Acta Biomaterialia*, 2(6):609–618.

[Barker, 2009] Barker, A. T. (2009). *Parallel monolithic fluid-structure interaction algorithms with application to blood flow simulation*. PhD thesis, University of Colorado.

[Barker and Cai, 2010] Barker, A. T. and Cai, X.-C. (2010). Scalable parallel methods for monolithic coupling in fluid-structure interaction with application to blood flow modeling. *Journal of Computational Physics*, 229(3):642–659.

[Bavier et al., 2012] Bavier, E., Hoemmen, M., Rajamanickam, S., and Thornquist, H. (2012). Amesos2 and belos: Direct and iterative solvers for large sparse linear systems. *Scientific Programming*, 20(3):241–255.

[Bazilevs et al., 2007] Bazilevs, Y., Calo, V. M., Cottrell, J. A., Hughes, T. J. R., Reali, A., and Scovazzi, G. (2007). Variational multiscale residual–based turbulence modeling for large eddy simulation of incompressible flows. *Computer Methods in Applied Mechanics and Engineering*, 197(1–4):173–201.

[Bazilevs et al., 2008] Bazilevs, Y., Calo, V. M., Hughes, T. J. R., and Zhang, Y. (2008). Isogeometric fluid-structure interaction: theory, algorithms, and computations. *Computational Mechanics*, 43:3–37.

[Bazilevs et al., 2009a] Bazilevs, Y., Gohean, J. R., Hughes, T. J. R., Moser, R. D., and Zhang, Y. (2009a). Patient–specific isogeometric fluid-–structure interaction analysis of thoracic aortic blood flow due to implantation of the jarvik 2000 left ventricular assist device. *Computer Methods in Applied Mechanics and Engineering*, 198(45–46):3534–3550.

[Bazilevs et al., 2009b] Bazilevs, Y., Hsu, M.-C., Zhang, Y., Wang, W., Liang, X., Kvamsdal, T., Brekken, R., and Isaksen, J. G. (2009b). A fully-coupled fluid-structure interaction simulation of cerebral aneurysms. *Computational Mechanics*, 46(1):3–16.

[Bazilevs and Hughes, 2007] Bazilevs, Y. and Hughes, T. (2007). Weak imposition of dirichlet boundary conditions in fluid mechanics. *Computers & Fluids*, 36:12–26.

[Bazilevs et al., 2013a] Bazilevs, Y., Takizawa, K., and Tezduyar, T. (2013a). *Computational Fluid–Structure Interaction. Methods and Applications*. Wiley Series in Computational Mechanics. Wiley.

[Bazilevs et al., 2013b] Bazilevs, Y., Takizawa, K., and Tezduyar, T. E. (2013b). *Computational fluid-structure interaction: methods and applications*. John Wiley & Sons.

[Bearman and Obasaju, 1981] Bearman, P. and Obasaju, E. (1981). An experimental study of pressure fluctuations on fixed and oscillating square–section cylinders. *Journal of Fluid Mechanics*, 119:297–321.

[Becker and Rannacher, 2001] Becker, R. and Rannacher, R. (2001). An optimal control approach to a posteriori error estimation in finite element methods. *Acta Numerica*, 10:1–102.

Bibliography

[Bègue et al., 1989] Bègue, C., Bernardi, C., Debit, N., Maday, Y., Karniadakis, G. E., Mavriplis, C., and Patera, A. T. (1989). Nonconforming spectral element-finite element approximations for partial differential equations, in *Proceedings of the Eighth International Conference on Computing Methods in Applied Sciences and Engineering (Versailles, 1987). Computer Methods in Applied Mechanics and Engineering*, (1-3):109–125.

[Belgacem, 1999] Belgacem, F. B. (1999). The mortar finite element method with Lagrange multipliers. *Numerische Mathematik*, 84(2):173–197.

[Ben Belgacem et al., 2001] Ben Belgacem, F., Buffa, A., and Maday, Y. (2001). The mortar finite element method for 3d maxwell equations: first results. *SIAM Journal on Numerical Analysis*, 39(3):880–901.

[Ben Belgacem et al., 2003] Ben Belgacem, F., Chilton, L. K., and Seshaiyer, P. (2003). The hp-mortar finite-element method for the mixed elasticity and stokes problems. *Computers & Mathematics with Applications*, 46(1):35–55.

[Ben Belgacem et al., 1999] Ben Belgacem, F., Hild, P., and Laborde, P. (1999). Extension of the mortar finite element method to a variational inequality modeling unilateral contact. *Mathematical Models and Methods in Applied Sciences*, 9(02):287–303.

[Bernardi and Maday, 2000] Bernardi, C. and Maday, Y. (2000). Mesh adaptivity in finite elements using the mortar method. *Revue européenne des éléments finis*, 9(4):451–465.

[Bernardi et al., 1993] Bernardi, C., Maday, Y., and Patera, A. T. (1993). Domain decomposition by the mortar element method. In *Asymptotic and numerical methods for partial differential equations with critical parameters (Beaune, 1992)*, volume 384 of *NATO Adv. Sci. Inst. Ser. C Math. Phys. Sci.*, pages 269–286. Kluwer Acad. Publ., Dordrecht.

[Bernardi et al., 1994] Bernardi, C., Maday, Y., and Patera, A. T. (1994). A new nonconforming approach to domain decomposition: the mortar element method. In *Nonlinear partial differential equations and their applications. Collège de France Seminar, Vol. XI (Paris, 1989–1991)*, volume 299 of *Pitman Res. Notes Math. Ser.*, pages 13–51. Longman Sci. Tech., Harlow.

[Bernardi et al., 2004] Bernardi, C., Maday, Y., and Rapetti, F. (2004). *Discrétisations variationnelles de problèmes aux limites elliptiques*, volume 45 of *Mathématiques & Applications (Berlin) [Mathematics & Applications]*. Springer-Verlag, Berlin.

[Boehler, 1987] Boehler, J. (1987). Introduction to the invariant formulation of anisotropic constitutive equations. In Boehler, J., editor, *Applications of tensor functions in solid mechanics*, number 292 in Courses and Lectures of CISM, pages 13–30. Springer.

[Boffi et al., 2011] Boffi, D., Cavallini, N., and Gastaldi, L. (2011). Finite element approach to immersed boundary method with different fluid and solid densities. *Mathematical Models and Methods in Applied Sciences*, 21(12):2523–2550.

[Bouillault et al., 2003] Bouillault, F., Buffa, A., Maday, Y., and Rapetti, F. (2003). The mortar edge element method in three dimensions: application to magnetostatics. *SIAM Journal on Scientific Computing*, 24(4):1303–1327.

[Brands et al., 2008] Brands, D., Klawonn, A., Rheinbach, O., and Schröder, J. (2008). Modelling and convergence in arterial wall simulations using a parallel FETI solution strategy. *Computer Methods in Biomechanics and Biomedical Engineering*, 11:569–583.

[Brenan et al., 1989] Brenan, K. E., Campbell, S. L. V., and Petzold, L. R. (1989). *Numerical solution of initial-value problems in differential-algebraic equations.* North-Holland.

[Brivadis et al., 2015] Brivadis, E., Buffa, A., Wohlmuth, B. I., and Wunderlich, L. (2015). Isogeometric mortar methods. *Computer Methods in Applied Mechanics and Engineering*, 284:292–319.

[Buffa et al., 2001] Buffa, A., Maday, Y., and Rapetti, F. (2001). A sliding mesh-mortar method for a two dimensional eddy currents model of electric engines. *ESAIM: Mathematical Modelling and Numerical Analysis-Modélisation Mathématique et Analyse Numérique*, 35(2):191–228.

[Buhmann, 2003] Buhmann, M. D. (2003). *Radial basis functions: theory and implementations*, volume 12. Cambridge university press.

[Bukac et al., 2016] Bukac, M., Canic, S., Deparis, S., Forti, D., and Quaini, A. (2016). A monolithic approach to solving fluid-structure interaction between multilayered structures and incompressible, viscous fluids. Submitted.

[Čanić et al., 2006] Čanić, S., Hartley, C., Rosenstrauch, D., Tambača, J., Guidoboni, G., and Mikelić, A. (2006). Blood flow in compliant arteries: An effective viscoelastic reduced model, numerics, and experimental validation. *Annals of Biomedical Engineering*, 34(4):575–592.

[Canuto et al., 2006] Canuto, C., Hussaini, M. Y., Quarteroni, A., and Zang, T. A. (2006). *Spectral Methods. Fundamentals in Single Domains.* Springer, Heidelberg.

[Canuto et al., 2007] Canuto, C., Hussaini, M. Y., Quarteroni, A., and Zang, T. A. (2007). *Spectral Methods. Evolution to Complex Geometries and Applications to Fluid Dynamics.* Springer, Heidelberg.

[Caputo et al., 2013] Caputo, M., Chiastra, C., Cianciolo, C., Cutrì, E., Dubini, G., Gunn, J., Keller, B., Migliavacca, F., and Zunino, P. (2013). Simulation of oxygen transfer in stented arteries and correlation with in-stent restenosis. *International Journal for Numerical Methods in Biomedical Engineering*, 29(12):1373–1387.

Bibliography

[Causin et al., 2005] Causin, P., Gerbeau, J. F., and Nobile, F. (2005). Added-mass effect in the design of partitioned algorithms for fluid-structure problems. *Computer Methods in Applied Mechanics and Engineering*, 194(42-44):4506–4527.

[Cellier and Kofman, 2006] Cellier, F. E. and Kofman, E. (2006). *Continuous System Simulation*. Springer-Verlag New York, Inc., Secaucus, NJ, USA.

[Chandramouli, 2010] Chandramouli, R. (2010). *Textbook of Physiology*. Jaypee Brothers Medical Publishers, 3rd edition.

[Cho et al., 2005] Cho, Y.-S., Jun, S., Im, S., and Kim, H.-G. (2005). An improved interface element with variable nodes for non-matching finite element meshes. *Computer Methods in Applied Mechanics and Engineering*, 194(27):3022–3046.

[Codina, 2002] Codina, R. (2002). Stabilized finite element approximation of transient incompressible flows using orthogonal subscales. *Computer Methods in Applied Mechanics and Engineering*, 191(39–40):4295–4321.

[Codina et al., 2007] Codina, R., Principe, J., Guasch, O., and Badia, S. (2007). Time dependent subscales in the stabilized finite element approximation of incompressible flow problems. *Computer Methods in Applied Mechanics and Engineering*, 196(21–24):2413–2430.

[Colciago, 2014] Colciago, C. M. (2014). *Reduced Order Fluid-Structure Interaction Models for Hemodynamics Applications*. PhD thesis, Lausanne.

[Colciago et al., 2014] Colciago, C. M., Deparis, S., and Quarteroni, A. (2014). Comparisons between reduced order models and full 3d models for fluid–structure interaction problems in haemodynamics. *Journal of Computational and Applied Mathematics*, 265:120–138.

[Colomés et al., 2015] Colomés, O., Badia, S., Codina, R., and Principe, J. (2015). Assessment of variational multiscale models for the large eddy simulation of turbulent incompressible flows. *Computer Methods in Applied Mechanics and Engineering*, 285:32–63.

[Cottet et al., 2008] Cottet, G.-H., Maitre, E., and Milcent, T. (2008). Eulerian formulation and level set models for incompressible fluid-structure interaction. *Mathematical Modelling and Numerical Analysis*, 42(3):471–492.

[Cottrell et al., 2009] Cottrell, J. A., Hughes, T. J. R., and Bazilevs, Y. (2009). *Isogeometric Analysis. Towards Integration of CAD and FEA*. Wiley, Chichester.

[Crosetto, 2011] Crosetto, P. (2011). *Fluid-Structure Interaction Problems in Hemodynamics: Parallel Solvers, Preconditioners, and Applications*. PhD thesis, EPFL.

[Crosetto et al., 2011] Crosetto, P., Deparis, S., Fourestey, G., and Quarteroni, A. (2011). Parallel algorithms for fluid-structure interaction problems in haemodynamics. *SIAM Journal on Scientific Computing*, 33(4):1598–1622.

[De Boer et al., 2007] De Boer, A., Van Zuijlen, A. H., and Bijl, H. (2007). Review of coupling methods for non-matching meshes. *Computer Methods in Applied Mechanics and Engineering*, 196(8):1515–1525.

[De Lorenzis et al., 2012] De Lorenzis, L., Wriggers, P., and Zavarise, G. (2012). A mortar formulation for 3d large deformation contact using nurbs-based isogeometric analysis and the augmented lagrangian method. *Computational Mechanics*, 49(1):1–20.

[Dedè, 2007] Dedè, L. (2007). Optimal flow control for navier–stokes equations: drag minimization. *International Journal for Numerical Methods in Fluids*, 55(4):347–366.

[Degroote et al., 2009] Degroote, J., Bathe, K.-J., and Vierendeels, J. (2009). Performance of a new partitioned procedure versus a monolithic procedure in fluid–structure interaction. *Computers & Structures*, 87:793–801.

[Deparis et al., 2006a] Deparis, S., Discacciati, M., Fourestey, G., and Quarteroni, A. (2006a). Fluid-structure algorithms based on Steklov-Poincaré operators. *Computer Methods in Applied Mechanics and Engineering*, 195:5797–5812.

[Deparis et al., 2006b] Deparis, S., Discacciati, M., and Quarteroni, A. (2006b). A domain decomposition framework for fluid-structure interaction problems. In Groth, C. and Zingg, D., editors, *Computational Fluid Dynamics 2004*, pages 41–58. Springer Berlin Heidelberg.

[Deparis et al., 2015a] Deparis, S., Forti, D., Gervasio, P., and Quarteroni, A. (2015a). INTERNODES: an accurate interpolation-based method for coupling the Galerkin solutions of PDEs on subdomains featuring non-conforming interfaces. Submitted. Available as Mathicse technical report 21.2015.

[Deparis et al., 2015b] Deparis, S., Forti, D., Grandperrin, G., and Quarteroni, A. (2015b). FaCSI: A block parallel preconditioner for fluid-structure interaction in hemodynamics. Submitted. Available as Mathicse technical report 13.2015.

[Deparis et al., 2015c] Deparis, S., Forti, D., Heinlein, A., Klawonn, A., Quarteroni, A., and Rheinbach, O. (2015c). A comparison of preconditioners for the steklov-poincaré formulation of the fluid-structure coupling in hemodynamics. *Proceedings in Applied Mathematics and Mechanics*, 15:93–94.

[Deparis et al., 2014a] Deparis, S., Forti, D., and Quarteroni, A. (2014a). A Rescaled Localized Radial Basis Function Interpolation on Non-Cartesian and Nonconforming Grids. *SIAM Journal on Scientific Computing*, 36:A2745–A2762.

Bibliography

[Deparis et al., 2015d] Deparis, S., Forti, D., and Quarteroni, A. (2015d). A fluid-structure interaction algorithm using radial basis function interpolation between non-conforming interfaces. Accepted for publication as book Chapter in "Advances in Computational Fluid-Structure" (available as Mathicse report 16.2015).

[Deparis et al., 2014b] Deparis, S., Grandperrin, G., and Quarteroni, A. (2014b). Parallel preconditioners for the unsteady Navier–Stokes equations and applications to hemodynamics simulations. *Computers & Fluids*, 92:253 – 273.

[Dettmer and Perić, 2007] Dettmer, W. G. and Perić, D. (2007). A fully implicit computational strategy for strongly coupled fluid–solid interaction. *Archives of Computational Methods in Engineering*, 14(3):205–247.

[Dickopf and Krause, 2009] Dickopf, T. and Krause, R. (2009). Efficient simulation of multi-body contact problems on complex geometries: A flexible decomposition approach using constrained minimization. *International Journal for Numerical Methods in Engineering*, 77:1834–1862.

[Dubief and Delcayre, 2000] Dubief, Y. and Delcayre, F. (2000). On coherent-vortex identification in turbulence. *Journal of turbulence*, 1(1):11.

[Dunne, 2007] Dunne, T. (2007). *Adaptive Finite Element Approximation of Fluid-Structure Interaction Based on Eulerian and Arbitrary Lagrangian-Eulerian Variational Formulations*. PhD thesis, Ruprechts-Karls Universität Heidelberg.

[Ehrl et al., 2014] Ehrl, A., Popp, A., Gravemeier, V., and Wall, W. (2014). A dual mortar approach for mesh tying within a variational multiscale method for incompressible flow. *International Journal for Numerical Methods in Fluids*, 76(1):1–27.

[Elman et al., 2006] Elman, H., Howle, V. E., Shadid, J., Shuttleworth, R., and Tuminaro, R. (2006). Block preconditioners based on approximate commutators. *SIAM Journal on Scientific Computing*, 27(5):1651–1668.

[Elman et al., 2008] Elman, H., Howle, V. E., Shadid, J., Shuttleworth, R., and Tuminaro, R. (2008). A taxonomy and comparison of parallel block multi-level preconditioners for the incompressible Navier-Stokes equations. *Journal of Computational Physics*, 227(3):1790–1808.

[Faggiano and Antiga, 2015] Faggiano, E. and Antiga, L. (2015). An open-source tool for patient-specific fluid-structure vessel mesh generation. In preparation.

[Farhat et al., 1998] Farhat, C., Lesoinne, M., and Le Tallec, P. (1998). Load and motion transfer algorithms for fluid/structure interaction problems with non-matching discrete interfaces: Momentum and energy conservation, optimal discretization and application to aeroelasticity. *Computer Methods in Applied Mechanics and Engineering*, 157(1):95–114.

[Faucher and Combescure, 2003] Faucher, V. and Combescure, A. (2003). A time and space mortar method for coupling linear modal subdomains and non-linear subdomains in explicit structural dynamics. *Computer Methods in Applied Mechanics and Engineering*, 192(5):509–533.

[Fernández and Moubachir, 2003] Fernández, M. A. and Moubachir, M. (2003). An exact block-Newton algorithm for solving fluid-structure interaction problems. *C. R. Math. Acad. Sci. Paris*, 336(8):681–686.

[Fernández et al., 2015] Fernández, M. A., Mullaert, J., and Vidrascu, M. (2015). Generalized robin–neumann explicit coupling schemes for incompressible fluid-structure interaction: Stability analysis and numerics. *International Journal for Numerical Methods in Engineering*, 101(3):199–229.

[Figueroa et al., 2006] Figueroa, C. A., Vignon-Clementel, I. E., Jansen, K. E., Hughes, T. J. R., and Taylor, C. A. (2006). A coupled momentum method for modeling blood flow in three-dimensional deformable arteries. *Computer Methods in Applied Mechanics and Engineering*, 195(41):5685–5706.

[Fischer and Wriggers, 2005] Fischer, K. A. and Wriggers, P. (2005). Frictionless 2d contact formulations for finite deformations based on the mortar method. *Computational Mechanics*, 36(3):226–244.

[Flemisch et al., 2005] Flemisch, B., Puso, M. A., and Wohlmuth, B. I. (2005). A new dual mortar method for curved interfaces: 2D elasticity. *International Journal for Numerical Methods in Engineering*, 63(6):813–832.

[Formaggia et al., 2009] Formaggia, L., Quarteroni, A., and Veneziani, A., editors (2009). *Cardiovascular mathematics*, volume 1 of *MS&A. Modeling, Simulation and Applications*. Springer-Verlag Italia, Milan. Modeling and simulation of the circulatory system.

[Forti and Dedè, 2015] Forti, D. and Dedè, L. (2015). Semi–implicit BDF time discretization of the Navier–Stokes equations with VMS–LES modeling in High Performance Computing framework. *Computers & Fluids*, 117:168–182.

[Gamnitzer et al., 2010] Gamnitzer, P., Gravemeier, V., and Wall, W. A. (2010). Time-dependent subgrid scales in residual-based large eddy simulation of turbulent channel flow. *Computer Methods in Applied Mechanics and Engineering*, 199(13–16):819–827.

[Gear, 1971] Gear, C. (1971). Simultaneous numerical solution of differential-algebraic equations. *Circuit Theory, IEEE Transactions on*, 18(1):89–95.

[Gee et al., 2010] Gee, M. W., Küttler, U., and Wall, W. A. (2010). Truly monolithic algebraic multigrid for fluid-structure interaction. *International Journal for Numerical Methods in Engineering*, 26:52–72.

Bibliography

[Gee et al., 2006] Gee, M. W., Siefert, C. M., Hu, J. J., Tuminaro, R. S., and Sala, M. G. (2006). ML 5.0 smoothed aggregation user's guide. Technical Report SAND2006-2649, Sandia National Laboratories.

[Gerbeau and Vidrascu, 2003] Gerbeau, J. F. and Vidrascu, M. (2003). A quasi-Newton algorithm based on a reduced model for fluid-structure interaction problems in blood flows. *Mathematical Modelling and Numerical Analysis*, 37(4):631–647.

[Germano et al., 1991] Germano, M., Piomelli, U., Moin, P., and Cabot, W. H. (1991). A dynamic subgrid-scale eddy viscosity model. *Physics of Fluids A*, 3(7):1760–1765.

[Gerstenberger and Wall, 2008] Gerstenberger, A. and Wall, W. A. (2008). An extended finite element method/lagrange multiplier based approach for fluid–structure interaction. *Computer Methods in Applied Mechanics and Engineering*, 197(19):1699–1714.

[Gervasio et al., 2006] Gervasio, P., Saleri, F., and Veneziani, A. (2006). Algebraic fractional-step schemes with spectral methods for the incompressible navier–stokes equations. *Journal of Computational Physics*, 214(1):347–365.

[Ghia et al., 1982] Ghia, U., Ghia, K., and Shin, C. (1982). High-Re Solutions for Incompressible Flow Using the Navier-Stokes Equations and a Multigrid Method. *Journal of Computational Physics*, 48:387–411.

[Grandperrin, 2013] Grandperrin, G. (2013). *Parallel Preconditioners for Navier-Stokes Equations and Fluid-Structure Interaction Problems: Application to Hemodynamics*. Phd thesis, EPFL.

[Gravemeier et al., 2010] Gravemeier, V., Gee, M. W., Kronbichler, M., and Wall, W. A. (2010). An algebraic variational multiscale-–multigrid method for large eddy simulation of turbulent flow. *Computer Methods in Applied Mechanics and Engineering*, 199:853—-864.

[Gurtin, 1982] Gurtin, M. E. (1982). *An introduction to continuum mechanics*. Academic press.

[Heil, 2004] Heil, M. (2004). An efficient solver for the fully coupled solution of large-displacement fluid–structure interaction problems. *Computer Methods in Applied Mechanics and Engineering*, 193(1-2):1–23.

[Heil et al., 2008] Heil, M., Hazel, A. L., and Boyle, J. (2008). Solvers for large–displacement fluid–structure interaction problems: segregated versus monolithic approaches. *Computational Mechanics*, 43(1):91–101.

[Heroux et al., 2005] Heroux, M. A., Bartlett, R. A., Howle, V. E., Hoekstra, R. J., Hu, J. J., Kolda, T. G., Lehoucq, R. B., Long, K. R., Pawlowski, R. P., Phipps, E. T., Salinger, A. G., Thornquist, H. K., Tuminaro, R. S., Willenbring, J. M., Williams, A., and Stanley, K. S. (2005). An overview of the trilinos project. *ACM Transactions on Mathematical Software*, 31(3):397–423.

[Hoffman, 2005] Hoffman, J. (2005). Computation of mean drag for bluff body problems using adaptive DNS/LES. *SIAM Journal on Scientific Computing*, 27(1):184–207.

[Holzapfel and Gasser, 2001] Holzapfel, G. and Gasser, T. (2001). A viscoelastic model for fiber-reinforced composites at finite strains: continuum basis, computational aspects and applications. *Computer Methods in Applied Mechanics and Engineering*, 190:4379–4403.

[Holzapfel et al., 2000] Holzapfel, G., Gasser, T., and Ogden, R. (2000). A new constitutive framework for arterial wall mechanics and a comparative study of material models. *Journal of Elasticity*, 61:1–48.

[Holzapfel et al., 2002] Holzapfel, G. A., Stadler, M., and Schulze-Bauer, C. A. J. (2002). A layer-specific three-dimensional model for the simulation of balloon angioplasty using magnetic resonance imaging and mechanical testing. *Annals of biomedical engineering*, 30(6):753–767.

[Hron and Turek, 2006] Hron, J. and Turek, S. (2006). A monolithic fem/multigrid solver for an ALE formulation of fluid-structure interaction with applications in biomechanics. In Bungartz, H.-J. and Schäfer, M., editors, *Fluid-structure interaction*, volume 53 of *Lecture Notes in Computational Science and Engineering*, pages 146–170.

[Hsu et al., 2012] Hsu, M., Akkerman, I., and Bazilevs, Y. (2012). Wind turbine aerodynamics using ale–vms: validation and the role of weakly enforced boundary conditions. *Computational Mechanics*, 50:499–511.

[Hsu et al., 2010] Hsu, M. C., Bazilevs, Y., Calo, V. M., Tezduyar, T. E., and Hughes, T. J. R. (2010). Improving stability of stabilized and multiscale formulations in flow simulations at small time steps. *Computer Methods in Applied Mechanics and Engineering*, 199(13–16):828 – 840.

[Hughes, 1995] Hughes, T. J. R. (1995). Multiscale phenomena: Green's functions, the dirichlet-to-neumann formulation, subgrid scale models, bubbles and the origins of stabilized methods. *Computer Methods in Applied Mechanics and Engineering*, 127(1–4):387 – 401.

[Hughes, 2012] Hughes, T. J. R. (2012). *The finite element method: linear static and dynamic finite element analysis*. Courier Corporation.

[Hughes et al., 2005] Hughes, T. J. R., Calo, V. M., and Scovazzi, G. (2005). Variational and multiscale methods in turbulence. In Gutkowski, W. and Kowalewski, T. A., editors, *Mechanics of the 21st Century*, pages 153–163. Springer Netherlands.

[Hughes et al., 2000] Hughes, T. J. R., Mazzei, L., and Jansen, K. E. (2000). Large eddy simulation and the variational multiscale method. *Computing and Visualization in Science*, 3(1-2):47–59.

Bibliography

[Hughes et al., 2001a] Hughes, T. J. R., Mazzei, L., Oberai, A. A., and Wray, A. A. (2001a). The multiscale formulation of large eddy simulation: Decay of homogeneous isotropic turbulence. *Physics of Fluids*, 13(2):505–512.

[Hughes et al., 2001b] Hughes, T. J. R., Oberai, A. A., and Mazzei, L. (2001b). Large eddy simulation of turbulent channel flows by the variational multiscale method. *Physics of Fluids*, 13(6):1784–1799.

[Hughes et al., 2004] Hughes, T. J. R., Scovazzi, G., and Franca, L. P. (2004). *Multiscale and Stabilized Methods.* John Wiley & Sons, Ltd.

[Itskov and Ehret, 2009] Itskov, M. and Ehret, A. E. (2009). A universal model for the elastic, inelastic and active behaviour of soft biological tissues. *GAMM-Mitteilungen*, 32(2):221–236.

[Janssen and Wick, 2010] Janssen, B. and Wick, T. (2010). Block preconditioning with Schur complements for monolithic fluid-structure interactions. In *Proceedings of V European Conference on Computational Fluid Dynamics ECCOMAS CFD 2010*, Lisbon, Portugal,.

[Jeong and Hussain, 1995] Jeong, J. and Hussain, F. (1995). On the identification of a vortex. *Journal of Fluid Mechanics*, 285:69–94.

[Karypis et al., 1998] Karypis, G., Schloegel, K., and Kumar, V. (1998). METIS: A Software Package for Partitioning Unstructured Graphs, Partitioning Meshes, and Computing Fill-Reducing Orderings of Sparse Matrices. Technical report, Univ MN.

[Karypis et al., 2003] Karypis, G., Schloegel, K., and Kumar, V. (2003). ParMETIS: Parallel Graph Partitioning and Sparse Matrix Ordering library. Technical report, Univ MN.

[Kim et al., 1987] Kim, J., Moin, P., and Moser, R. D. (1987). Turbulence statistics in fully developed channel flow at low reynolds number. *Journal of Fluid Mechanics*, 177:133–166.

[Klawonn and Rheinbach, 2010] Klawonn, A. and Rheinbach, O. (2010). Highly scalable parallel domain decomposition methods with an application to biomechanics. *Zeitschrift für Angewandte Mathematik und Mechanik. Journal of Applied Mathematics and Mechanics*, 90(1):5–32.

[Klöppel et al., 2011] Klöppel, T., Popp, A., Küttler, U., and Wall, W. A. (2011). Fluid-structure interaction for non-conforming interfaces based on a dual mortar formulation. *Computer Methods in Applied Mechanics and Engineering*, 200:3111–3126.

[Koobus and Farhat, 2004] Koobus, B. and Farhat, C. (2004). A variational multiscale method for the large eddy simulation of compressible turbulent flows on unstructured meshes–application to vortex shedding. *Computer Methods in Applied Mechanics and Engineering*, 193(15–16):1367–1383.

184

[Ku, 1997] Ku, D. N. (1997). Blood flow in arteries. *Annual Review of Fluid Mechanics*, 29(1):399–434.

[Küttler et al., 2010] Küttler, U., Gee, M. W., Förster, C., Comerford, A., and Wall, W. A. (2010). Coupling strategies for biomedical fluid-structure interaction problems. *International Journal for Numerical Methods in Biomedical Engineering*, 26(3-4):305–321.

[Küttler and Wall, 2008a] Küttler, U. and Wall, W. A. (2008a). The dilemma of domain decomposition approaches in fluid-structure interactions with fully enclosed incompressible fluids. In Langer, U., Discacciati, M., Keyes, D., Widlund, O., and Zulehner, W., editors, *Domain Decomposition Methods in Science and Engineering XVII*, volume 60 of *Lecture Notes in Computational Science and Engineering*, pages 575–582. Springer Berlin Heidelberg.

[Küttler and Wall, 2008b] Küttler, U. and Wall, W. A. (2008b). Fixed-point fluid–structure interaction solvers with dynamic relaxation. *Computational Mechanics*, 43(1):61–72.

[Lamichhane et al., 2005] Lamichhane, B. P., Stevenson, R. P., and Wohlmuth, B. I. (2005). Higher order mortar finite element methods in 3d with dual lagrange multiplier bases. *Numerische Mathematik*, 102(1):93–121.

[Lamichhane and Wohlmuth, 2004] Lamichhane, P. B. and Wohlmuth, B. I. (2004). Mortar finite elements for interface problems. *Computing*, 72(3):333–348.

[Langer and Yang, 2012] Langer, U. and Yang, H. (2012). Domain decomposition solvers for some fluid-structure interaction problems. *Proceedings in Applied Mathematics and Mechanics*, 12(1):375–376.

[Langer and Yang, 2015] Langer, U. and Yang, H. (2015). Partitioned solution algorithms for fluid-structure interaction problems with hyperelastic models. *Journal of Computational and Applied Mathematics*, 276:47–61.

[Laursen et al., 2012] Laursen, T. A., Puso, M. A., and Sanders, J. (2012). Mortar contact formulations for deformable–deformable contact: past contributions and new extensions for enriched and embedded interface formulations. *Computer Methods in Applied Mechanics and Engineering*, 205:3–15.

[Le Tallec and Mouro, 2001] Le Tallec, P. and Mouro, J. (2001). Fluid structure interaction with large structural displacements. *Computer Methods in Applied Mechanics and Engineering*, 190:3039–3067.

[Lilly, 1992] Lilly, D. K. (1992). A proposed modification of the germano subgrid-scale closure method. *Physics of Fluids A*, 4(3):633–635.

Bibliography

[Lombardi et al., 2012] Lombardi, M., Parolini, N., Quarteroni, A., and Rozza, G. (2012). Numerical simulation of sailing boats: Dynamics, fsi, and shape optimization. In Buttazzo, G. and Frediani, A., editors, *Variational Analysis and Aerospace Engineering: Mathematical Challenges for Aerospace Design*, pages 339–377. Springer.

[Lyn et al., 1995] Lyn, D. A., Einav, S., Rodi, W., and Park, J. H. (1995). A laser-doppler velocimetry study of ensemble-averaged characteristics of the turbulent near wake of a square cylinder. *Journal of Fluid Mechanics*, 304:285–319.

[Maday et al., 1988] Maday, Y., Mavripilis, C., and Patera, A. T. (1988). Nonconforming mortar element methods: application to spectral discretizations. In T.F.Chan, R.Glowinski, J. and O.B.Widlund, editors, *Second International Conference on Domain Decomposition Methods for Partial Differential Equations*, Philadelphia. SIAM.

[Maday et al., 2002] Maday, Y., Rapetti, F., and Wohlmuth, B. I. (2002). The influence of quadrature formulas in 2D and 3D mortar element methods. In *Recent developments in domain decomposition methods (Zürich, 2001)*, volume 23 of *Lect. Notes Comput. Sci. Eng.*, pages 203–221. Springer.

[Marchandise et al., 2012] Marchandise, E., Crosetto, P., Geuzaine, C., Remacle, J. F., and Sauvage, E. (2012). Quality open source mesh generation for cardiovascular flow simulations. In Ambrosi, D., Quarteroni, A., and Rozza, G., editors, *Modeling of Physiological Flows*, pages 395–414. Springer Milan.

[Masud and Calderer, 2009] Masud, A. and Calderer, R. (2009). A variational multiscale stabilized formulation for the incompressible navier–stokes equations. *Computational Mechanics*, 44(2):145–160.

[Matthies et al., 2006] Matthies, H. G., Niekamp, R., and Steindorf, J. (2006). Algorithms for strong coupling procedures. *Computer Methods in Applied Mechanics and Engineering*, 195(17-18):2028–2049.

[Mayer et al., 2010] Mayer, U. M., Popp, A., Gerstenberger, A., and Wall, W. A. (2010). 3d fluid–structure-contact interaction based on a combined xfem fsi and dual mortar contact approach. *Computational Mechanics*, 46(1):53–67.

[Mayr et al., 2015] Mayr, M., Klöppel, T., Wall, W. A., and Gee, M. W. (2015). A temporal consistent monolithic approach to fluid-structure interaction enabling single field predictors. *SIAM Journal on Scientific Computing*, 37(1):B30–B59.

[Michler et al., 2004] Michler, C., Hulshoff, S. J., Van Brummelen, E. H., and De Borst, R. (2004). A monolithic approach to fluid–structure interaction. *Computers & fluids*, 33(5):839–848.

[Mittal and Iaccarino, 2005] Mittal, R. and Iaccarino, G. (2005). Immersed boundary methods. In *Annual review of fluid mechanics. Vol. 37*, volume 37 of *Annu. Rev. Fluid Mech.*, pages 239–261. Annual Reviews, Palo Alto, CA.

[Mohrman and Heller, 2013] Mohrman, D. and Heller, L. J. (2013). *Cardiovascular Physiology*. McGraw Hill Professional, 8th edition.

[Moser et al., 1999] Moser, R. D., Kim, J., and Mansour, N. N. (1999). Direct numerical simulation of turbulent channel flow up to $Re_\tau = 590$. *Physics of Fluids*, 11(4):943–945.

[Newmark, 1959] Newmark, N. M. (1959). A method of computation for structural dynamics. *Journal of the Engineering Mechanics Division*, 85(3):67–94.

[Nicoud and Ducros, 1999] Nicoud, F. and Ducros, F. (1999). Subgrid-scale stress modelling based on the square of the velocity gradient tensor. *Flow, Turbulence and Combustion*, 62(3):183–200.

[Nobile., 2001] Nobile., F. (2001). *Numerical approximation of fluid-structure interaction problems with application to haemodynamics*. PhD thesis, EPFL.

[Nobile et al., 2014] Nobile, F., Pozzoli, M., and Vergara, C. (2014). Inexact accurate partitioned algorithms for fluid–structure interaction problems with finite elasticity in haemodynamics. *Journal of Computational Physics*, 273(0):598 – 617.

[Nobile and Vergara, 2008] Nobile, F. and Vergara, C. (2008). An effective fluid-structure interaction formulation for vascular dynamics by generalized Robin conditions. *SIAM Journal on Scientific Computing*, 30(2):731–763.

[Ogden, 1997] Ogden, R. W. (1997). *Non-linear elastic deformations*. Courier Corporation.

[Ogden and Holzapfel, 2006] Ogden, R. W. and Holzapfel, G. A. (2006). *Mechanics of biological tissue*. Springer-Verlag.

[Parolini and Quarteroni, 2005] Parolini, N. and Quarteroni, A. (2005). Mathematical models and numerical simulations for the america's cup. *Computer Methods in Applied Mechanics and Engineering*, 194(9):1001–1026.

[Patankar and Spalding, 1972] Patankar, S. V. and Spalding, D. B. (1972). A calculation procedure for heat, mass and momentum transfer in three dimensional parabolic flows. *International Journal of Heat and Mass Transfer*, 15:1787–1806.

[Pernice and Tocci, 2001] Pernice, M. and Tocci, M. D. (2001). A multigrid-preconditioned Newton-Krylov method for the incompressible Navier-Stokes equations. *SIAM Journal on Scientific Computing*, 23(2):398–418.

[Peskin, 2002] Peskin, C. S. (2002). The immersed boundary method. *Acta Numerica*, 11:479–517.

[Pope, 2000] Pope, S. B. (2000). *Turbulent flows*. Cambridge university press.

Bibliography

[Popp, 2012] Popp, A. (2012). *Mortar Methods for Computational Contact Mechanics and General Interface Problems.* PhD thesis, Technische Universität München, Münich.

[Popp et al., 2009] Popp, A., Gee, M. W., and Wall, W. A. (2009). A finite deformation mortar contact formulation using a primal–dual active set strategy. *International Journal for Numerical Methods in Engineering*, 79(11):1354–1391.

[Popp et al., 2010] Popp, A., Gitterle, M., Gee, M. W., and Wall, W. A. (2010). A dual mortar approach for 3d finite deformation contact with consistent linearization. *International Journal for Numerical Methods in Engineering*, 83(11):1428–1465.

[Popp et al., 2012] Popp, A., Wohlmuth, B. I., Gee, M. W., and Wall, W. A. (2012). Dual quadratic mortar finite element methods for 3d finite deformation contact. *SIAM Journal on Scientific Computing*, 34(4):B421–B446.

[Puso, 2004] Puso, M. A. (2004). A 3d mortar method for solid mechanics. *International Journal for Numerical Methods in Engineering*, 59(3):315–336.

[Puso and Laursen, 2003] Puso, M. A. and Laursen, T. A. (2003). Mesh tying on curved interfaces in 3d. *Engineering Computations*, 20(3):305–319.

[Puso and Laursen, 2004] Puso, M. A. and Laursen, T. A. (2004). A mortar segment-to-segment contact method for large deformation solid mechanics. *Computer methods in applied mechanics and engineering*, 193(6):601–629.

[Quarteroni, 2013] Quarteroni, A. (2013). *Numerical Models for Differential Problems.* 2nd edition. Series MS&A, Vol. 2. Springer, Milano.

[Quarteroni et al., 2007] Quarteroni, A., Sacco, R., and Saleri, F. (2007). *Numerical Mathematics.* 2nd edition. Texts in Applied Mathematics. Springer-Verlag, Berlin.

[Quarteroni and Valli, 1994] Quarteroni, A. and Valli, A. (1994). *Numerical approximation of partial differential equations.* Springer.

[Quarteroni and Valli, 1999] Quarteroni, A. and Valli, A. (1999). *Domain decomposition methods for partial differential equations.* Oxford University Press.

[Rannacher and Richter, 2010] Rannacher, R. and Richter, T. (2010). An adaptive finite element method for fluid-structure interaction problems based on a fully eulerian formulation. In et al., H.-J. B., editor, *Fluid Structure Interaction II*, pages 159–192. Springer-Verlag Berlin Heidelberg. Lecture Notes in Computational Science and Engineering 73.

[Rao, 2009] Rao, G. (2009). *Numerical Analysis.* New Age International Publishers.

[Rapetti et al., 2000] Rapetti, F., Bouillault, F., Santandrea, L., Buffa, A., Maday, Y., and Razek, A. (2000). Calculation of eddy currents with edge elements on non-matching grids in moving structures. *Magnetics, IEEE Transactions on*, 36(4):1351–1355.

[Reymond et al., 2013] Reymond, P., Crosetto, P., Deparis, S., Quarteroni, A., and Stergiopulos, N. (2013). Physiological simulation of blood flow in the aorta: comparison of hemodynamic indices as predicted by 3-d fsi, 3-d rigid wall and 1-d models. *Medical engineering & physics*, 35(6):784–791.

[Rheinbach, 2009] Rheinbach, O. (2009). Parallel iterative substructuring in structural mechanics. *Archives of Computational Methods in Engineering. State of the Art Reviews*, 16(4):425–463.

[Richter, 2010] Richter, T. (2010). A fully eulerian formulation for fluid–structure–interaction problems with large deformations and free structure movement. In *Proceedings of the V European Conference on Computational Fluid Dynamics ECCOMAS CFD 2010*, Lisbon, Portugal, 14-17 June 2010.

[Richter, 2013] Richter, T. (2013). A fully eulerian formulation for fluid–structure-interaction problems. *Journal of Computational Physics*, 233:227–240.

[Robertson et al., 2009] Robertson, A. M., Sequeira, A., and Owens, R. G. (2009). Rheological models for blood. In Formaggia, L., Quarteroni, A., and Veneziani, A., editors, *Cardiovascular Mathematics*, volume 1 of *MS&A*, pages 211–241. Springer-Verlag.

[Rodi et al., 1997] Rodi, W., Ferziger, J., Breuer, M., and Pourquié, M. (1997). Status of large eddy simulation: Results of a workshop. *Journal of fluids engineering*, 119(2):248–262.

[Saad and Schultz, 1986] Saad, Y. and Schultz, M. H. (1986). GMRES: a generalized minimal residual algorithm for solving nonsymmetric linear systems. *SIAM Journal on Scientific and Statistical Computing*, 7(3):856–869.

[Sagaut, 2006] Sagaut, P. (2006). *Large eddy simulation for incompressible flows: an introduction.* Springer Science & Business Media, 3 edition.

[Sala and Heroux, 2005] Sala, M. and Heroux, M. (2005). Robust algebraic preconditioners with IFPACK 3.0. Technical report, Sandia National Laboratories.

[Sansour, 2008] Sansour, C. (2008). On the physical assumptions underlying the volumetric-isochoric split and the case of anisotropy. *European Journal of Mechanics A/Solids*, 27:28–39.

[Schäfer and S.Turek, 1996] Schäfer, M. and S.Turek (1996). Benchmark computations of laminar flow around a cylinder. In Hirschel, E., editor, *Flow Simulation with High-Performance Computers II. DFG priority research program results 1993-1995, number 52 in Notes Numer. Fluid Mech.*, pages 547–566. Vieweg, Weisbaden.

[Schröder and Neff, 2003] Schröder, J. and Neff, P. (2003). Invariant formulation of hyperelastic transverse isotropy based on polyconvex free energy functions. *International Journal of Solids and Structures*, 40:401–445.

[Schröder et al., 2004] Schröder, J., Neff, P., and Balzani, D. (2004). A variational approach for materially stable anisotropic hyperelasticity. *International Journal of Solids and Structures*, 42(15):4352–4371.

[Schröder et al., 2005] Schröder, J., Neff, P., and Balzani, D. (2005). A variational approach for materially stable anisotropic hyperelasticity. *International Journal of Solids and Structures*, 42(15):4352–4371.

[Sherwin and Karniadakis, 1995] Sherwin, S. and Karniadakis, G. (1995). A triangular spectral element method; applications to the incompressible Navier-Stokes equations. *Computer Methods in Applied Mechanics and Engineering*, 123:189–229.

[Simo, 1987] Simo, J. (1987). On a fully three-dimensional finite-strain viscoelastic damage model: formulation and computational aspects. *Computer Methods in Applied Mechanics and Engineering*, 60:153–173.

[Simo, 1998] Simo, J. (1998). Numerical analysis and simulation of plasticity. In Ciarlet, P. G. and Lions, J. L., editors, *Handbook of numerical analysis*, number 6. Elsevier Science.

[Simo and Hughes, 2006] Simo, J. C. and Hughes, T. J. R. (2006). *Computational inelasticity*, volume 7. Springer-Verlag.

[Smagorinsky, 1963] Smagorinsky, J. (1963). General circulation experiments with the primitive equations: I. the basic experiment*. *Monthly weather review*, 91(3):99–164.

[Sohankar et al., 2000] Sohankar, A., Davidson, L., and Norberg, C. (2000). Large eddy simulation of flow past a square cylinder: comparison of different subgrid scale models. *Journal of Fluids Engineering*, 122(1):39–47.

[Souli et al., 2000] Souli, M., Ouahsine, A., and Lewin, L. (2000). {ALE} formulation for fluid–structure interaction problems. *Computer Methods in Applied Mechanics and Engineering*, 190(5–7):659 – 675.

[Spiller et al., 1983] Spiller, P., Schmiel, F. K., Pölitz, B., Block, M., Fermor, U., Hackbarth, W., Jehle, J., Körfer, R., and Pannek, H. (1983). Measurement of systolic and diastolic flow rates in the coronary artery system by x-ray densitometry. *Circulation*, 68:337–347.

[Takizawa and Tezduyar, 2011] Takizawa, K. and Tezduyar, T. E. (2011). Multiscale space–time fluid–structure interaction techniques. *Computational Mechanics*, 48(3):247–267.

[Tezduyar and Sathe, 2003] Tezduyar, T. E. and Sathe, S. (2003). Stabilization parameters in supg and pspg formulations. *Journal of Computational and Applied Mechanics*, 4(1):71–88.

[Tezduyar and Sathe, 2007] Tezduyar, T. E. and Sathe, S. (2007). Modelling of fluid–structure interactions with the space–time finite elements: solution techniques. *International Journal for Numerical Methods in Fluids*, 54(6-8):855–900.

[Tezduyar et al., 2008] Tezduyar, T. E., Sathe, S., Schwaab, M., and Conklin, B. S. (2008). Arterial fluid mechanics modeling with the stabilized space–time fluid–structure interaction technique. *International Journal for Numerical Methods in Fluids*, 57(5):601–629.

[Tezduyar et al., 2006] Tezduyar, T. E., Sathe, S., and Stein, K. (2006). Solution techniques for the fully discretized equations in computation of fluid-structure interactions with the space-time formulations. *Computer Methods in Applied Mechanics and Engineering*, 195(41-43):5743–5753.

[Toselli and Widlund, 2005] Toselli, A. and Widlund, O. (2005). *Domain decomposition methods: algorithms and theory.* Springer.

[Tricerri, 2014] Tricerri, P. (2014). *Mathematical and Numerical Modeling of Healthy and Unhealthy Cerebral Arterial Tissues.* PhD thesis, Lausanne.

[ur Rehman et al., 2008] ur Rehman, M., Vuik, C., and Segal, G. (2008). Preconditioners for the steady incompressible Navier-Stokes problem. *International Journal of Applied Mathematics*, 38:223–232.

[ur Rehman et al., 2009] ur Rehman, M., Vuik, C., and Segal, G. (2009). SIMPLE-type preconditioners for the Oseen problem. *International Journal for Numerical Methods in Fluids*, 61:432–452.

[Van Brummelen, 2009] Van Brummelen, E. H. (2009). Added mass effects of compressible and incompressible flows in fluid-structure interaction. *Journal of Applied mechanics*, 76(2):021206–1–021206–7.

[Van Brummelen, 2011] Van Brummelen, E. H. (2011). Partitioned iterative solution methods for fluid–structure interaction. *International Journal for Numerical Methods in Fluids*, 65(1-3):3–27.

[Vorp et al., 1998] Vorp, D. A., Raghavan, M. L., and Webster, M. W. (1998). Mechanical wall stress in abdominal aortic aneurysm: Influence of diameter and asymmetry. *Journal of Vascular Surgery*, 27(4):632 – 639.

[Wall et al., 2006] Wall, W. A., Gerstenberger, A., Gamnitzer, P., Förster, C., and Ramm, E. (2006). Large deformation fluid-structure interaction–advances in ale methods and new fixed grid approaches. In *Fluid-structure interaction*, pages 195–232. Springer.

[Wall et al., 2010] Wall, W. A., Gerstenberger, A., Küttler, U., and Mayer, U. M. (2010). An XFEM based fixed-grid approach for 3d fluid-structure interaction. In et al.,

Bibliography

H.-J. B., editor, *Fluid Structure Interaction II*, pages 327–349. Springer-Verlag Berlin Heidelberg. Lecture Notes in Computational Science and Engineering 73.

[Wang et al., 2008] Wang, H., Chessa, J., Liu, W. K., and Belytschko, T. (2008). The immersed/fictitious element method for fluid-structure interaction: volumetric consistency, compressibility and thin members. *International Journal for Numerical Methods in Engineering*, 74(1):32–55.

[Wendland, 1995] Wendland, H. (1995). Piecewise polynomial, positive definite and compactly supported radial functions of minimal degree. *Advances in computational Mathematics*, 4(1):389–396.

[Wiesner, 2015] Wiesner, T. (2015). *Flexible Aggregation-based Algebraic Multigrid Methods for Contact and Flow Problems*. Phd thesis, Technische Universität München.

[Wohlmuth, 2000] Wohlmuth, B. I. (2000). A mortar finite element method using dual spaces for the Lagrange multiplier. *SIAM Journal on Numerical Analysis*, 38:989–1012.

[Wohlmuth and Krause, 2003] Wohlmuth, B. I. and Krause, R. (2003). Monotone multigrid methods on nonmatching grids for nonlinear multibody contact problems. *SIAM journal on scientific computing*, 25(1):324–347.

[Wu and Cai, 2014] Wu, Y. and Cai, X.-C. (2014). A fully implicit domain decomposition based ALE framework for three-dimensional fluid-structure interaction with application in blood flow computation. *Journal of Computational Physics*, 258:524–537.

[Zhao et al., 2008] Zhao, A. R., Field, M. L., Digges, K., and Richens, D. (2008). Blunt trauma and acute aortic syndrome: a three-layer finite-element model of the aortic wall. *European Journal of Cardio-Thoracic Surgery*, 34(3):623–629.

Davide Forti

Curriculum Vitae

Personal Information

Date of birth	July 13, 1987
Nationality	Italian
Status	Married
Place of birth	Gallarate (Varese)
Address	Rue de la Gare 20, 1131 Tolochenaz, Switzerland
E-mail	forti_d@hotmail.it

Work Experience

Nov. 2012 - Present **Doctoral Assistant**

Chair of Modeling and Scientific Computing, EPFL, Lausanne, Switzerland.

Education

Nov. 2012 - Present **Ph.D. student in Mathematics**

Ecole Polytechnique Fédérale de Lausanne

Laboratory Chair of Modeling and Scientific Computing

Thesis title "Parallel algorithms for the solution of large-scale fluid-structure interaction problems in hemodynamics"

Advisors Prof. Alfio Quarteroni, Dr. Simone Deparis

2009-2012 **Master of Science in Aeronautical Engineering (specialization in Structures)**.

Thesis title "Comparison of shape parametrization techniques for fluid-structure Interaction problems"

Advisors Prof. Alfio Quarteroni, Prof. Gianluigi Rozza

Grade 110/110

2006-2009 **Bachelor of Science in Aerospace Engineering**.

Thesis title "Dynamics and control of a quad-rotor helicopter"

Advisors Prof. Marco Lovera, Dr. Mara Tanelli

Grade 108/110

Publications

- D. Forti and G. Rozza. *Efficient geometrical parametrisation techniques of interfaces for reduced-order modelling: application to fluid-structure interaction coupling problems*. Int. J. Comput. Fluid D., 28(3-4), 158-169, 2014.

- S. Deparis, D. Forti, and A. Quarteroni. *A rescaled localized radial basis functions interpolation on non-Cartesian and non-conforming grids*. SIAM J. Sci. Comput. 36(5), A2745-A2762, 2014.

- D. Balzani, S. Deparis, S. Fausten, D. Forti, A. Heinlein, A. Klawonn, A. Quarteroni, O. Rheinbach and J. Schröder. *Aspects of Arterial Wall Simulations: Nonlinear Anisotropic Material Models and Fluid Structure Interaction*. In Proceedings of the WCCM XI conference, Barcelona, Spain, 2014.

- D. Forti and L. Dedè. *Semi–implicit BDF time discretization of the Navier-Stokes equations with VMS-LES modeling in High Performance Computing framework*. Comp. Fluids 117, 168–182, 2015.

- S. Deparis, D. Forti, and A. Quarteroni. *A fluid-structure interaction algorithm using radial basis function interpolation between non-conforming interfaces*. Accepted for publication as book Chapter In Y. Bazilevs, K. Takizawa (eds.) Advances in Computational Fluid-Structure, *Modeling and Simulation in Science, Engineering and Technology. Birkhäuser Basel, 2015*.

- S. Deparis, D. Forti, A. Heinlein, A. Klawonn, A. Quarteroni and O. Rheinbach. *A comparison of Preconditioners for the Steklov-Poincaré Formulation of the Fluid-Structure Coupling in Hemodynamics*. PAMM, 15(1), 93–94, 2015.

- D. Balzani, S. Deparis, S. Fausten, D. Forti, A. Heinlein, A. Klawonn, A. Quarteroni, O.Rheinbach and J. Schröder. *Numerical modeling of fluid-structure interaction in arteries with anisotropic polyconvex hyperelastic and anisotropic viscoelastic material models at finite strains*. Int. J. Numer. Method Biomed. Eng., In press, 2015.

- S. Deparis, D. Forti, G. Grandperrin and A. Quarteroni. *FaCSI: A Block Parallel Preconditioner for Fluid-Structure Interaction in Hemodynamics*. Submitted, 2015.

- S. Deparis, D. Forti, P. Gervasio, A. Quarteroni. *INTERNODES: an accurate interpolation-based method for coupling the Galerkin solutions of PDEs on subdomains featuring non-conforming interfaces*. Submitted, 2015.

- D. Forti, M. Bukac, A. Quaini, S. Canic, S. Deparis. *A monolithic approach to solving fluid-structure interaction between multilayered structures and incompressible, viscous fluids*. Submitted, 2016.

Conferences and workshops

- **Swiss Numerics Colloquium 2013**. Poster Session. EPFL, Lausanne, Switzerland. Poster session, April 5, 2013.

- **DD22**, 22nd International conference on Domain Decomposition Methods. Invited talk in a minisymposium. September 16-20, 2013. USI, Lugano, Switzerland.

- **EUROTUG 2014**, Contributed talk. Swiss National Supercomputing Center, Lugano, Switzerland. 30 June-1 July, 2014.

- **PDESoft 2014**, Contributed talk. Heidelberg, Germany. July 14-16, 2014.

- **43th SPEEDUP** Workshop on High Performance Computing. Poster session. University of Geneva, Geneva, Switzerland. September 4-5, 2014.

- **International workshop on numerical methods and applications in fluid-structure interactions**. Contributed talk. Laboratoire Jean Kuntzmann, Grenoble, France. November 24-25, 2014.

- **PASC15**, Platform of Advanced Scientific Computing Conference. Poster session. ETH, Zurich, Switzerland. June 1-3, 2015.

- **USNCCM13**, 13th U.S. National Congress on Computational Mechanics. Invited talk in a minisymposium. San Diego, California, United States. July 27-30, 2015.

Teaching activities

- **Teaching assistant** of the bachelor course *Analyse numérique* held by MER S. Deparis in the spring semester 2012-2013, 2013-2014, 2014-2015.

- **Teaching assistant** of the master course *Programming concepts in scientic computing* held by MER S. Deparis in the autumn semester 2013-2014, 2014-2015, and by Dr. G. Anciaux in the autumn semester 2015-2016.

- **Co-advisor of the master thesis** *FETI-DP Domain Decomposition method: application to the Navier-Stokes equations* by Christoph Jäggli. École Polithecnique Fédérale de Lausanne, 2014.

Supervision of the following semester projects
- *Computational Fluid Dynamics of Hydrofoils*, by Christian Kanesan, autumn semester 2013-2014.
- *HydroContest - Computational Fluid Dynamics of Hydrofoils*, by Fabio Stradelli, spring semester 2013-2014.
- *High Performance Computing of flows around hydrofoils*, by Raimondo Pictet, autumn semester 2014-2015.